
The Effects of Surface Condition on an Ultrasonic Inspection: Engineering Studies Using Validated Computer Model

Prepared by
M. S. Greenwood

Pacific Northwest National Laboratory

Prepared for
U.S. Nuclear Regulatory Commission

NUREG/CR-6589
PNNL-11751

The Effects of Surface Condition on an Ultrasonic Inspection: Engineering Studies Using Validated Computer Model

Manuscript Completed: October 1997
Date Published: April 1998

Prepared by
M. S. Greenwood

Pacific Northwest National Laboratory
Richland, WA 99352

D. Jackson, NRC Project Manager

Prepared for
Division of Engineering Technology
Office of Nuclear Regulatory Research
U.S. Nuclear Regulatory Commission
Washington, DC 20555-0001
NRC Job Code B2289 and W6275

DISCLAIMER

This report was prepared as an account of work sponsored by an agency of the United States Government. Neither the United States Government nor any agency thereof, nor any of their employees, makes any warranty, express or implied, or assumes any legal liability or responsibility for the accuracy, completeness, or usefulness of any information, apparatus, product, or process disclosed, or represents that its use would not infringe privately owned rights. Reference herein to any specific commercial product, process, or service by trade name, trademark, manufacturer, or otherwise does not necessarily constitute or imply its endorsement, recommendation, or favoring by the United States Government or any agency thereof. The views and opinions of authors expressed herein do not necessarily state or reflect those of the United States Government or any agency thereof.

Abstract

This report documents work performed at Pacific Northwest National Laboratory (PNNL) on the effects of surface roughness on the reliability of an ultrasonic inservice inspection. The primary objective of this research is to develop ASME Code recommendations in order to limit the adverse effects of a rough surface and thereby increase the reliability of ultrasonic inservice inspections. In order to achieve this objective engineering studies were conducted that included experimental validation of computer codes, developed at the Center for Nondestructive Evaluation (CNDE) at Iowa State University as a result of a cooperative effort between the Electric Power Research Institute (EPRI) and the Nuclear Regulatory Commission.

The basic problem associated with a rough surface in an inservice inspection is that, as the transducer rotates slightly to accommodate the rough surface, the beam direction in the metal changes and the time-of-flight of the echo changes as well. One problem is the excessive weld crown, where weld material protrudes above the adjoining surfaces. In this research this condition is modeled by considering a step discontinuity on the top surface. CNDE developed several models of increasing complexity in order to model an inservice inspection. This report describes the validation of four computer codes.

These codes were used to mimic an inservice inspection in order to understand effects associated with rotation of the transducer as it traverses a step discontinuity. Systematic engineering studies were conducted using these computer codes and as a result ASME Section XI Code recommendations were developed. Briefly, Recommendation I is that the wedge be tilted by no more than 5° . A 5° tilt of the transducer wedge results in the angle of the ultrasonic beam in steel changing from 45° to 60° . Recommendation II is that the angle of inclination of the transducer wedge on a wavy or blended surface be limited to 14° . This means that, for a 45° beam in steel, the angle can range from 31° up to 59° . Recommendation III is that the excessive weld crown should be reduced uniformly until flush with the adjacent surface or until the 5° limit stated in Recommendation I can be maintained. Also, for new welds and repair welds the method of contour grinding should not be used.

Contents

Abstract	iii
Executive Summary	xi
Acknowledgments	xiii
1 Introduction	1.1
2 Description of Computer Models	2.1
2.1 Model I	2.1
2.2 Model II	2.1
2.3 Model III and Model IV	2.1
3 Modeling an Ultrasonic Inservice Inspection	3.1
3.1 Introduction	3.1
3.2 Model Calculations	3.1
3.3 Case 1 Calculations	3.2
3.3.1 Smooth Surface	3.3
3.3.2 Varying the Flaw Location Relative to the Step	3.5
3.3.3 Flaw Close to Step	3.5
3.3.4 Flaw at Intermediate Distance	3.6
3.3.5 Flaw at a Greater Distance from Step	3.9
3.4 Case 2 Calculations	3.10
3.4.1 Conclusion	3.12
3.4.2 Additional Calculations for 80° and 85° Flaw Angle	3.14
3.4.3 Other Types of Inspections	3.14
3.5 Using a Slanted Surface Instead of a Step Discontinuity	3.16
3.6 No-Tilt Inspection	3.19
3.7 Maximum Angle of Tilt	3.21
3.8 Different Step Heights	3.22
3.9 Summary	3.22
4 Interference Effects Due to a Step Discontinuity in an Inservice Inspection	4.1
4.1 Introduction	4.1
4.2 Interference Effects: Calculations Using Toneburst Signal	4.1
4.3 Interference Effects: Input Signals with Large Bandwidth	4.3
4.4 Conclusions	4.6
4.5 Experiments Validating Interference Effects	4.6

Contents

5	Discussion and ASME Code Recommendations.....	5.1
5.1	Results of Computer Modeling Studies	5.1
5.2	ASME Code Recommendations	5.2
5.2.1	Wavy or Blended Surface	5.3
6	References	6.1
	Appendix A - Validation of Model I and Model II Codes.....	A.1
	Appendix B - Validation of Model III and Model IV Codes.....	B.I

Figures

1.1	Schematic diagram of the experimental set-up for comparing the pressure measured by the microprobe with the predictions of Model I.....	1.3
1.2	Schematic diagram of the experimental set-up for comparing the reflections from a perpendicular flaw with the predictions of Model II. The experimental apparatus is placed in an immersion tank, and the transducer is fastened to the arm of a laboratory x-y scanner	1.3
1.3	Schematic diagram of the experimental set-up for comparing the experimental pulse-echo measurements with the predictions of Model III. The transducer is placed on a plastic wedge and the flaw is perpendicular to the bottom surface	1.4
1.4	The experimental set-up is similar to Figure 1.3 except that the flaw can be at any angle relative to the bottom surface. The experimental measurements will be compared with the predictions of Model IV	1.5
2.1	Illustration of the four parts of the Model I computer code to describe the propagation of ultrasound: 1) from the transducer to the interface, 2) through the interface, 3) through the metal plate, and 4) through the bottom surface into the water. The analytical solutions are shown by the shaded regions and the arrows indicate the ray-tracing solutions	2.2
3.1	The five parts describing the motion of a transducer wedge across a step discontinuity	3.2
3.2a	Peak-to-peak amplitude versus the x-coordinate of the exit point (XW) for Case 1 for a smooth surface	3.4
3.2b	Peak-to-peak amplitude versus the x-coordinate of the central ray on the bottom surface (XBOTSUR) for Case 1 for a smooth surface.....	3.4
3.3	Response for a flaw located at 0.5 cm from the step.....	3.5
3.4	Response for a flaw located at 0.9 cm from the step.....	3.6
3.5	Response for a flaw located at 1.44 cm from the step.....	3.7
3.6	Response for a flaw located at 1.74 cm from the step.....	3.7
3.7a	Peak-to-peak amplitude versus the x-coordinate of the exit point (XW) for a flaw located at 2.04 cm from the step.....	3.8
3.7b	Peak-to-peak amplitude versus the x-coordinate of the central ray on the bottom surface (XBOTSUR) for a flaw located at 2.04 cm from the step	3.8
3.8	Response for a flaw located at 2.54 cm from the step.....	3.9
3.9	Response for a flaw located at 3.04 cm from the step.....	3.10
3.10	Response for a flaw located at 1.34 cm from the step for Case 2	3.12

Figures

3.11	Response for a flaw located at 1.64 cm from the step.....	3.13
3.12	Response for a flaw located at 2.24 cm from the step.....	3.13
3.13	Response for a flaw located at 2.54 cm from the step.....	3.14
3.14	Transducer wedge, traveling left to right, approaching a slanted section (stage 6)	3.16
3.15	Transducer wedge moving across the slanted section, but the central ray strikes the lower flat surface (stage 15)	3.17
3.16	Transducer wedge moving across the slanted section, but the central ray strikes the slanted surface (stage 18)	3.17
3.17	Transducer wedge rotating toward the top surface (stage 25).....	3.18
3.18	Transducer wedge moving on the top surface (stage 29).....	3.18
3.19	Response for a flaw located at 1.34 cm from the top of slanted surface	3.20
3.20	Response for a flaw located at 1.64 cm from the top of slanted surface	3.20
3.21	Response for a flaw located at 2.54 cm from the top of slanted surface	3.21
3.22	Response for a flaw located at 1.64 cm from the step during a no-tilt inspection	3.23
3.23	Response for a flaw located at 1.94 cm from the step during a no-tilt inspection	3.23
3.24	Response for a flaw located at 2.24 cm from the step during a no-tilt inspection.....	3.24
3.25	Response for a flaw located at 2.54 cm from the step during a no-tilt inspection	3.24
4.1	The steel plate has a thickness of 2.54 cm and the step height is 0.152 cm. The perpendicular flaw has a half-elliptical shape with a maximum depth of 0.254 cm and is 1.27 cm across the base. In the initial studies the transducer has a center frequency of 2.25 MHz and a diameter of 1.27 cm	4.1
4.2	Results of modeling calculations using a toneburst signal where the amplitude of the echo is plotted versus the step height. XW is 0.05 cm	4.2
4.3	Several types of signals that are used as input into the Model III code	4.3
4.4	Graph showing the fast Fourier transform of a signal having a center frequency of 2.25 MHz and a 20% bandwidth	4.4
4.5	Graph showing the fast Fourier transform of a signal having a center frequency of 2.25 MHz and an 88% bandwidth	4.4
4.6	Results of modeling calculations showing the variation in amplitude as a function of step height for four signals	4.5

4.7	Results of modeling calculations using a signal having a center frequency of 5.5 MHz and a 25% bandwidth	4.7
4.8	Results of modeling calculations using a signal having a center frequency of 5.2 MHz and a 31% bandwidth	4.8
4.9	Response from 0.152 cm step height using a toneburst signal. In (a) a gel couplant, such as Ultrigel II, was used and in (b) water (carbopol) was used as the couplant. The flaw and bottom surface are in air	4.10
4.10	Response from 0.229 cm step height using a toneburst signal. In (a) a gel couplant, such as Ultrigel II, was used and in (b) water (carbopol) was used as the couplant. The flaw and bottom surface are in air	4.11
4.11	Response from a 0.152 cm step height using a signal of short time duration. In (a) a gel couplant was used and in (b) water (carbopol) was used as the couplant. The flaw and bottom surface are in air	4.12
4.12	Response from a 0.229 cm step height using a signal of short time duration. In (a) a gel couplant was used and in (b) water (carbopol) was used as the couplant. The flaw and bottom surface are in air	4.13
5.1	Transducer on a wavy or blended surface	5.4

Tables

3.1	Parameters for each location in the scan	3.3
3.2	Maximum peak-to-peak amplitude for various locations of the flaw. The amplitude must be compared with the amplitude of 0.461 that was obtained for a smooth surface	3.10
3.3	Parameters for each stage in scan for Case 2	3.11
3.4	Maximum peak-to-peak amplitude for various flaw locations.....	3.15
3.5	Parameters for each stage where the surface has a slanted section rather than a step discontinuity	3.19
3.6	Parameters for each stage where the wedge moves vertically upward, for all stages NWANGST is 45.0° and TILTANG is 0.0°	3.22
3.7	Comparison of the tilt angle of the wedge and the resulting angle in steel for water and for the couplant Ultragel II	3.25
3.8	Summary of eight case studies for modeling an ultrasonic inservice inspection	3.26
4.1	Summary of results for CAA cases	4.6
4.2	Summary of results for WAA cases	4.6
4.3	Input signal parameters used in the calculations	4.7
4.4.	Peak-to-peak amplitude response obtained using Ultragel II and water and a toneburst signal and signal. with a larger bandwidth for various step heights. For each step height the first row gives the data obtained using an analog oscilloscope, while the second line is that obtained using a digital oscilloscope.	4.14
5.1	Maximum step height as a function of transducer wedge length	5.3

Executive Summary

The primary objective of this research is to develop ASME Code recommendations in order to limit the adverse effects of a rough surface and thereby increase the reliability of ultrasonic inservice inspections. In order to achieve this objective engineering studies were conducted that included experimental validation of computer codes, developed at the Center for Non-destructive Evaluation (CNDE) at Iowa State University as a result of a cooperative effort between the Electric Power Research Institute (EPRI) and the Nuclear Regulatory Commission (NRC). Once the computer models have been validated, they can be used as engineering tools to study the effect of surface conditions and then used as a basis to develop the ASME Code recommendations. Currently, there are no ASME Section XI Code requirements dealing with surface conditions during an ultrasonic inspection. A summary of the research and conclusions are as follows:

Computer Codes

- Model I describes the propagation of ultrasound through a steel plate with a step discontinuity on the top surface. This model predicts the pressure measured by a microprobe as it scans several millimeters from the bottom surface.
- Model II describes an immersion pulse-echo inspection in which the transducer and metal plate are placed in water. The ultrasound propagates through a rough top surface, through the metal, and is reflected by a perpendicular flaw on the bottom surface, where it returns to the transducer. Model II predicts the pulse-echo response of the transducer for a given transducer location.
- Model III describes a pulse-echo inspection in which the transducer is mounted on a wedge, which can traverse a rough top surface. A perpendicular flaw is located on the bottom surface.
- Model IV is very similar to Model III except that the flaw can be at any angle.

Computer Predictions and Experimental Results

- In experiments to validate Model I the ultrasound insonified three step discontinuities having depths of 0.152 cm (60 mils), 0.0762 cm (30 mils), and 0.0254 cm (10 mils). Data were obtained when the ultrasonic beam was normal to the top surface. By placing the beam at an angle to the top surface, 45° longitudinal and 45° shear waves were produced in the plate. The comparison between the experimental data and the theoretical calculations produced very good agreement.
- In experiments to validate Model II the ultrasound insonified a step discontinuity with a height of 0.152 cm. Data were obtained from three flaws having different depths and different distances from the step. Data were obtained using an eight-cycle toneburst and also a negative uni-polar pulse. Data were obtained using 45° shear waves and 45° longitudinal waves. There was good agreement between the experimental data and the theoretical curves. In addition, the theory showed the ability to produce the shape of the pulse obtained from a negative uni-polar pulse. In an experiment one can measure the amplitude of an echo for a smooth surface and when a step discontinuity is on the top surface. This ratio can be called $V_{\text{step}}/V_{\text{smooth}}$, which remains constant.
- In experiments to validate Model III a transducer wedge was mounted on the end of a scanning arm of an x-y scanner. The plate and transducer were placed in an immersion tank so that the base of the wedge was about 1 cm above the plate surface. The scanning arm could be rotated so that the wedge was tilted as it would be in an inservice inspection. Data were obtained during a scan in which the angle of tilt was constant. Data were obtained for 45° shear waves, 45° longitudinal waves, and 60° shear waves. The theoretical calculations were in very good agreement with the experimental data

Executive Summary

- for the 45° shear waves and 45° longitudinal waves, but in poor agreement for 60° shear waves. Data were also obtained for step heights of 0.229 cm (90 mils) and 0.305 cm (120 mils). Comparison of theoretical calculations with this data showed good agreement for a step height of 0.229 cm, but not for a step height of 0.305 cm.
- In experiments to validate Model IV the ends of steel blocks were cut at an angle to produce through-wall flaws having angles ranging from 79° through 101°. Pulse-echo measurements were obtained for this series of through-wall flaws and compared with theoretical predictions. The results showed very good agreement for angles 90° or less, but poor agreement for angles larger than 90°.
- In order to develop ASME Code recommendations Model III and Model IV were used to model a pulse-echo inservice inspection for 45° shear waves at 2.25 MHZ. The step height was 0.152 cm. The motion of the transducer wedge consisted of several steps: (1) the wedge approaches the step on a flat lower surface, (2) when the front of the wedge reaches the step, the front end rotates to the top of the step, (3) the wedge slides along the edge of the step until about half of its length transverses the step, (4) then, the wedge rotates to the top surface of the step, (5) the wedge moves along the top surface. The calculations were carried out for a variety of flaw shapes and couplants. In the calculations the flaw was located at different distances from the step to see where it might be most difficult to detect a flaw. The results showed that at some distance (depending upon the wedge length) a flaw could be seen only during step 2 (above). A flaw in this location would be difficult to detect. Flaws at other distances from the step could be seen during step 2, step 3, and step 5. The inspector needs to be aware of this. Otherwise, a single flaw might be recorded several times.
- The calculations to model an inservice inspection showed that, as the wedge is tilted, the angle of the beam in steel changes. When the wedge is tilted by about 5°, the angle in steel changes from 45° to 60°. For a reliable inspection this change in angle must be limited.
- There are two basic effects of the step. One is the tilt of the wedge just discussed. The other is that interference effects occur. For example, consider a transducer wedge located so that the central ray passes very close to the tip of the step (and the front end of the wedge is flat on the top surface of the step). In that case about half of the beam passes from the wedge directly into the steel. However, the other half passes through the couplant and then into the steel. These two partial beams can interfere constructively or destructively. Calculations were carried out for this situation, where the step height was varied in multiples of 0.007 cm. A graph of amplitude versus step height showed oscillatory behavior due to interference effects. These effects were also validated experimentally. These results show that a small step height can exhibit destructive interference as well as a larger step height.
- The ASME Code recommendations are as follows:
 - *Recommendation I:* The wedge should be tilted by no more than 5°. A 5° tilt of the transducer wedge results in the angle of the ultrasonic beam in steel changing from 45° to 60°.
 - *Recommendation II:* The angle of inclination of the transducer wedge on a wavy or blended surface should be limited to 14°. This means that, for a 45° beam in steel, the angle can range from 31° up to 59°.
 - *Recommendation III:* The excessive weld crown should be reduced uniformly until flush with the adjacent surface or until the 5° limit stated in Recommendation I can be maintained. Also, for new welds and repair welds the method of contour grinding should not be used.

Acknowledgments

This work is supported by the U.S. Nuclear Regulatory Commission under Contract DE-AC06-76RL0 1830; NRC JCN B2289 and W6275; Dr. Joseph Muscara, Mr. Allen Hiser, Jr., and Deborah A. Jackson, program monitors; Dr. Steve Doctor, PNNL program manager.

Dr. R. Bruce Thompson and Dr. Ali Minachi at CNDE at Iowa State University (ISU) provided information about the theoretical models and provided the UT modeling computer codes, enabling effective implementation of these codes at PNNL.

The Electric Power Research Institute provided support for the computer modeling at ISU. Dr. Mike Avioli and subsequently Mr. T. Thomas Taylor were the program monitors.

There are many people to thank who contributed to this work. Dr. Steve Doctor was the program manager and provided helpful suggestions about the experimental measurements. Dr. Morris S. Good introduced Margaret Greenwood to the research on surface roughness evaluation. He and Aaron A. Diaz performed several of the validation experiments. Jerry Posakony constructed the microprobes used in validation experiments for Model I. Bob Ferris was very helpful in setting up experiments using the laboratory x-y scanner. Josef L. Mai, a Science and Engineering Research Semester (SERS) appointee, assisted in the experimental measurements and analysis of data for validation of the Model I code. Catherine Mount, also a SERS appointee, assisted with validation of Model II. Scott McCloskey assisted in the validation of Model III and Model IV. Marsha Brehm and Kay Hass assisted in typing this report.

1 Introduction

This report summarizes work started as part of the surface-condition subtask of the Nuclear Regulatory Commission (NRC) program entitled "Evaluation and Improvement in the Nondestructive Evaluation (NDE) Reliability for Inservice Inspection (ISI) of Light Water Reactors" and was completed under the NRC program entitled "Assessment of the Reliability of UT and Improved Programs for ISI." The goal of these programs is to determine the reliability of current inservice inspection techniques and to develop recommendations that will ensure a suitably high inspection reliability. The objectives of this program include determining the reliability of ISI performed on the primary systems of commercial light-water reactors (LWRs); using probabilistic fracture mechanics analysis to determine the impact of NDE unreliability on the structural integrity of LWR components; and evaluating the reliability improvements that can be achieved with improved and advanced technology. A final objective is to formulate recommended revisions to regulatory and American Society of Mechanical Engineers (ASME) Code requirements. This final objective is the major goal of the surface-condition subtask that is to develop ASME Section XI Code recommendations to limit the adverse effect of surface conditions on an ultrasonic inspection to insure that nuclear reactor components are inspected reliably. Currently, there are no ASME Code requirements dealing with surface conditions for UT inspection.

The work reported herein is the result of the cooperative effort between The Center for Nondestructive Evaluation (CNDE) at Iowa State University, sponsored by Electric Power Research Institute (EPRI), and the Pacific Northwest National Laboratory (PNNL), funded by the NRC. CNDE developed several models of increasing complexity in order to model an inservice inspection. These models were experimentally validated at PNNL.

This task began in 1987 when Morris Good (Good 1987) investigated the severe problems caused by surface conditions. He obtained pulse-echo measurements from three 10% through-wall flaws, three 20% through-wall flaws, and two 50% through-wall flaws. The flaws were perpendicular notches machined into a steel plate having

a thickness of 1.67 cm. He measured the maximum response when the probe passed over a 1.5-mm step discontinuity, with the flaws located at different distances from the step. These measurements were compared with those obtained when the probe passed over a smooth top surface. The dB change in the two signals was determined. For a transducer having a diameter of 13 mm, the dB change ranged from -1 dB through -12 dB, depending upon the through-wall thickness and the distance from the notch to the step discontinuity. For a notch with a 10% through-wall thickness, changing the distance between the notch and the step discontinuity by 1.9 mm resulted in the dB change going from -1 dB to -12 dB. The results were also dependent upon the diameter of the transducer. A transducer having a diameter of 6 mm gave different values for the dB change than one with a diameter of 13 mm. The flaw location, the height and shape of the surface discontinuity, and the flaw characteristics would also affect the dB change. Therefore, it seemed impractical to study the effects of surface conditions experimentally, since so many parameters would have to be varied and the results are sensitive to small changes in these parameters.

In the same study Morris Good (Good 1987) reviewed the 1968, 1971, and 1986 versions of the ASME Section III Boiler and Pressure Vessel Code pertaining to circumferential welds in order to ascertain the surface conditions permitted. Most LWRs were constructed to the older Codes. He concludes:

"Therefore, no objective guidelines are given in the Code since surface condition remains to be a subjective judgment of the radiographer. It is conceivable, although not probable due to common sense and judgment, that an abrupt change of 4.8 mm exists in the field. Since a taper is required for allowable offsets, it is reasonable that welders and the authorized nuclear inspector would not accept an abrupt change until a significant reduction had been achieved; e.g., a factor of three. Thus, a 1.6-mm abrupt change might be expected to be common in both new construction since this results from 4.8 mm divided by 3 and old construction as stated earlier."

Introduction

Morris Good (Good 1990) identified a variety of surface conditions, primarily near welds in pipes, that will limit the ability to detect a flaw during an ultrasonic inspection:

- (1) Diametrical shrink, in which the circumferential weld has a smaller diameter than the pipe and deforms the original pipe material. The radius of curvature is formed by shrinkage of the weld metal during welding.
- (2) Excessive weld crown, where excessive weld material protrudes above the adjoining surfaces being welded together. This weld reinforcement, as it is commonly called, may be in the as-welded, partially ground, or blended ground state. Usually a step-like protrusion exists from a partially ground condition.
- (3) Weld splatter, in which welding material has splattered to and adhered to the pipe.
- (4) Over-ground condition, where the grinding operation, designed to blend the weld reinforcement into the pipe, typically makes a wavy surface along the pipe circumference. When a probe is applied to the surface, either a gap may exist under the probe or a convex surface may exist on which the probe may rock and pivot.

In order to study the effects of surface conditions systematically, the cooperative effort between CNDE at Iowa State University (sponsored by EPRI) and the Pacific Northwest National Laboratory (funded by the NRC) was established in 1987. The plan was to develop models of increasing sophistication and to validate these models experimentally.

The first step was to describe the propagation of ultrasound through a rough surface and into an isotropic metal. Model I is illustrated in Figure 1.1 for a step discontinuity. The object is to predict theoretically the pressure measured by the microprobe and to compare it with experimental measurements. The first validation experiments for longitudinal waves were carried out by Morris Good and Aaron Diaz in 1991. The comparison of the experimental data with the predictions of the theory have been reported (Minachi, Thompson, Good, and Diaz, 1991).

In 1991 Margaret Greenwood also became involved in the surface-conditions subtask. The basic problem associated with a rough surface in an ultrasonic inspection is that, as the transducer rotates slightly to accommodate the rough surface, the beam direction in the metal changes along with the challenge to maintain good acoustic coupling. To gain insight into this problem she (Greenwood 1991) developed a simple model to trace the path of the central ray of the transducer as the probe passed over a weld crown (or step discontinuity) on a steel pipe. It also served as an introduction to the sophisticated three-dimensional computer models, developed at CNDE. When the probe is tilted as it travels over a step discontinuity, the gel occupies the space between the probe and the horizontal steel surface. Since the speed of sound in the gel is smaller than that in steel or the plastic wedge, significant refraction occurs at the wedge-gel and gel-steel interfaces. Consider the situation in which a probe, 2.95 cm long and designed to produce 45° shear waves in steel, travels across a 1.5 mm step on a 1.5-cm thick pipe. The calculations show that, as the probe travels over the step discontinuity, the angle of the central ray with the vertical changes from 51° (due to the initial rotation to cross the step) to 54° (for greater inclination of the probe). Therefore, as a result of the rough surface, the angle of the central ray can change by as much as 9° in this example. In addition, the round-trip time for the central ray increases by as much as 20% compared to that when the probe is resting on a flat surface. The conclusions were: (1) the effect of the rotation results in some areas not being scanned effectively by the central ray of the transducer and (2) the response from a crack might suggest, due to the increased round-trip time, that the crack is positioned farther away than it actually is. Hence it will be harder to distinguish it from the root signal. Also, crack tip signals will be located farther away leading to systematic undersizing.

In November 1991 Greenwood, now the sub-task leader, began validation experiments for Model I, including investigations with longitudinal and shear waves. An overview of these results have been reported (Greenwood 1993).

After the successful validation of Model I, agreement was reached between PNNL and CNDE on the development of successive models. We agreed that the next level of

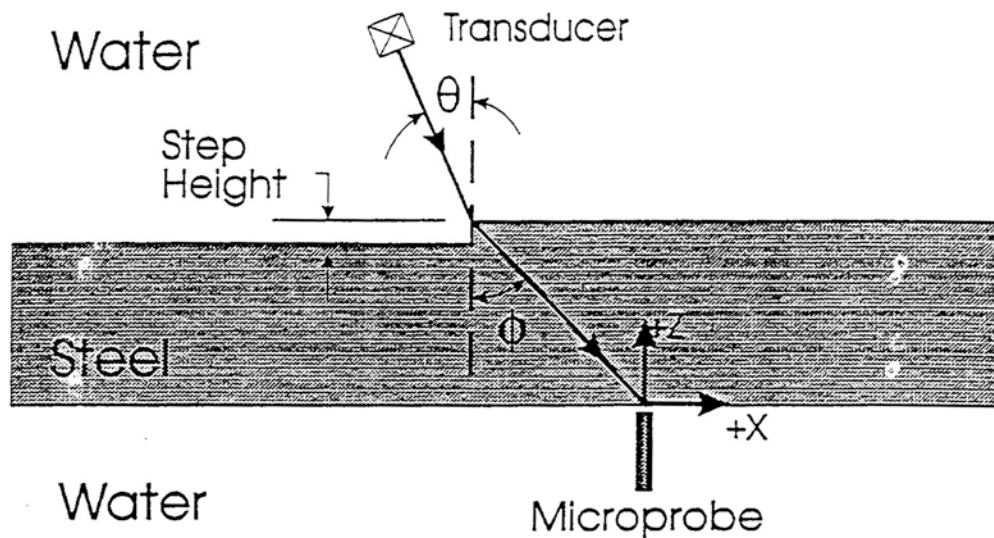


Figure 1.1 Schematic diagram of the experimental set-up for comparing the pressure measured by the microprobe with the predictions of Model I

sophistication should be to develop a code to describe pulse-echo measurements from a perpendicular flaw located at the bottom surface of a metal plate. Figure 1.2 depicts this situation, in which the transducer and metal

plate are placed in an immersion tank. This represents the case of immersion testing of LWR components. The transducer is attached to the arm of a laboratory x-y scanner. The transducer will travel in the direction

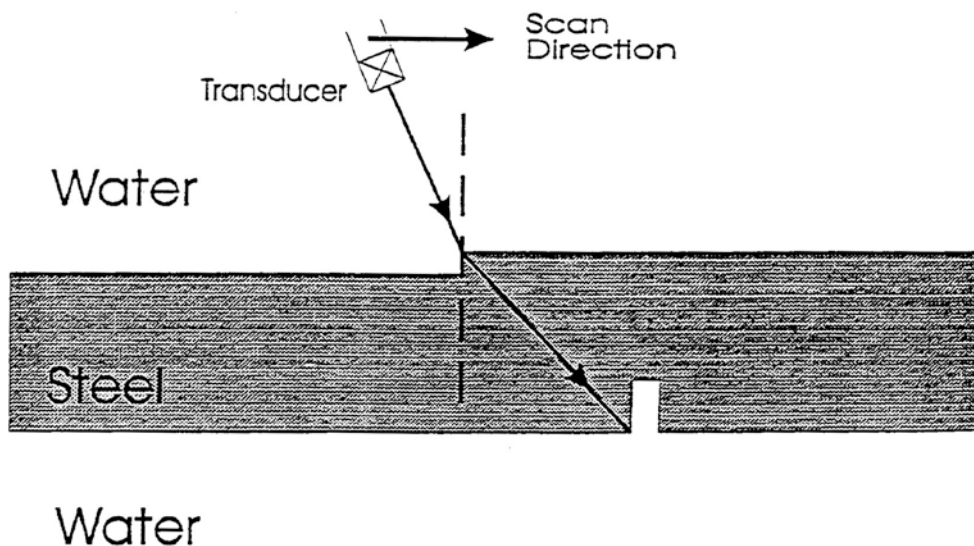


Figure 1.2 Schematic diagram of the experimental set-up for comparing the reflections from a perpendicular flaw with the predictions of Model II. The experimental apparatus is placed in an immersion tank, and the transducer is fastened to the arm of a laboratory x-y scanner.

Introduction

indicated and the echo will be recorded as a function of the transducer position. To validate this model, the experimental echo will be compared with that predicted theoretically.

Model III is illustrated in Figure 1.3. Here, the transducer is mounted on a wedge as in a contact technique for in-service inspection and this code describes the pulse-echo measurements from a perpendicular flaw located at the bottom surface of a metal plate.

Model IV is similar to Model III, except that the flaw can be at **any angle**, as is shown in Figure 1.4. That is, it need not be perpendicular to the bottom surface of the metal plate.

In the experiments designed to test the validity of Model I through Model IV, only a step discontinuity was used, even though the codes are capable of describing other types of surface features. The reason for this choice is that the step discontinuity provides the most critical test of the model. That is, if there is agreement between experimental data and the theoretical calculations for a step discontinuity, then more gradual changes in the surface features should be well described by the model. This position is based upon the reasoning that the greatest change between two parts of the beam occurs for a step discontinuity.

Once validated, these models can be used as engineering tools to study the effects of surface conditions and to develop ASME Code recommendations. The first step will be to decide upon the criteria (or, possibly several sets of criteria) to define what reduction in signal is acceptable. This will be determined by running the computer code(s) to quantify the effect of varying certain parameters and possibly carrying out some additional experiments. One must ensure that the signal remains at least 6 dB above the noise level. The tip signal, used for sizing the flaw, is about 15 dB below that from a corner trap. Thus, the importance of detecting the tip signal must also be taken into account. In connection with Model IV, where the angle of the flaw can vary, another feature must be considered: the worst-case flaw. Research by Green et al. (Green 1992) and Greenwood (Greenwood 1994) has shown that, for some flaw angle, the amplitude is greatly reduced at the inspection frequency of 2.25 MHz compared with that for a corner trap. In this situation, the signal will be reduced because the flaw is a worst-case flaw and further reduced due to surface conditions. All of these situations must be weighed in arriving at criteria to define acceptable versus unacceptable surface conditions. Based upon the selected criteria, ASME Code recommendations can then be formulated.

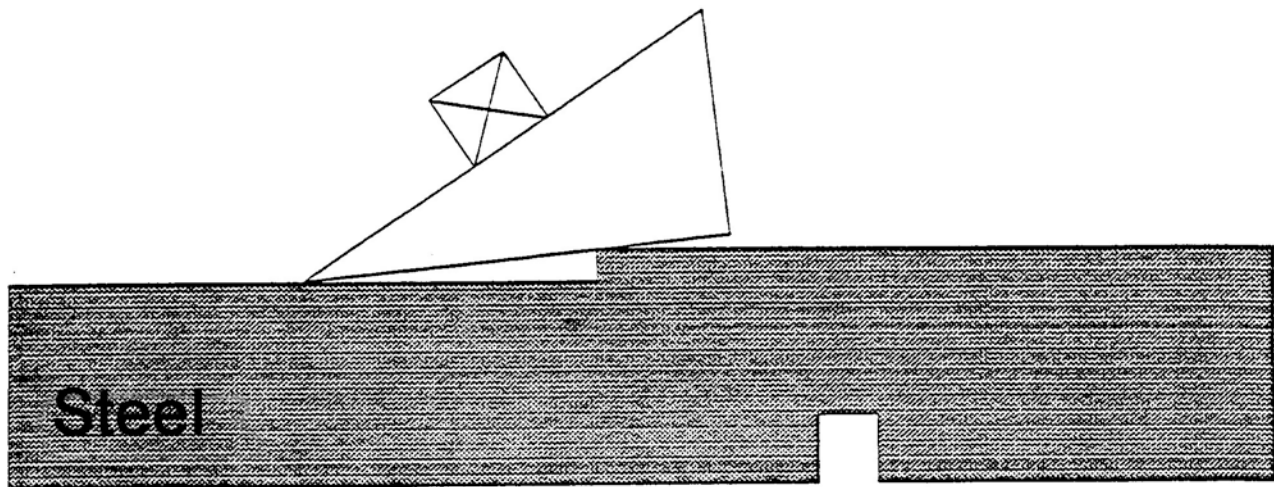


Figure 1.3 Schematic diagram of the experimental set-up for comparing the experimental pulse-echo measurements with the predictions of Model III. The transducer is placed on a plastic wedge and the flaw is perpendicular to the bottom surface.

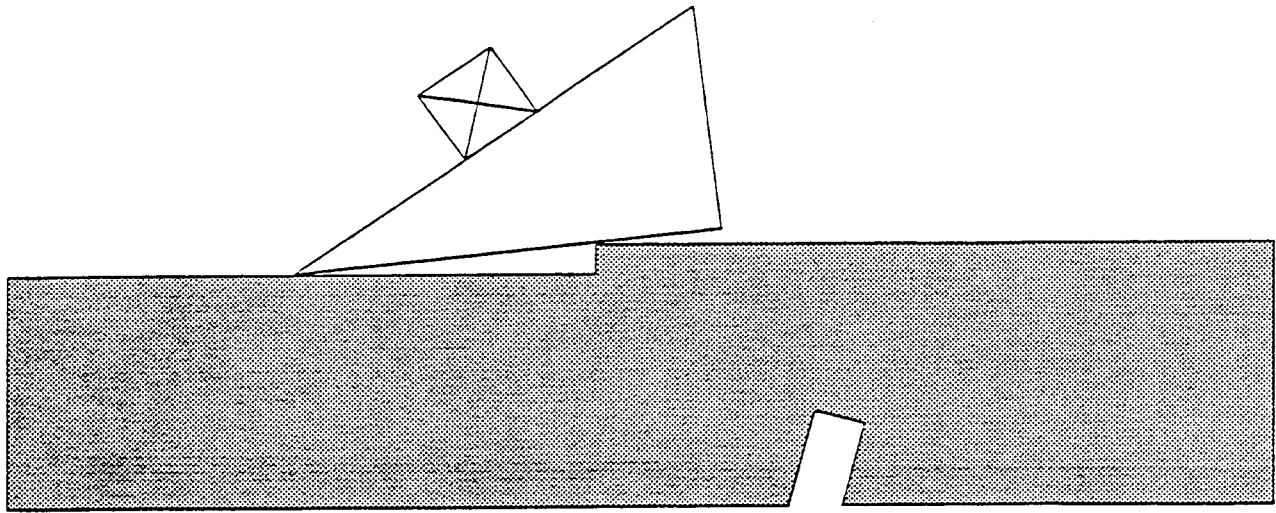


Figure 1.4 The experimental set-up is similar to Figure 1.3 except that the flaw can be at any angle relative to the bottom surface. The experimental measurements will be compared with the predictions of Model IV.

Since the ASME Code recommendations are the primary emphasis of this report, the use of the Model III and Model IV codes to model an ultrasonic inservice inspection comprise the main body of the text. Section 2 provides a brief description of the models. Section 3 describes how the computer codes are used to model an inservice inspection as the transducer wedge is tilted to go over a step discontinuity. Section 4 considers the height of the step discontinuity and the role that it plays in the inspection. Section 5 describes the development of the

ASME Code recommendations. The experimental validation of the four models are given in appendices. Appendix A compares the results of theoretical calculations using Model I and Model II with experimental data. It also presents some basic concepts that are needed to understand the propagation of ultrasound from a planar transducer through a step discontinuity. Features of the computer code for Model I are also described. Appendix B describes the validation of Model III and Model IV codes.

2 Description of Computer Models

2.1 Model I

The objective of the Model I code is to predict theoretically the pressure measured by the microprobe in Figure 1.1.

Essentially, the Model I code consists of the following four parts:

- (1) The pressure generated by the transducer is an analytical solution to the wave equation, which has the form of a series of Gaussian-Hermite basis functions. This solution is used to predict the beam profile at the surface interface.
- (2) A ray-tracing model is then used to approximate the change in the beam as it propagates across the irregular interface. The interface is described by a square grid of points, describing the x, y, and z coordinates of each point and the components of a vector normal to the surface at that grid point. A ray is projected from each grid point onto a so-called transmitted plane.
- (3) The fields are re-expressed in terms of the Gaussian-Hermite analytical solution, which is used to describe the subsequent propagation from the transmitted plane to the bottom surface.
- (4) The next step involved propagating rays from the metal into the water below the plate. This describes the pressure measured by the microprobe, usually several millimeters below the metal plate.

Figure 2.1 illustrates these four steps for an ultrasound beam normal to a surface with a step discontinuity. Note that the density of arrows in the illustration is indicative of the pressure.

These four steps provide an overview of how the computer code for Model I operates. Additional details are presented in Appendix A, but keep in mind that a complete theoretical description of this model is beyond the scope of this report. Rather, the intention is to provide enough information about the theory to give the reader a basic notion of how the computer code operates.

2.2 Model II

The Model II code describes the pulse-echo inspection of a vertical crack on the bottom surface of a sample. The goal is to predict the electrical voltage signal that arises from the corner-trap reflection from the flaw. The reciprocity relationship derived by B. A. Auld (1979) was used to determine the echo response due to the perpendicular flaw. This is described further in Appendix B.

2.3 Model III and Model IV

In Model III, the transducer is mounted on a wedge. The propagation of the ultrasonic wave through the planar wedge-couplant interface is an additional step in Model III. The flaw is perpendicular to the base of the plate in Model III, but the flaw can be at any angle in Model IV. These two models are described in Appendix C and Appendix D.

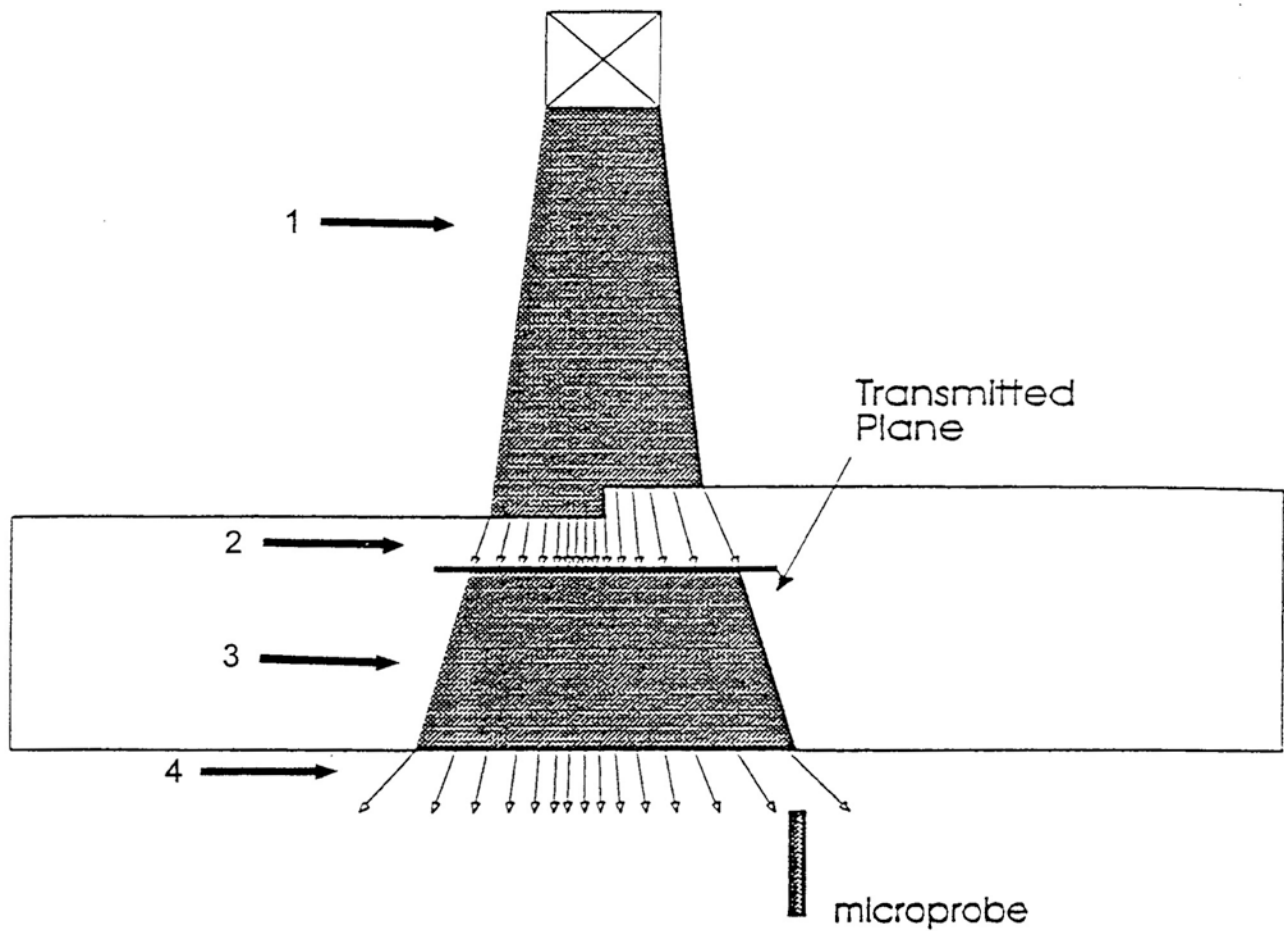


Figure 2.1 Illustration of the four parts of the Model I computer code to describe the propagation of ultrasound: 1) from the transducer to the interface, 2) through the interface, 3) through the metal plate, and 4) through the bottom surface into the water. The analytical solutions are shown by the shaded regions and the arrows indicate the ray-tracing solutions.

3 Modeling an Ultrasonic Inservice Inspection

3.1 Introduction

One goal of this study is to model an ultrasonic inservice inspection and to determine the effect of a step discontinuity on the surface over which the transducer wedge travels. We shall be concerned with how the step affects the amplitude of the signal and also whether there are locations of a flaw, relative to the step location, that might make such a flaw difficult to detect or size.

The motion of the wedge across the step discontinuity can be broken down into five parts:

- (1) The wedge travels on a flat surface and is approaching the step.
 - (2) The front end of the wedge is at the step and it is rotated to lift the front end to the top of the step.
 - (3) The wedge moves across the step until about half of its length has moved over the step.
 - (4) The wedge rotates to bring the front end of the wedge to the top surface.
 - (5) The wedge moves across a flat surface on the top surface.
- (1) TILTANG is the angle of tilt of the wedge above the horizontal.
 - (2) The coordinates (XW, ZW) locate the exit point of the central ray from the base of the wedge.
 - (3) The coordinates (XSURF, ZSURF) denote the location of the central ray on the top surface of the plate. (These coordinates are not shown in Figure 3.1.)
 - (4) The coordinates (XBOTSUR, ZBOTSUR) denote the location of the central ray on the bottom surface of the plate.
 - (5) The horizontal distance between the crack and the step is denoted by HDCRSTP.
 - (6) The angle NWANGST (or "new angle in steel") is the angle that the central ray makes with the normal to the surface. When a wedge that has been designed to produce a 45° sheaf wave in steel is tilted, the angle in steel is larger than 45°.

In order to determine how the rotation of the transducer affects an inservice inspection, calculations were carried out in which the following parameters were varied:

- (1) step height, (2) location of flaw relative to step, (3) angle of flaw, (4) type of couplant, and (5) whether flaw is in air or water. Calculations were also carried out in which the transducer wedge did not rotate as it traversed the step. In addition, calculations were performed for the case where the step was machined and blended.

3.2 Model Calculations

Figure 3.1 shows the motion of the wedge just described. The third panel shows the definition of parameters that are required for input to the ISU code, relative to a coordinate system located at the top of the step:

Each position of the wedge corresponds to a case that is run using the ISU computer code for Model III. The first step is to determine some of the input parameters. To do that another code was developed and, based upon the geometry of the wedge and its orientation, the angle of tilt of the wedge (TILTANG) and the coordinates XW, ZW, XSURF, and ZSURF are determined. Also the coordinates XBOTSUR and ZBOTSUR are very helpful in determining how the central ray interacts with the flaw. This program is then used to generate a series of input cases for the ISU code. The location of the flaw HDCRSTP (horizontal distance between crack and step) is specified on the input file.

An eight-cycle toneburst at a frequency of 2.25 MHz is input to the ISU code. The output is also an eight-cycle toneburst and the peak-to-peak amplitude of this signal is determined. The value of HDCRSTP is input into the code and the amplitude is calculated at each point in the scan.

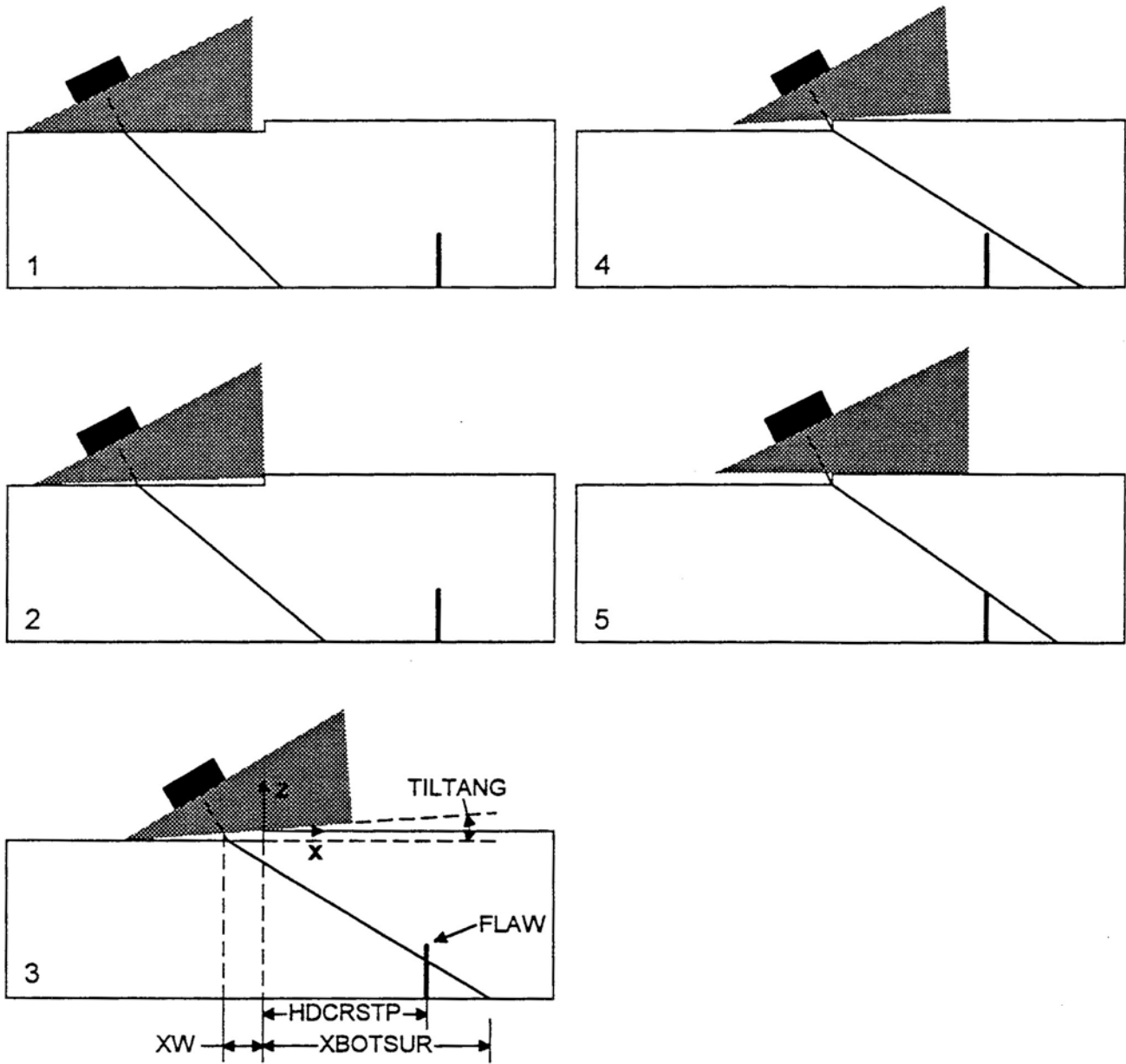


Figure 3.1 The five parts describing the motion of a transducer wedge across a step discontinuity

The output of the ISU code provides a **relative** amplitude. Therefore, in order to determine the effect of a step discontinuity on a flaw, one must carry out a calculation where there **is** a step discontinuity and compare it with the calculation where there **is no** step discontinuity.

3.3 Case 1 Calculations

The first case considered for the modeling of an inservice inspection has the following parameters:

plate thickness = 2.54 cm
 flaw = 0.64 cm high and 0.64 cm long, perpendicular to
 the base
 step height = 0.152 cm wedge length = 3.44 cm
 transducer frequency = 2.25 MHZ wedge design = 45°
 shear in steel couplant = Ultragel II

Table 3.1 shows the parameters describing the position of the wedge. Note that when the wedge is tilted, the angle in steel NWANGST can be as large as 60°.

One objective is to place the flaw at different distances (HDCRSTP) from the step and to see how the response is affected by the step discontinuity. First, we shall consider the signal from the flaw when the surface is smooth so that the signal in the presence of a step can be compared with it.

3.3.1 Smooth Surface

Figure 3.2a shows a plot of the peak-to-peak amplitude versus the x-coordinate of the exit point (XW). The maximum amplitude is 0.461. In the inspection, the amplitude of the signal is obviously important, but also important is the distance over which the wedge travels and receives a strong signal. For example, Figure 3.2a shows that the wedge travels a distance of about 0.8 cm over which the signal is equal to or greater than 0.23, which is half its maximum value.

Figure 3.2b shows a plot of the peak-to-peak amplitude versus the x-coordinate of the central ray on the bottom surface (XBOTSUR). This graph shows that the maximum amplitude occurs when the central ray is directed to the base of the flaw.

The calculations shown in Figures 3.2a and 3.2b were obtained by considering a flaw located at a distance of 4.29 cm from the step. This distance is so great that the step has no influence.

Table 3.1 Parameters for each location in the scan

STAGE	XW	XBOTSUR	NWANGST	TILTANG
Motion across lower flat surface				
1	-2.37000	0.0180001	45.0000	0.00000
2	-2.20333	0.184667	45.0000	0.00000
3	-2.03667	0.351333	45.0000	0.00000
4	-1.87000	0.518000	45.0000	0.00000
Rotation to top of step				
5	-1.87017	0.718849	47.2094	0.843343
6	-i.87068	0.944928	49.5010	1.68669
7	-1.87153	1.20340	51.8901	2.53003
Motion across step				
8	-1.65674	1.47474	52.3806	2.69846
9	-1.44200	1.75631	52.9469	2.89089
10	-1.22732	2.05123	53.6084	3.11284
11	-1.01272	2.36403	54.3916	3.37167
12	-0.798233	2.70162	55.3343	3.67738
13	-0.583909	3.07510	56.4919	4.04395
14	-0.369822	3.50359	57.9502	4.49153
15	-0.156095	4.02338	59.8502	5.05023
Rotation back to top surface				
16	-0.156433	3.24157	54.3768	3.36682
17	-0.156636	2.70081	49.4919	1.68341
Motion on top flat surface				
18	-0.156703	2.29030	45.0000	0.00000
19	0.0932968	2.63330	45.0000	0.00000
20	0.343297	2.88330	45.0000	0.00000
21	0.593297	3.13330	45.0000	0.00000
22	0.843297	3.38330	45.0000	0.00000

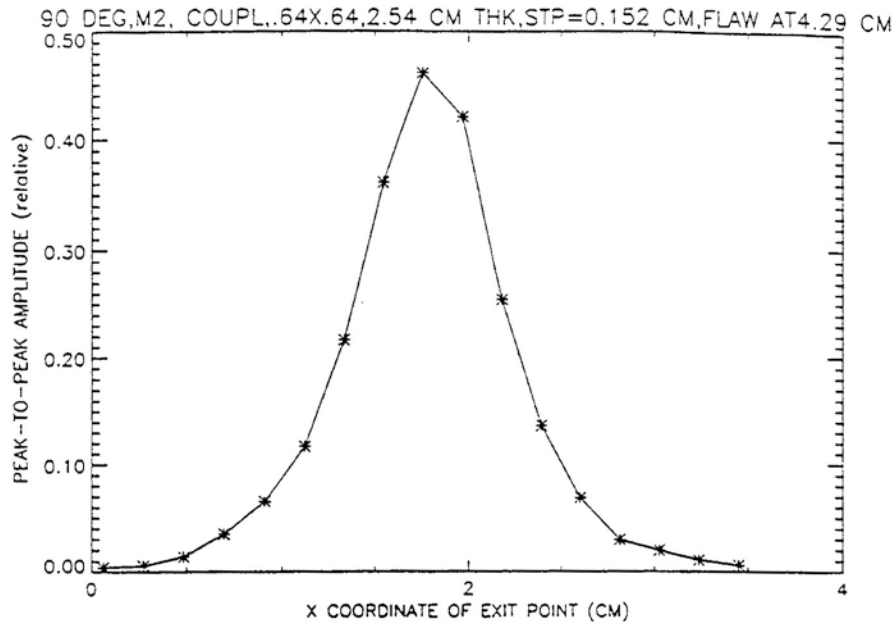


Figure 3.2a Peak-to-peak amplitude versus the x-coordinate of the exit point (XW) for Case 1 for a smooth surface

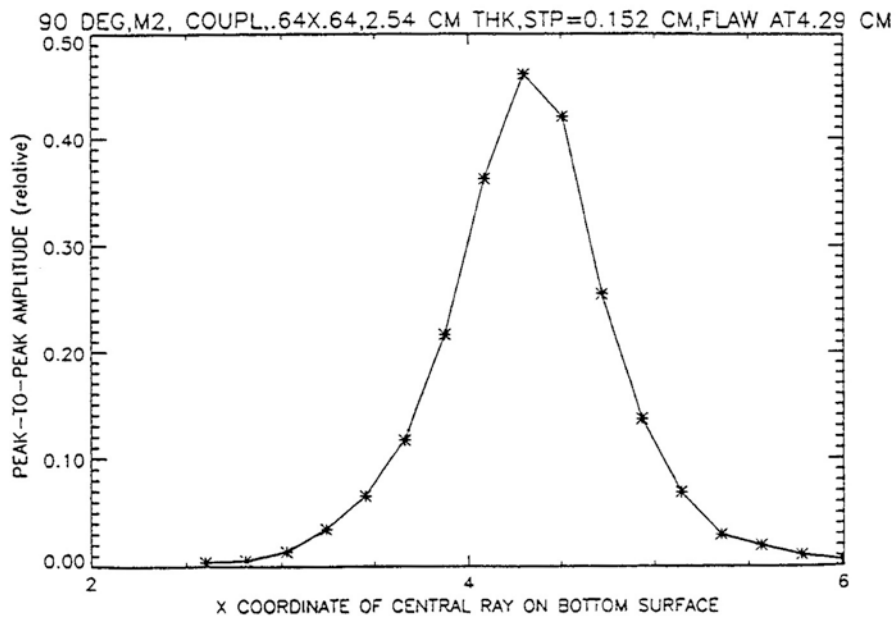


Figure 3.2b Peak-to-peak amplitude versus the x-coordinate of the central ray on the bottom surface (XBOTSUR) for Case 1 for a smooth surface

3.3.2 Varying the Flaw Location Relative to the Step

Calculations were carried out in which the distance between the step and the flaw (HDCRSTP) are as follows: 0.5 cm, 0.9 cm, 1.44 cm, 1.74 cm, 2.04 cm, 2.54 cm, 3.04 cm, 3.34 cm, and 3.64 cm.

The flaw locations can be separated into three categories:

- (1) If the flaw is close to the step, then, as the wedge approaches the step on the lower surface, a response will be observed before the wedge is rotated to go over the step.
- (2) If the flaw is farther away from the step, then the wedge is tilted to go over the step before a response is observed.
- (3) If the flaw is far away from the step, then a response will be observed when the wedge is on the top surface of the step discontinuity.

The goal is to delineate these three categories and to compare the response with that on a smooth surface.

3.3.3 Flaw Close to Step

- **HDCRSTP = 0.5 cm** - Figure 3.3 shows the response for a flaw located at 0.5 cm from the step. The first four points correspond to the motion along the bottom surface, as the values of XW in Table 3.1 show. The next three points correspond to rotating the tip of the wedge to go over the step. The remaining points occur when the wedge is tilted and travels across the step. The maximum amplitude is just about the same as for a smooth surface. However, it is observed over a much shorter distance during the scan. The amplitude is half its maximum value or larger for only about 0.4 cm.
- **HDCRSTP = 0.9 cm** - Figure 3.4 shows the response for a flaw located at 0.9 cm from the step. The motion is similar to that in Figure 3.3. The first four points correspond to motion along the bottom surface. The next three points correspond to rotating the tip of

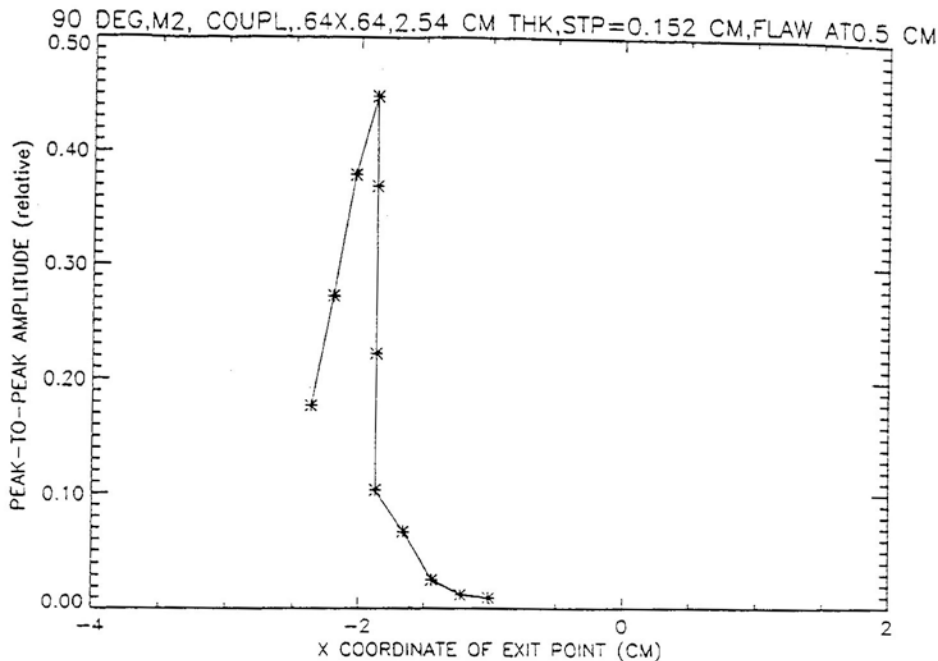


Figure 3.3 Response for a flaw located at 0.5 cm from the step

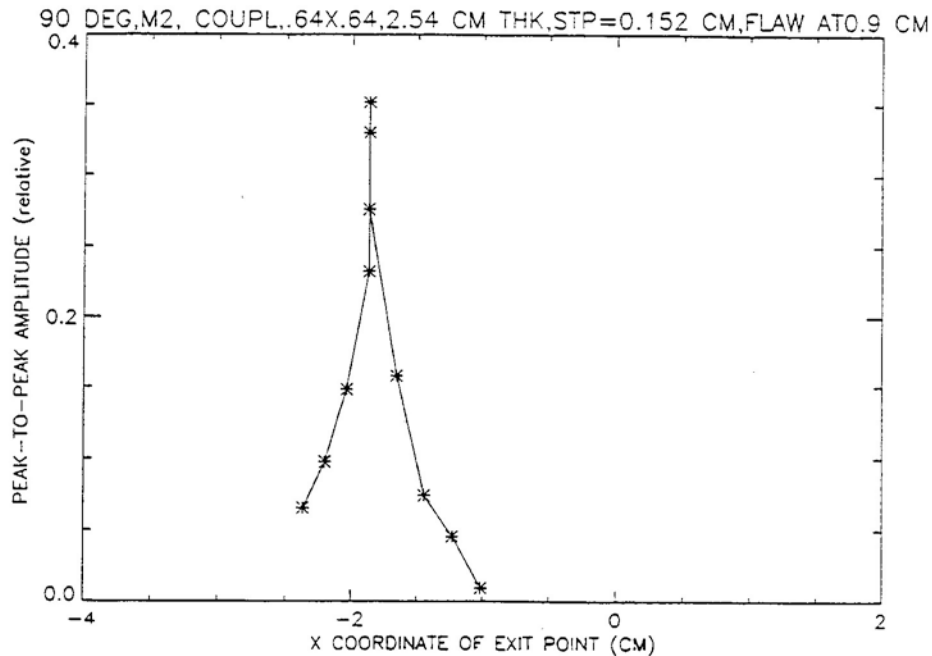


Figure 3.4 Response for a flaw located at 0.9 cm from the step

the wedge to go over the step. It is here that the maximum amplitude of 0.35 occurs. This can be compared with the maximum amplitude of 0.46 for a smooth surface. As the scan takes place the signal will be of short duration. The amplitude is half its maximum value of 0.17 (or larger) for only about 0.3 cm during the scan. A flaw in this location will be difficult to detect.

- **HDCRST = 1.44 cm** - Figure 3.5 shows a plot of the amplitude versus XW for a flaw located at 1.44 cm. The peak that occurs at XW = -1.66 cm is due to motion of the tilted wedge across the step, while that at XW = -0.157 cm is due to motion on the top flat surface. In this case we see that the largest signal occurs as the wedge travels across the step, where its amplitude is 0.285. Due to the tilt and an angle in steel (NWANGST) greater than 45°, the signal will occur at a larger time than expected. This will be discussed further for another flaw in a later section. Only a trace of a signal appears when the wedge travels across the flat surface.

- **HDCRSTP = 1.74 cm** - Figure 3.6 for a flaw at 1.74 cm is very similar to Figure 3.5. However, one difference is that the signal is larger when the wedge travels on the top surface.

3.3.4 Flaw at Intermediate Distance

- **HDCRSTP = 2.04 cm** - Figure 3.7a shows a plot of amplitude versus XW for a flaw located at 2.04 cm from the step. The points are labeled to describe the motion of the wedge and are as follows:
 - Points 6 and 7-rotation of wedge to reach top of step.
 - Points 8 through 15- motion of wedge across step.
 - Points 16 through 18 -rotation back to the top flat surface
 - Points 19 through 21 - motion of wedge on top flat surface

Figure 3.7b is of interest because it shows how the transducer central ray travels back and forth across the bottom surface as the wedge travels across the step discontinuity.

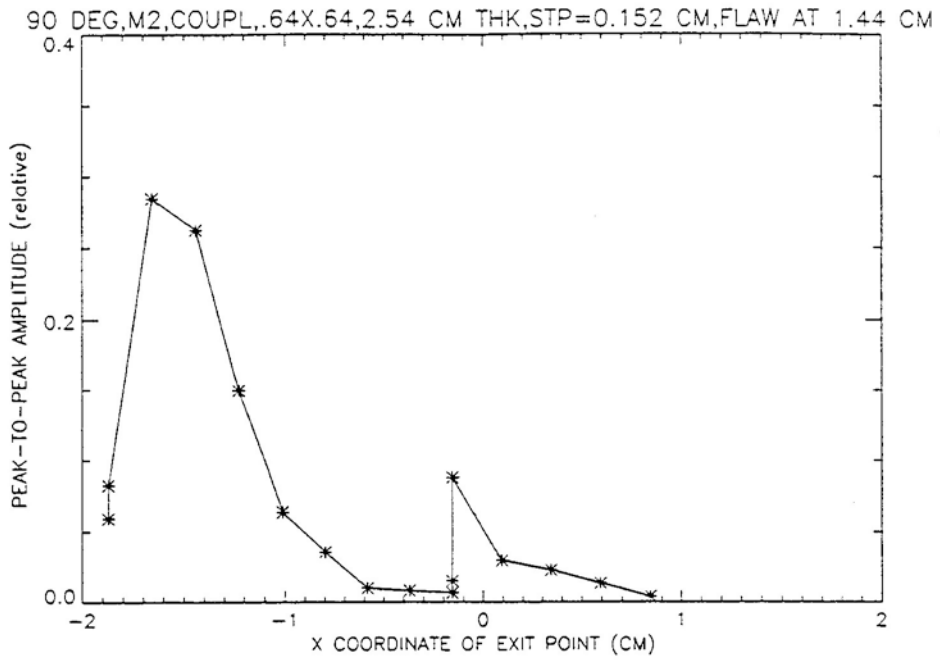


Figure 3.5 Response for a flaw located at 1.44 cm from the step

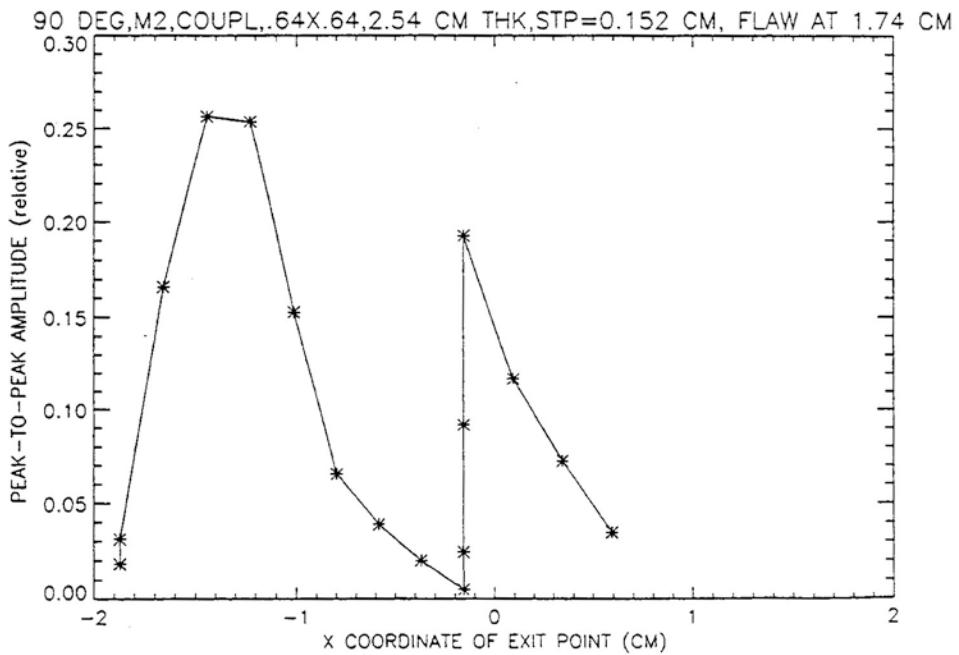


Figure 3.6 Response for a flaw located at 1.74 cm from the step

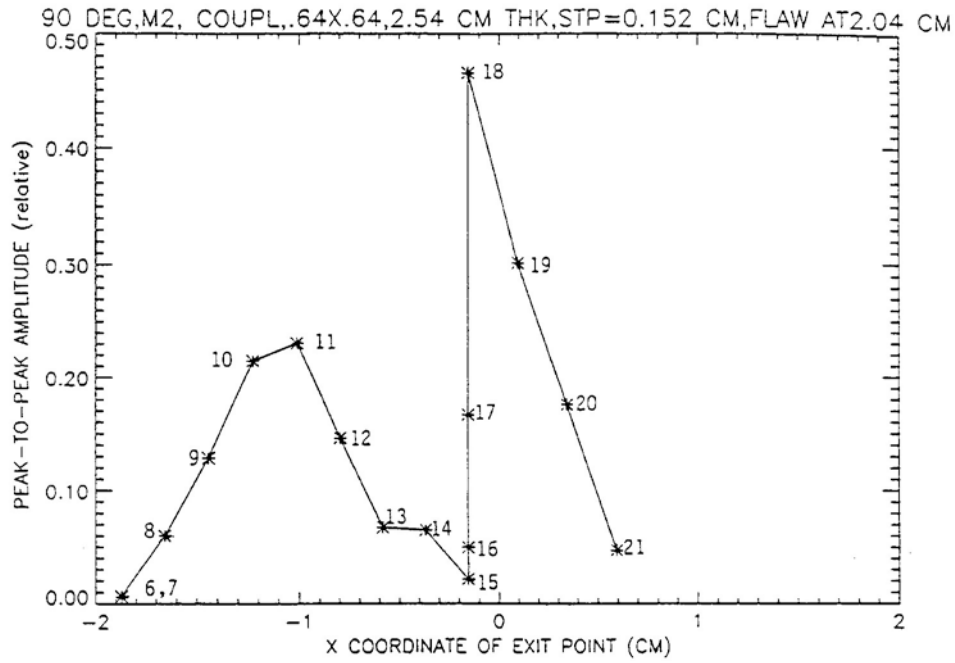


Figure 3.7a Peak-to-peak amplitude versus the x-coordinate of the exit point (XW) for a flaw located at 2.04 cm from the step

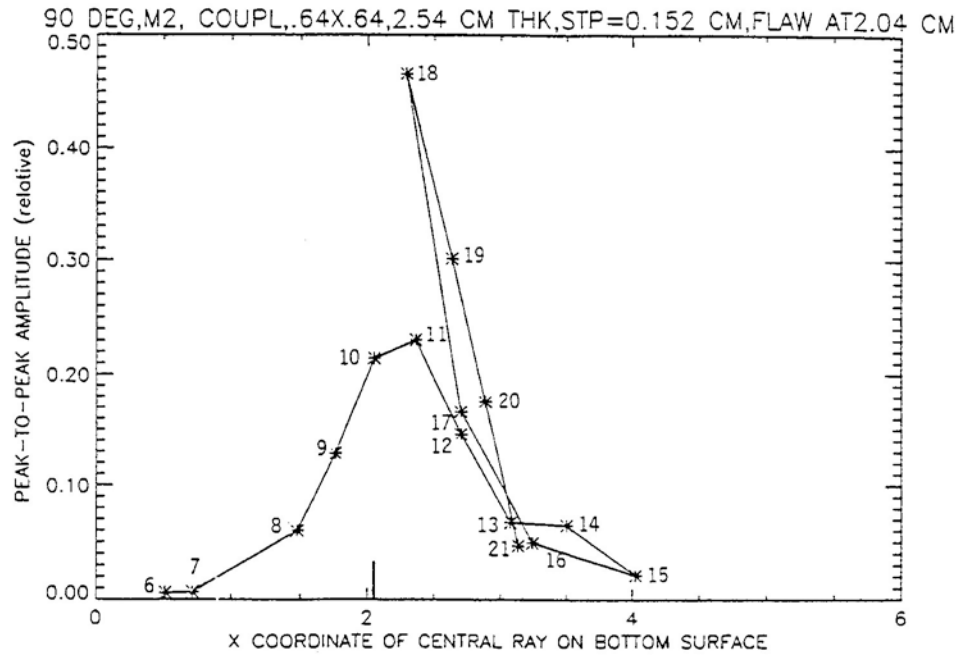


Figure 3.7b Peak-to-peak amplitude versus the x-coordinate of the central ray on the bottom surface (XBOTSUR) for a flaw located at 2.04 cm from the step

In this case the flaw is observed twice: once, as the tilted wedge travels across the step and second, as it travels on the top flat surface. Its maximum amplitude in the first case is 0.23 and is 0.47, in the second. This is to be compared with the amplitude of 0.461 for a smooth surface. These two signals will also be observed at different times. The reason for this can be seen from Table 3.1. For the first signal the maximum amplitude occurs at position #11 where the angle in steel (NWANGST) is 54.4° and the angle of tilt (TILTANG) is 3.37°. The increase in time, compared to traveling at 45° in steel, is given by

$$\begin{aligned} \text{time increase} &= [2(2.54 \text{ cm})/0.323 \text{ cm/microsec}] \\ &\quad [1/\text{COS}54.4 - 1/\text{COS}45] \\ &= 4.77 \text{ microsec} \end{aligned}$$

This example shows that when the transducer is tilted, the time at which the signal is recorded is increased by approximately 5 microseconds. This factor will have to be taken into account during an inservice

inspection. In addition, Table 3.1 shows that NWANGST is as large as 59.9°.

- **HDCRSTP = 2.54 cm** - Figure 3.8 shows that a flaw at 2.54 cm is also observed twice. Now, however, the signal when the wedge is on the top surface is the larger of the two. The maximum amplitude is 0.388 compared to 0.461 for a smooth surface, showing the effect of the step discontinuity.

3.3.5 Flaw at a Greater Distance from Step

- **HDCRSTP = 3.04 cm** - Figure 3.9 shows the flaw is now far enough away from the step that the largest signal is due to the wedge traveling across the top flat surface. The amplitude is now nearly the same as for a smooth surface. Only a trace of a signal appears as the tilted wedge travels across the step.

Flaws at a distance of 3.34 cm and 3.64 cm exhibit a similar behavior as at 3.04 cm.

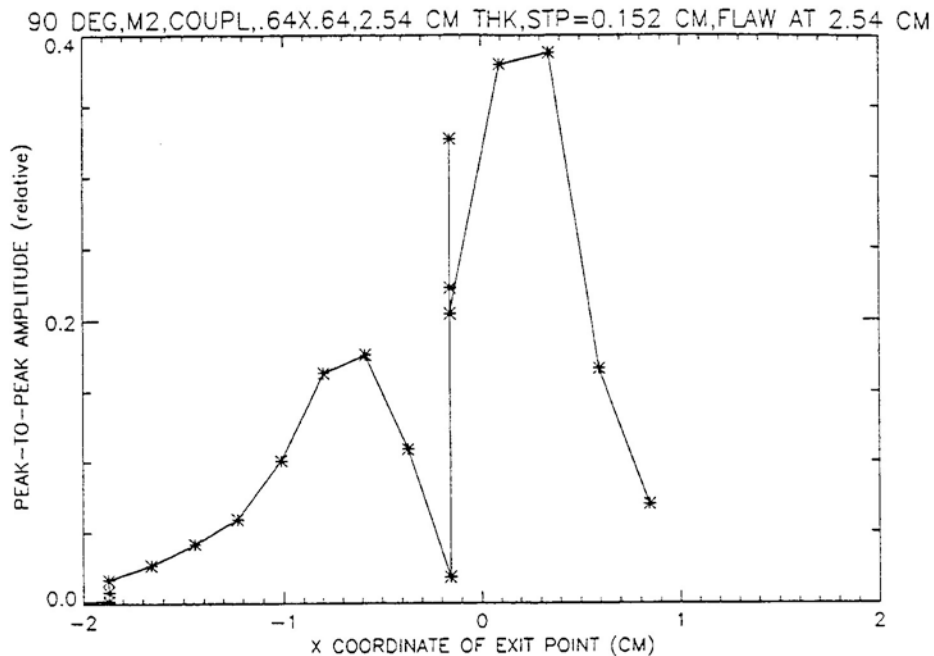


Figure 3.8 Response for a flaw located at 2.54 cm from the step

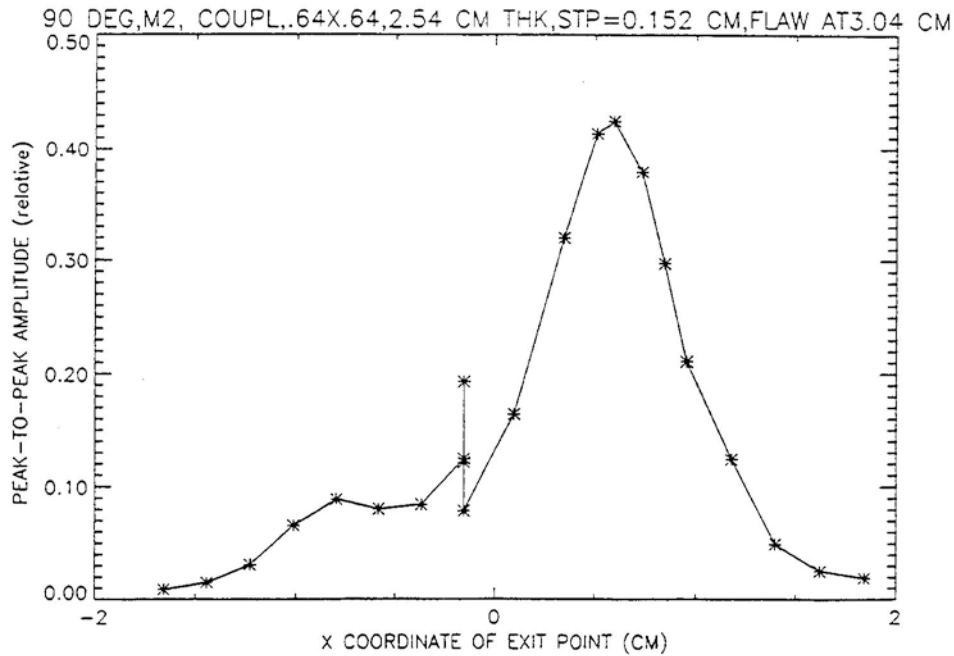


Figure 3.9 Response for a flaw located at 3.04 cm from the step

Table 3.2 summarizes the maximum peak-to-peak amplitude for the various flaw locations and shows some interesting results. As the wedge moves across the step, the flaw located at 1.44 cm from the step has a larger amplitude (0.285) than for a flaw located at 2.54 cm (0.176). The reason for this is that the tilt angle is smaller for the 1.44 cm flaw than that required for the 2.54 cm flaw. As the tilt angle increases, theory has shown that the amplitude decreases.

3.4 Case 2 Calculations

In these calculations the flaw shape was changed to be more like a flaw encountered in an inservice inspection.

Table 3.2 Maximum peak-to-peak amplitude for various locations of the flaw. The amplitude must be compared with the amplitude of 0.461 that was obtained for a smooth surface.

Horizontal distance between crack and step HDCRSTP, cm	Maximum amplitude moving across step or moving on bottom flat surface	Maximum amplitude rotating back to flat or moving across flat top surface
0.5	0.352	-
0.9	0.448	-
1.44	0.285	0.088
1.74	0.256	0.192
2.04	0.230	0.466
2.54	0.176	0.388
3.04	0.089	0.425
3.34	0.093	0.456
3.64	-	0.448

The flaw has the shape of half of an ellipse. Also a shorter wedge was used. This case has the following parameters:

- plate thickness = 2.54 cm
- flaw is half elliptical in shape, height = 0.254 cm, length = 1.27 cm
- step height = 0.152 cm
- wedge length = 2.34 cm
- transducer frequency = 2.25 MHZ
- wedge design = 45° shear in steel
- couplant = Ultragel II flaw in air bottom surface in air

Table 3.3 shows the transducer parameters for each stage in the scan. It is interesting to note that this shorter transducer wedge means that the angle of tilt as it goes over the step is increased to 7.4° and the angle in steel (NW ANGST) is increased to a maximum of 69.4°. A wedge of this length is often used in inservice inspections.

When the wedge travels across a smooth surface (no step) the maximum amplitude is 0.342 for this case, while it was 0.461 for Case 1. This shows that the response from this flaw is reduced by about 26%, compared to that for Case 1.

The object of these calculations is to change the distance between the flaw and the step and to observe how the amplitude changes. The behavior for this second case is similar to that for Case 1.

- **HDCRSTP = 1.04 cm** - The calculations show that a flaw at this distance will be observed when the wedge is traveling on the lower surface before reaching the step. Therefore, flaws having a smaller value of HDCRSTP need not be investigated.
- **HDCRSTP = 1.34 cm** - Figure 3.10 shows a plot of the amplitude versus the x coordinate of the exit point (XW). Comparing the values of XW on this graph with those in Table 3.3, one sees that the amplitude increases as the wedge approaches the step while on the lower surface, but that the amplitude decreases when the tip of the wedge is raised to go over the step. There is essentially no signal when the wedge moves over the top surface.

Table 3.3 Parameters for each stage in scan for Case 2

STAGE	XW	XBOTSUR	NWANG	
			ST	TILTANG
Motion across lower flat surface				
5	-1.66000	0.728000	45.0000	0.00000
6	-1.52250	0.865500	45.0000	0.00000
7	-1.38500	1.00300	45.0000	0.00000
8	-1.24750	1.14050	45.0000	0.00000
9	-1.11000	1.27800	45.0000	0.00000
Rotation to top of step				
10	-1.11029	1.57840	48.2730	1.23885
11	-1.11115	1.94011	51.7387	2.47770
12	-1.11259	2.39340	55.4566	3.71656
Motion across step				
13	-1.01532	2.55906	55.9629	3.87766
14	-0.918077	2.73385	56.5220	4.05335
15	-0.820875	2.91981	57.1427	4.24567
16	-0.723720	3.11963	57.8362	4.45712
17	-0.626620	3.33696	58.6166	4.69068
18	-0.529587	3.57694	59.5022	4.95002
19	-0.432639	3.84696	60.5170	5.23962
20	-0.335797	4.15825	61.6938	5.56510
21	-0.239090	4.52869	63.0782	5.93354
22	-0.142556	4.98891	64.7374	6.35401
23	-0.0462500	5.59697	66.7760	6.83832
24	0.0497497	6.80118	69.3730	7.40210
Rotation back to step				
25	0.0498774	5.25898	63.9937	6.16841
26	0.0499819	4.35547	59.4494	4.93473
27	0.0500632	3.73462	55.4081	3.70105
28	0.0501213	3.26828	51.7088	2.46737
29	0.0501562	2.89733	48.2590	1.23368
Motion on top flat surface				
30	0.0501678	2.59017	45.0000	0.00000
31	0.261932	2.80193	45.0000	0.00000
32	0.473697	3.01370	45.0000	0.00000
33	0.685462	3.22546	45.0000	0.00000
37	1.53252	4.07252	45.0000	0.00000

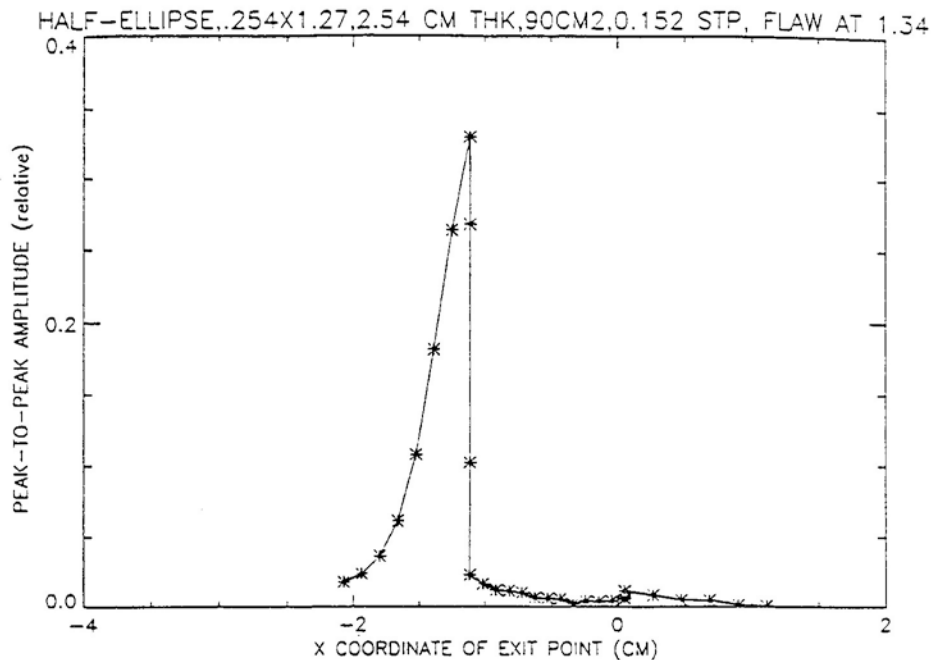


Figure 3.10 Response for a flaw located at 1.34 cm from the step for Case 2

- **HDCRSTP = 1.64 cm** - Figure 3.11 shows the results of calculations for a flaw located at 1.64 cm from the step. Here one sees that the flaw is observed only while the wedge is rotating to the top of the step. Such a flaw might easily be missed in an inservice inspection. A trace of a signal is also observed as the wedge rotates back to the flat top surface.
- **HDCRSTP = 1.94 cm** - The results of calculations for a flaw located at 1.94 cm from the step are very similar to that for 1.64 cm, but as the wedge rotates back to the flat top surface the signal is larger.
- **HDCRSTP = 2.24 cm** - Figure 3.12 shows that, for a flaw at 2.24 cm, there is no signal as the wedge moves across the lower surface toward the step. As the tip of the wedge rotates to go over the step, the amplitude increases. As the tilted wedge moves across the step, the amplitude decreases. Then, as the wedge rotates to the top flat surface the signal again increases and decreases as it moves over the top surface. Note that in each place where the signal is strong, the wedge travels only about 0.5 cm before the signal drops off.

- **HDCRSTP = 2.54 cm** - For a flaw located at 2.54 cm from the step, Figure 3.13 shows that a strong signal is observed when the tilted wedge moves across the step, when it rotates back to the flat top surface, and when it moves along the top flat surface.

Calculations for flaws at 2.84 cm and 3.14 cm are similar to those for 2.54 cm.

3.4.1 Conclusion

A comparison of Case 1 and Case 2 shows that very similar behavior can be noted in both cases. It is the **location** of the flaw in relation to the step location that is important and the shape of the flaw determines the amplitude of the signal. Another conclusion from these calculations is that the worst case flaw occurs when the flaw is located at 1.64 cm from the step in the second case. Here the flaw is seen only during the rotation of the wedge from the lower flat surface to the top of the step. In contrast, the flaw located at 2.54 cm from the step is quite easily observed.

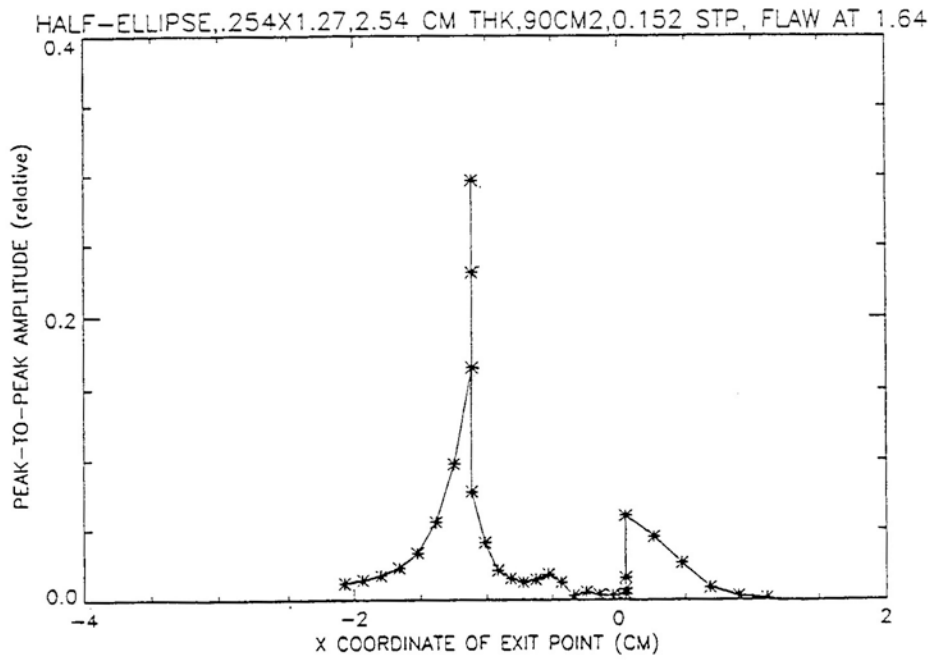


Figure 3.11 Response for a flaw located at 1.64 cm from the step

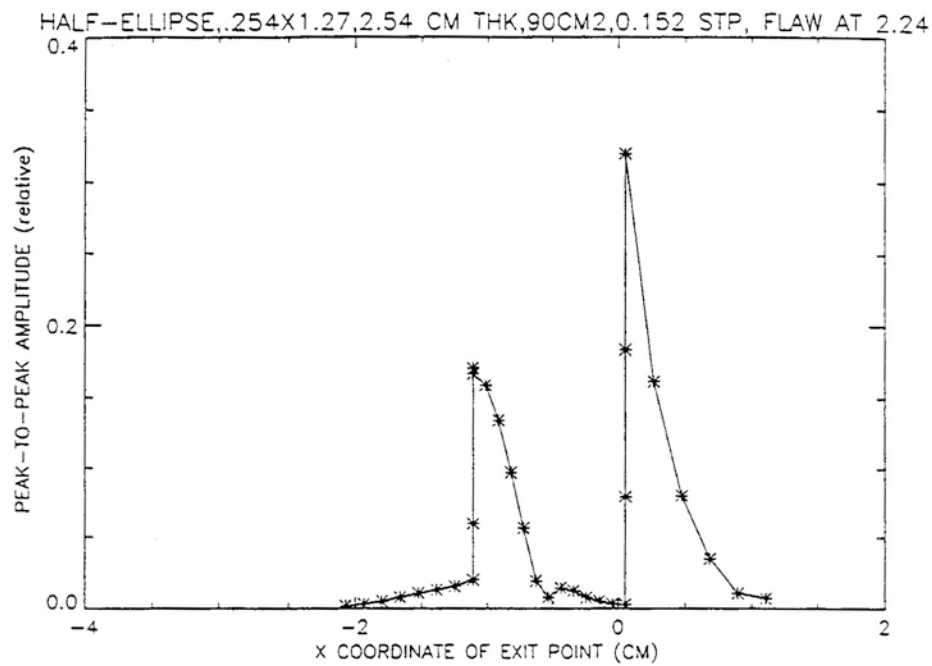


Figure 3.12 Response for a flaw located at 2.24 cm from the step

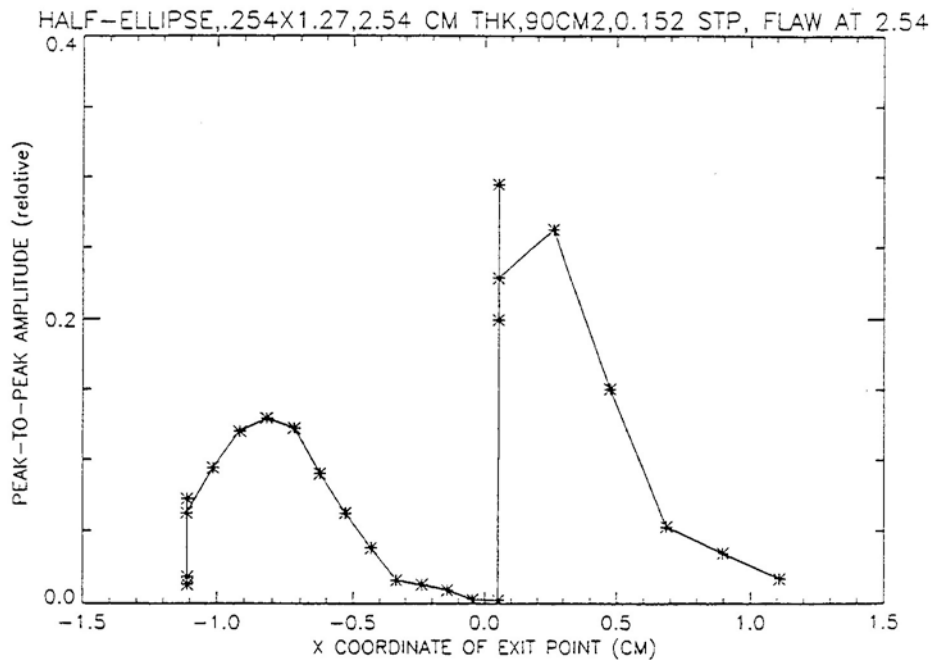


Figure 3.13 Response for a flaw located at 2.54 cm from the step

3.4.2 Additional Calculations for 80° and 85° Flaw Angle

The calculations described so far have considered the flaw to be perpendicular to the bottom surface. Calculations were also carried out for the half-elliptical flaw and changing only the flaw angle to 85° and 80°. These calculations used a couplant such as Ultrigel II and the flaw and bottom surface are considered to be in air. The results show that the amplitude changes somewhat, but the overall shape of the scan does **not** change in character. Table 3.4 summarizes these results and previous results for the semi-elliptical flaw.

3.4.3 Other Types of Inspections

Some inspections are carried out in which the couplant is water and the flaw and bottom surface are in air. For example, an inspection of this type would occur for a remotely-controlled inspection inside a reactor pressure vessel. This type of inspection will be denoted by "WAA."

In another type of inspection the flaw and bottom surface are in water and the couplant is a gel couplant, like Ultrigel II. An example is the inspection of a pipe carrying water. This type of inspection will be denoted by "CWW."

Calculations have been carried out for both of these inspections for the half-elliptical flaw of Case 2.

The results of all of the studies using the half-elliptical flaw are tabulated in Table 3.4.

The amplitude for a flaw angle of 90° must be compared with the amplitude of 0.342 that was obtained for a smooth surface with no step. For a flaw angle of 85° and a smooth surface, the maximum amplitude was 0.323. For a flaw angle of 80° and a smooth surface, the maximum amplitude was 0.273. The preceding values are for the situation in which a couplant (like Ultrigel II) is used and the bottom surface and flaw are in air. These cases are labeled CAA. Calculations were also carried out where the water acts as the couplant and the bottom surface and

Table 3.4 Maximum peak-to-peak amplitude for various flaw locations

	Horizontal distance between crack and step HDCRSTP flaw, cm	Maximum amplitude on flat surface angle	Maximum amplitude moving across step or moving across flat below step	Maximum amplitude rotating back to flat top surface
1.04	90CAA	0.335	-	—
	85CAA	0.348		
	80CAA	0.285		
	90WAA	0.296		
	90CWW	0.317		
1.34	90CAA	0.330	—	—
	85CAA	0.325		
	80CAA	0.270		
	90WAA	0.278		
	90CWW	0.297		
1.64	90CAA	—	0.296 (rotation)	0.060 (rotation)
	85CAA		0.298 (rotation)	0.056 (rotation)
	80CAA		0.229 (rotation)	0.046 (rotation)
	90WAA		0.255 (rotation)	0.094 (rotation)
	90CWW		0.271 (rotation)	0.053 (rotation)
1.94	90CAA	—	0.256 (rotation)	0.152 (rotation)
	85CAA		0.282 (rotation)	0.139 (rotation)
	80CAA		0.183 (rotation)	0.112 (rotation)
	90WAA		0.211 (rotation)	0.187 (rotation)
	90CWW		0.238 (rotation)	
2.24	90CAA	—	0.171	0.319 (rotation)
	85CAA		0.207 (rotation)	0.299 (rotation)
	80CAA		0.135 (rotation)	0.247 (rotation)
	90WAA		0.119	0.126 (rotation)
	90CWW		0.167	0.280
2.54	90CAA	—	0.129	0.294
	85CAA		0.192	0.246
	80CAA		0.123	0.203
	90WAA		0.082	0.088
	90CWW		0.136	0.230
2.84	90CAA	—	0.084	0.263
	85CAA		0.183	0.258 (rotation)
	80CAA		0.119	0.202
3.14	90CAA	—	0.098	0.329
	85CAA		0.153	0.31
	80CAA		0.099	0.260

flaw are in air. These cases are labeled WAA. For a smooth surface, the maximum amplitude is 0.273. In addition, calculations were carried out where couplant (like Ultrigel II) is used and the bottom surface and crack are in water. These cases are labeled CWW. For a smooth surface, the maximum amplitude is 0.358. For easy reference, the following maximum amplitudes are listed:

smooth CAA	90	0.342
smooth WAA	90	0.273
smooth CWW	90	0.358

3.5 Using a Slanted Surface Instead of a Step Discontinuity

In the studies for Case 1 we found that a flaw located at 0.9 cm from the step would be very difficult to detect in an inservice inspection (see Figure 3.4). Similarly, for Case 2 a flaw located at 1.64 cm from the step would be difficult to detect (see Figure 3.11). The basic difference in these two cases is the length of the wedge used in each

case. This suggests the possibility that performing an inservice inspection with wedges of two different lengths would permit detecting all flaws with one or both of the wedges. Another possibility was also considered. Suppose that the step discontinuity was machined so that it became a slanted surface rather than a step. Figures 3.14 through Figure 3.18 show the motion of a wedge across a slanted surface using the same plate and flaw parameters as for Case 2. The additional parameters are:

- wedge length = 2.34 cm
- vertical height of slanted section = 0.152 cm
- horizontal length of slanted section = 0.608 cm
- couplant = Ultrigel II
- flaw and bottom surface in air

Table 3.5 shows the parameters describing the motion of the wedge. The "stage" number in this table corresponds to the "stage" number shown on the graphs in Figures 3.14 through 3.18. Table 3.5 shows that some stages have an angle in steel (NWANGST) less than 45°. This is due to the central ray striking the slanted surface. The application of Snell's law yields this unexpected result.

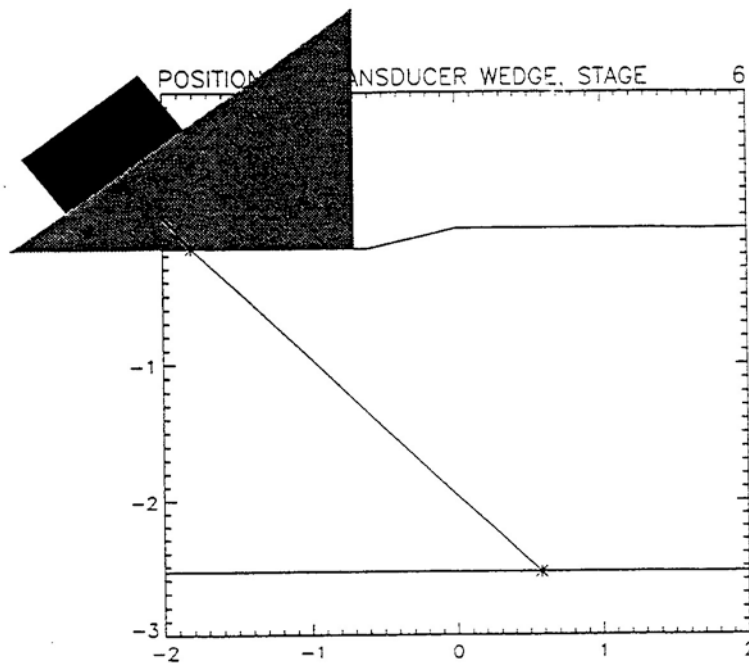


Figure 3.14 Transducer wedge, traveling left to right, approaching a slanted section (stage 6)

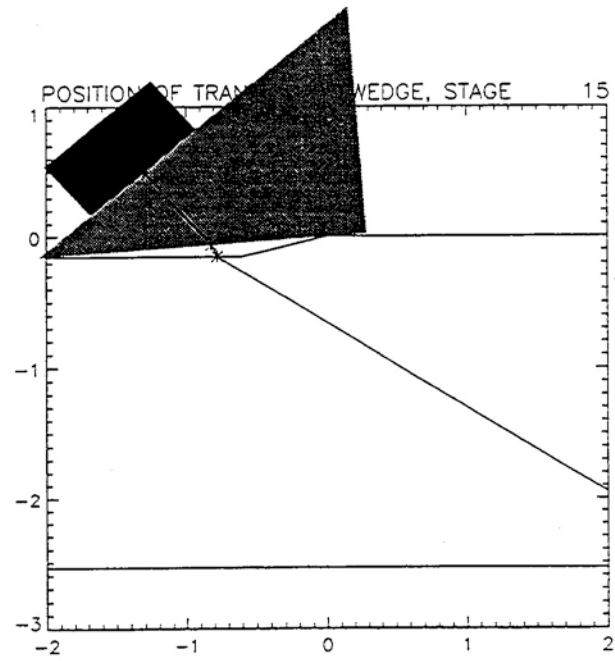


Figure 3.15 Transducer wedge moving across the slanted section, but the central ray strikes the lower flat surface (stage 15)

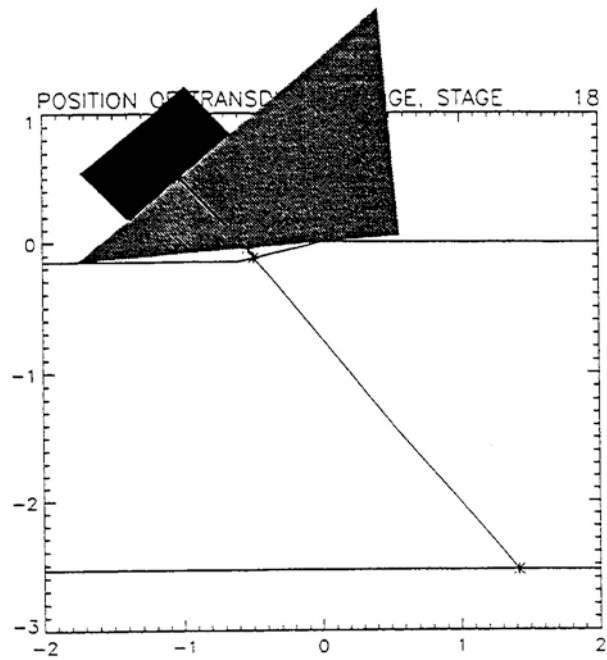


Figure 3.16 Transducer wedge moving across the slanted section, but the central ray strikes the slanted surface (stage 18)

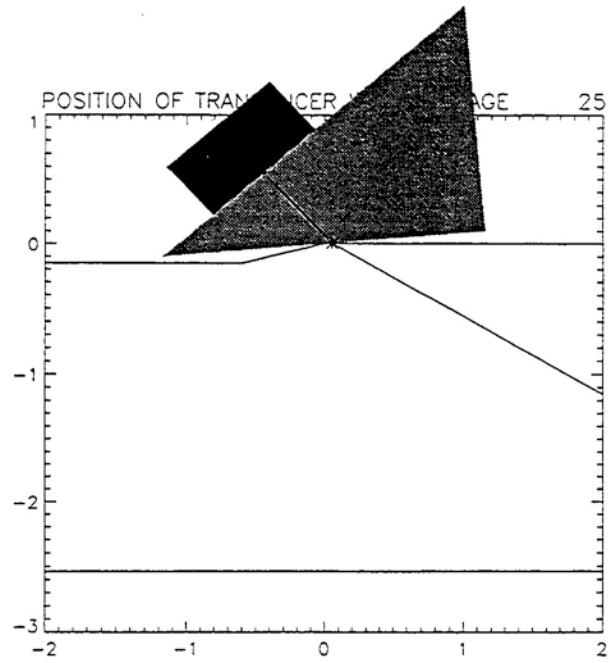


Figure 3.17 Transducer wedge rotating toward the top surface (stage 25)

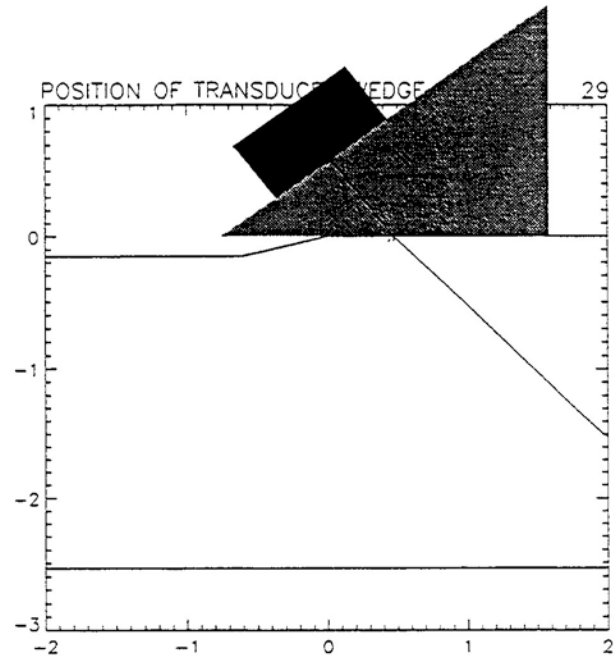


Figure 3.18 Transducer wedge moving on the top surface (stage 29)

Table 3.5 Parameters for each stage where the surface has a slanted section rather than a step discontinuity

STAGE	XW	OBOTSUR	NWANGST	TILTANG
Wedge moves across lower flat surface				
1	-2.27	0.118	45.0	0.0
2	-2.17	0.210	45.0	0.0
3	-2.08	0.302	45.0	0.0
4	-1.99	0.394	45.0	0.0
5	-1.90	0.486	45.0	0.0
6	-1.81	0.578	45.0	0.0
7	-1.71	0.670	45.0	0.0
Wedge moves across slanted surface				
Central ray strikes the lower flat surface				
8	-1.59	0.966	47.0	0.74
9	-1.47	1.281	49.0	1.49
10	-1.35	1.62	51.0	2.23
11	-1.23	1.99	53.2	2.98
12	-1.11	2.40	55.5	3.72
13	-1.01	2.55	56.0	3.88
14	-0.92	2.73	56.5	4.05
15	-0.82	2.92	57.1	4.25
16	-0.72	3.12	57.8	4.45
17	-0.63	3.34	58.6	4.69
Wedge moves across slanted surface				
Central ray strikes the slanted surface				
18	-0.53	1.41	38.3	4.95
19	-0.43	1.56	38.9	5.23
20	-0.34	1.72	39.6	5.57
21	-0.24	1.88	40.4	5.93
22	-0.14	2.06	41.3	6.35
23	-0.05	2.25	42.3	6.83
Wedge moves across slanted surface				
Central ray strikes the top flat surface				
24	0.05	6.80	69.4	7.40
Wedge rotates toward the top flat surface				
25	0.05	4.36	59.5	4.93
26	0.05	3.26	51.7	2.46
27	0.05	2.59	45.0	0.0
Wedge moves across top flat surface				
28	0.262	2.80	45.0	0.0
29	0.473	3.01	45.0	0.0
30	0.685	3.22	45.0	0.0
31	0.897	3.43	45.0	0

Figure 3.19 shows a graph of amplitude versus XW for a flaw located at 1.34 cm from the top of the slanted section. Comparing it with Figure 3.10 one sees that it is not greatly different, but has a slightly wider peak.

Figure 3.20 shows the results for a flaw located at 1.64 cm. When this is compared with Figure 3.11, one sees that the peak is now much wider as a result of the slanted section and represents an improvement for detecting the flaw.

Figure 3.21 shows the results for a flaw located at 2.54 cm. Here, the flaw is seen several times as the central ray travels back and forth past the flaw as the wedge moves and rotates.

The flaw at 0.9 cm for Case 1 and the flaw at 1.34 cm for Case 2 are observed only when the tip of the wedge is rotated to the top of the step. In an inservice inspection, this is a very difficult motion to do consistently and detect the flaw. By having a slanted surface, the motion of the wedge is more regulated and the flaw will be much easier to detect. However, the use of two wedges of different lengths would also seem an appropriate method to improve detecting flaws of this type.

3.6 No-Tilt Inspection

Many of the problems in an inservice inspection, as discussed above, arise from tilting the wedge. This causes the angle in steel to change from 45° to a larger angle usually, and even a smaller angle for a slanted surface. Also, due to the different angle in steel, the echo will return at a different time than expected. Suppose instead that the wedge is not tilted as it goes over a step, but is held level with the couplant between the wedge base and the surface. The discussion so far has considered the wedge approaching the step on the lower surface and then proceeding onto the top surface. If the wedge were not to be tilted, then in an actual inspection, the wedge would approach the step on the top surface. The wedge would push the couplant out of the way as it was moved to the lower surface. However, the calculations do not depend upon which direction the wedge moves. In this case, the motion of the wedge is as follows:

- (1) The wedge moves toward the step on the lower surface.

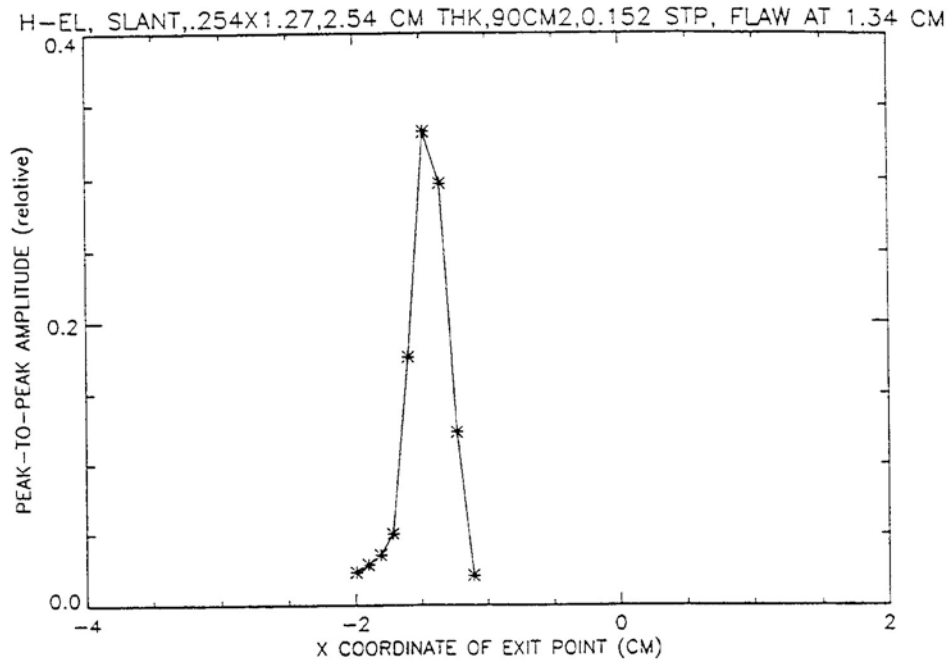


Figure 3.19 Response for a flaw located at 1.34 cm from the top of slanted surface

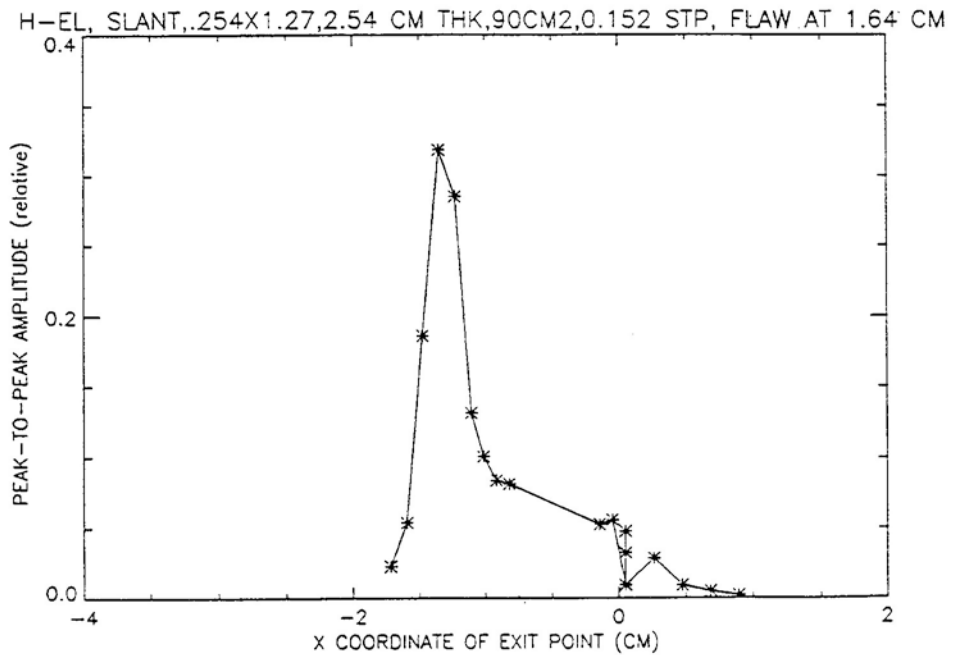


Figure 3.20 Response for a flaw located at 1.64 cm from the top of slanted surface

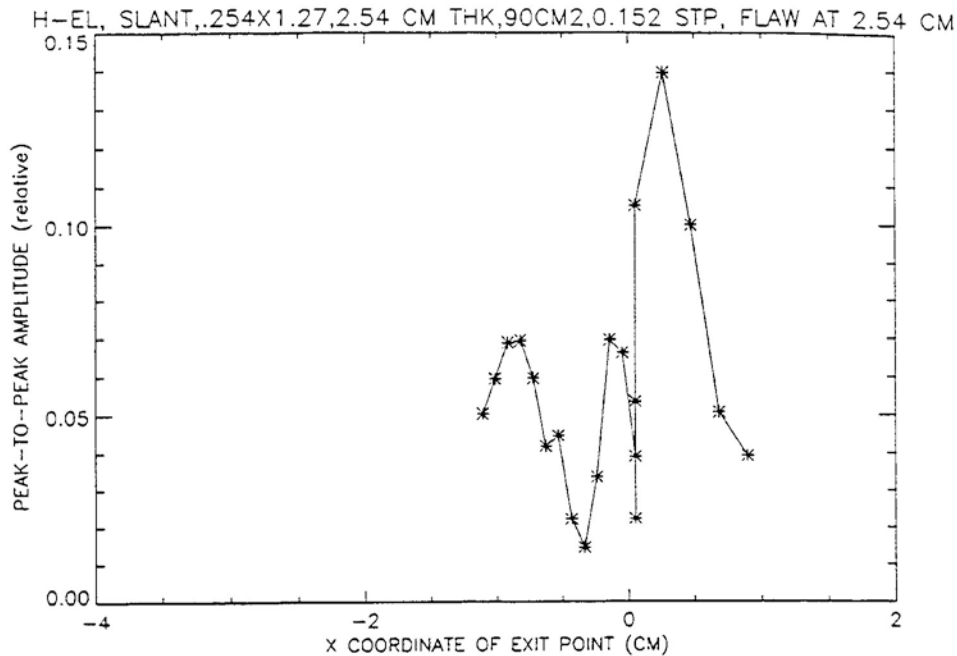


Figure 3.21 Response for a flaw located at 2.54 cm from the top of slanted surface

- (2) When the tip of the wedge reaches the step, the wedge moves vertically upward.
- (3) The wedge moves across the top surface. This means that the ultrasound will travel through an even layer of couplant before entering the steel part, during the first part of this motion.

Table 3.6 shows the parameters for each stage of this motion and calculations were carried out using couplant, such as Ultrigel II, and the flaw and bottom surface are in air.

Figure 3.22 shows the amplitude versus XW for a flaw at a distance of 1.64 cm from the step. From Table 3.6 the maximum amplitude occurs when XBOTSUR is 1.70 cm and is the result one expects. Here the amplitude is very strong and is to be compared to Figure 3.15 where the wedge is tilted to go over the flaw. There is a great deal of difference between these two responses. This shows that the flaw at 1.64 cm will be detected if the wedge is held level as it goes over the step rather than being tilted.

Figure 3.23 shows a similar graph for a flaw at 1.94 cm.

In Figures 3.24 and 3.25 for flaws at 2.24 cm and 2.54 cm, the amplitude is smaller than in Figures 3.22 and 3.23. The reason for this is that the exit point of the central ray is close to the top of the step.

3.7 Maximum Angle of Tilt

Validation experiments have been carried out and show that there is agreement between theory and experimental data for step heights as large as 0.2286 cm. For a wedge having a length of 2.34 cm, the tip of the wedge would have to be tilted by 5.6° to go over a step with a height of 0.2286 cm. As the wedge moved over the step the angle would increase to about 10.8° after half the length of the wedge had traversed the step. As the tilt angle increases so does the angle in steel.

Table 3.7 shows the angle that the central ray makes with the normal to the surface when the couplant is water and when it is a gel couplant, such as Ultrigel II. These results are obtained by using Snell's law at the wedge-couplant interface and also at the couplant-steel interface and thus, are determined by geometry alone.

Table 3.6 Parameters for each stage where the wedge moves vertically upward. For all stages NWANGST is 45.0° and TELTANG is 0.0°

STAGE	XW	XBOTSUR
Wedge moves across lower flat surface		
1	-2.21	0.178
2	-2.07	0.316
3	-1.93	0.453
4	-1.79	0.590
5	-1.66	0.728
6	-1.52	0.866
7	-1.38	1.00
8	-1.24	1.14
9	-1.11	1.28
Wedge moves vertically upward to top surface		
10	-1.11	1.28
11	-1.11	1.29
12	-1.11	1.31
13	-1.11	1.32
14	-1.11	1.34
Wedge moves across top surface		
15	-0.90	1.49
16	-0.69	1.70
17	-0.47	1.91
18	-0.26	2.13
19	-0.05	2.33
20	0.16	2.70
21	0.37	2.91
22	0.58	3.12
23	0.80	3.34

One important question then is, what angle in steel is acceptable? The answer will then limit the angle of tilt of the wedge. A tilt of about 5° seems to be a reasonable limit. Recall also that this will result in a signal being observed at a greater time, since the central ray travels a longer distance.

One obvious way to limit the angle of tilt is to use a longer transducer wedge. For a wedge length of 4.00 cm, the tilt due to a step height of 0.2286 cm is 3.27 degrees.

3.8 Different Step Heights

A step height of 0.152 cm has been used in most of the calculation described so far. However, the theory has been validated for step heights as large as 0.2286 cm. The next chapter describes calculations when the wedge is nearly centered over the step where interference effects come into play.

3.9 Summary

Table 3.8 summarizes the parameters used in the calculations for the eight case studies and the main conclusion from each case study.

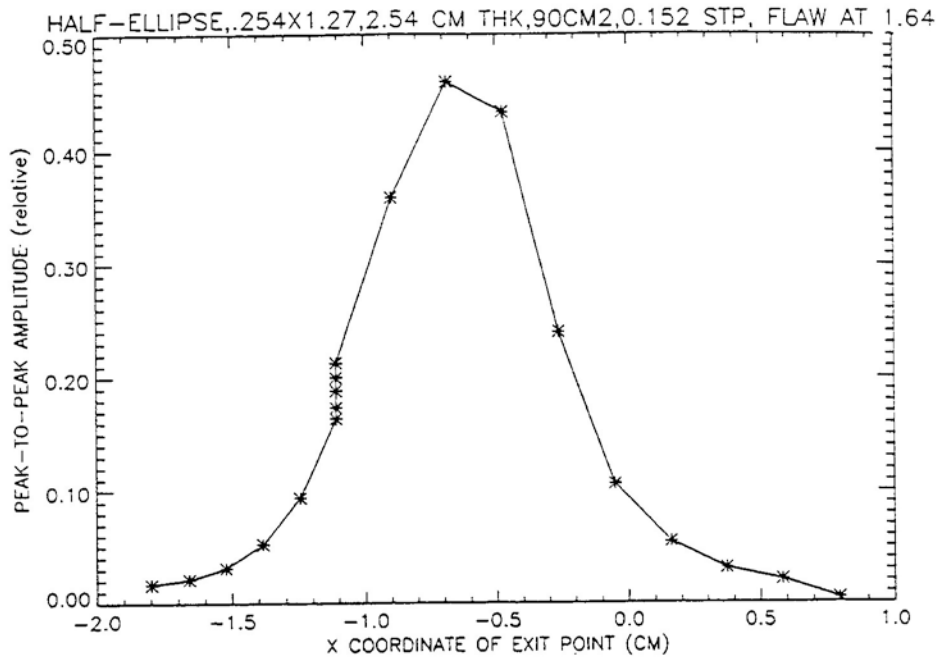


Figure 3.22 Response for a flaw located at 1.64 cm from the step during a no-tilt inspection

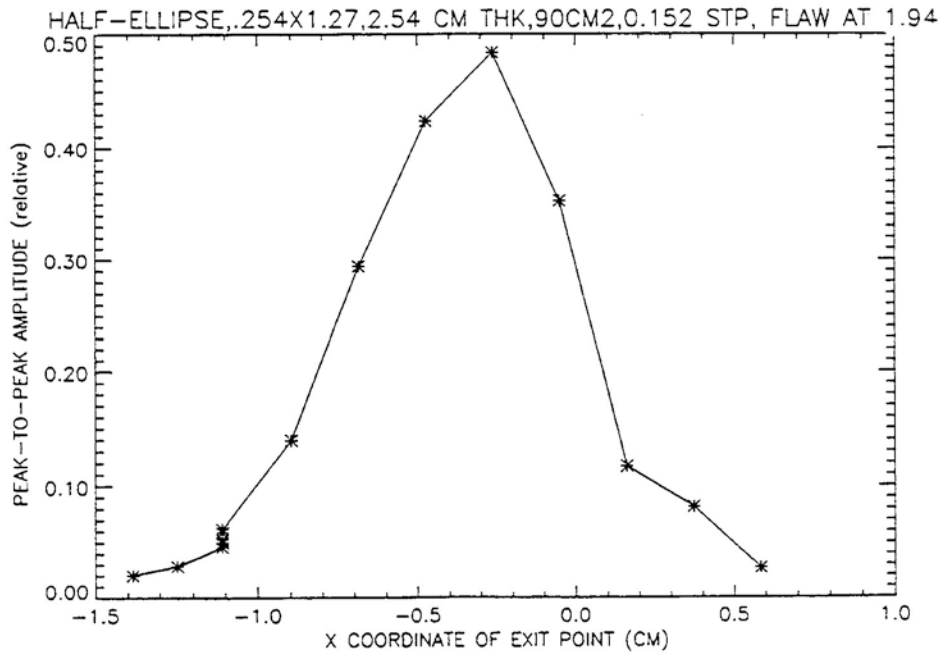


Figure 3.23 Response for a flaw located at 1.94 cm from the step during a no-tilt inspection

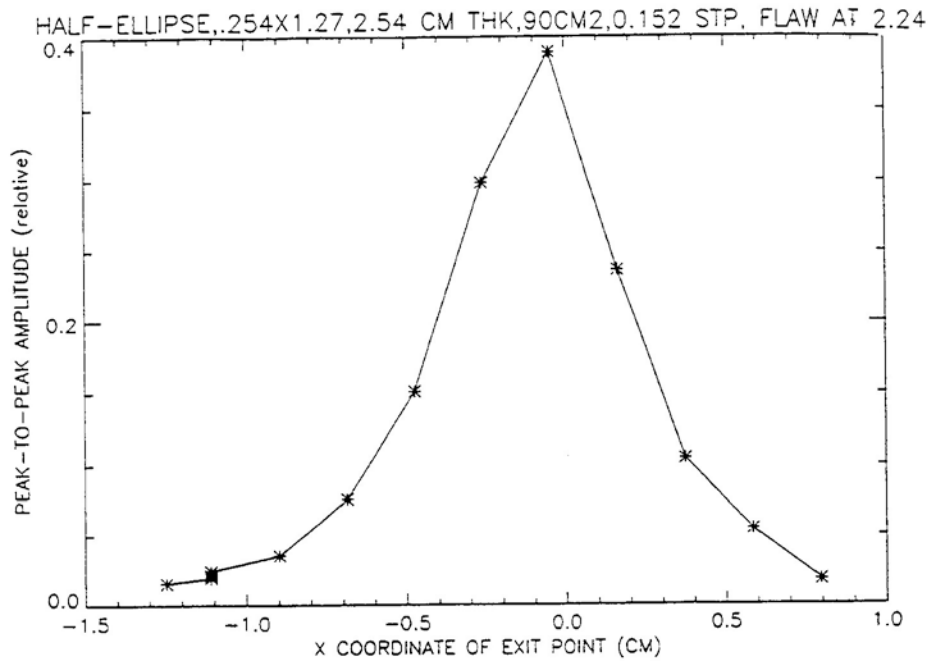


Figure 3.24 Response for a flaw located at 2.24 cm from the step during a no-tilt inspection

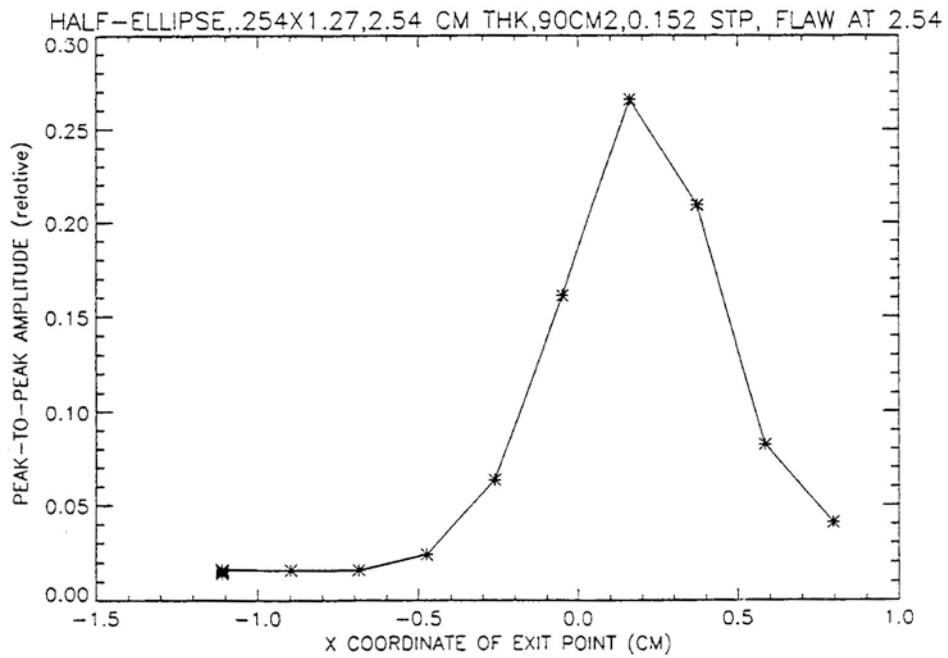


Figure 3.25 Response for a flaw located at 2.54 cm from the step during a no-tilt inspection

Table 3.7 Comparison of the tilt angle of the wedge and the resulting angle in steel for water and for the couplant Ultragel II

Wedge tilt angle	Angle in steel couplant = water	Angle in steel couplant = Ultragel II
0	45	45
1.86	50.7	50.0
3.71	57.1	55.5
5.57	64.8	61.7
5.82	65.9	62.6
6.37	68.7	64.8
7.03	72.7	67.6
7.85	79.3	71.7
8.34	87.4	74.5
8.88	not possible	78.5
9.51	not possible	86.6
10.2	not possible	not possible

Table 3.8 Summary of eight case studies for modeling an ultrasonic inservice inspection

All of the calculations were carried out using an eight-cycle toneburst having a frequency of 2.25 MHz. The transducer was mounted on a wedge designed to produce 45 ° shear waves in steel. In case 1 the flaw was rectangular in shape with a height of 0.64 cm and a length of 0.64 cm. In all other cases the flaw had the shape of a half-ellipse, with a height of 0.254 cm and a length of 1.27 cm. The plate thickness in all cases was 2.54 cm.

Case	Angle (deg)	Flaw step height (cm)	Couplant	Flaw and bottom Surface	Distance between flaw and step (cm)
1	90	0.152	gel	air	0.5,0.9,1.44,1.74,2.04,2.54,3.04
<p>Conclusions: A flaw at a distance of 0.9 cm from the step is difficult to observe because it is only detected as the tip of the wedge rotates to go over step and as wedge moves across step. Some flaws are seen only when the wedge travels across the lower surface (0.5 cm and smaller distances). Others are seen only when the wedge travels on the upper surface (3.34 cm and larger). Some flaws are seen several times (2.74 cm, 2.04 cm, and 2.54 cm). Due to tilt of wedge the angle in steel is greater than 45° and the signal will be observed at a greater time than expected.</p>					
2	90	0.152	gel	air	1.04,1.34,1.64,1.94,2.24,2.54, 2.84,3.14
<p>Conclusions: The worst case flaw is at a distance of 1.64 cm from the step and this flaw will be difficult to detect. The wedge length in this case is different from that in case 1. Carrying out the inspection with wedges of two different lengths would improve flaw detection.</p>					
3	85 & 80	0.152	gel	air	1.04,1.34,1.64,1.94,2.24,2.54, 2.84,3.14
<p>Conclusions: The results show that the amplitude is slightly reduced, but the overall shape of the scan does not change in character due to a smaller flaw angle.</p>					
4	90	0.152	water	air	1.04,1.34,1.64, 1.94,2.24,2.54, 2.84,3.14
<p>Conclusions: The character of the scan remains the same, when the couplant is changed. In case 2 calculations were carried out where the couplant was gel. When case 2 and 4 were compared, the surprising result was that the amplitudes for a flaw at 2.54 cm differed by a factor of 3.3! This led to considering constructive and destructive interference of waves for steps of different heights.</p>					
5	90	0.152	gel	water	1.04,1.34,1.64,1.94,2.24,2.54, 2.84,3.14
<p>Conclusions: The amplitude of the signal does not change significantly and the character of the scan remains the same.</p>					
6	90	0.229	water	air	1.04,1.34,1.64,1.94,2.24,2.54,2.84, 3.14
<p>Conclusions: When a wedge of this length is used for a step height of 0.229 cm (90 mils), the angle in steel is so large that this is unacceptable. For larger step heights a wedge of longer length should be used so that the angle in steel can be limited to 60° or less.</p>					
7	90	0.152 with slanted surface	gel	air	1.04,1.34,1.64, 1.94,2.24,2.54
<p>Conclusions: The step was replaced by a slanted section having a horizontal length of 0.608 cm and a vertical height of 0.152 cm. The results show that the flaw at 1.64 cm is easier to detect because the signal is observed for a larger fraction of the scan. An alternative to grinding a step down is to use wedges of two different lengths.</p>					
8	90 no-tilt	0.152	gel	air	
<p>Conclusions: Many of the problems in an inspection arise from the tilting of the wedge. This causes the angle in steel to change and causes the echo to return at a different time than expected. Here the wedge is not tilted as it goes over a step, but is held level and there is a layer of couplant between the wedge and surface. The amplitude is strong for all flaw distances from step and a good signal is received.</p>					

4 Interference Effects Due to a Step Discontinuity in an Inservice Inspection

4.1 Introduction

Let us direct our attention to Table 3.4 and the entries for the flaw at 2.54 cm. Four entries have an amplitude of about 0.2 to 0.3 and one of only 0.088. The amplitude for CAA is 0.294 and for WAA is 0.088. This is a factor of 3.3, but the only difference in the calculations is the couplant, which in one case is gel couplant, and, in the other, water. All other parameters in the calculations are the same. (The inputs to these two cases were checked and confirmed to be correct.) The situation described by these calculations is shown in Figure 4.1. The flaw is located so that the central ray traveling at a 45° angle in the steel will strike the base of the flaw. With this orientation of the wedge the step will have its maximum impact. In this case, approximately half of the beam will pass through steel only, while the other half will pass through the couplant and then through the steel. Why such a difference? For water the speed of sound is 0.148 cm/microsec and for the gel couplant it is 0.165 cm/microsec. The density of the gel couplant is

1.049 g/cm³. Since the speeds are different, the difference in amplitudes may be due to interference effects. That is, if one considers the beam divided into two parts, the two beams will interfere constructively or destructively based upon the path difference between them. If that is so, then changing the step height should also show interference effects. The next section describes the calculations carried out using a toneburst signal, which has a very narrow bandwidth. This is followed by calculations using signals obtained from a spike pulser or a square wave pulser, which have a larger bandwidth.

4.2 Interference Effects: Calculations Using Toneburst Signal

A toneburst signal having a frequency of 2.25 MHz was input to the computer code. It has a bandwidth of 12%. The calculations were carried out using water or Ultrigel II as the couplant.

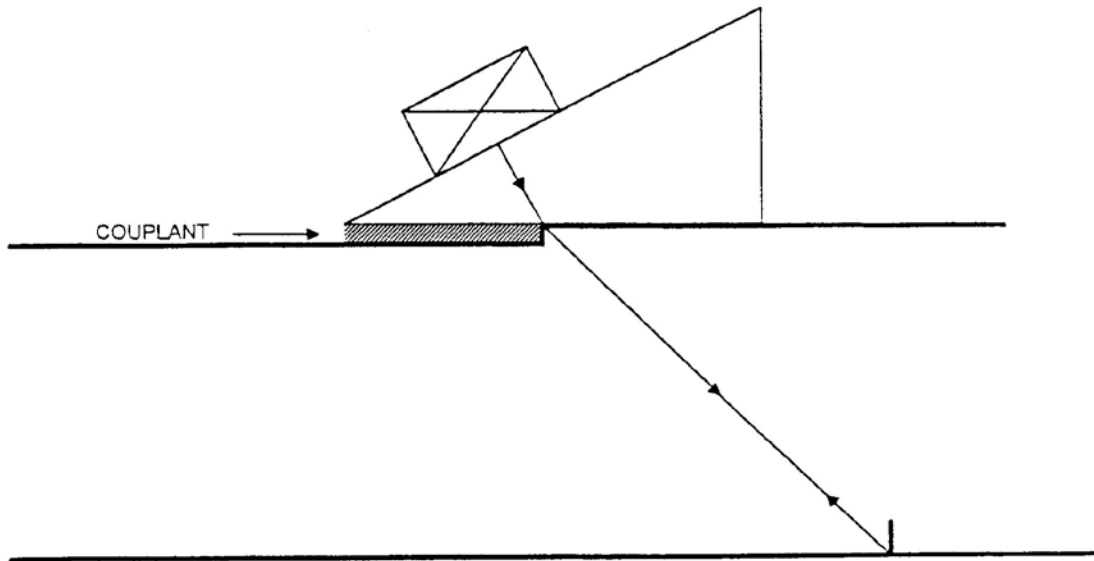


Figure 4.1 The steel plate has a thickness of 2.54 cm and the step height is 0.152 cm. The perpendicular flaw has a half-elliptical shape with a maximum depth of 0.254 cm and is 1.27 cm across the base. In the initial studies the transducer has a center frequency of 2.25 MHz and a diameter of 1.27 cm.

Interference Effects

At 2.25 MHz the wavelength in water is 0.066 cm. In order to see the effects of constructive and destructive interference the step height was changed in integral multiples of 0.007 cm, which is about 1/10 of the wavelength. These values were used for both water and the gel couplant. The results of the calculations are shown in graphs in Figure 4.2. XW is the distance between the tip of die step and the exit point of the central ray from the wedge. The notation "CAA" indicates that a gel couplant was used and that the crack and base of the plate are in air. Similarly, the notation "WAA" indicates that water was used as the couplant.

The results show the periodic behavior of the amplitude. When the step height is about 0.07 cm and 0.19 cm, the amplitude for the CAA case is at a minimum. But, for a

step height of 0.13 cm it is at a maximum. For the WAA case, the amplitude is maximum for a step height of 0.11 cm and 0.21 cm; it is at a minimum for a step height of 0.06 cm and 0.16 cm.

The periodic behavior is due to the fact that the toneburst input signal is close to a pure frequency, since its bandwidth is only 12%. In that case a small step discontinuity may yield results similar to those for a large step. However, inservice inspections are usually carried out using a spike pulser or a square wave pulser. These signals are of much shorter time duration and hence, have a larger bandwidth. In the following section we compare the results of using signals of larger bandwidth and see how the interference effects change.

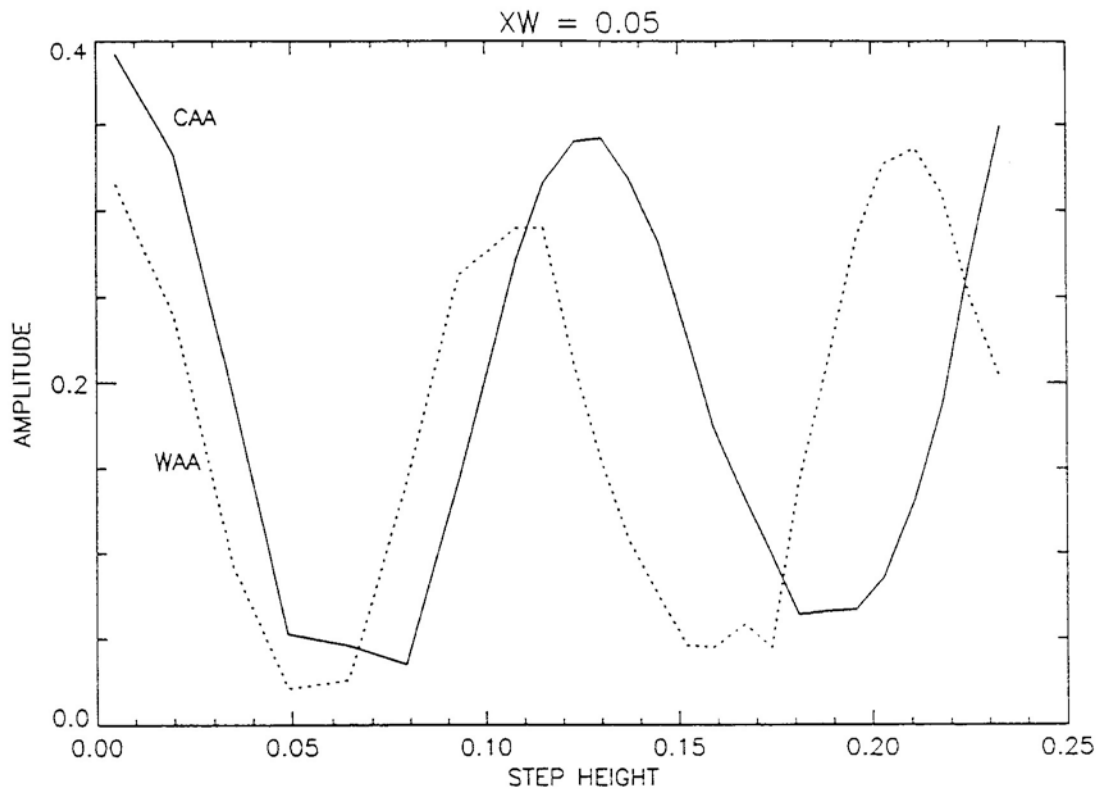


Figure 4.2 Results of modeling calculations using a toneburst signal where the amplitude of the echo is plotted versus the step height. XW is 0.05 cm.

4.3 Interference Effects: Input Signals with Large Bandwidth

A pulse-echo experiment was set up using a variety of transducers and the signal was generated with a square wave pulser or a spike pulser. The echo signal was digitized. In order to obtain the bandwidth the fast Fourier transform (FFT) of each signal was obtained. From 14 signals five signals were selected for use in the model calculations. Four signals had a center frequency of 2.25 MHz and a bandwidth of 20%, 50%, 71%, and 88%. A signal with a center frequency of 4.0 MHz and a bandwidth of 41% was also selected to see the effect of a higher frequency. Figure 4.3 shows the five input signals, and Figure 4.4 and Figure 4.5 show the FFT of two signals.

Calculations were carried out for the CAA and WAA cases and varying the step height. One set of calculations was carried out for each of the five input signals. The output of the calculations is a signal very similar in shape

to the input signal, but of a smaller amplitude. The amplitude is defined as the difference between the maximum (or positive) peak height and the minimum (or negative) peak height. Some results are shown in Figure 4.6. As the bandwidth increases, the ratio between the maximum amplitude and the minimum amplitude decreases. Table 4.1 shows the ratio of the maximum amplitude to the minimum (mini) and the ratio to the minimum (min2) for the CAA case and Table 4.2, for the WAA case. The minimum mini is to the left of the maximum peak and minimum min2, to the right. Table 4.1 and Table 4.2 contains two entries for the 4.0 MHz transducer, because there are two peaks in Figure 4.6 for the 4 MHz curve. Table 4.1 and Table 4.2 show that as the bandwidth is increased, the ratio decreases. This is expected since more frequencies are now used in the calculation. Essentially, what is happening is that destructive interference may occur at one frequency (or wavelength) and constructive interference for another frequency. Therefore, when the bandwidth is large, the summation of constructive interference at some frequencies and destructive interference at other

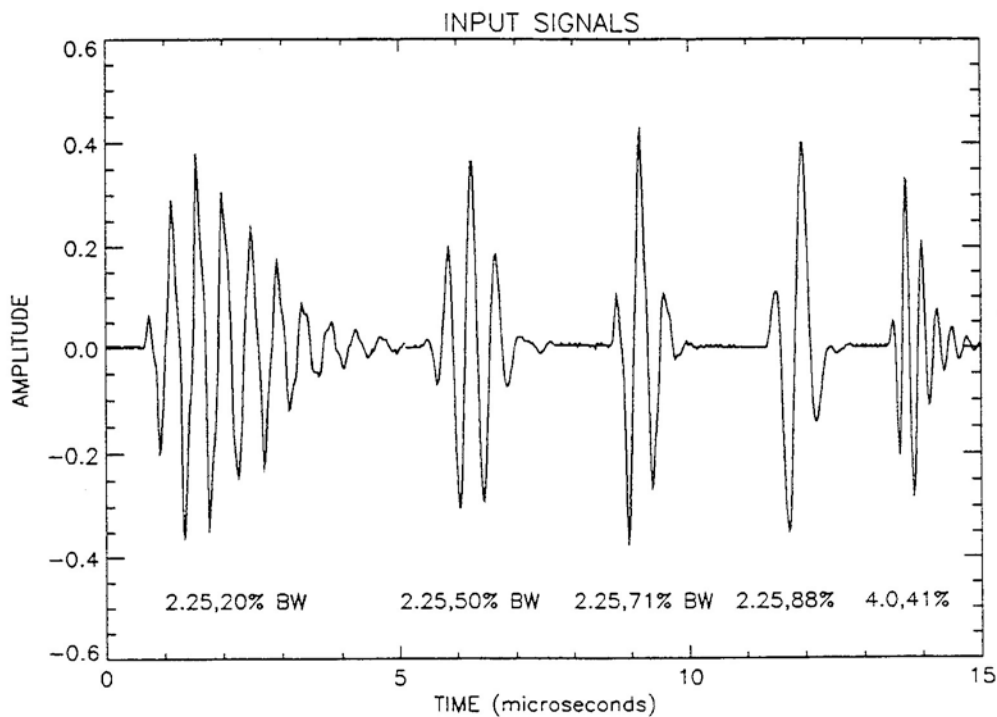


Figure 4.3 Several types of signals that are used as input into the Model III code

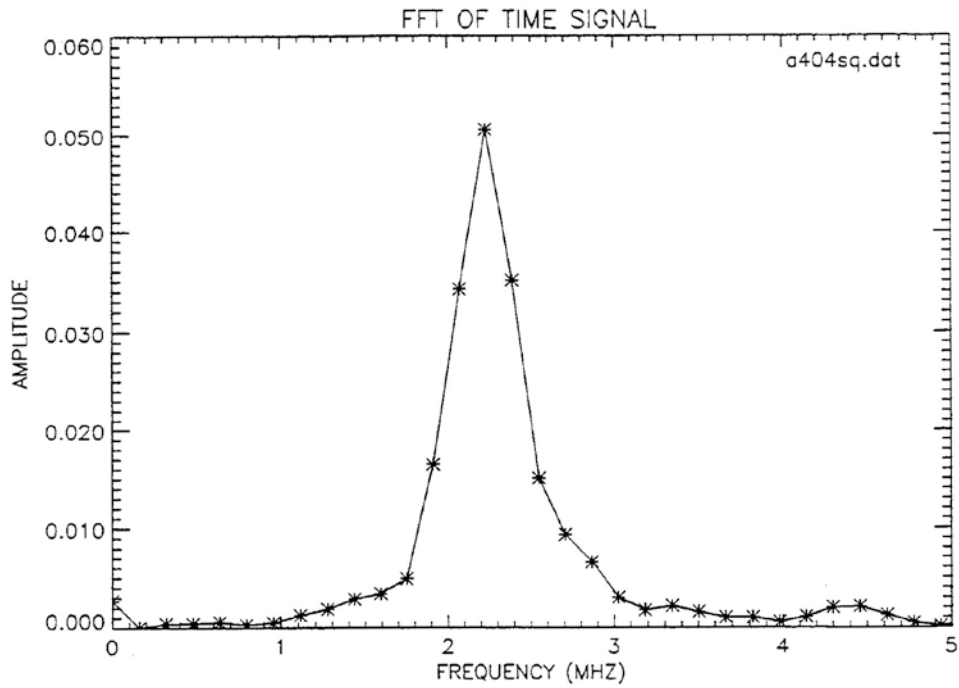


Figure 4.4 Graph showing the fast Fourier transform of a signal having a center frequency of 2.25 MHz and a 20% bandwidth

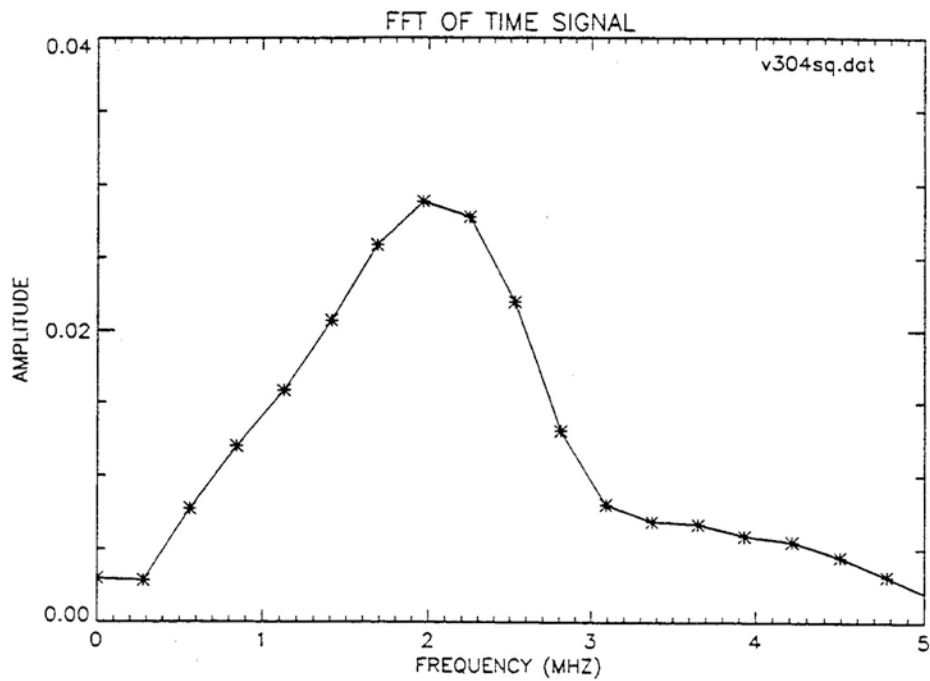


Figure 4.5 Graph showing the fast Fourier transform of a signal having a center frequency of 2.25 MHz and an 88% bandwidth

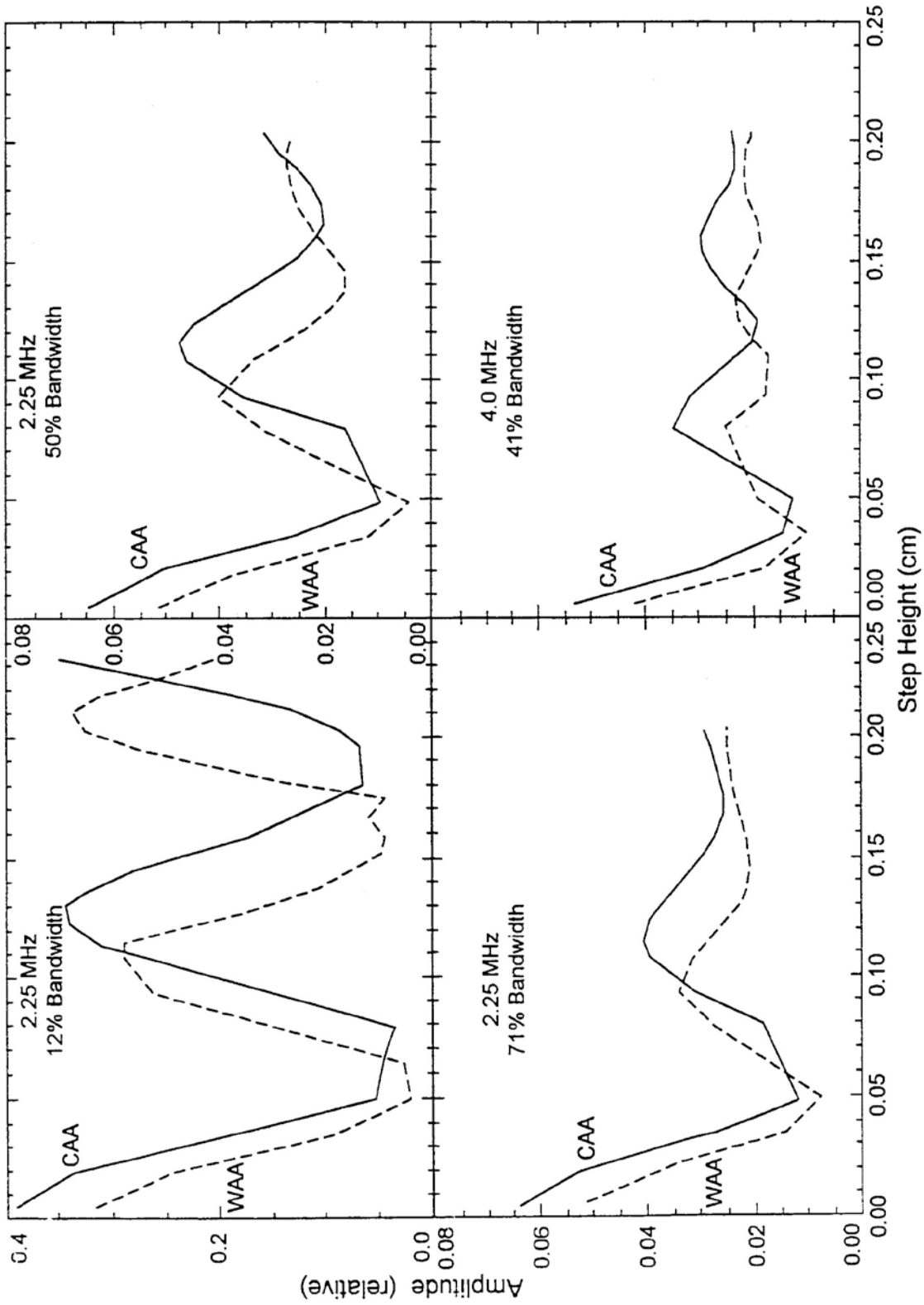


Figure 4.6 Results of modeling calculations showing the variation in amplitude as a function of step height for four signals

Table 4.1 Summary of results for CAA cases.

Frequency, MHz	Bandwidth	Ratio = max/mini	Ratio = max/min2
2.25	12%	9.77	5.34
2:25	20%	6.81	4.00
2.25	50%	5.10	2.33
2.25	71%	3.49	1.55
2.25	88%	3.27	1.42
4.00	41%	2.73	1.82
4.00	41%	1.53	1.26

Table 4.2 Summary of results for WAA cases

Frequency, MHz	Bandwidth	Ratio = max/mini	Ratio = max/min2
2.25	12%	14.10	6.58
2.25	20%	11.42	4.46
2.25	50%	10.33	2.45
2.25	71%	4.74	1.63
2.25	88%	4.17	1.45
4.00	41%	2.55	1.47
4.00	41%	1.36	1.24

frequencies tend to average, and the maxima and minima are not as pronounced. One of the most interesting results of the series of calculations is the results for the 4.0 MHz transducer. Figure 4.6 visually shows that the maxima and minima in the graph are not pronounced. This is likewise noted in the ratio values in Table 4.1 and Table 4.2, which are very small.

In order to understand how the 2.25 MHz and 4.0 MHz transducers produce such different results, let us examine how the input signals are used in the model calculations. The input signal is read from a file and the FFT of the signal is obtained. An amplitude threshold is used to select the range of frequencies over which the calculations

are carried out. Usually this threshold is very low.

Table 4.3 shows the parameters for the five signals used here. When the initial and final frequency values in Table 4.3 are compared, the range of frequencies for the 4 MHz transducer is much larger than for the other cases. Calculations were also run for a 5 MHz transducer using signals generated by the spike pulser and the square wave pulser. Table 4.3 also shows the frequency range for these two cases. Figures 4.7, and 4.8 show the results for these cases. The results suggest that using a larger frequency transducer minimizes the effect of the step.

4.4 Conclusions

There are several important conclusions from these studies.

First of all, one might have the preconceived notion that the larger step height would cause greater problems in an inservice inspection. These studies show that the interference effects can occur for **any** step height. Further, the interference effects are dependent upon the type of couplant used in the inspection. For example, Figure 4.6 (2.25 MHz, 71% BW) shows that there is a deep minimum for the CAA curve for a step height of 0.07 cm, a maximum amplitude for a step height of 0.12 cm, and another minimum for a step height of 0.17 cm. However, the change from the maximum to the second minimum is not nearly as great as for the first minimum. The two ratio values shown in Table 4.1 and Table 4.2 also bear this out. Comparison of the third and fourth columns in these two tables suggest that the undesirable effects of a step discontinuity are **larger** for some smaller step heights.

Secondly, the calculations for transducers having a center frequency of 4 and 5 MHz show that the effects of the step height are much less pronounced than for transducers having a center frequency of 2.25 MHz.

4.5 Experiments Validating Interference Effects

Experiments were carried out to validate the interesting and important effects noted in the modeling studies. The transducer wedge was placed over the step as shown in

Table 4.3 Input signal parameters used in the calculations

Frequency and bandwidth	No. of points in signal file	No. of frequencies	Initial frequency (MHz)	Final frequency (MHz)	Frequency separator (MHz)
2.25, 12%	256				
2.25, 20%	256	9	1.367	2.930	0.195
2.25, 50%	128	6	1.563	3.516	0.391
2.25, 71%	128	12	0.391	4.688	0.391
2.25, 88%	128	9	0.391	3.516	0.391
4.00, 41%	128	15	1.563	7.031	0.391
5.5, 25%	128	10	3.51	7.03	0.391
5.2, 31%	128	13	1.95	6.64	0.391

NOTE: The second column gives the number of points in the data file. The third column gives the number of frequencies used by the Model III code in carrying out the calculation. The fourth column gives the initial frequency and the fifth column, the final frequency used in the calculation. The last column gives the frequency separation of the frequencies used in the calculation.

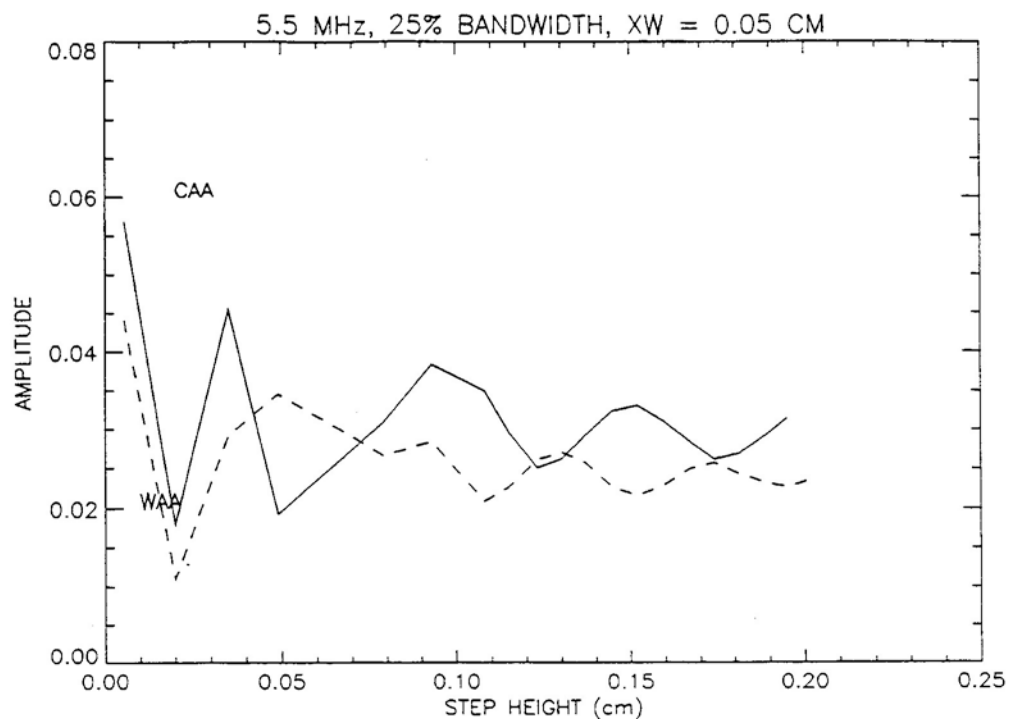


Figure 4.7 Results of modeling calculations using a signal having a center frequency of 5.5 MHz and a 25% bandwidth

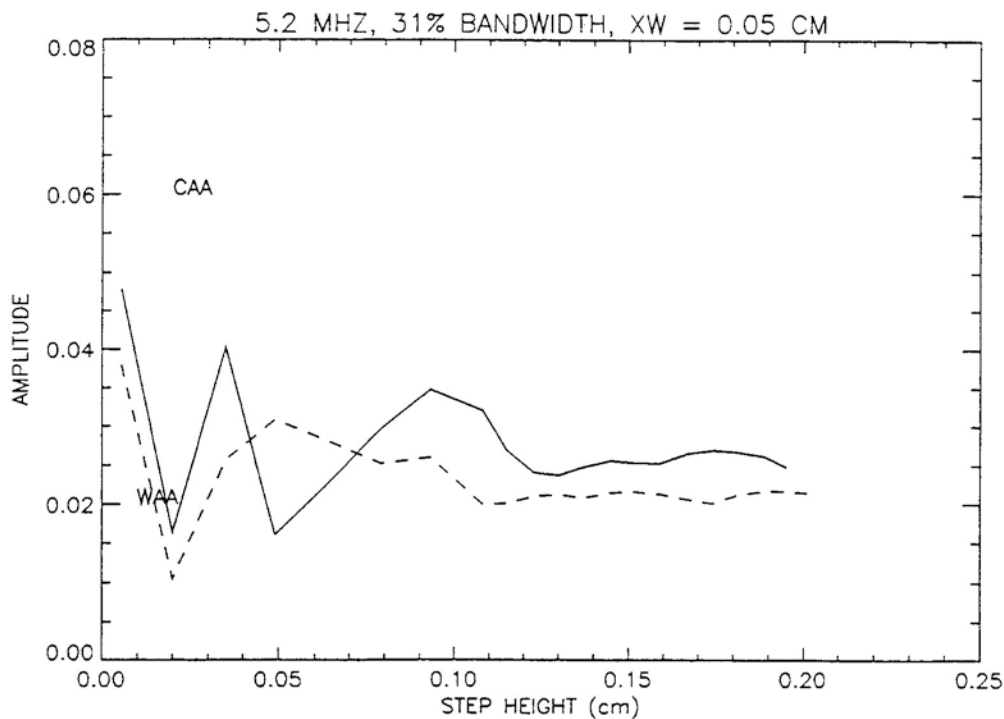


Figure 4.8 Results of modeling calculations using a signal having a center frequency of 5.2 MHz and a 31% bandwidth

Figure 4.1. Steel plates (thickness = 3.11 cm) having step heights of 0.152 cm (60 mils), 0.229 cm (90 mils), and 0.305 cm (120 mils) were used. In each plate the rectangular flaw had a depth of 0.635 cm and a length of 1.59 cm. The horizontal distance between the flaw and the step was 3.11 cm. Thus, similar to Figure 4.1, the central ray passing through the top of the step would strike the base of the flaw. The transducer wedge was designed to produce 45° shear waves in steel. The transducer had a center frequency of 2.25 MHz. These steel plates were used in the validation experiment described in Appendix C. The objective of the experiment was to use a gel couplant, such as Ultrigel II, and water and measure the amplitude of the signal in each case and to compare the results. Also, using the different step heights should show the interference effects noted in Figure 4.2.

In these experiments the flaw and bottom surface of the plate were in air, while the couplant was either Ultrigel II or water. Using water presented a problem since an immersion experiment could not be carried out. This was

solved by using a polymer called carbopol. When a solution of 0.15% carbopol by weight is placed in water, a gelatinous liquid is formed, but the density and speed of sound are extremely close to water. This mixture of carbopol was used in these experiments.

A pulse-echo experiment was set up, the echo was amplified, and the signal observed on an oscilloscope. Two sets of experiments were carried out. In the first set, an analog oscilloscope was used and the cursors determined the peak-to-peak voltage. In the second set a digital oscilloscope was used and an immediate printout of the scope screen was obtained.

A toneburst generator was used to produce the signal to excite the transducer. In the modeling studies we found that using a larger bandwidth signal reduced the interference effects of the step. That is, the ratio of the maximum amplitude to the minimum amplitude was reduced. To see if this effect was observed in the experiments, two types of signals were used: (1) a typical toneburst signal, and (2) a signal of short time duration was obtained

by reducing the toneburst signal to one cycle. Figure 4.9a shows the response for a 0.152 cm step using a toneburst signal and Ultrigel II as the couplant. In Figure 4.9b the only difference is that the couplant is water (carbopol). Figures 4.10a and 4.10b show similar results for a 0.229 cm step. Figures 4.11 and 4.12 show similar data for the two step heights using a signal with a larger bandwidth.

Theoretical calculations were also carried out for each case. Table 4.4 displays the experimental data and the results of the calculations. Both sets of experimental data are shown. The first line gives the data obtained using an analog scope, and the second line, the digital oscilloscope. These two lines show the error in the measurements due to different manual pressure exerted on the wedge and slightly different orientations of the wedge. In order to compare the experimental measurements with the theoretical calculation, the experimental data are normalized to the no-step case for each type of signal, using the average values of the two measurements. The theoretical calculations are normalized in the same way.

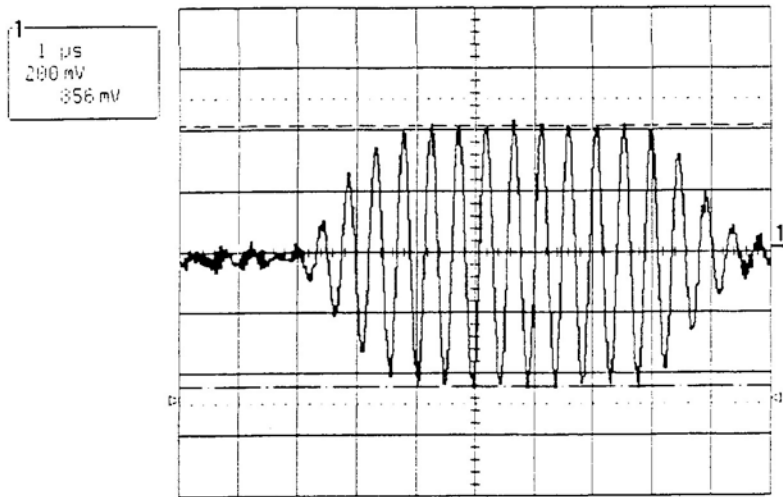
Table 4.4 shows some very interesting results. Even though the only difference in the experiments is the type of couplant used, columns 4 and 5 show quite different normalized responses for all values of the step height. This is in general agreement with the results of the modeling calculations shown in Figure 4.2. For a step height of 0.152 cm, the ratio of the normalized responses is 0.78/0.42, or 1.9. For a step height of 0.229 cm, this ratio is 0.28/0.64, or 0.44. These ratios indicate a characteristic noted in Figure 4.2. The curves for CAA and for WAA show maxima and minima, but they do not

occur at the same step height. For one step height, the response will be larger for CAA than WAA, but for another step height the reverse is true.

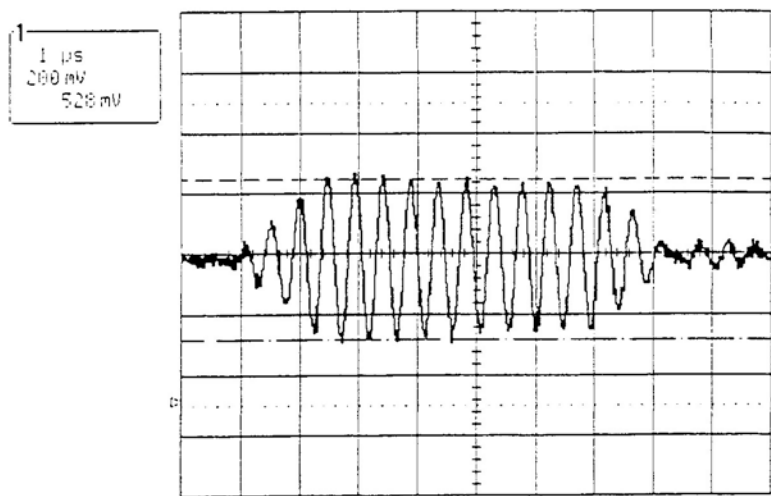
Table 4.4 also shows that the response due to different step heights varies, but not in a way that can easily be predicted. For example, column 4 shows that as the step height increases the normalized response goes from 0.78, to 0.28, and then to 0.54. Similarly, column 5 shows a trend of 0.42, to 0.64, and then to 0.33. These experimental results are in agreement with the oscillatory nature of the response shown in Figure 4.2.

The lower half of Table 4.4 shows that when a signal of larger bandwidth is used, the effect of the step is reduced. For example, column 4 shows that as the step height increases the normalized response goes from 0.69, to 0.38, and then to 0.40. This shows that the change in amplitude with a change in step height is not as large as for a toneburst signal, where the corresponding normalized response goes from 0.78, to 0.28, to 0.54. This is in agreement with the results of the modeling calculation shown in Table 4.1, where the ratio of the maximum to the minimum decreased when bandwidth of the signal increased.

The theoretical calculations (for step heights of 0.152 cm and 0.229 cm) are in good agreement with the experimental data, given the uncertainties in the experiments. The exception to this is the theoretical calculation for a step height of 0.229 cm for the gel type couplant, where the theoretical calculations are larger than the experimental data. This comparison shows the ability of the computer code to predict with reasonable accuracy the results of an inservice inspection.

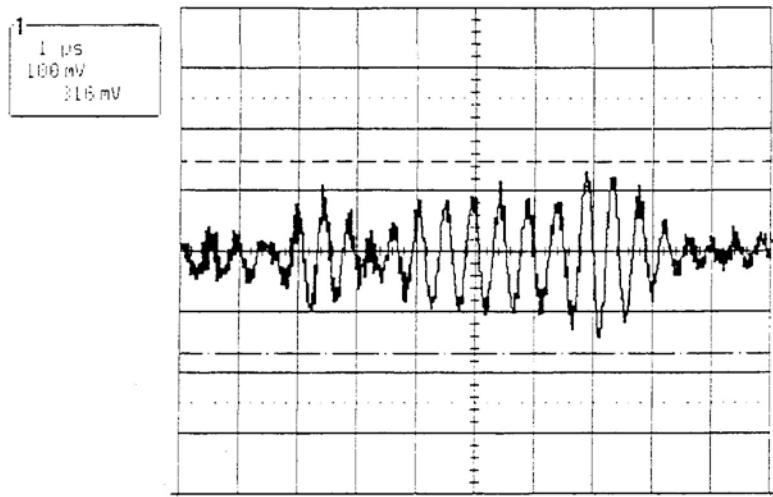


(a)

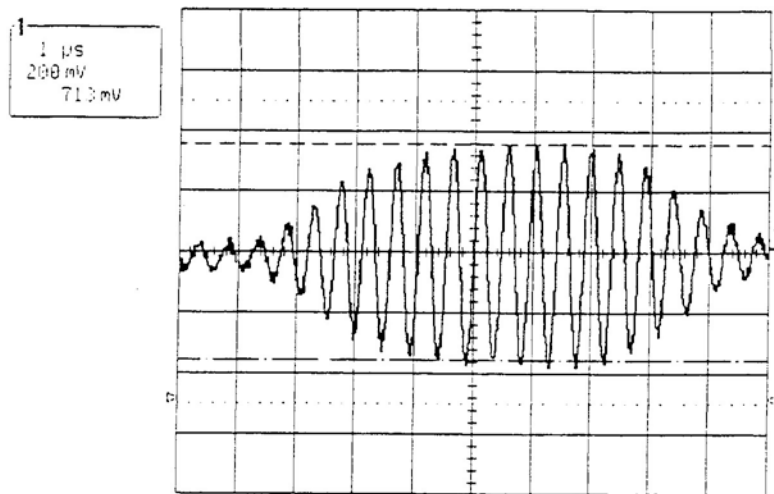


(b)

Figure 4.9 Response from 0.152 cm step height using a toneburst signal. In (a) a gel couplant, such as Ultragel II, was used and in (b) water (carbopol) was used as the couplant. The flaw and bottom surface are in air.

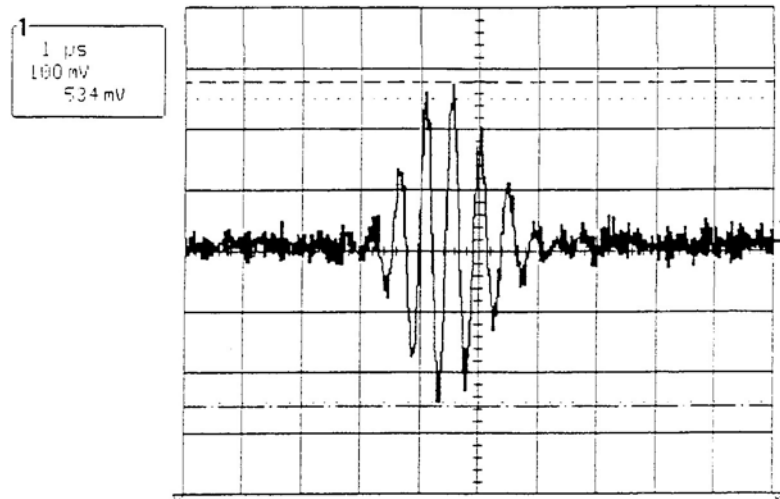


(a)

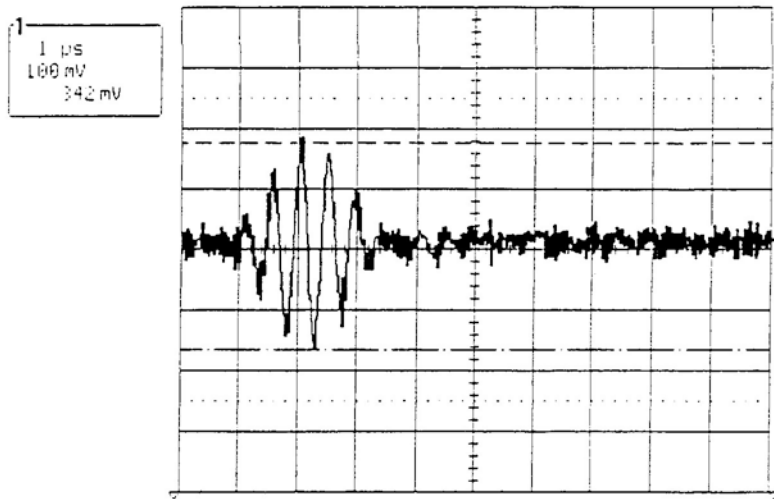


(b)

Figure 4.10 Response from 0.229 cm step height using a toneburst signal. In (a) a gel couplant, such as Ultragel II, was used and in (b) water (carbopol) was used as the couplant. The flaw and bottom surface are in air.

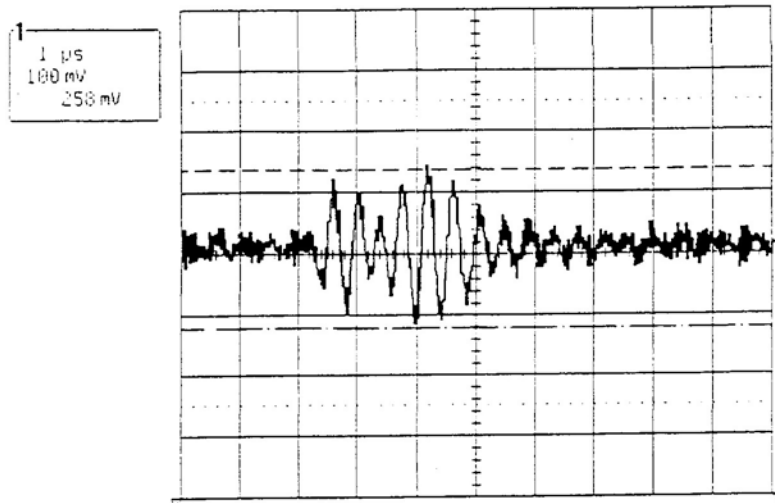


(a)

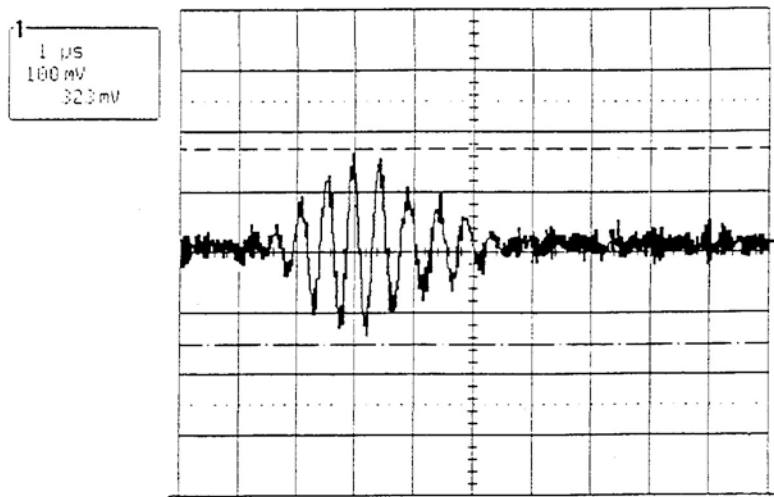


(b)

Figure 4.11 Response from a 0.152 cm step height using a signal of short time duration. In (a) a gel couplant was used and in (b) water (carbopol) was used as the couplant. The flaw and bottom surface are in air.



(a)



(b)

Figure 4.12 Response from a 0.229 cm step height using a signal of short time duration. In (a) a gel couplant was used and in (b) water (carbopol) was used as the couplant. The flaw and bottom surface are in air.

Table 4.4. Peak-to-peak amplitude response obtained using Ultrigel II and water and a toneburst signal and signal with a larger bandwidth for various step heights. For each step height the first row gives the data obtained using an analog oscilloscope, while the second line is that obtained using a digital oscilloscope.

Step height, cm	Gel response, volts	Water response, volts	Experimental		Theoretical		
			Gel normalized response	Water normalized response	Gel normalized response	Water normalized response	
Toneburst:							
none	1.10	0.96	--	--	--	--	
none	1.14	0.99	1.0	0.87	1.0	0.83	
0.152	0.89	0.42	--	--	--	--	
0.152	0.86	0.53	0.78	0.42	0.63	0.31	
0.229	0.35	0.72	--	--	--	--	
0.229	0.27	0.71	0.28	0.64	0.84	0.62	
0.305	0.67	0.43	--	--	--	--	
0.305	0.63	0.30	0.54	0.33	--	--	
Larger Bandwidth:							
none	0.75	0.63	--	--	--	--	
none	0.72	0.68	1.0	0.89	1.0	0.83	
0.152	0.49	0.38	--	--	--	--	
0.152	0.53	0.34	0.69	0.49	0.53	0.32	
0.229	0.30	0.36	--	--	--	--	
0.229	0.26	0.30	0.38	0.45	0.62	0.42	
0.305	0.27	0.21	--	--	--	--	
0.305	0.31	0.17	0.40	0.26	--	--	

5 Discussion and ASME Code Recommendations

5.1 Results of Computer Modeling Studies

As a basis for making ASME Code recommendations, some of the important results obtained from the modeling studies will be summarized and discussed:

- (1) One result was that the location of the flaw relative to the step is an important parameter. It is possible for a flaw to be located so that it is observed during an inspection only when the transducer wedge, having reached the step, rotates upward to go over the step. Such a flaw will give only a momentary small signal and thus, will be difficult to detect. Computer studies were carried out with wedges of two different lengths. The results showed that the location of the hard-to-detect flaw depended upon the wedge length. This suggests that an inspection carried out with wedges of two different lengths would detect the flaw during an inspection with one or both wedges.
- (2) In contrast, flaws at some locations will be observed three times due to the tilting of the wedge and motion along the surface. It is important for the person carrying out the inspection to realize that this can occur and not to record three flaws, rather than only one flaw.
- (3) When the wedge is tilted, the central rays makes an angle greater than 45° in steel. The reason is that refraction occurs at the wedge-couplant interface and also at the couplant-steel interface. For example, when the wedge is tilted by only 3.4° , the angle in steel changes from 45° to 54.4° . As a result, the central ray travels a longer distance in steel and the round-trip time is increased by nearly 5 microseconds for a steel plate 2.54 cm thick.
- (4) Modeling studies carried out using a step height of 0.229 cm and a short wedge showed that the angle of tilt could be as great as nearly 10° . In this case, depending upon the couplant used, the angle of the central ray in steel was about 85° . For a different couplant, the central ray was completely reflected at the couplant-steel interface. Clearly, this condition is unacceptable in an inspection and the angle of tilt must be limited.
- (5) There is another reason that the angle of tilt of the wedge must be limited. Figure 3.7b shows the path of the central ray on the bottom surface of the plate. In this case the maximum angle of tilt of the wedge (see Table 3.1) was about 5° . Figure 3.7b shows that, as the wedge is tilted to go over the step, the path of the central ray travels about 2 cm over the bottom surface. If the tilt is increased to a larger angle, the distance over the bottom surface will be still larger.
- (6) As noted in (1) a flaw at some location relative to the step will be difficult to detect. Modeling studies in which the step is replaced by a slanted surface show that such a flaw is easier to detect because the signal is observed for a larger fraction of the scan. Instead of rotation when it reaches the step, the rotation of the wedge is more gradual as the tip of the step moves along the slanted portion of the surface.
- (7) Another type of scan is one in which the wedge is simply not tilted as the wedge encounters a step. This is a no-tilt inspection in which the wedge is not tilted but a layer of couplant is used between the wedge and the steel surface. The results show that the amplitude is strong for all flaw distance from the step and a strong signal is observed. This may be difficult to implement and would require that the scan be carried out by traveling over the high part of the step first and then pushing the wedge down through the couplant to the lower part of the step.
- (8) There are two effects of the step. The first is that the wedge must be tilted to go over the step and these effects have been discussed above. The second is that, when the central ray emerging from the wedge strikes near the top of the step, interference effects due to the step discontinuity come into play. That is, part of the ultrasonic beam passes through a layer of couplant and then enters the steel surface on the lower portion of the step. Another part of the beam

passes through the top portion of the step. These two parts of the beam can interfere, either constructively or destructively. Modeling studies carried out for this situation using a tone-burst signal showed maxima and minima, depending upon the step height and the couplant used. **The important conclusion is that interference effects, resulting in a reduced signal strength, can occur for any step height.** This is a very important result, because there seems to be a tendency to think that a large step height will cause problems in an inspection, while a small one will not. The results of these modeling studies show that this tendency or this preconceived idea is simply not correct.

- (9) Studies of the interference effects also used signals ranging in bandwidth from 20% to 88%. In contrast, a tone-burst signal has a bandwidth of about 12%. These results showed that the difference between the maxima and the minima could be reduced by increasing the bandwidth. These studies also showed that the interference effects were further reduced by using a signal having a center frequency of 4 MHz, rather than 2.25 MHz. Thus, the interference effects due to the step can be reduced if the inspection is carried out at 4 MHz or 5 MHz, rather than 2.25 MHz, and if the bandwidth of the system is, say, 60%. However, there are problems with this. At a frequency of 4 MHz, the signal is more strongly attenuated and the return signal will be therefore, much harder to detect. Also, using a signal of large bandwidth will cause the signal to noise ratio to decrease, which also will lead to increased difficulty in interpreting the inspection data. It is possible that in some inspections it may well be possible to use a higher frequency and larger bandwidth signal, while in other this is simply not the case. It is difficult to quantify the situation, but it is important that the person carrying out the inspection is aware of these possibilities to eliminate the undesirable effects of surface roughness.
- (10) The validation studies for Model III in Appendix B were carried out for a the wedge tilted at a given angle for the entire scan. These angles were 0°, 1°, 2°, 3°, and 4°. Data were obtained when the ultrasound passed through a step discontinuity and compared with data obtained for a smooth surface. These studies show some unexpected results. Table B.3 shows, for 0° tilt, that a step height of

0.152 cm (60 mils) causes the amplitude to be reduced by nearly a factor of 2 compared to the no-step data. For a 4° tilt the amplitude for the no-step case is smaller than for a 0.152 cm step. These results are surprising. However, in Chapter 4 we learned that constructive and destructive interference effects depend upon the step height as well as the type of couplant. Therefore, while these results are surprising, they are understandable.

- (11) Validation experiments carried out for step heights of 0.229 cm (90 mils) and 0.305 cm (120 mils) also show some unexpected results. For these larger steps the amplitude varies much less than for the 0.152 cm step. For the 0.229 cm step the amplitude was reduced by only a factor of 1.5 (3.5 dB) for a 4° tilt compared to the no-step level case. For a similar comparison for the 0.305 cm step, the reduction is greatest for a tilt of 2° and it is a factor of 2.5 (8 dB). These results are shown in Table B.6.

5.2 ASME Code Recommendations

Let us first consider the flaw that is hard to detect due to its location. This is addressed in (1) and (5) above. The possibilities are as follows: (1) wedges of two different lengths can be used, (2) the surface can be ground to form a slanted surface, and (3) a wedge designed to produce a larger angle in steel, say, 60°, can be used. In this last case, the hard-to-detect flaw would be observed before the tip of the wedge reached the step, assuming that the 45° and 60° wedges had the same length. Also, the 60° beam angleinsonified the total volume that required inspection that was not covered by the 45° inspection angle. However, rather than making an ASME Code recommendation, this information could be listed as a precautionary measure in the Weld Inspection Procedure.

It is clear that tilting the wedge causes undesirable effects. However, an important effect is documented in the validation studies for Model III for a step height of 0.152 cm, which are given in Appendix B. These results show that as the transducer wedge is tilted the amplitude of the signal decreases and the signal also becomes somewhat distorted at a tilt angle of 4° for a step height of 0.152 cm. These results are discussed in (10) above and in more detail in Appendix B. This would seem to indicate that the tilt angle be limited to 4°. However,

there are some additional considerations. The validation experiments and calculations were carried out when the wedge was tilted to a certain angle for the entire scan. This is quite different from an inservice inspection where the tilt angle is continually changing. Therefore, another look should be given to the model calculations for an inservice inspection. Some observations are as follows:

- (1) For a wedge having a length of 3.44 cm (Case 1), Table 3.1 shows that the maximum angle of tilt is 5° (stage 15). This maximum tilt occurs only for a short time during the scan. Table 3.2 compares the amplitude from the calculations with that from a smooth surface (0.461). The amplitude of the response for all flaw locations seems quite acceptable, except for the hard-to-detect flaw at 0.9 cm.
- (2) For a wedge having a length of 2.34 cm (Case 2), Table 3.3 shows that the maximum tilt angle is 7.4° and the maximum angle in steel is 69.4° . Table 3.4 shows that compared to the smooth surface case (0.342) reasonable amplitudes are again obtained, except for the hard-to-detect flaw at 1.64 cm.

The validation experiments for two larger steps show that the amplitude is decreased by a **smaller** amount than for the 0.152 cm step. This is discussed in item (11) above and in Appendix B.

When the wedge is tilted to go over a step, the angle in steel becomes greater than 45° . This has been discussed in item (3) above. A tilt of 5° corresponds to an angle in steel of 60° . Considering all of these factors it seems reasonable to limit the angle of tilt of the transducer wedge to 5° or less. Therefore, the ASME Code recommendation is that the wedge be tilted by no more than 5° .

The 5° limit can be maintained during an inspection by considering the wedge length and the step height. We shall consider the same scenario used in the modeling of an inservice inspection in Ch. 3. That is, the wedge approaches the step and the tip of the wedge is rotated to go over the step. Next, the wedge slides over the step for **half its length** and then rotates back so that the wedge is on top surface. Table 5.1 shows the length of the wedge and the step height permitted so that the 5° limit is not exceeded. The weld crown can be ground to ensure, that with the choice of the transducer wedge, the height is sufficiently reduced to maintain the 5° limit.

Table 5.1 Maximum step height as a function of transducer wedge length^(a)

Wedge length, cm	Maximum permitted step height, cm
1.79	0.055
1.91	0.083
2.54	0.111
3.18	0.139
3.81	0.166
4.45	0.194
5.08	0.221
5.59	0.244
6.35	0.274

(a) This table displays the maximum step height that can be traversed by a transducer wedge of a given length and not exceed the 5° angle of tilt limitation. After traveling half its length across the step, the wedge rotates back to the top surface of the step.

The information obtained from this research can be used to add notes in the procedures: (1) When welds are repaired the 5° limit should be considered and the surface prepared accordingly. (2) For analysis of inspection of welds it is important to have an accurate profile to know where the sound beam has propagated in the component. (3) Where weld profiles exist, the inspector can review them and select search units and angles so that there are no problems with the inspection.

5.2.1 Wavy or Blended Surface

Some inspections will encounter a wavy or blended surface. Figure 5.1 shows such a surface with the transducer wedge in two locations. When the transducer wedge travels over a slightly curved section, the base of the wedge will be approximately perpendicular to the normal to the surface. When the central ray travels into the steel component, it will make a 45° angle with the normal to the surface. However, the angle that the central ray makes with the normal to the bottom surface is not 45° . If the surface is inclined at an angle of 14° , then, for the transducer position on the left in Figure 5.1, the

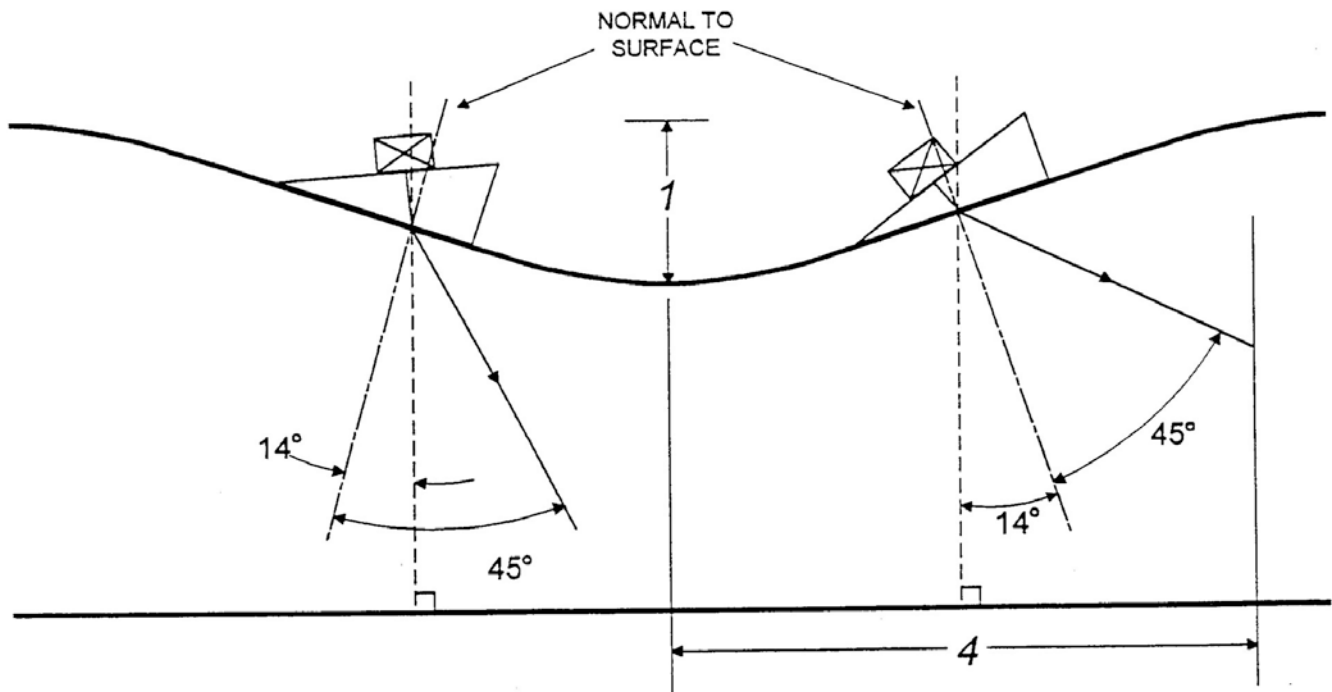


Figure 5.1 Transducer on a wavy or blended surface

effective angle in steel is 31° relative to the normal to the bottom surface. Similarly, for the position on the right, the effective angle is 59° .

The reason for the choice of 14° is that the maximum permitted angle in steel is about 60° , which was also the angle used to limit the transducer tilt to 5° . The tangent of 14° is 0.25 and therefore, the slope of the inclination has a 1 to 4 ratio, as is also shown in Figure 5.1.

Therefore, the ASME Code recommendation is that for a wavy or blended surface the angle of inclination be limited to 14° , or to a ratio of one to four ($\tan 14^\circ = 0.25$).

Because the wavy or blended surface causes problems, in new work this can be eliminated. Therefore, the third recommendation is that for new welds and repair welds the method of contour grinding should not be used. The excessive weld crown should be reduced uniformly until flush with the adjacent surface or until the 5° limit in the first recommendation can be maintained.

The ASME Code recommendations are summarized as follows:

Recommendation I: During an inspection the angle at which the wedge is tilted can be no more than 5° . This 5° limit can be maintained by considering the wedge length and the step height.

Recommendation II: During an inspection of a wavy or blended surface, the angle of inclination of the surface is limited to 14° , or to a ratio of 4 to 1 for the inclination.

Recommendation III: For new welds and repair welds the method of contour grinding should not be used. The excessive weld crown should be reduced uniformly until flush with the adjacent surface or until the 5° limit stated in Recommendation I can be maintained.

6 References

- Auld, B. A. 1979. "General Electromechanical Reciprocity Relations Applied to the Calculation of Elastic Wave Scattering Coefficients," *Wave Motion*, Vol. 1, 1979, pp. 3-10.
- Barger, V. D. and M. G. Olsson. 1987. *Classical Electricity and Magnetism: A Contemporary Perspective*. Allyn and Bacon, Inc., Boston.
- Beyer, R. T. and S. V. Letcher. 1969. *Physical Ultrasonics*. Academic Press, New York.
- Cavanagh, E. and B. D. Cook. 1981. "Lens in the Nearfield of a Circular Transducer: Gaussian-Laguerre Formulation," *Journal of the Acoustical Society of America*, Vol. 69, 1981, pp. 345-351.
- Cook, B. D. and W. J. Arnoult III. 1976. "Gaussian-Laguerre/Hermite Formulation for the Nearfield of an Ultrasonic Transducer," *Journal of the Acoustical Society of America*, Vol. 59, No. 1, January 1976, pp. 9-11.
- Good, M. S. 1988. "Appendix A: Significance of Surface Condition upon Ultrasonic Inspection," in *Nondestructive Examination (NDE) Reliability of Inservice Inspection of Light Water Reactors, Semi-Annual Report April-September 1987*, NUREG/CR-4469, Vol. 7.
- Good, M.S. 1990. "Appendix A: Matrix of Surface Conditions and Ultrasonic Inspection Parameters for EPRI/NDE Study," in *Nondestructive Examination (NDE) Reliability for Inservice Inspection of Light Water Reactors, Semi-Annual Report October 1988-March 1989*, NUREG/CR-4469, Vol. 10.
- Good, M.S. 1991. "Phase Mapping of Ultrasonic Fields Passed through Centrifugally Cast Stainless Steel," *Review of Progress in Quantitative Nondestructive Evaluation*, Vol. 10B. Plenum Press, New York, New York. pp. 1975-1982.
- Green, E. R., S. R. Doctor, R. L. Hockey, and A. A. Diaz. 1992. *Development of Equipment Parameter Tolerances for the Ultrasonic Inspection of Steel Components: Application to Components Up to 3 Inches Thick*, NUREG/CR-5871, Vol. 1.
- Greenwood, M. S. 1992. "Appendix A: Modeling of a Step Discontinuity," in *Nondestructive Examination (NDE) Reliability of Inservice Inspection of Light Water Reactors, Semi-Annual Report April 1991-September 1991*, NUREG/CR-4469, Vol. 14.
- Greenwood, M. S., J. L. Mai, A. Minachi, I. Yalda-Mooshabad, and R. B. Thompson. 1993. "Ultrasonic Propagation through a Surface with a Step Discontinuity: Validation of a Hybrid, Gauss-Hermite Ray Tracing Beam Model," *Review of Progress in Quantitative Nondestructive Evaluation*, Vol. 12A, Plenum Press, New York, New York, pp. 203-210.
- Greenwood, M. S. 1994. *Development of Equipment Parameter Tolerances for the Ultrasonic Inspection of Steel Components: Application to Components up to 12 Inches Thick and to Circular Components*, to be published as NUREG/CR-5871, Vol. 2.
- Greenwood, M. S. and J. J. Walters. 1994. "A Two-Dimensional Ray Tracing Model for Studying Flaw Detection Reliability of Circular Steel Components," *Review of Progress in Quantitative NDE*, Vol. 13 A, Plenum Press, New York, New York, pp. 93-100.
- Kinsler, L. E., A. R. Frey, A. B. Coppens, and J. V. Sanders. 1982. *Fundamentals of Acoustics*, 3rd Edition. John Wiley and Sons. New York.
- Minachi, A., R. B. Thompson, M. S. Good, and A. A. Diaz. 1991. "Ultrasonic Wave Propagation through an Interface with a Step Discontinuity," *Review of Progress in Quantitative Nondestructive Evaluation*, Vol. 11 A, Plenum Press, New York, New York, pp. 161-168.
- Thompson, R. B., T. A. Gray, J. H. Rose, V. G. Kogan, and E. F. Lopes. 1987. "The Radiation of Elliptical and Bicylindrically Focus Piston Transducers," *Journal of the Acoustical Society of America*, Vol. 82, No. 5, November 1987, pp. 1818-1828.

Appendix A

Validation of Model I and Model II Codes

Appendix A

Validation of Model I and Model II Codes

A.1 Introduction

Appendix A describes the validation of the Model I and Model II codes. Section A.2 provides a description of Model I. Section A.3 presents some basic concepts that are needed to discuss the propagation of ultrasound from a planar transducer in Section A.4. Section A.5 discusses additional features of the computer code for Model I and the input parameters. Section A.6 describes the apparatus and the experimental measurements. Section A.7 compares the results of theoretical calculation using Model I with experimental data. Section A.8 presents the theoretical basis for Model II and provides a description of the computer code. In Section A.9 the experimental apparatus for the validation of Model II is described and the data analysis procedures are reported. Section A.10 presents the comparison of the experimental data with the predictions of Model II. Section A.11 summarizes the research for Model I and Model II and the conclusions obtained.

A.2 Description of Model I

The objective of the Model I code is to predict theoretically the pressure measured by the microprobe in Figure A.1.

Essentially, the Model I code consists of the following four parts:

- (1) The pressure generated by the transducer is an analytical solution to the wave equation, which has the form of a series of Gaussian-Hermite basis functions. This solution is used to predict the beam profile at the surface interface.
- (2) A ray-tracing model is then used to approximate the change in the beam as it propagates across the irregular interface. The interface is described by a

square grid of points, describing the x, y, and z coordinates of each point and the components of a vector normal to the surface at that grid point. A ray is projected from each grid point onto a so-called transmitted plane.

- (3) The fields are re-expressed in terms of the Gaussian-Hermite analytical solution, which is used to describe the subsequent propagation from the transmitted plane to the bottom surface. The initial version of the code gives the amplitude versus the x-coordinate using the coordinate system described in Figure A.1.
- (4) The next improvement to the model involved propagating rays from the metal into the water below the plate, using a procedure similar to that employed at the entry surface. This describes the pressure measured by the microprobe, usually several millimeters below the metal plate.

Figure A.1 illustrates these four steps for an ultrasound beam normal to a surface with a step discontinuity. Note that the density of arrows in the illustration is indicative of the pressure.

These four steps provide an overview of how the computer code operates. With this introduction we shall now discuss these steps in more detail keeping in mind that a complete theoretical description of this model is beyond the scope of this report. Rather, the intention is to provide enough information about the theory to give the reader a basic notion of how the computer code operates.

A.3 Some Basic Concepts

This section defines some of the fundamental concepts that are used to discuss the propagation of ultrasound from a planar transducer in Section A.4.

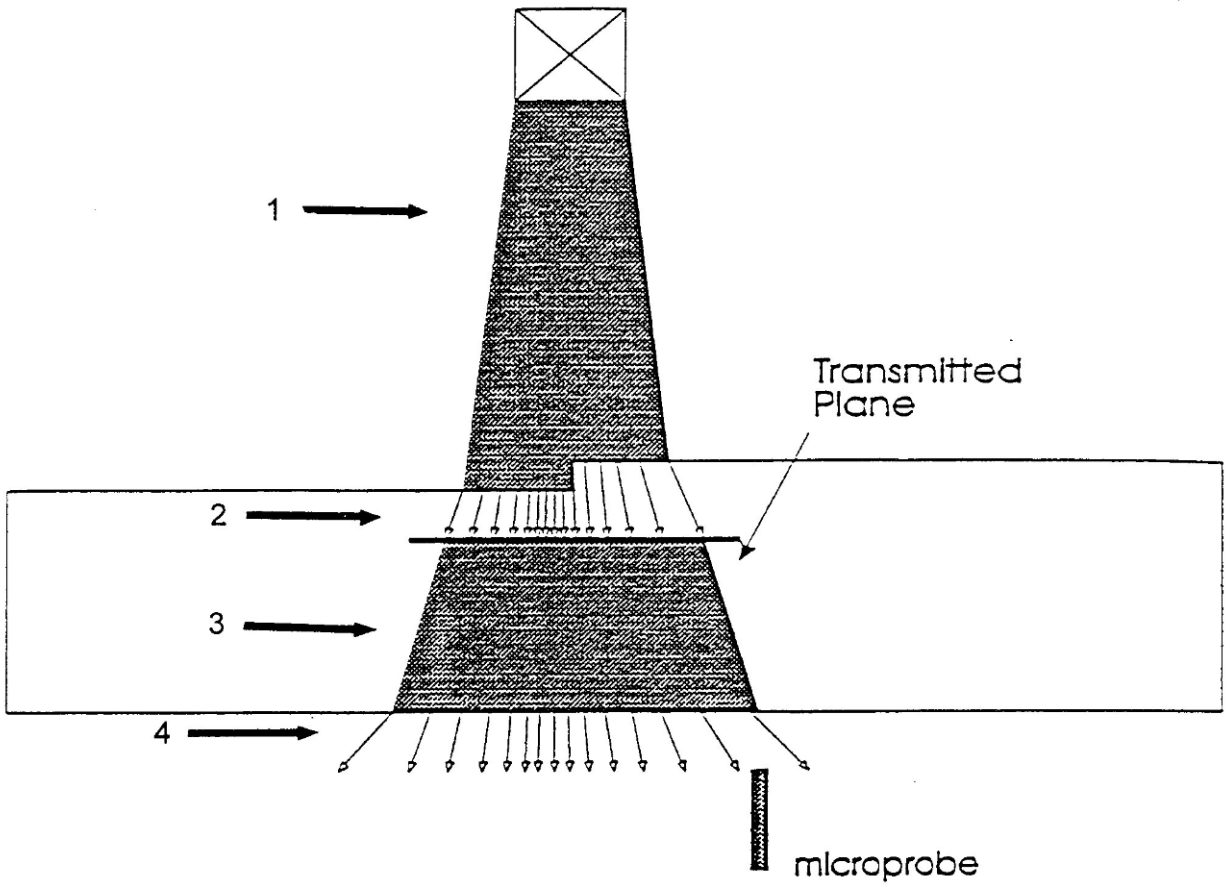


Figure A.1 Illustration of the four parts of the Model I computer code to describe the propagation of ultrasound: 1) from the transducer to the interface, 2) through the interface, 3) through the metal plate, and 4) through the bottom surface into the water. The analytical solutions are shown by the shaded regions and the arrows indicate the ray-tracing solutions.

A.3.1 Relationships Between Pressure, Displacement, and Velocity

Consider a very small fluid element dV that moves with the fluid. The fluid is subjected to an acoustic wave causing the element to be displaced from its equilibrium position. Let the vector displacement be designated by ξ . Application of Newton's second law of motion to the element dV results in the following relationship:

$$\nabla p = -\rho \frac{\partial^2 \xi}{\partial t^2} \quad (\text{A.1})$$

where ρ is the density of the fluid and p is the pressure.

The velocity of the element dV is given by

$$u = \frac{\partial \xi}{\partial t} \quad (\text{A.2})$$

Equation (A.1) becomes

$$\nabla p = -\rho \frac{\partial u}{\partial t} \quad (\text{A.3})$$

A.3.2 Velocity Potential

The velocity potential Φ is defined as follows:

$$u = \nabla \Phi \quad (\text{A.4})$$

Substituting Equation (A.4) into Equation (A.3) results in the following relationship:

$$p = -\rho \frac{\partial \Phi}{\partial t} \quad (\text{A.5})$$

This establishes the relationship between the pressure and the velocity potential. If one solves for the velocity potential, then the pressure can be easily determined.

A.3.3 Wave Equations

Both the pressure and the velocity potential satisfy the wave equation.

$$\nabla^2 p = \frac{1}{c^2} \frac{\partial^2 p}{\partial t^2} \quad (\text{A.6})$$

$$\nabla^2 \Phi = \frac{1}{c^2} \frac{\partial^2 \Phi}{\partial t^2} \quad (\text{A.7})$$

where c is the speed of sound.

A.4 Propagation of Ultrasound from a Planar Transducer

The propagation of ultrasound from a transducer has been the subject of several important papers (Cook and Arnoult, 1976; Cavanagh and Cook, 1981; and Thompson et al., 1987). In the following discussion we shall make references to these papers. In addition, to clarify some points of the discussion, we shall use numerical examples by considering a planar transducer that has a radius of 0.635 cm (0.25 inches) and a center frequency of 2.0 MHz. When immersed in water, this transducer produces ultrasound that has a wavelength of 0.0742 cm and has a wave number, defined by $k = 2\pi/\lambda$, equal to 84.67 cm^{-1} .

Let us consider a planar transducer located at $z = 0$ with a beam propagation along the z axis. Then the velocity potential is given by

$$\Phi = \psi(x, y, z) \exp j(\omega t - kz) \quad (\text{A.8})$$

When Equation (A.8) is substituted into the wave equation, Equation (A.7), then $\psi(x, y, z)$ must satisfy the differential equation

$$\left(\frac{\partial^2}{\partial x^2} + \frac{\partial^2}{\partial y^2} + \frac{\partial^2}{\partial z^2} \right) \psi - \partial_{jk} \frac{\partial \psi}{\partial z} = 0 \quad (\text{A.9})$$

If Ψ varies slowly in the z direction, then $\left| \frac{\partial^2 \Psi}{\partial z^2} \right|$ will be

much smaller than $k \left| \frac{\partial \Psi}{\partial z} \right|$ and the smaller term can be

neglected. In the numerical example discussed above, the wave number k is equal to 84.67 cm^{-1} . Therefore, it is reasonable to neglect the smaller term and the velocity potential described by Equation (A.8) must satisfy the following differential equation:

$$\left(\frac{\partial^2}{\partial x^2} + \frac{\partial^2}{\partial y^2}\right)\Psi - \partial jk \frac{\partial \Psi}{\partial x} = 0 \quad (\text{A.10})$$

A.4.1 Lowest Order Solution in Cylindrical Coordinates

We can gain some insight into the propagation of ultrasound if Equation (A.10) is expressed in cylindrical coordinates (Cook and Arnoult, 1976):

$$\left(\frac{\partial^2}{\partial r^2} + \frac{1}{r} \frac{\partial}{\partial r} + \frac{1}{r^2} \frac{\partial^2}{\partial \theta^2}\right)\Psi - \partial jk \frac{\partial \Psi}{\partial z} = 0 \quad (\text{A.11})$$

The lowest order solution is given by

$$\Psi_{\infty} = \left(\frac{2}{\pi}\right)^{1/2} \frac{1}{W(z)} \exp\left\{-j\frac{\pi}{\lambda} \frac{r^2}{R(z)} - \frac{r^2}{W^2(z)} + j\Theta(z)\right\} \quad (\text{A.12})$$

The terms W , R , and Θ are defined as functions of z as

$$W(z) = W_0 \left[1 + \left(\frac{\lambda z}{\pi W_0^2}\right)^2\right]^{1/2} \quad (\text{A.13})$$

$$R(z) = z + \left(\frac{\pi W_0^2}{\lambda}\right) \frac{1}{z} \quad (\text{A.14})$$

$$\Theta(z) = \tan^{-1}\left(\frac{\lambda z}{\pi W_0^2}\right) \quad (\text{A.15})$$

W_0 specifies the radius of the beam at $z = 0$ and W describes how the radius changes with the distance z . The term $R(z)$ describes the radius of curvature of the wavefront.

A.4.2 An Example Using the Lowest Order Solution

A.4.2.1 Beam Radius and Radius of Curvature

As an example, consider a transducer immersed in water, where the transducer has a radius of 0.635 cm and a center frequency of 2.0 MHz. Here $W_0 = 0.635$ cm, and the

wavelength is 0.0742 cm. Using Equations (A.13) and (A.14), the radius of the beam spot W and the radius of curvature R of the wavefront are given by:

$$W = W_0 \left[1 + 0.003431 z^2\right]^{1/2} \quad (\text{A.16})$$

and

$$R = z + \frac{291.47}{z} \quad (\text{A.17})$$

Figures A.2 and A.3 show graphs of W versus z and R versus z . Note that when z is zero, the radius of curvature is infinite, indicating a plane wave.

A.4.2.2 Pressure Variation with Radius

Next, let us consider the location $z = 10$ cm and see how the pressure varies with radius for the lowest order solution. The pressure can be obtained from the velocity potential using Equation (A.5). The lowest order velocity potential is given by

$$\Phi_{\infty} = \Psi_{\infty}(r, z) e^{j(\omega t - kz)} \quad (\text{A.18})$$

Using Equation (A.5) one obtains

$$p = -j\omega\rho\Psi_{\infty}(r, z) e^{j(\omega t - kz)} \quad (\text{A.19})$$

Substituting Equation (A.12) into Equation (A.19) one finds:

$$p = -j\omega\rho \left(\frac{2}{\pi}\right)^{1/2} \frac{1}{W(z)} e^{-r^2/w^2(z)} e^{-j\left(kz + \frac{\pi}{\lambda} \frac{r^2}{R(z)} - \Theta(z)\right)} e^{j\omega t} \quad (\text{A.20})$$

The measured pressure corresponds to the real part of this expression and it is given by

$$p = -\omega\rho \left(\frac{2}{\pi}\right)^{1/2} \frac{1}{W(z)} e^{-r^2/w^2(z)} \sin\left(\omega t - kz - \frac{\pi}{\lambda} \frac{r^2}{R(z)} + \Theta(z)\right) \quad (\text{A.21})$$

Let us compare Equation (A.21) with a plane wave that can be written in the form

$$p = A e^{j(\omega t - kz)} \quad (\text{A.22})$$

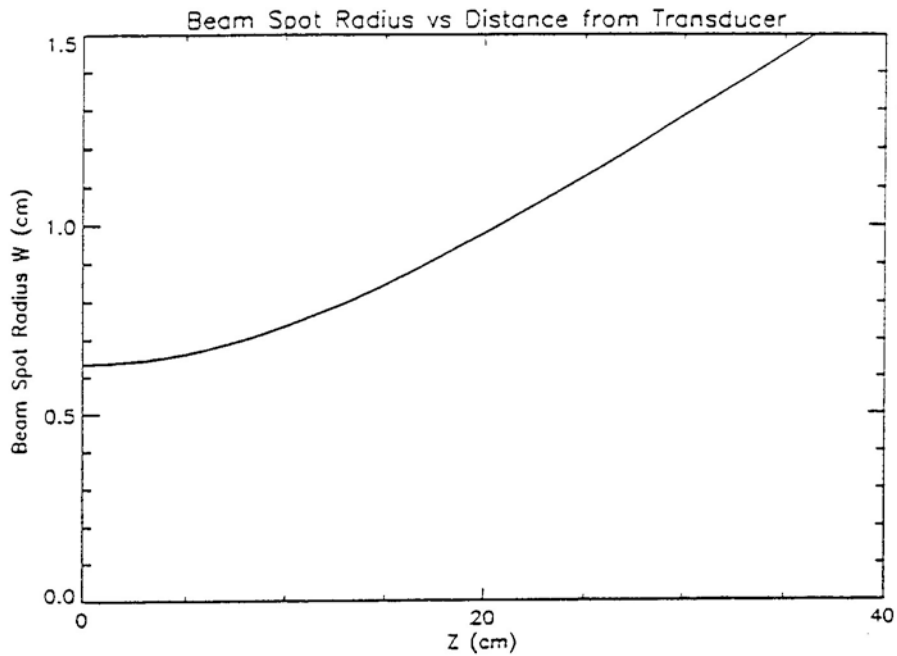


Figure A.2 Graph showing how the beam spot radius W varies with the distance z from the transducer

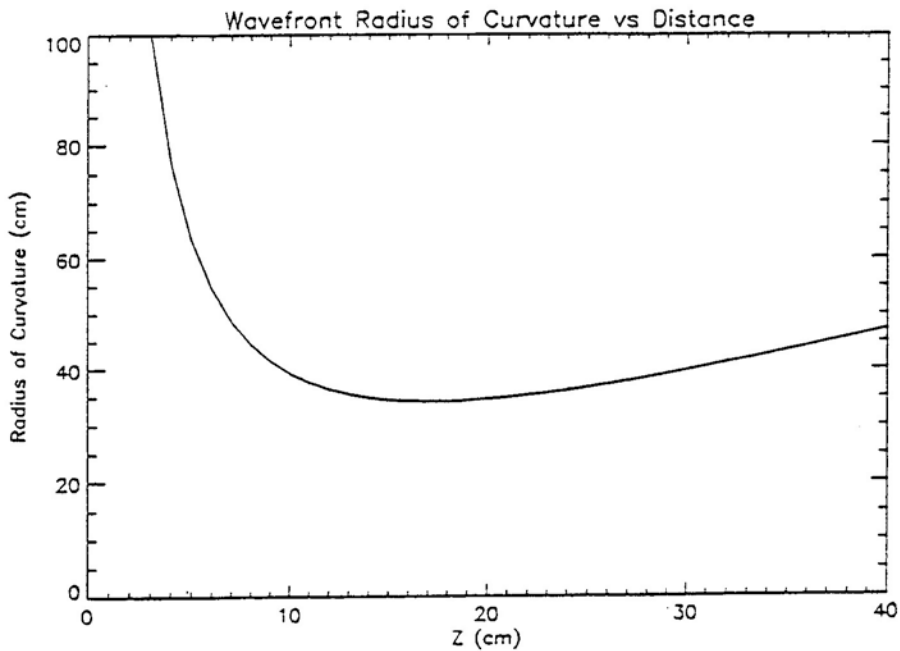


Figure A.3 Graph showing how the radius of curvature R of the wavefront varies with the distance z from the transducer

The actual pressure is the real part of this expression and we obtain

$$p = A \cos(\omega t - kz) \quad (\text{A.23})$$

One can view this expression in two ways: (1) pick a certain time and plot the wave form as a function of z ; (2) pick a certain value of z and plot the variation with respect to the time t .

This comparison shows that the amplitude is given by

$$\text{Amplitude} = \frac{\text{constant}}{W(z)} e^{-r^2/w^2(z)} \quad (\text{A.24})$$

and that it varies with both z and r . The dependence upon r shows a Gaussian term and, hence, the reason for that name in the description. Figure A.4 shows how the amplitude varies as a function of r when $z = 10$ cm, for a transducer having a radius of 0.635 cm and frequency of 2 MHz. The radius of the beam spot is defined as the distance required for the pressure to drop to $1/e$ of its value on the z -axis.

A.4.2.3 Surfaces of Constant Phase and Direction of Rays

For a plane wave in Equation (A.22) the phase of the wave is determined by choosing a value for t , such as $t = 0$, and the quantity kz is called the phase. Here we see that the phase does not depend upon x and y , as is expected for a plane wave. However, for Equation (A.21), with $t = 0$, we see that the phase depends upon both z and r and the phase is given by

$$\text{phase} = -kz - \frac{\pi}{\lambda} \frac{r^2}{R(z)} + \Theta(z) \quad (\text{A.25})$$

For $z = 10$ cm, $k = 84.67 \text{ cm}^{-1}$, wavelength = 0.0742 cm, and $W_0 = 0.635$ cm, the phase is given by

$$\text{phase (10 cm)} = -847.17 - 1.0816r^2 + \Theta(z) \quad (\text{A.26})$$

This shows that as r changes, the phase changes and, therefore, it is not a plane wave.

$$\text{phase (9.6 cm)} = -812.832 - 1.0595 r^2 \text{ radians} \quad (\text{A.27})$$

When $z = 10$ cm and $r = 0$, Equation (A.26) shows that the phase is given by -846.17 radians. For $z = 9.6$ cm, Equation (A.27) shows that, when $r = 5.6094$ cm, the phase is also -846.17 radians. Therefore, the points having $z = 10$ cm with $r = 0$ and those having $z = 9.6$ cm with $r = 5.6094$ cm lie on a surface having constant phase. Next, let us see that this surface is a sphere.

According to Equation (A.14), the point having $z = 10$ cm and $r = 0$ has a radius of curvature of 39.147 cm and its center lies at $z = -29.147$ cm. A point having $z = 9.6$ cm and $r = 5.6094$ cm from this center has a radius of curvature given by

$$R = \left[(29.147 + 9.6)^2 + 5.6094^2 \right]^{0.5} \quad (\text{A.28})$$

$$= 39.15 \text{ cm}$$

It is interesting to see that even though the assumption in Equation (A.8) is a wave traveling in the z direction, the fact that $\Psi(x,y,z)$ has a solution that has an imaginary exponential term leads to a phase that varies with both z and r .

The surface of constant phase is also an important idea when considering rays. Later we shall discuss the need for ray tracing. A ray is considered to travel perpendicular to the surface of constant phase, as illustrated in Figure A.5. Therefore, at the point at $z = 10$ cm and $r = 0$, a ray travels along the z -axis. However, a ray from a point $z = 9.6$ cm and $r = 5.6094$ cm makes an angle equal to $\tan^{-1}(5.6094/38.747) = 8.3^\circ$ with the z axis.

A.4.3 General Solution in Rectangular Coordinates

The general solution is described in detail by R. B. Thompson (Thompson et al. 1987) and only the general outline shall be presented here. The general solution to Equation (A.8) can be written as

$$\Phi(x, y, z) = \sum_{m,n} c_{mn} \Psi_m(x, z) \Psi_n(y, z) e^{j(\omega t - kz)} \quad (\text{A.29})$$

where Ψ_m and Ψ_n are called the Gauss-Hermite polynomials. When $m = n = 0$, the Gauss-Hermite solution reduces to the propagation of a Gaussian beam that has been described above.

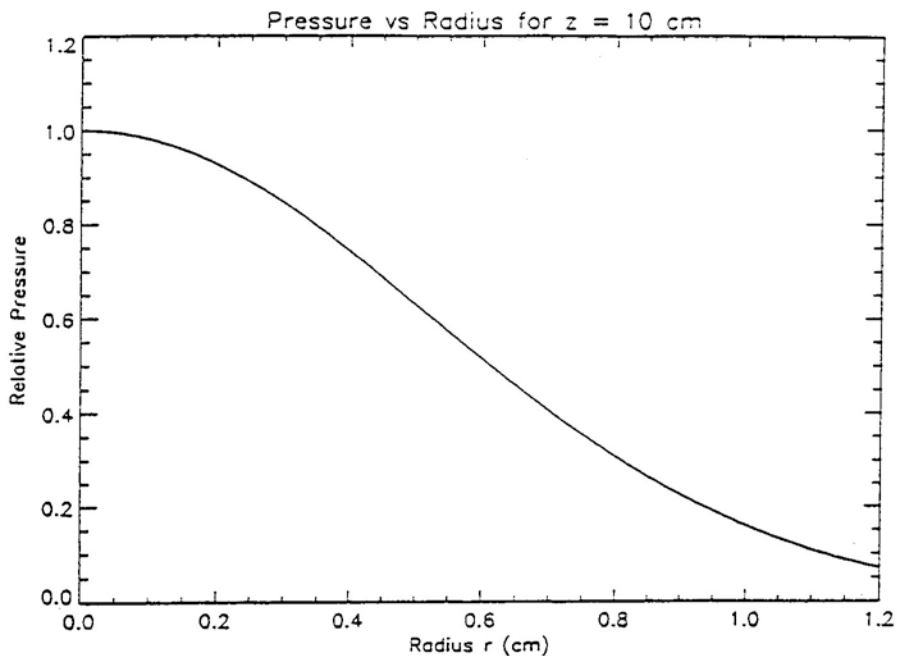


Figure A.4 Amplitude variation as a function of the coordinate r when $z = 10$ cm

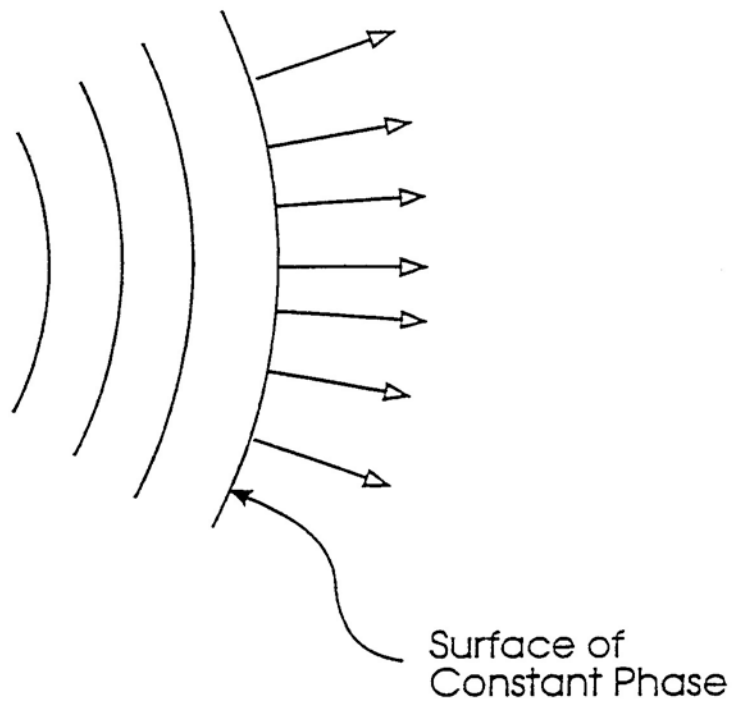


Figure A.5 Rays traveling perpendicular to surface of constant phase

If the velocity potential ϕ is known on a plane, then the coefficients can be determined by using orthogonality relationships for the polynomials. Equation (A.4) shows that this is equivalent to determining the velocity on a plane. For a planar transducer located at $z = 0$, this means that the velocity on the $z = 0$ plane is known and this velocity determines the sound wave that is propagated from it. Increasing the voltage of a tone burst applied to the transducer increases the velocity of the transducer face at $z = 0$ and causes an increase in the pressure.

A.5 Computer Code for Model I and Input Parameters

In Section 2.0 the computer code was described as consisting of four parts. The preceding section described concepts concerning the propagation of ultrasound from a planar transducer, which corresponds to the first part or step in the program. We shall discuss the remaining three

parts by considering a sample set of input to the program and each additional part of the program as it arises in the computer code.

Experimental setup: Figure 1.1 illustrates the experimental set up. The transducer has a radius of 0.635 cm and a center frequency of 2 MHz. The central ray from the transducer makes an angle θ of 10.3° with the vertical so that 45° longitudinal waves are produced in the steel plate (thickness = 1.585 cm). The central ray strikes the top of the step discontinuity. The distance from the transducer face, along the central ray, to the top of the step is 6.4 cm. The microprobe is located 3 mm below the metal plate.

Table A.1 shows the program input for this experimental setup.

Figure A.6 shows a diagram defining some of the parameters and coordinate systems used to define solutions in the computer code.

Table A.1 Example of input file (in45L30.DAT) for Model I Code

Line	
1	0 0.635 0.635 1.e30 1.e30 2.0: itype,radiusx,radiusy,focusx,focusy,frequency
2	25 25 0.0 0.0 0 50: G-H expansion,G-H integration,alfa0x,alfa0y,G-H printout option
3	10.355 45.0 1.0e30 1.0e30 6.4: th1,th2,bx,by,z0
4	0.1485 0.0 1.0 1: v11,v1s,rho1,niw
5	0.5842 0.3048 7.9 1: v21,v2s,rho2,ntw
6	0.1485 0.0 1.0 1: v31,v3s,rho3,ntw3
7	0.0 169.645 0.0 -1.1490 0.0 6.2960: rot. and transl. transf. from int. to transc.
8	0.7071 0.0 -0.7071 0.0: equation of transmitted plane w.r.t. int. coord. sys.
9	0.0 135.0 0.0 0.0 0.0 0.0: rot. and transl. transf. from int. to transm. coord. s
10	0.0 0.0 1.0 -0.30: equation of observation plane.
11	grd30.dat: file which contain grid points
12	-3 .1 61: initial x, step size, and number of points in x dir.
13	0 0 1: initial y, step size, and number of points in y dir.
14	2.2410: z distance from trsm. coord. sys. to the observation coordinate system
15	0 135 0: rot. transf. from trsm. coord. sys. to the observation coord. sys.
16	out45130.dat: an output file name

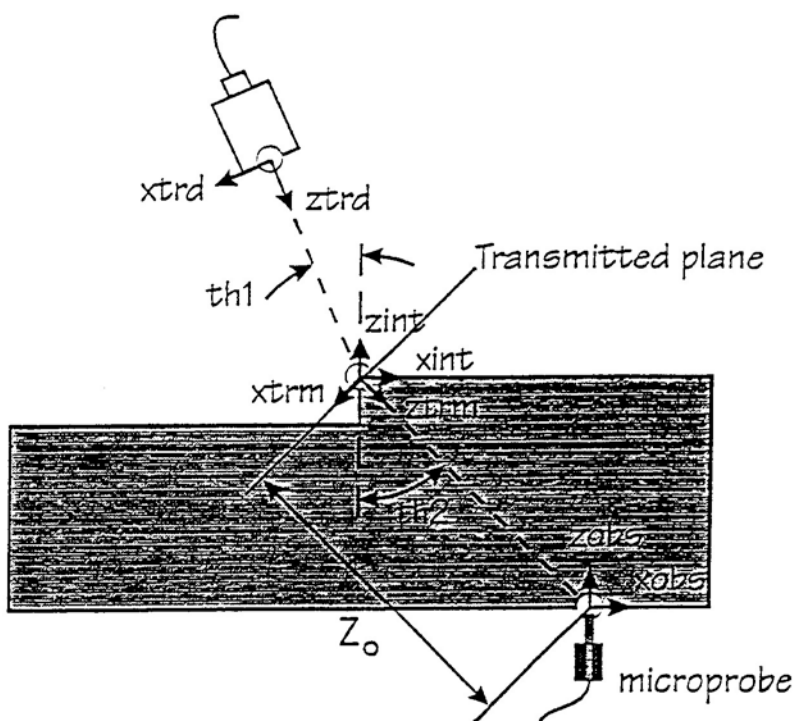


Figure A.6 Definition of some parameters used in computer code for Model I

The input parameters on each line of Table A.1 will be described as follows:

Line 1. Transducer Information

itype:

set to zero

rx,ry:

semi-axis of an elliptical transducer along the x and y axes. For a circular transducer $r_x = r_y = 0.635$ cm.

f0x,f0y:

transducer focal lengths along the x and y axes. For a planar transducer, the focal lengths are infinite and f0x and f0y are set equal to $1.0e30$.

freq:

frequency in MHz, $freq = 2.0$

Line 2. Gauss-Hermite (G-H) beam information

nc:

number of terms used in the G-H expansion, $nc = 25$

ni:

number of integration points to determine the constants C_{mn} in the expansion, $ni = 25$

alfa0x, alfa0y:

initial parameters defining the beam width. Set to zero.

Line 3. Incidence, interface, and transmission configuration

th1:

angle of incidence measured from normal to the interface, $th1 = 10.355^\circ$

Appendix A

th2:
angle of transmission measured from normal to the interface, $th2 = 45^\circ$

bx,by:
radii of curvature of the interface. For a planar interface, $bx=by=1.e30$

z0:
distance from the transducer to the interface along the central ray of transducer, $z0 = 6.4$ cm

Line 4. Material properties of incident medium

v11, v1s:
longitudinal and shear wave speeds. For water, $v11 = 0.1485$ cm/ μ s and $v1s = 0$

rho1:
density. For water, $rho1 = 1$ g/cm³

niw:
incident wave type, 1 for longitudinal waves and 2 for shear waves

Line 5. Material properties of the transmitted medium

v21, v2s:
longitudinal and shear wave speeds. For steel, $v2 = 0.5842$ cm/ μ s and $v2s = 0.3048$ cm/ μ s

rho2:
density. For steel, $rho2 = 7.9$ g/cm³

ntw:
transmitted wave type, 1 for longitudinal waves and 2 for shear waves

Line 6. Material properties of the final medium

The microprobe measures the pressure in water.

v31, v3s:
longitudinal and shear wave speeds. For water, $v31 = 0.1485$ cm/ μ s and $v3s = 0.3048$ cm/ μ s.

rho3:
density. For water, $rho3 = 1$ g/cm³

ntw:
wave type, 1 for longitudinal waves and 2 for shear waves

Line 7. Transformation parameters from the interface coordinate system to the transducer coordinate system

alfa1, beta1, gamma1:
rotational angles

x1,y1,z1:
translational parameters

The surface is described in the interface coordinate system and the surface is defined by a grid of points on the surface. The file for this grid is given in Line 11.

The analytical solution, defined by a series of Gauss-Hermite polynomials, is given in terms of the transducer coordinate system. In order to determine where the ultrasound strikes the surface, the grid points will have to be defined in terms of the transducer coordinate system. The parameters on this line define the rotation matrix to change from the interface coordinate system to the transducer coordinate system and to take into account the different origins of the two coordinate systems. All rotational transformations are performed about three angles about the z, y, and x axes and the right-hand rule is followed for all rotations.

Figure A.7 shows a diagram of the two coordinate systems. The interface coordinate system must be rotated by an angle of 169.645° about the +y axis (directed into the paper) in order to have the same orientation as the transducer coordinate system. The translational values are indicated in this figure.

Line 8. Equation of the transmitted plane with respect to the interface coordinate system

In order to consider the transmission of ultrasound through a step discontinuity or any other irregular surface, a ray tracing procedure is used. The amplitude and phase are determined at each grid point on the interface surface. In order to determine the direction of the ray at each point in the grid, the surfaces of constant phase are determined. The concepts are the same as those discussed in Section 4.2.3 dealing with surfaces of constant phase for the zeroth order solution to the wave equation. The normal to the surface indicates the direction of the ray.

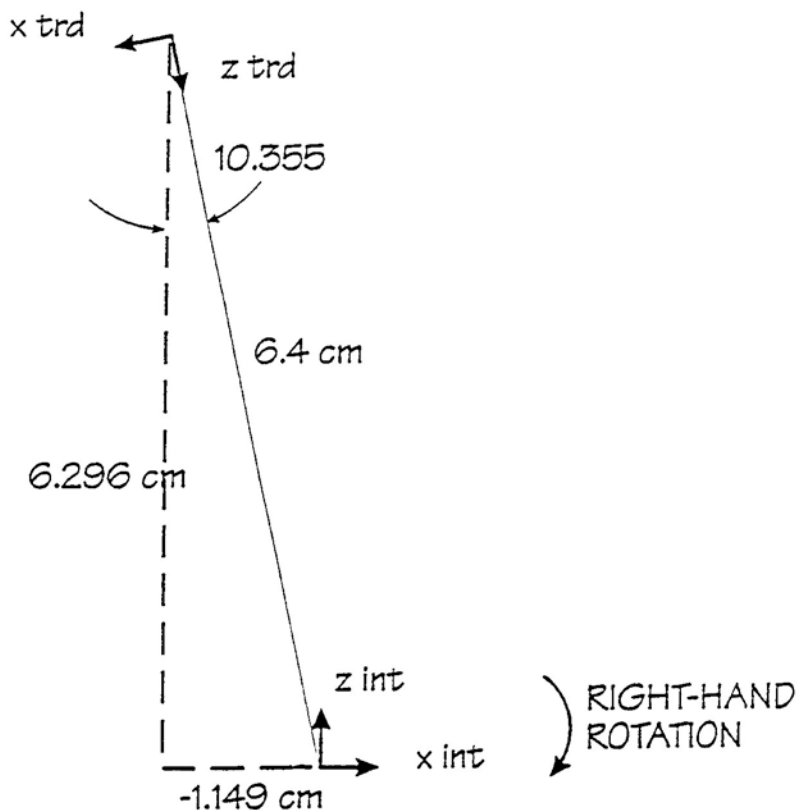


Figure A.7 Relationship between the transducer coordinate system and the interface coordinate system

Snell's law is used to determine the direction of a ray inside the second medium, which, in this case, is steel. Transmission coefficients are calculated and the amplitude is multiplied by the transmission coefficient to yield the amplitude inside the second medium. The ray is then traced until it reaches the transmitted plane. The rays on the transmitted plane are separated by a different distance than on the interface. In order to conserve energy, the amplitude on the transmitted plane is corrected by comparing the distance between two grid points with the distance between the two rays on the transmitted plane. The phase on the transmitted plane is adjusted by considering the distance between the grid point and the transmitted plane and the wavelength. For example, if a ray traveled a distance equal to 0.75λ , then the phase change is 270° .

In Section 4.3 we discussed the concept that, if the velocity potential is known on a plane, then the coefficient C_{mn} in Equation (A.29) can be determined. Therefore, the

amplitude and phase values on the transmitted planes are used to find the new constants C_{mn} which describe the propagation of ultrasound in the transmitted coordinate system. Thus, the propagation of ultrasound through the steel plate is described.

Figure A.6 shows a diagram of transmission through a surface with a step discontinuity. Rays from grid points to the left of the step can be projected toward the transmitted plane. For grid points to the right of the step, the amplitude and phase are obtained by projecting "backwards" to the transmitted plane. That is, for grid points to the right of the step, one obtains the amplitude and phase that they must have on the transmitted plane to account for the phase and amplitude at the corresponding grid points.

The transmitted plane is described by defining the equation of the plane with respect to the interface coordinate system. A vector normal to the transmitted plane is

The transmitted plane is described by defining the equation of the plane with respect to the interface coordinate system. A vector normal to the transmitted plane is always in the direction of the transmission in the second medium. The equation of the plane is defined as

$$(xcoef)x + (ycoef)y + (zcoef)z = \text{constant.}$$

The parameters on line 8 are: xcoef, ycoef, zcoef, const.

Line 9. Transformation parameters from the interface coordinate system to the transmitted coordinate system

alfa2, beta2, gama2:
rotational angles

x2,y2,z2:
translation parameters

Since angle th2 in Figure A.6 is 45°, the interface coordinate system must be rotated about the +y axis by 135° to have the same orientation as the transmitted coordinate system.

Line 10. Equation of the observation plane relative to the observation coordinate system shown in Figure A.6, using the standard definition for the equation of a plane

For the input shown in Table A.I, the microprobe was 0.3 cm below the bottom surface of the steel plate.

When the transmitted wave intersects the bottom surface, a procedure similar to that for the ray tracing through the rough surface is used. The direction of rays striking the bottom surface are determined and transmission coefficients are calculated in order to determine the amplitude and phase of the wave that is transmitted into the water.

Line 11. Name of file containing the grid points on the interface which describes the surface

This file can describe a step discontinuity or any surface, rough or smooth. A ray is generated at each grid point and traced across the interface, using Snell's law, until it reaches the transmitted plane.

First line in this file states the grid dimension, nptsx by nptsy. For example, the grid may contain 51 by 51 points.

The rest of the lines in this file state the (x,y,z) coordinates of each of the grid points and the x, y, and z components of a vector normal to the surface at the grid point.

Let us consider a grid of points with x ranging from -3.0 cm to +3.0 and y ranging from -3.0 cm to +3.0 cm. For a 51 by 51 grid, the points are separated by 0.12 cm. Let the step height be 0.0762 cm (30 mils). The first two lines are as follows:

```
51 51
-3.0 -3.0 -0.0762 0.0 0.0 0.0
```

In the succeeding lines x remains constant at -3.0 cm, and y is incremented from -3.0 to +3.0 by 0.12 cm. After that x is set to -2.88 cm, and y is again incremented from -3.0 to +3.0 cm by 0.12 cm, etc. When x = 0, then z is set equal to 0.0 and the definition of the grid points continues until x = +3.0 cm. The file will contain 51x51 such lines.

Line 12. Information for obtaining the transmitted beam profile along the x axis

x0, xstep, npx:
initial position, step size, and the number of points

x0 = -3.0 cm, xstep = 0.1 cm, and npx = 61.

Line 13. Information for obtaining the transmitted beam profile along the y axis

y0, ystep, nyp:
initial position, step size, and number of points. If a profile is not desired along y axis, the set y0 = 0, ystep = 0, nyp = 1.

Line 14. Translational parameter z0

This parameter is defined as the distance from the origin of the transmitted coordinate system to the point where the central ray of the transducer intersects the bottom surface of the plate. The origin of the observer coordinate system is located at this point, as shown in Figure A.6.

Since the thickness of the plate is 1.585 cm and angle th2 is 45°, z0 = 2.241 cm.

Line 15. Rotational parameters from the observation coordinate system to the transmitted coordinate system

rotz, roty, rotx:
rotational angles

For the example in Table A.I, the observation coordinate system must be rotated about the +y axis by 135° so that it has the same orientation as the transmitted coordinate system.

Line 16. A file to store the beam profile, e.g., out45130.dat.

A.6 Model I Experimental Measurements

This section describes the experimental apparatus that was used to validate Model I and the procedures employed to analyze this data. When a 45° longitudinal wave is produced in steel, it is accompanied by a 21.7° shear wave. The time difference between these two signals is derived and this influenced the choice of signal applied to the transducer.

A.6.1 Experimental Apparatus for Validating Model I

Figure A.8 shows a diagram of the experimental apparatus. The steel plate has a thickness of 1.585 cm and three step discontinuities were machined on the top surface. Region A has a depth of 0.152 cm (60 mils); region B, 0.0762 cm (30 mils); and region C, 0.0254 cm (10 mils). This forms three step discontinuities. The transducers were mounted on a Plexiglas bracket that was designed to produce the desired incident angle and the bracket was fastened to the steel plate using epoxy. Figure A.8 shows the bracket oriented so that the two transducers produce a beam normal to two steps. This permits experimental data to be acquired for two steps, before changing the orientation of the bracket.

When the incident angle Θ is 10.4° , a longitudinal wave ($\Phi = 45^\circ$) as well as a shear wave ($\Phi = 21.7^\circ$) are produced in the steel. When the incident angle Φ is 20.2° , only a shear wave ($\Phi = 45^\circ$) is produced in the steel. In

order to produce 45° longitudinal waves, the surface of the Plexiglas bracket was machined at an angle of 10.4° and the transducer mounted upon the angled surface. Two such angled mounting holes were machined in the bracket. Another Plexiglas bracket was constructed and the only difference was that the surface was angled at 20.2° in order to produce 45° shear waves. The bracket was oriented so that the central ray of the transducer was aimed at the top of the step.

The distance between the transducer and the top of the step was chosen so that the top of the step was in the far field. The near-field distance N is calculated to be 5.4 cm for a frequency of 2 MHz in water. The distance between the center of the transducer and the top of the step was 6.3 cm for the normal orientation, 6.4 cm for 45° longitudinal wave generation, and 6.7 cm for 45° shear generation.

The microprobes used in these experiments were constructed at PNNL by Jerry Posakony and are described by Good et al. (1991). They are transducers that have a diameter of only 0.0254 cm (10 mils). Their use permits measurement of the pressure at a "point."

When the experiment was performed, the steel plate with the attached bracket was placed in an immersion tank **upside-down**, so that the completely smooth surface was now on top. A microprobe was attached to the laboratory x-y scanner and used to measure the pressure over a 5.08 cm x 5.08 cm scan, every 0.0254 cm (10 mils) in the x and y directions at a distance of 3 mm from the top surface. For convenience, we shall continue to discuss the experiment using the conventional orientation of the apparatus as shown in Figure 1.1. At each position in the scan, a computer records an A-scan, which is defined as the voltage observed by the microprobe versus the time. For the dimensions of the scan stated, a total of 200 x 200 A-scans are recorded.

A.6.2 Separation of Longitudinal and Shear Signals

When a 45° longitudinal wave is generated in the steel, a shear wave at 21.7° is also generated. Both can be detected by the microprobe. One certainly needs to assess under what conditions there might be interference between these two signals and to take precautions so that this is not a problem.

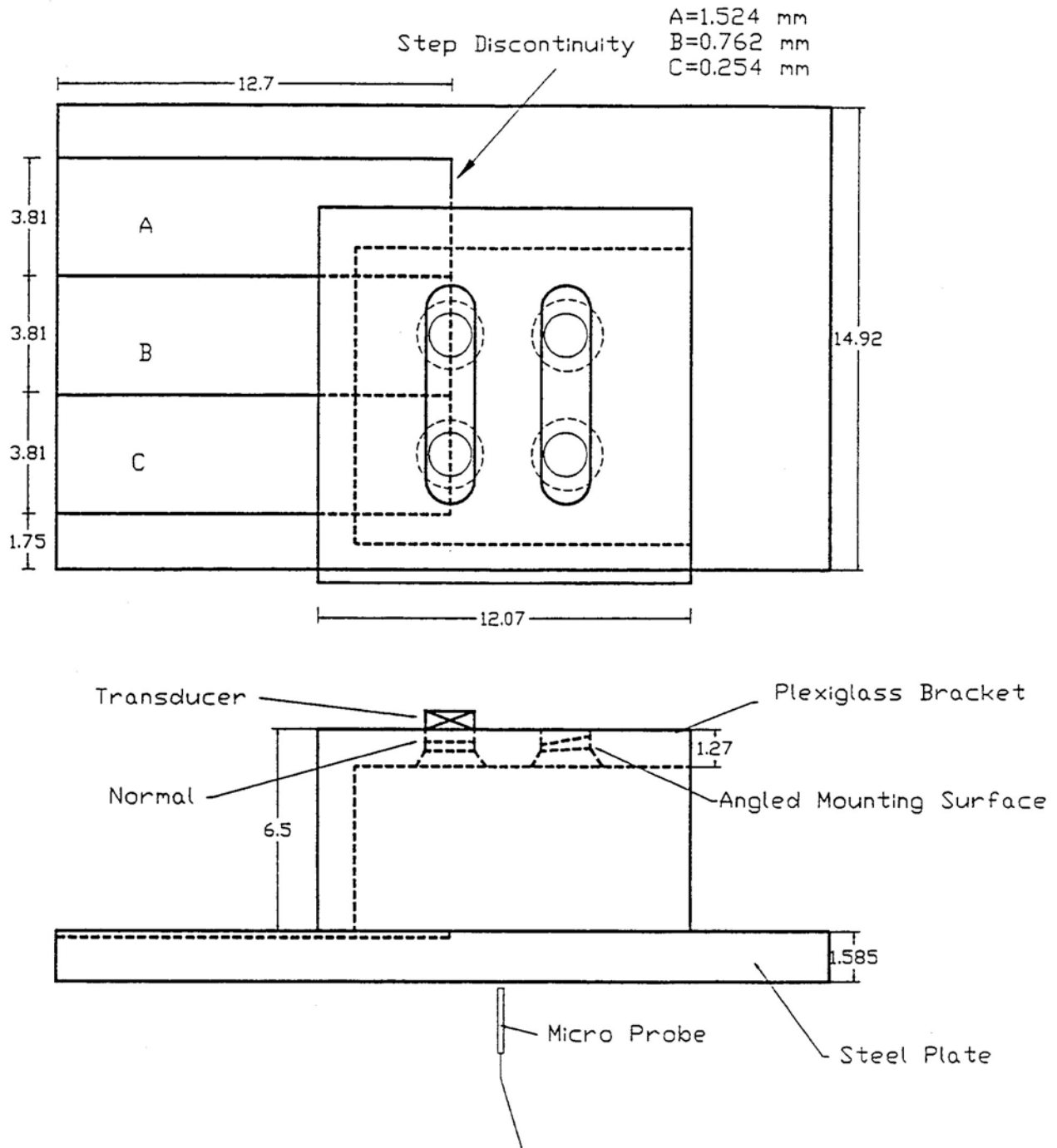


Figure A.8 Diagram showing steel plate containing three step discontinuities and the Plexiglas mounting bracket for the transducers. Unless indicated otherwise, the distances are expressed in centimeters.

Figure A.9 shows a **plane** wave leaving point A and traveling through the material at an angle Θ with the normal to the surface. A microprobe at point B records the arrival of the wave. The wavefront at point B is the same as that at point C. Therefore, in order to calculate the time of arrival of the wavefront at the microprobe, one needs to determine the distance AC and divide by the speed of the wave. Trigonometric relations show the following:

$$\frac{AC}{c} = \frac{D}{c} \cos \Theta + \frac{x}{c} \sin \Theta \quad (\text{A.30})$$

where c is the speed of sound in the medium.

Using Equation (A.30) the time of arrival at the microprobe for a 45° longitudinal wave is given by

$$(\text{time})_{\text{long}} = 1.918 + x \left(\sin \frac{45}{c_L} \right) \quad (\text{A.31})$$

where $D = 1.585$ cm, $\Theta = 45^\circ$, and $c_L = 0.584$ cm/ μ s. Similarly the time of arrival for a shear wave at the microprobe is given by

$$(\text{time})_{\text{shear}} = 4.832 + x \left(\sin \frac{21.7}{c_s} \right) \quad (\text{A.32})$$

where $c_s = 0.3048$ cm/ μ s. The difference in the arrival time is given by

$$(\text{time})_{\text{shear}} - (\text{time})_{\text{long}} = 2.91 \mu\text{s} \quad (\text{A.33})$$

The terms involving x in Equations (A.31) and (A.32) cancel because, due to Snell's law,

$$\sin \frac{45}{c_L} = \sin \frac{21.7}{c_s} \quad (\text{A.34})$$

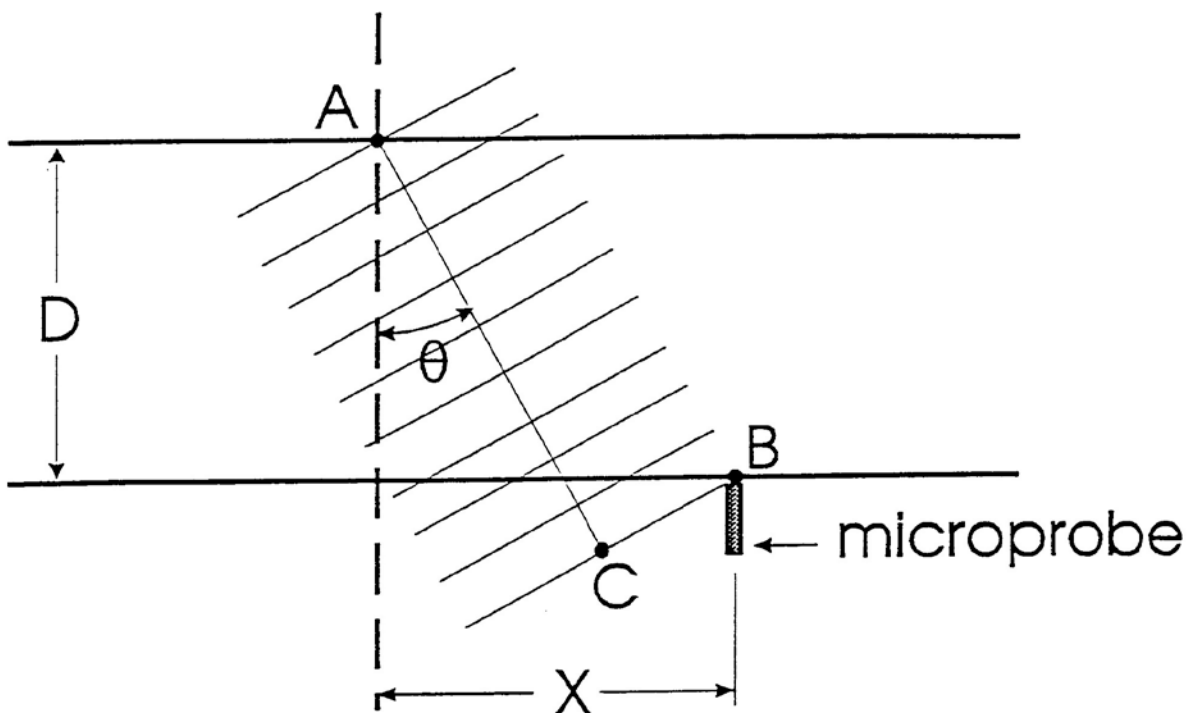


Figure A.9 Plane wave with a wavefront that reaches points B and C simultaneously

Therefore, for plane waves emerging from point A, the shear waves will arrive about 3 μ s after the longitudinal waves and this time is independent of the position of the microprobe. For this reason, we used a 4-cycle tone burst (2 microseconds in length) in obtaining the longitudinal data at 45° (in Data Set I).

A.6.3 Data Analysis

The A-scan data were analyzed in two ways: (1) obtaining the maximum voltage of a tone burst signal by using a gated composite C-scan, and (2) a fast Fourier transform (FFT) analysis.

In the first method, a point is chosen on a given A-scan (voltage versus time). For example, this point might be the maximum value of the fourth peak in an 8-cycle tone burst. Then, the computer code permits successive A-scans to be viewed and, for five more A-scans, a similar point is chosen; e.g., in this example, the fourth peak in the 8-cycle tone burst for five A-scans. The computer code calculates the location in time of a similar point on all of the A-scans in that particular run. Then a gate of a certain width (here, 1 microsecond) is selected and is centered over that point in all of the A-scans. The computer code selects the maximum amplitude of the A-scan signal within the gate.

The FFT analysis was carried out using the software PV-WAVE for the SUN Workstation. PV-WAVE is a mathematical analysis plus graphics package, which has its own very powerful computer language. For example, the computer files for a single run are quite large, but each A-scan of the 40,000 total on the file has the same number of bytes. Rather than reading in the entire file into the computer program, PV-WAVE considers the file to be broken up into 40,000 similar parts and permits only one part at a time to be read into the computer program. One line of the scan (5.08 cm long and scanned every 0.0254 cm) contains 200 A-scans. Thus, to analyze the A-scans, the fast Fourier transform of 200 signals needs to be obtained for only one run. In order to make the data analysis manageable, an A-scan was graphed and the cursor selected a point on the left and right of the desired signal. The time for the left cursor position and the right cursor position were recorded. A similar procedure was carried out for nine more A-scans spread over the possible 200. For, say, the left cursor a graph of the cursor-time versus the scan location (1 to 200) was obtained and a

polynomial fit to these 10 data points was obtained and, similarly, for the right cursor. This permitted the position (or time location) of the signal to be obtained for all 200 A-scans. With this information, the FFT of the signals in 200 A-scans could be obtained. The amplitude at 2 MHz was then obtained, which subsequently was compared with the theoretical predictions at 2 MHz.

The data were analyzed using both methods for the 4-cycle tone bursts used to acquire the 45° longitudinal data in Data Set I. The results showed little difference between the two methods. However, a second set of data was obtained using a negative bi-polar pulse and, in this case, it was essential to analyze the data using the FFT method.

A.7 Comparison of Experimental Data with Model I Theoretical Calculations

In this section the experimental data are compared with the theoretical calculations using the Model I code. The first subsection describes how the grid point separation distance, one of the Model I code parameters, was chosen. The remaining subsections deal with the comparison of three sets of experimental data with theoretical calculations. Data Set I and Data Set II consist of the more recent data obtained for longitudinal and shear waves, and the other set comprises the longitudinal data initially obtained at PNL.

A.7.1 Grid Point Separation Distance

The separation distance between the grid points that describe the rough surface is a parameter in the computer code. Initially, the calculations were carried out using a grid point separation of 0.12 cm. For a frequency of 2 MHz, the wavelength in water is 0.074 cm, the wavelength for longitudinal waves in steel is 0.292 cm, and the wavelength for shear waves in steel is 0.1524 cm. Since 0.12 cm is significantly greater than the wavelength in water, calculations were carried out using a smaller grid separation to see if there were changes in the theoretical curves. In the original code, many of the memory allocations were 100 x 100. In order to use a larger number of grid points, the memory allocations were increased to 301 x 301. Calculations were carried out using grid point separations of 0.06 cm, 0.03 cm, and 0.02 cm. The results showed that the calculation for 45° shear waves in steel

are affected more by smaller separation distance than are the calculations for 45° longitudinal waves. This is understandable because the shear waves have a smaller wavelength by about a factor of two compared to the longitudinal waves. The calculations for a grid separation of 0.02 cm were very similar to those for a grid separation of 0.03 cm. For a grid separation of 0.03 cm, the calculation on the SUN Workstation required 48 minutes. The theoretical calculations were carried out using a grid separation distance of 0.03 cm.

A.7.2 Data Set I

Data were obtained using an 8-cycle tone burst for the normal orientation and also to produce 45° shear waves in steel. A 4-cycle tone burst was used in obtaining the longitudinal data at 45°.

Figures A.10, A.11, and A.12 show the comparison of the experimental data obtained from the FFT analysis with the theoretical calculations. The experimental data and the theoretical calculations were normalized to 1.0 at their maximum value. Figure 1.1 shows the origin of the coordinate system, which is used for the theoretical calculations. Essentially, $x = 0$ corresponds to the location of the central ray on the bottom surface of the steel plate. Care was taken to ensure that the experimental data were placed appropriately upon the graph by determining the location of the step for both theory and experiment.

When the data were taken, the microprobe was moved to the location under the step and its position in the scan was recorded. Figure 1.1 also shows the location of the step relative to the origin of the coordinate system.

Figure A.10 shows very good agreement between the experimental data for the normal orientation (Data Set I) and the theoretical calculations for all of the steps. Similar data had been obtained by other researchers at PNL and compared with theoretical calculations carried out at Iowa State University. These results (Minachi, Thompson, Good, and Diaz, 1991) are shown in Figure A.13 for the normal orientation and in Figure A.14 for the propagation of 45° longitudinal waves. It should be pointed out that the theoretical calculations in this reference describe the pressure on the bottom surface of the plate. This corresponds to the first three parts of the computer code described in Section 1.1. However, the measurements were obtained with the microprobe several

millimeters below the surface of the plate. A short time later a modification to the code was made to calculate the pressure recorded by the microprobe located several millimeters below the surface of the plate, which corresponds to the fourth part described in Section 1.1. Therefore, differences will be noted in the theoretical curves shown by Minachi et al. (1991) in Figures A.13 and A.14 and those reported here.

When comparing the data shown in Figure A.11 for the 45° longitudinal case with data obtained by Minachi et al. (1991) in Figure A.14, one sees comparable results for the 10-mil step. However, for the 30- and 60-mil steps, the data in Figure A.14 shows a sizeable secondary peak to the right of the main peak while in Data Set I only traces of this secondary peak are evident. The data for the 30-mil and 60-mil steps obtained by Minachi et al. (1991) were re-examined. A composite C-scan was obtained by placing a gate of 0.7 microseconds over the first cycle of the 8-cycle tone burst. This type of gating was used to eliminate any interference between the longitudinal and shear waves. However, the results were the same as had been reported by Minachi et al. (1991).

For Data Set I, the theoretical fit to the 45° shear data in Figure A.11 appears to be better than that to the 45° longitudinal data in Figure A.12.

A.7.3 Data Set II

A second set of data was also obtained. Essentially the same experimental set-up was used, but a negative bipolar pulse (1 cycle) was applied to the transducer. The pulse width was 0.44 microseconds and the pulser output voltage was 375 V. The resulting A-scans were analyzed using the FFT method. The A-scans were obtained by incrementing the laboratory x-y scanner by 0.0381 cm. Figure A.15 shows the data obtained for the 60-mil step for the 45° longitudinal case and Figure A.16, for the 45° shear case for all steps.

Three sets of data were obtained for the 60-mil step for 45° longitudinal waves: Figure A.11 (Data Set I), Figure A.15 (Data Set II), and Figure A.14 (Minachi et al. 1991). We see a strong secondary peak in Data Set II, a weaker secondary peak from Minachi et al. (1991), and only a trace of it in Data Set I. The most likely explanation for these differences is a slightly different orientation of the transducer bracket upon the plate. For example,

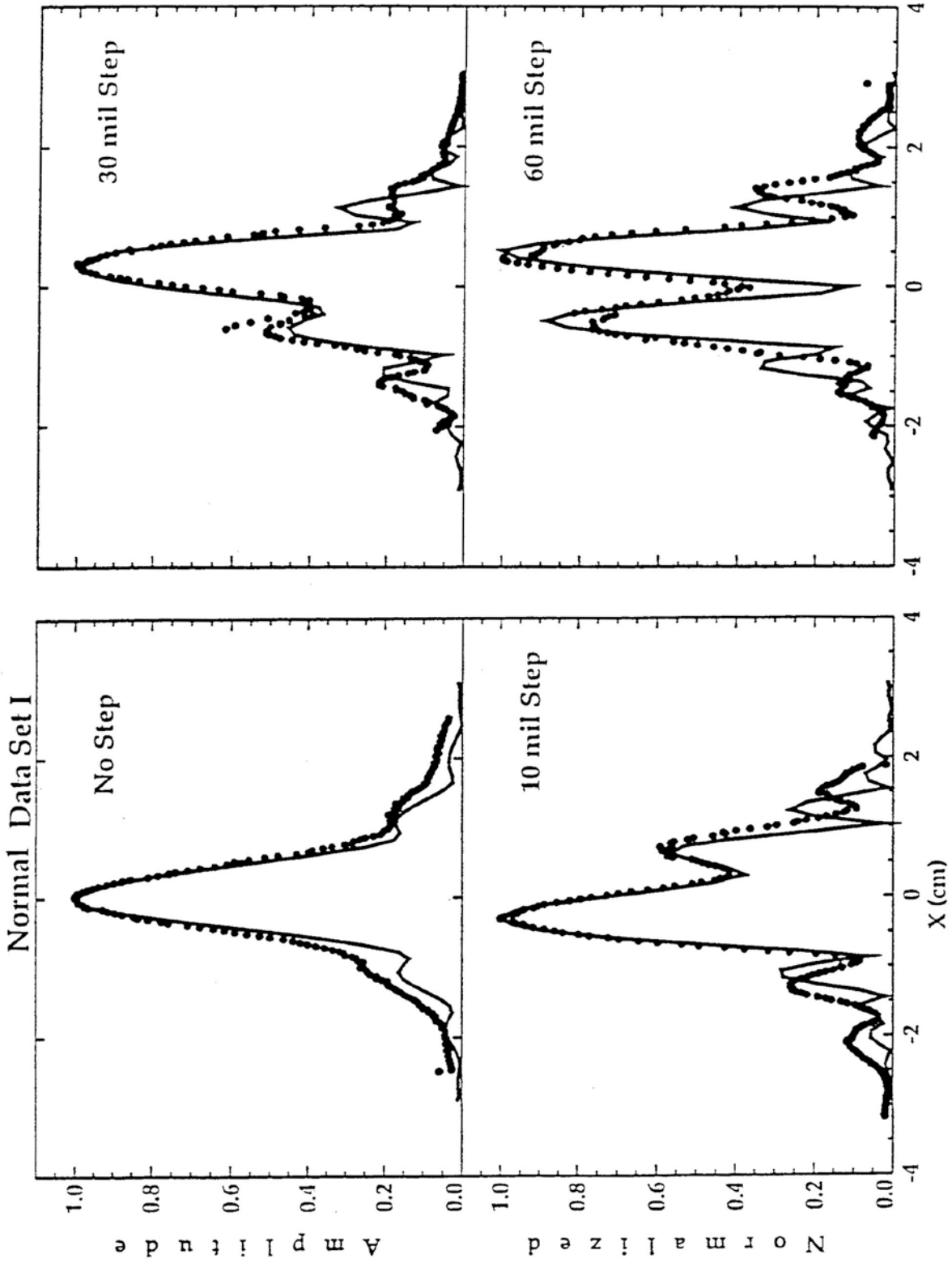


Figure A.10 Comparison of experimental data (Data Set I) with theoretical calculation for the normal orientation. In this figure, and all that follow, the experimental data are indicated by solid circles and the theoretical curves, by a solid line.

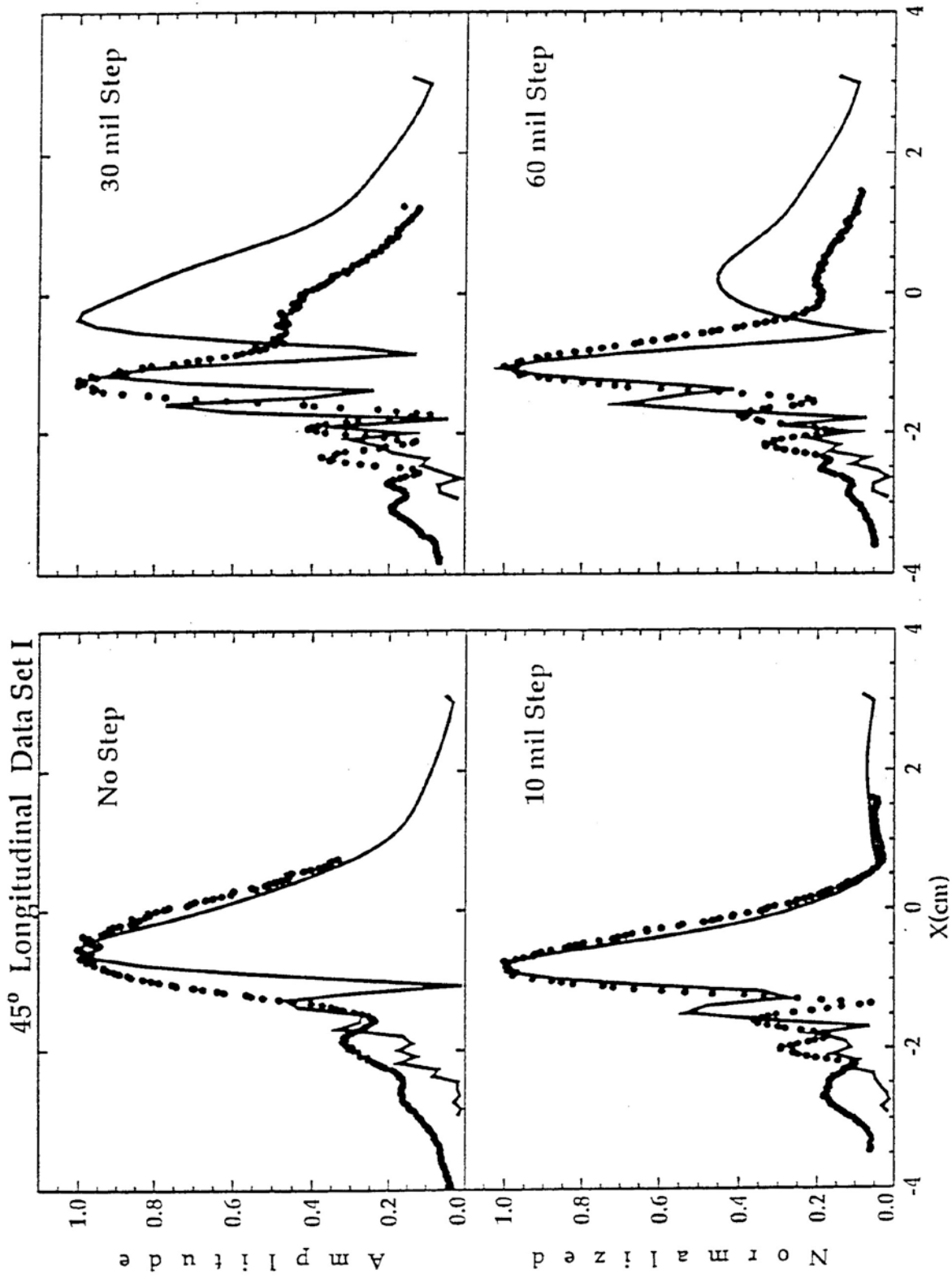


Figure A.11 Comparison of experimental data (Data Set D) with theoretical calculation for 45° longitudinal waves.

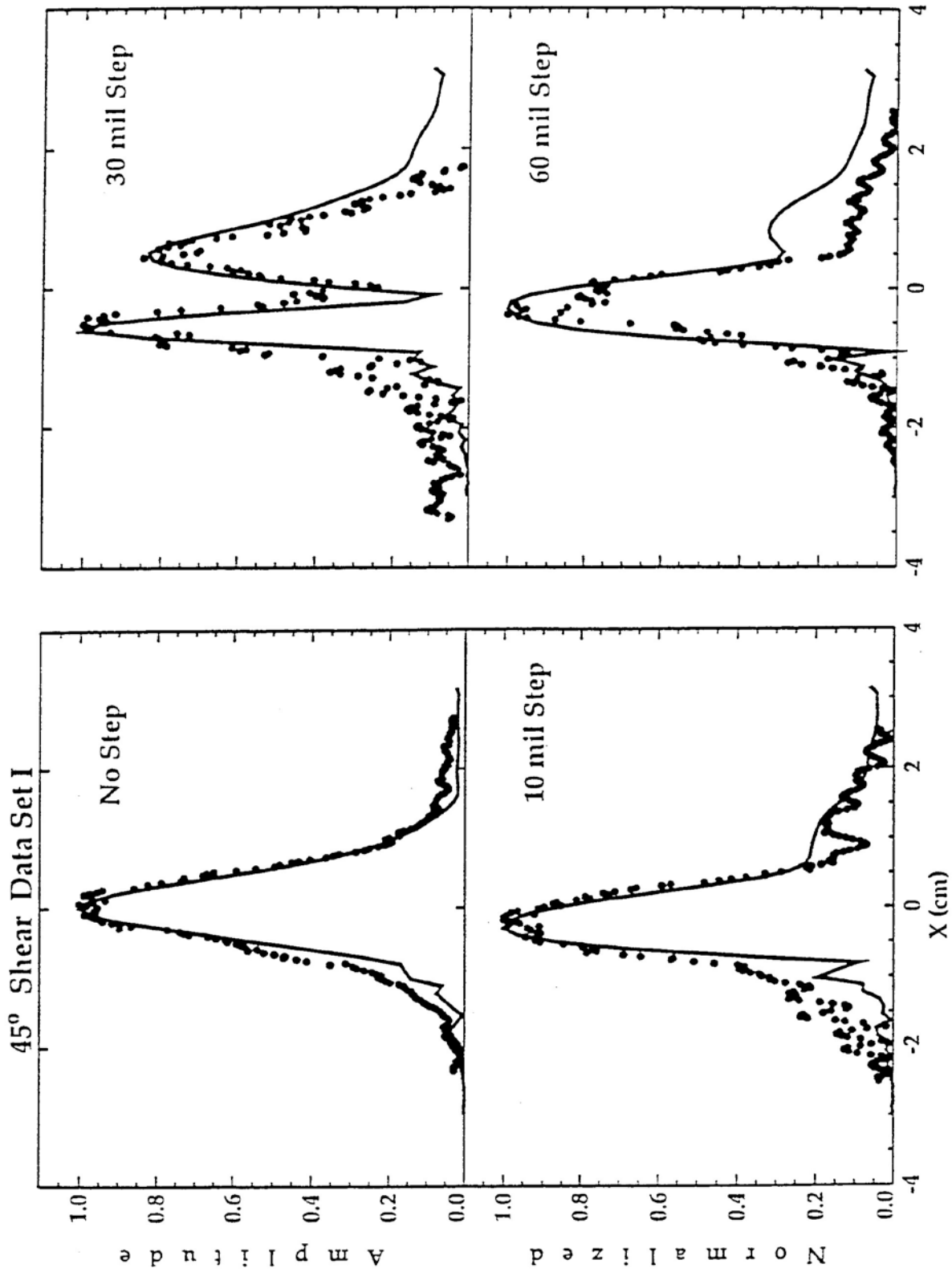


Figure A.12 Comparison of experimental data (Data Set I) with theoretical calculations for 45° shear waves

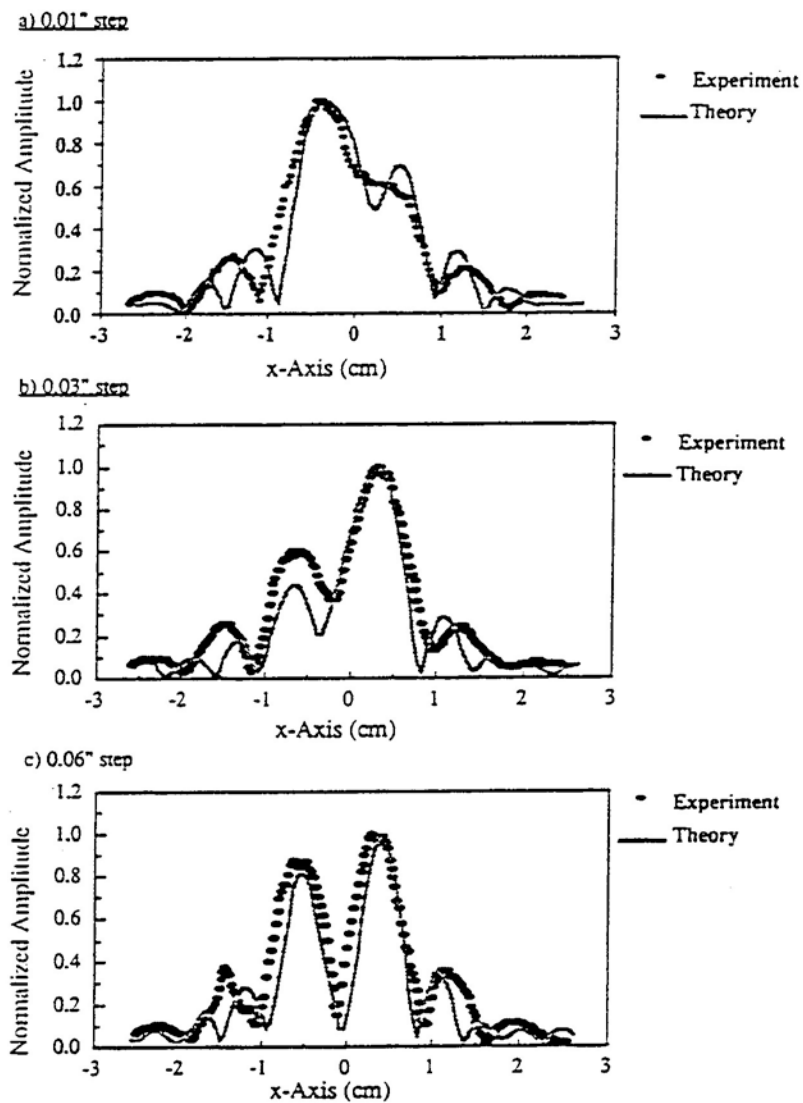


Figure A.13 Experimental data for the normal orientation and comparison with theoretical calculations (Minachi, Thompson, Good, and Diaz, 1991)

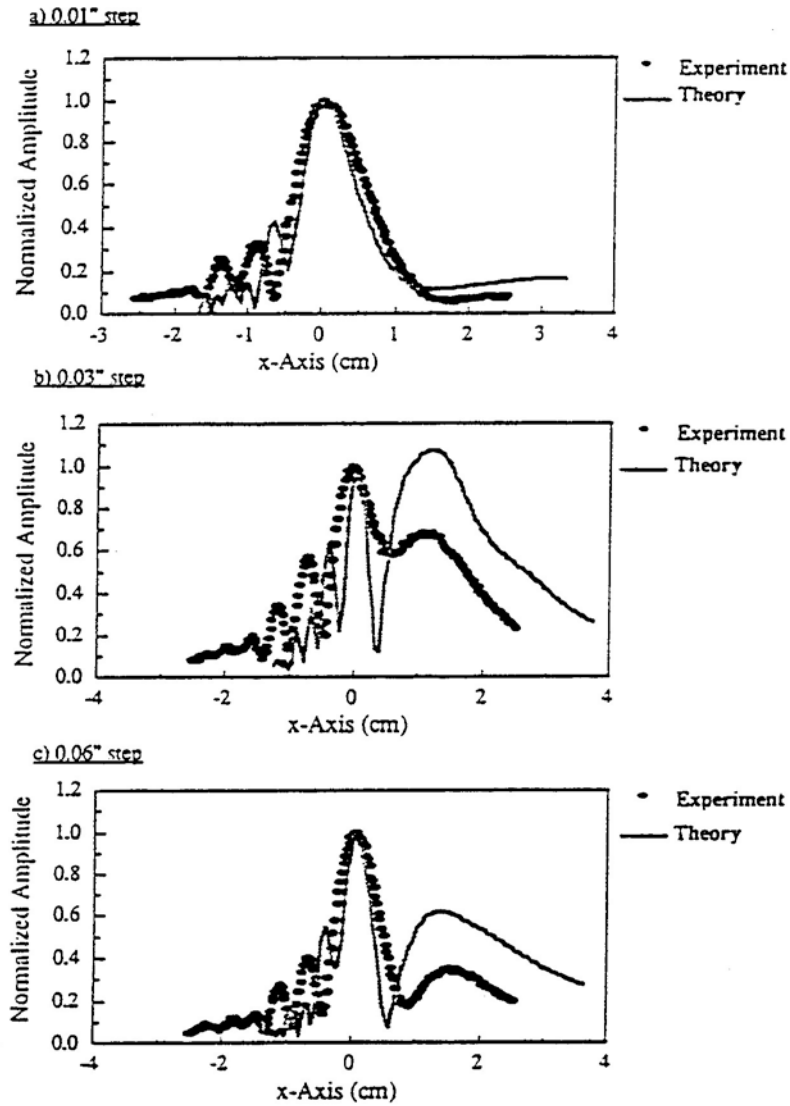


Figure A.14 Experimental data for 45° longitudinal waves and comparison with theoretical calculations (Minachi, Thompson, Good, and Diaz, 1991)

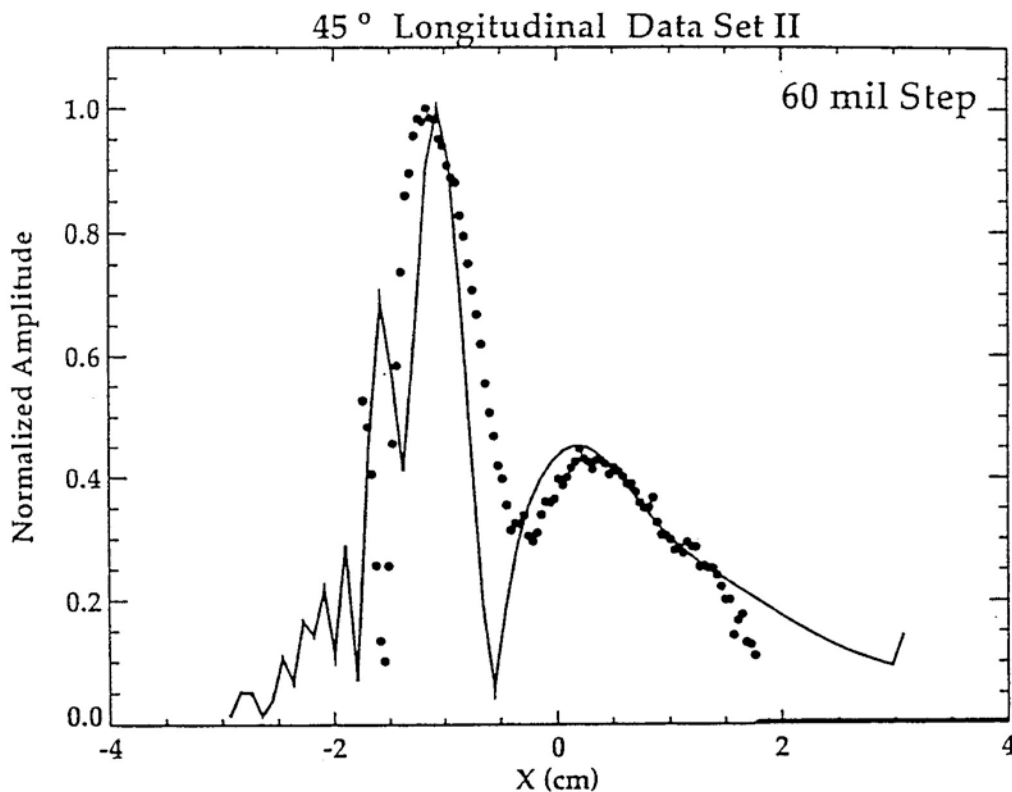


Figure A.15 Comparison of experimental data (Data Set II) for the 60 mil step with theoretical calculations for 45° longitudinal waves

theoretical calculations show that, if the central ray of the transducer is displaced only 1 mm along the x-axis from the top of the step, significant changes occur in the theoretical curve. It is important to note that in Figure A.15 the agreement between the data and the theoretical curve is very good.

Figure A.16 shows the data obtained for 45° shear waves and the corresponding theoretical curves. The agreement between the experimental data and the theoretical calculations is very good. We can compare the results for Data Set I and Data Set II. For the no-step case, the agreement between theory and experiment is better for Data Set I (Figure A.12). One notes that the experimental data is broader for Data Set II (Figure A.16). For the 10-mil step, the small peaks to the right of the main peak are more pronounced for Data Set II. For the 30-mil step, the theoretical calculations agree very favorably with the experimental data for Data Set I, and only slightly less so

for Data Set II. The reason for this is that the peak on the left side is not as broad for Data Set I as for Data Set II and the minimum between the two peaks has a smaller value in Data Set I. For the 60-mil step, the theory agrees very well with the data for Data Set II due to the existence of a secondary peak that is absent for Data Set I. The differences in the two sets of data are probably due to slightly different alignments of the transducer bracket relative to the plate.

A.7.4 Conclusions

In conclusion, this model provides a very good description of the data for the normal orientation, for 45° longitudinal wave generation, and for 45° shear wave generation. Thus, the hybrid Gauss-Hermite ray-tracing model is validated for the step discontinuity for the goal of ascertaining the adverse effects of surface conditions.

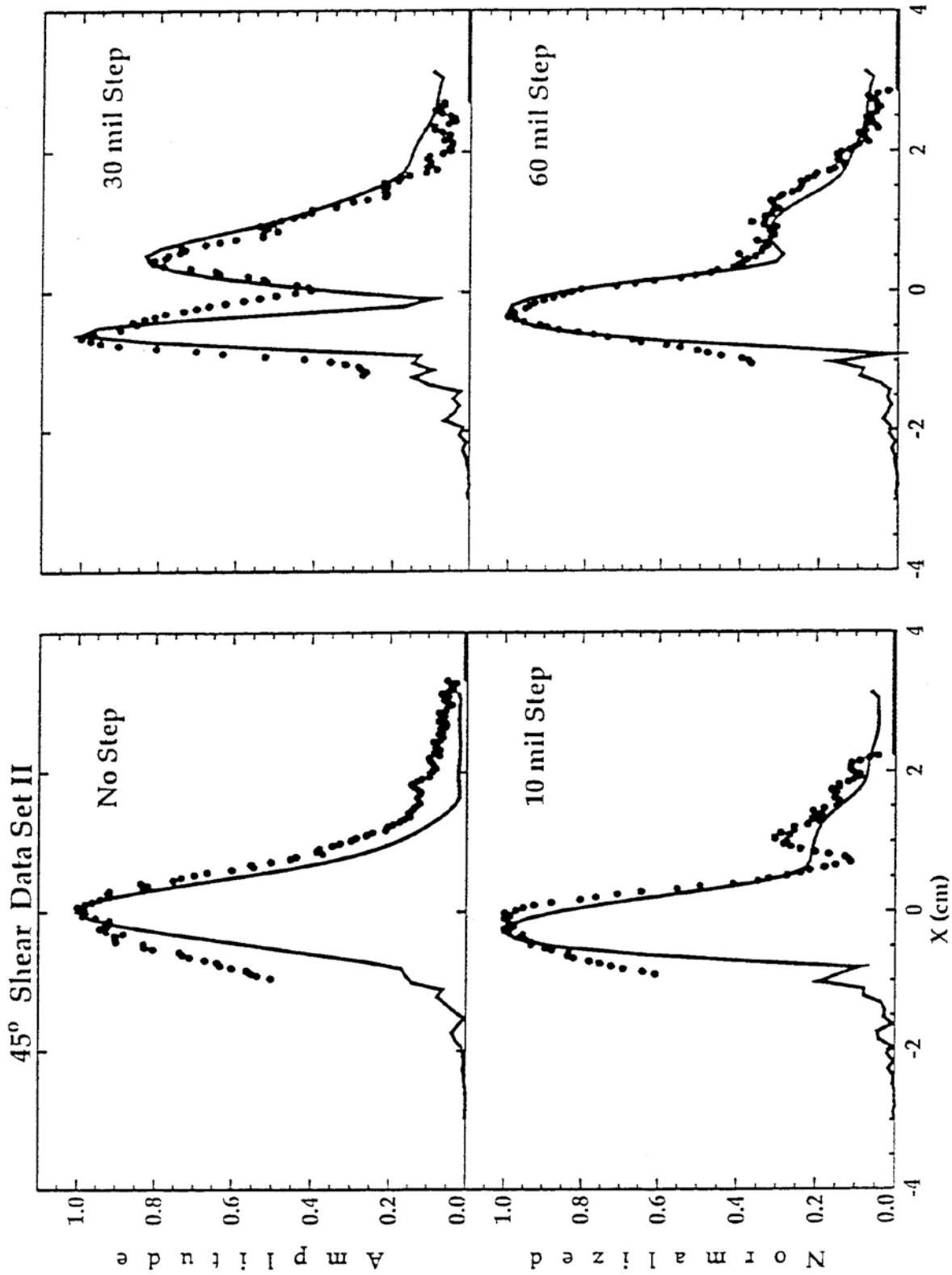


Figure A.16 Comparison of experimental data (Data Set II) with theoretical calculations for 45° shear waves

A.8 Theoretical Basis for Model II and Computer Code Description

The discussion in this section will center on the interaction of the ultrasound with the flaw, since the propagation of ultrasound through the rough surface and the propagation through the material has already been discussed for Model I. The variables needed for input to Model II will be described.

A.8.1 Theoretical Considerations

The reciprocity relationships derived by B. A. Auld (1979) will be used to determine the echo response due to a perpendicular flaw. Reciprocity relationships are theorems relating two different solutions to a differential equation. For example, Kinsler (1982, p. 165) discusses reciprocity relationships for the wave equation for velocity potential, Equation (A.7), and shows that, if the source and receiver are interchanged, the received signal will remain the same. Note that there are two situations to consider: (1) source and receiver in original positions, and (2) source and receiver positions are interchanged. Kinsler (1982, p. 185) also shows that a transducer has the same directional properties whether it is transmitting or receiving. Similarly, reciprocity relationships are used for electromagnetic waves to show that antenna power patterns are the same for transmitting or receiving (Barger and Olsson, 1987, p. 449).

The Model II code describes the pulse-echo inspection of a vertical crack at the bottom of a sample. The goal is to predict the electrical voltage signal which arises from the backscattering of ultrasonic waves from the perpendicular crack. Auld's reciprocity formula relates the ultrasonic fields in the vicinity of a crack to the electromagnetic signals in the cable which is attached to the transducer. A coaxial cable transports electrical energy to the transducer. A portion of this energy is converted to ultrasound, transmitted through one or more material layers to the site of the crack, and subsequently backscattered by the crack. This returning sound wave then produces an outgoing electromagnetic signal in the cable. A dimensionless reflection coefficient Γ is used to describe the reflected electromagnetic signal in the cable. For non-piezoelectric elastic media and general pitch/catch geometries, Auld (1979) has derived the following relationship for the change in Γ that is produced by the presence of a flaw:

$$\begin{aligned} \delta\Gamma &= \Gamma_{\text{flaw}} - \Gamma_{\text{n.f.}} \\ &= \frac{1}{4P} \int_A (\mathbf{v}_1 \cdot \mathbf{T}_2 - \mathbf{v}_2 \cdot \mathbf{T}_1) \cdot \hat{\mathbf{n}} \, dS \end{aligned} \quad (\text{A.35})$$

The subscript "1" refers to the situation when a flaw is not present for which the reflection coefficient is $\Gamma_{\text{n.f.}}$. The subscript "2" refers to the second situation when a flaw is present for which the reflection coefficient is Γ_{flaw} . Equation (A.35) describes the relationship between these two situations. P denotes the time-averaged electrical power carried by the incident electromagnetic field toward the transducer. The integration in Equation (A.35) may be performed over any closed surface that encloses the crack, and \mathbf{n} is the outward normal vector to that surface. \mathbf{v}_1 and \mathbf{T}_1 are the time-independent factors of the velocity and stress tensor (i.e., the factors that remain after $e^{i\omega t}$ term is removed), which occur in the absence of the flaw. \mathbf{v}_2 and \mathbf{T}_2 are the velocity and stress tensor, which occur in the presence of the flaw. The stress tensor \mathbf{T} is a 3 x 3 matrix and the dot product of a vector \mathbf{v} with the stress tensor \mathbf{T} is also a vector.

Equation (A.35) is valid for a single frequency. Thus, it is assumed that a steady-state situation exists in which the electromagnetic and sonic fields have a time dependence $e^{i\omega t}$, where $\omega = 2\pi f$. If the signal applied to the transducer is a broadband signal, the fast Fourier transform of this signal will give information about the relative contributions of each frequency. Each frequency can be treated separately and the change in the reflection coefficient obtained. One can then reconstruct the frequency spectrum of the return signal in the transducer and the inverse FFT will yield the signal as a function of time.

Let us now see how Equation (A.35) applies to the pulse-echo inspection of a vertical flaw. Since the net stress must vanish on the surface of a crack, the term $\mathbf{T}_2 \cdot \mathbf{n}$ is equal to zero and Equation (A.35) reduces to

$$\begin{aligned} \delta\Gamma &= \Gamma_{\text{flaw}} - \Gamma_{\text{n.f.}} \\ &= \frac{-1}{4P} \int_A \mathbf{v}_2 \cdot \mathbf{T}_1 \cdot \hat{\mathbf{n}} \, dS \end{aligned} \quad (\text{A.36})$$

Since the echo is due to the crack, the area A is reduced to that portion of the area of the crack that is insonified by the ultrasonic wave.

Further clarification of the two situations is needed in order to understand how Equation (A.36) can be applied to this problem.

Figure A.17a shows Situation 1, in which a flaw **is not** present. Note that the dashed line indicates the location of the flaw, when it is present. Two rays are shown in Figure A.17a. Ray #1 encounters the dashed line and continues in the same direction, because a flaw is not present here. Ray #2 strikes the bottom surface and it is reflected. It then also encounters the dashed line and its direction is unchanged. In Equation (A.36) the stress tensor has the subscript "1" and so it must be calculated using Situation 1.

Figure A.17b shows Situation 2, in which a flaw is present. In this case, each ray reflects from the flaw, as shown. In Equation (A.36) the velocity has the subscript "2" and so it must be calculated using Situation 2.

$$T_{ij} = c_{ijkl} u_{kl} \tag{A.37}$$

The components of the stress tensor T is calculated using Hooke's law of elasticity which states that each stress component is a linear function of each strain component (Beyer and Letcher, 1969). u_{kl} is the strain tensor, which is defined as

$$u_{kl} = \frac{1}{2} \left(\frac{\partial \xi_k}{\partial x_l} + \frac{\partial \xi_l}{\partial x_k} \right) \tag{A.38}$$

where ξ is the displacement. Note that the strain tensor has terms consistent with the elementary definition of strain, which is $\Delta L/L$. c_{ijkl} is a fourth-rank elastic modulus tensor that has 3^4 components, many of which are 0. For an isotropic solid the non-zero components can be determined from relationships involving the speed of longitudinal waves and the speed of shear waves in the solid.

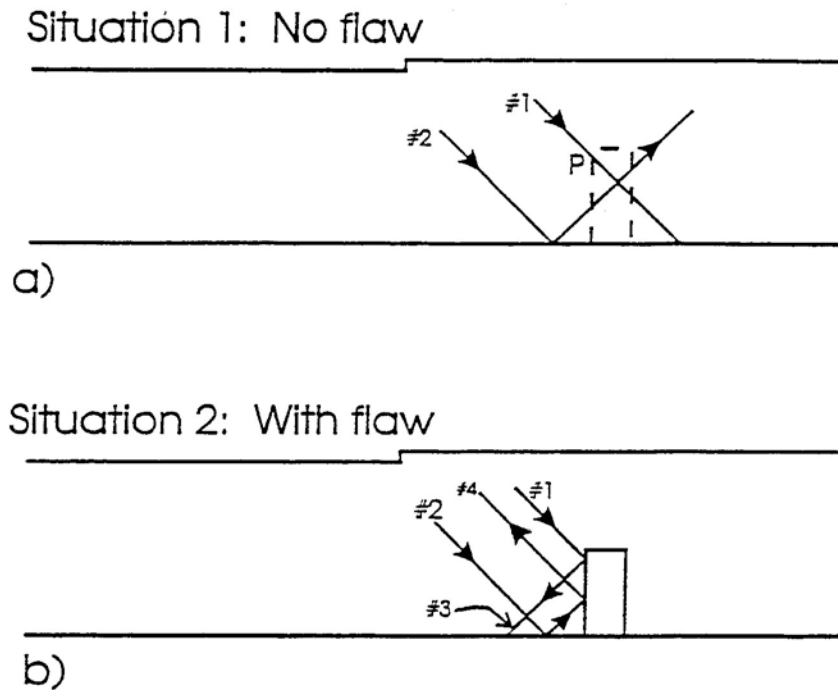


Figure A.17 a) Types of rays used in the calculation of the stress tensor T_1 for Situation 1, when no flaw is present; b) types of rays used in the calculation of the velocity V_2 , when a flaw is present.

Equation (A.37) can be expanded as

$$\begin{aligned} T_{ij} = & c_{ij11}u_{11} + c_{ij22}u_{22} + c_{ij33}u_{33} \\ & + 2c_{ij23}u_{23} + 2c_{ij13}u_{13} + 2c_{ij12}u_{12} \end{aligned} \quad (\text{A.39})$$

Therefore, since the elements of the tensor c_{ijkl} can be determined, the elements of the stress tensor T can be calculated from knowledge of the strain tensor u_{kl} , as shown by Equation (A.37).

The strain tensor, defined in Equation (A.38), must now be related to the calculations that are carried out in the Model II code. In Figure A.17a let us consider ray #1 first, where it intersects the dashed line (on the left). At this location, the program calculates the amplitude A of the displacement ξ . It is assumed that the wave in this region can be considered a plane wave:

$$\xi = A e^{j(\omega t - k \cdot r)} \quad (\text{A.40})$$

The program makes the assumption that all of the rays strike the flaw at the **same** angle. Therefore, the wave-number vector k is the same for all rays striking the flaw.

Next, let us consider ray #2 in Figure A.17a. For the sake of clarity, this ray does not pass through point P. However, there is another ray, similar to ray #2, that strikes the bottom surface first and is reflected so that it passes through point P. The two rays passing through point P produce a displacement that is the vector sum of the displacements produced by each ray separately, taking into account the relative phases of the two rays. For a ray similar to #2, the computer code calculates the amplitude B of the displacement at the intersection with the bottom surface. Then the reflection coefficient is calculated and the amplitude C of the displacement of the reflected ray is determined. The total displacement will be the vector sum of two terms similar to Equation (A.40). The components of the strain tensor u_{ik} are calculated by taking the derivatives of the total displacement, shown in Equation (A.38). With this information, the elements of the stress tensor T can be calculated.

The next step is to calculate the velocity v_2 . Figure A.17b shows four rays intersecting the surface of the flaw. The amplitude D of ray #3 is determined from the reflection coefficient and the amplitude A of ray #1. Similarly, the amplitude E of ray #4 is determined from the amplitude C

and the reflection coefficient. The total displacement will be the vector sum of four terms similar to Equation (A.40), involving the amplitudes A , C , D , and E . The velocity v_2 is obtained by taking the derivative with respect to time of the total displacement.

The surface of the flaw in the y - z plane is divided into a rectangular grid of points in order to carry out the numerical integration. The velocity v_2 and the stress tensor T_1 are evaluated at each point in the grid. The dot product operations, indicated in the integrand of Equation (A.37), are carried out and the numerical integration over the surface of the flaw is performed.

Let us recall that Equation (A.37) is valid for a single frequency and the power P refers to the power at that frequency. The computer code permits any type of voltage-versus-time signal, $f(t)$, to be applied to the transducer. One of the first steps is to take a fast Fourier transform (FFT) of $f(t)$ to obtain the function $F(f)$. A loop is carried out in the computer code to treat each frequency separately and then recombine the resulting responses in a way that will now be described. The power P refers to the power spectral density which is defined as

$$P(f) = |F(f)|^2 + |F(-f)|^2 \quad (\text{A.41})$$

For a given frequency f , the power spectral density $P(f)$ is substituted into Equation (A.37). Thus, the quantity on the left hand side of Equation (A.37) is evaluated for each frequency and one obtains the function $\delta\Gamma(f)$. The inverse fast Fourier transform of $\delta\Gamma(f)$ yields a function of time. The real part of this function is proportional to the voltage observed when an oscilloscope is attached to the cable.

A.8.2 Main Program Description

We shall discuss the Model II computer code by considering a sample set of input. Since there are many parameters in the Model II code that are the same as those in the Model I code, only the differences will be described. *Experimental Setup:* Figure 1.2 illustrates the experimental set up. The transducer has a radius of 0.635 cm and a center frequency of 2.25 MHz. The central ray from the transducer makes an angle of 18.9° with the vertical so that 45° shear waves are produced in the steel plate (thickness = 1.67 cm). The central ray strikes the top of the step discontinuity, which has a height of 0.152 cm.

The distance from the transducer face, along the central ray, to the top of the step is 7.62 cm. The perpendicular crack has a depth of 0.835 cm and a width of 2.54 cm. The face of the crack is a distance of 1.67 cm in from the step discontinuity in the top surface.

Table A.2 shows the program input for this experimental setup. Figure A.18 shows a diagram defining parameters and coordinate systems used in the code.

Line 1. Transducer information

rx,ry:
semi-axis of an elliptical transducer along the x and y axes. For a circular transducer rx = ry = 0.635 cm.

f0x, f0y:
transducer focal lengths along the x and y axes. For a planar transducer, f0x = f0y = 1.0e30.

Line 2. Gauss-Hermite (G-H) beam information

nc:
number of terms used in the G-H expansion, nc = 25.

Line 3. Incidence, interface, and transmission configuration

Same as line 3 for Model I code.

Line 4. Material properties of Incident medium

Same as line 4 for Model I code.

Line 5. Material properties of the transmitted medium

Same as line 5 for Model I code.

Line 6. Material properties of the medium adjacent to bottom surface

Same as line 6 for Model I code.

Line 7. Transformation parameters from the interface coordinate system to the transducer coordinate system

Same as line 7 for Model I code. The experimental data will be acquired by scanning the transducer and obtaining information as a function of position, relative to the step. When the central ray strikes the top of the step, then for this example

$$x1 = -7.62 \sin 18.9 = -2.468 \text{ cm}$$

$$\text{and } z1 = 7.62 \cos 18.9 = 7.209 \text{ cm}$$

However, for other positions in the scan, z1 is unchanged, but a different x1 coordinate is used, e.g., x1 = -2.671 cm. The calculations must be carried out for each transducer position.

Table A.2 Example of input file (ij247.d60) for Model II Code

Line	
1	0.635 0.635 1.E30 1.E30: radiusx, radiusy, focusx, focusy
2	25: G-H expansion
3	18.9 45.0 1.E30 1.E30 7.62: th1,th2, bx,by,z0
4	0.148 0.0 1.0 1: n11, v1s,rho1,ntw
5	0.590 0.323 7.62 2: v21,v2s,rho2,ntw
6	0.148 0.0 1.0: v31,v3s,rho3
7	0. 161.1 0 -2.468 0.0 7.209: rot. and transl. from int. to transd. sys.
8	0.7071 0.0 -0.7071 0.0: equation of transmitted plane w.r.t. int. sys.
9	0.0 135.0 0.0 0.0 0.0 0.0: rot. and transl. from int. to transm. sys.
10	0.0 135.0 0.0 -1.67 0.0 1.67: rot. and transl. from crack to transm. sys.
11	0.835 2.54 20 20: depth and width of the crack, no. of crack grid in 2 dir.
12	g9904.d60: file which contains interface grid points
13	trans8.dat: file for transducer parameters
14	oj247.d60: output file showing time signal

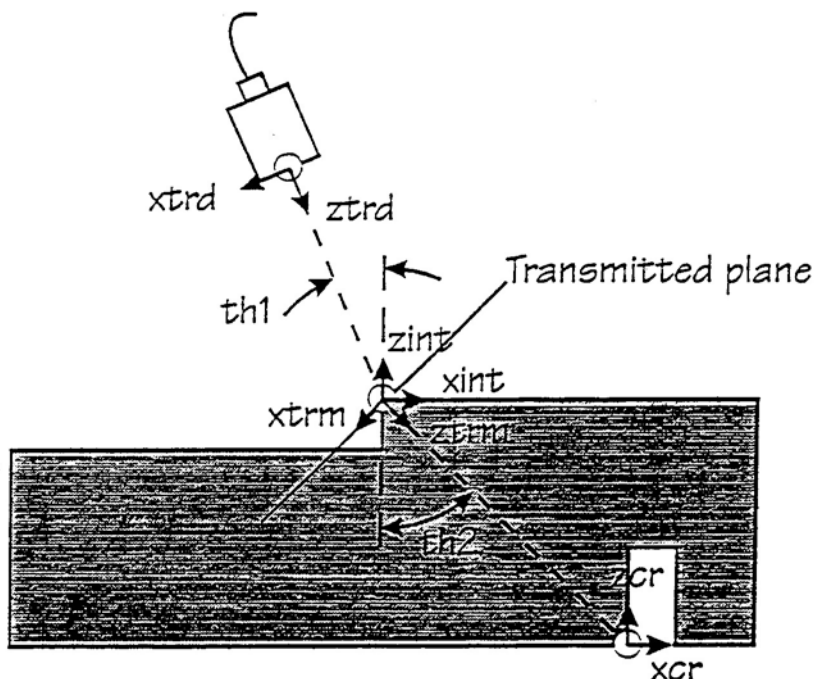


Figure A.18 Definition of coordinate systems used in computer code for Model II

Line 8. Equation of the transmitted plane with respect to the interface coordinate system

Same as line 8 for Model I code.

Line 9. Transformation parameters from the interface coordinate system to the transmitted coordinate system

Same as line 9 for Model I code.

Line 10. Transformation parameters from the crack coordinate system to the transmitted coordinate system

alfa3, beta3, gama3:
rotational angles

x3, y3, z3:
translation parameters

The parameters are obtained in the same way as the other coordinate transformations. The parameters x3 and z3 depend on the thickness of the plate.

Line 11. Description of the crack

dpth, wdth, grddp, grdwd

dpth:
depth of the crack measured along the z axis of crack coordinate system

lgh:
length of the crack measured along the y axis of crack coordinate system

grddp:
number of integration steps over the crack in the z direction

grdwd:
number of integration steps over the crack in the y direction

The minimum number of grid points was found to be 20 by 20.

Line 12. Name of file containing the grid points on the interface which describes the surface

Same as line 11 for Model I code.

The file name, g9904.d60, indicates that the surface is described by a grid having 99 by 99 points, separated by 0.04 cm, with a step discontinuity of 60 mils.

Line 13. File name for transducer efficiency

A reference pulse is the echo obtained when the ultrasound beam, directed normal to the smooth surface of the plate, is reflected from the top surface. The parameters that describe this reflection are given in this file for the transducer efficiency and will be described below. Next, let us consider the purpose of the reference pulse.

In these experiments, the experimental data were obtained by using a digitizer frequency of 25 MHz. This means that the voltage-versus-time pulse shape is defined by voltage values every 0.04 microseconds. One section of the code for Model II calculates the fast Fourier transform (FFT) of the reference pulse. If Δt is the time increment, then the frequency values for the FFT are separated by $\Delta f = 1/N \Delta t$, where N is equal to the number of samples in the reference pulse. For example, if $N = 256$ and $\Delta t = 0.04$ microseconds, then $\Delta f = 0.09766$ MHz. The FFT analysis of the reference pulse provides the power spectral density of each frequency contributing to it. The program begins with the smallest frequency, considers that the transducer produces ultrasound with that frequency only, and finds the echo produced by the flaw. The frequency is

incremented by Δf and these steps are repeated for each frequency contained by the reference pulse. Then contributions from each frequency are obtained by considering the power spectral density of that frequency. The inverse FFT produces a voltage-versus-time signal corresponding to the echo. This information is written to the output file, which gives the voltage versus the time incremented by Δt .

Line 14. Output file showing echo signal

In this example, the output file is called oj247.d60. It contains the results for flaw J in which the transducer is situated at $x = -2.47$ cm and the step height is 60 mils. If $\Delta t = 0.04$ microseconds and $N = 256$, the output file will also contain 256 points with $\Delta t = 0.04$ microseconds.

A.8.3 File for Transducer Efficiency

Table A.3 shows the program input for the file describing the transducer efficiency.

Line 1. Liquid medium parameters

Fluid density in g/cm^3 , longitudinal velocity in $cm/microseconds$

Line 2. Plate parameters

Density of plate in g/cm^3 , longitudinal velocity in $cm/microseconds$

Table A.3 File for transducer efficiency

Line	
1	1.0 0.184: Fluid density (g/cm^3), fluid acoustic velocity ($cm/microsec$)
2	7.62 0.590: Solid density (g/cm^3), solid velocity ($cm/microsec$)
3	0 1 : fluid alpha and n
4	0 1 : solid alpha and n
5	0.635 1.E30 : transducer radius (cm), transducer focal length (cm)
6	5 : Max frequency (MHz)
7	7.0 : Water path length (cm)
8	0.0 : Solid path length (cm)
9	SIGPERP8 : file containing ref. time signal
10	0.1 : Wiener filter (0 to 100%)

Line 3. Fluid parameters

alpha, n

Set alpha = 0 and n = 1

Line 4. Solid parameters

alpha, n

Set alpha = 0 and n = 1

Line 5. Transducer parameters

Transducer radius in cm, transducer focal length

Only circular transducers are considered at the present time.

Line 6. Maximum frequency

Maximum frequency in MHz

This is the highest frequency that will be considered in the calculations for the Model II code. If the center frequency of the transducer is 2.25 MHz, then a reasonable value for the maximum frequency is, say, 5.0 MHz.

Line 7. Liquid path length

Liquid path length in cm

This is the distance between the transducer face and the top of the steel plate.

Line 8. Solid path length

Solid path length in cm. For reflection from the top of the plate, set this parameter equal to 0.0.

Line 9. File name for reference time signal**Line 10. Filter**

Describes a Wiener filter, which ranges from 0 to 100%. A typical value is 0.1.

A.8.4 Description of File for Reference Time Signal

The first line of this file contains the integer N, where N is the number of points describing the reference time signal. N is defined by

$$N = 2^n,$$

where n is an integer less than or equal to 10. For example, for an eight cycle tone burst N was 256.

The following lines, N in number, contain the voltage values of the time signal. There is one value per line.

The last line contains the value of At in microseconds. Usually, At = 0.04 microseconds.

A.9 Model II Experimental Validation Measurements

This section describes the experimental apparatus that was used to validate Model II and the procedures employed to analyze this data. The nomenclature to describe the flaw and whether the ultrasound passed through a step or a smooth surface is defined. The measurement of a normal reference pulse, needed for input into the Model II code, is also discussed.

A.9.1 Experimental Apparatus

Figure 1.2 shows a diagram of the experimental apparatus. A steel plate with step discontinuities on the top surface is placed in an immersion tank and a transducer is attached to the arm of a laboratory x-y scanner. Pulse-echo measurements are obtained when ultrasound is reflected by a perpendicular flaw. Figure A.19 shows more detailed information about the steel plate. Figure A.19a shows the top view of the plate, in which all flaws are end-milled slots. The length of the flaw is 2.54 cm and smaller dimension is 1.27 cm. Figure A.19b, a cross-sectional view of the plate, shows three step discontinuities all having a step height of 0.152 cm (60 mils). The three flaws in this figure are labeled J, I, and C, and this

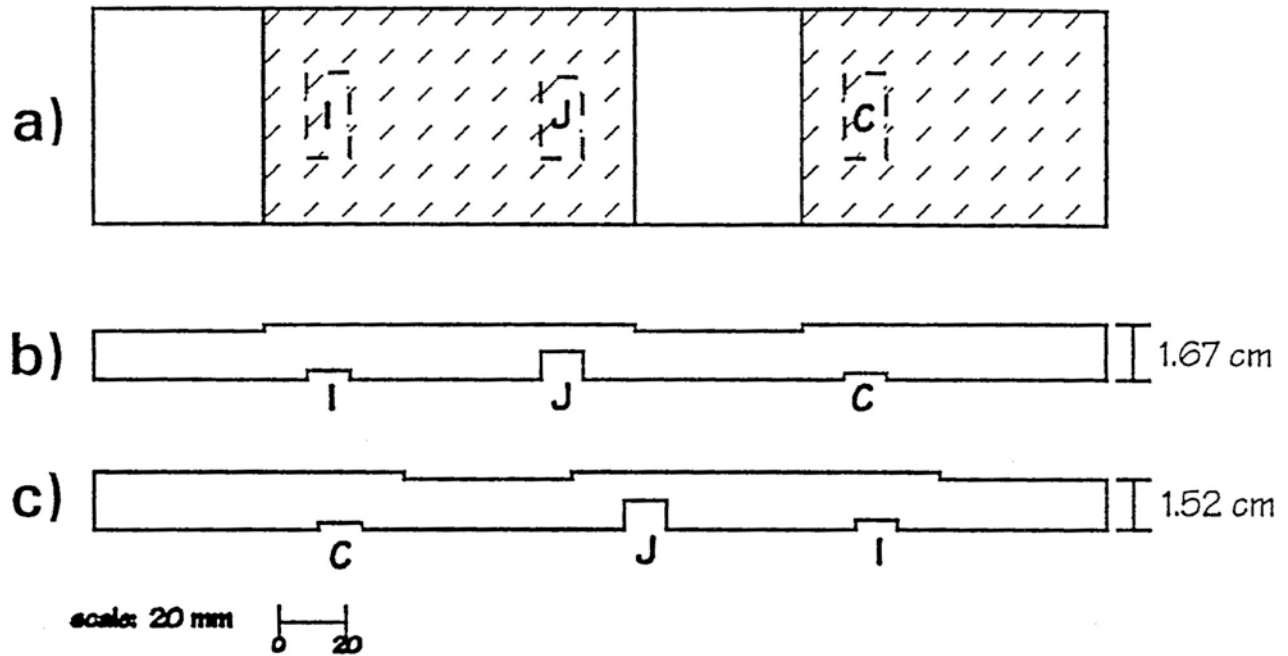


Figure A.19 Diagram of steel plate used in validation experiments for Model II. a) top view. The flaws are end-milled slots with dimensions 2.54 cm by 1.27 cm. b) cross-sectional view of plate with three step discontinuities of 0.152 cm depth. The three flaws are labeled J, I, and C for identification. The scan direction is left to right, c) cross-sectional view with the plate reversed. The scan direction is now left to right.

designation will be used throughout. Information about the flaw parameters is summarized in Table A.4. The third column indicates the horizontal distance between the step and the closer face of the flaw.

Table A.4 Flaw parameters

Flaw	Depth	Distance to flaw
J	0.834 cm	1.676 cm
I	0.318 cm	1.325 cm
C	0.169 cm	1.328 cm

The computer-controlled scan was set up to take an A-scan in increments of 0.1016 cm (40 mils) along the length of the plate through the centerline. In Figures A.19b and A.19c, the scan direction is left

to right. When the plate was oriented as shown in Figure A.19b, the ultrasound had to pass through a step discontinuity on the top surface in order to reach flaws I and C, but passed through a smooth surface for flaw J. In the discussions that follow, it will be convenient to use the following designations:

- (1) I with step
- (2) J no step
- (3) C with step

Since the scanner took a scan in only one direction, the plate was reversed as shown in Figure A.19c. In this case, the ultrasound passed through a smooth surface for flaws C and I and passed through a step for flaw J. The designations are:

- (4) C no step
- (5) J with step
- (6) I no step

When data for all six cases is obtained, one can then see how the presence of a step discontinuity affects the pulse-echo measurements for flaws of three different depths.

Measurement were obtained using a planar transducer having a radius of 0.635 cm and a center frequency of 2.25 MHz. The transducer was oriented at an angle of 18.9° with respect to the vertical in order to produce 45° shear waves in the steel plate. An eight-cycle tone burst was applied to the transducer. When the transducer was oriented at 10.2° , 45° longitudinal waves were produced and also 21.7° shear waves. The A-scan data showed that the echo due to the shear wave arrived about 3 microseconds after the echo from the longitudinal wave. In order to avoid interference between the two signals, a one-cycle negative uni-polar pulse was applied to the transducer.

A.9.2 Measurement of Normal Reference Pulse

Pulse-echo measurements were also obtained when the ultrasound beam was directed normal to the surface of the steel plate. The data of interest was the reflection from the top surface of the plate. As described earlier, a file containing the pulse shape (voltage versus time) serves as input for the computer code. This pulse shape serves as a reference for describing the type of pulse that insonifies the flaw. A fast Fourier transform of this pulse shape shows the power spectral density of frequencies that constitute the pulse.

A.9.3 Data Analysis

The data analysis was carried out using the software PV-WAVE available on the SUN Workstation. As described in Section 6.3, this software permits selection of a single A-scan to be stored in the computer memory in order to produce a graph of the A-scan. Figure A.20 shows an A-scan for flaw J with step for 45° shear waves.

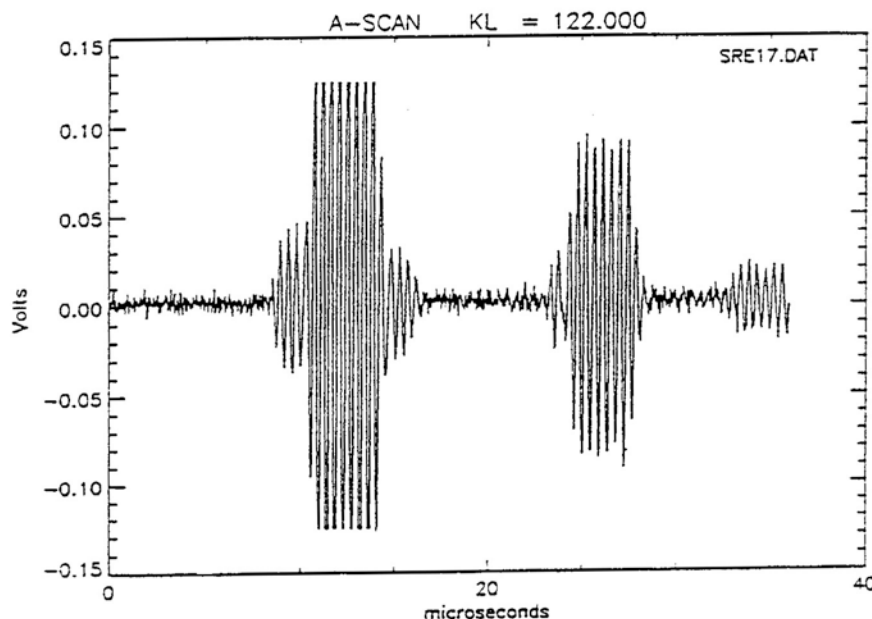


Figure A.20 A-scan of echo from flaw J for an eight-cycle tone burst insonifying the flaw after passing through a step on the top surface. The post-trigger delay was set to 92.96 microseconds. In order to obtain the elapsed time from the trigger, this post-trigger delay must be added to that shown on the graph.

The peak between 22 and 30 microseconds is due to shear waves reflected from flaw J. The peaks between 8 and 15 microseconds are due to ultrasound reflecting from the step discontinuity. Some of the beam is reflected from the top of the step and some from the bottom of it. The cursor is used to select a point on the left and right of the desired signal. Depending upon the application, there are several options available: (1) when an eight-cycle tone burst is used, the program can determine the maximum voltage value between the two cursor positions, or (2) the signal between the two cursor positions can be output to a file for subsequent comparison with theoretical calculations.

A.10 Comparison of Experimental Data with Theoretical Calculations for Model II

In this section the experimental data are compared with the theoretical calculations using the Model II code. The first subsection deals with the choice of two input parameters for the Model II code: the grid point separation distance and the integration step size over the surface of the flaw. The remaining subsections deal with the comparison of theoretical calculations with the experimental data. In particular, the normalization of theoretical curves with the data is described. The ability of the theory to delineate the effect of a step discontinuity, compared to a smooth surface, is discussed.

A.10.1 Grid Point Separation Distance and Integration over Surface of Flaw

Two parameters that influence the accuracy of the calculation are the interface grid point separation distance and the integration step size over the surface of the flaw. In Model I the interface grid point separation distance was shown to be an important factor. For Model II calculations, the effect of decreasing the grid point separation distance was also investigated by decreasing the grid size until very little change in the theoretical calculations was found. On the other hand, decreasing the size also results in a longer running time. For Model I, the grid points covered an area 6 cm by 6 cm. For Model II, the optimum

situation was a grid point separation distance of 0.04 cm with the grid covering an area 4 cm by 4 cm.

For the integration over the surface of the flaw, the flaw is subdivided using a grid of points. For flaws J, I, and C, the optimum flaw grid size was 20 by 20. Changing the flaw grid size to 30 by 30 had very little effect.

In the calculations reported here, the interface grid file (called g9904.d60) contains a grid point separation distance of 0.04 cm for a 99 x 99 point grid. The flaw grid was not less than 20 by 20. Figure A.21 shows the pulse-echo response from flaw J predicted by the Model II code when an eight-cycle tone burst 45° shear wave insonifies flaw J. The transducer is located at $x = -2.47$ cm.

A.10.2 Data Set I for 45° Shear Waves, Eight-cycle Tone Burst

In Data Set I the measurements for the normal reference pulse were obtained by applying an eight-cycle tone burst to the transducer. Care was taken to ensure that the pulser-receiver was not saturated. The amplifier settings were not changed when the pulse-echo measurements from the flaws were subsequently obtained for 45° shear waves.

The pulse-echo measurements were analyzed as described in Section 9.3 by obtaining the maximum voltage of the tone burst signal for each position of the transducer (or each A-scan). The scanning increment was 0.1016 cm. Figures A.22 through A.25 show the experimental data, in which the normalized amplitude is plotted versus the transducer position. The data are normalized in the following way. The peak voltage for J no-step is 0.098 volts. However, in order to obtain the best fit of the experimental data for all four cases, a normalization constant of 0.092 volts was used. All experimental data points for the four cases were normalized by dividing each voltage by 0.092 volts. Thus, the peak relative amplitude for flaw J no-step is 1.07 as shown in Figure A.22. As would be expected, the flaw with the greatest depth gives the largest echo voltage. Thus, flaw J gives the largest echo, followed by flaw I.

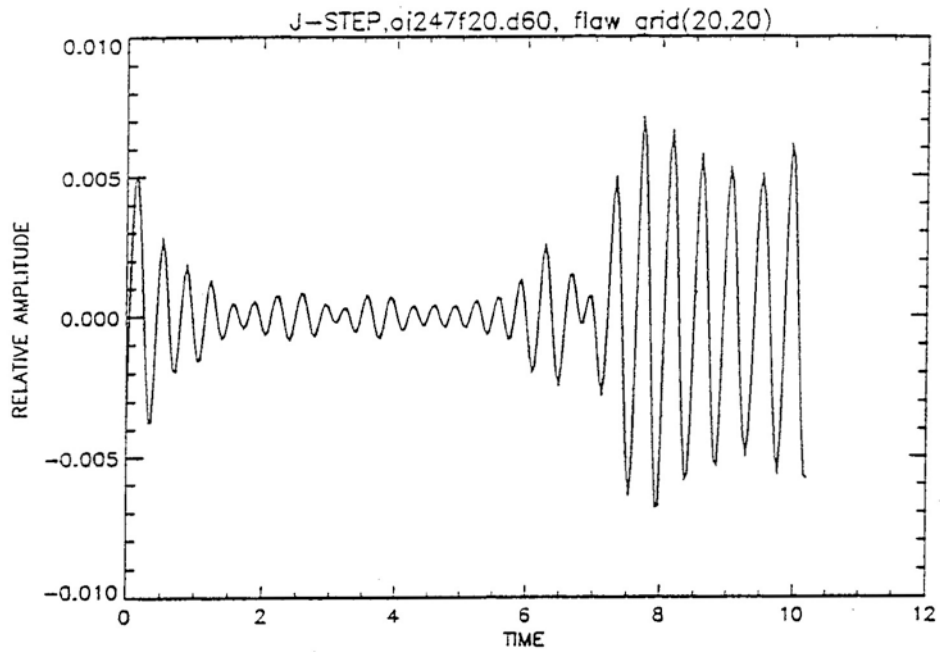


Figure A.21 Output from the Model II code for an eight-cycle tone burst, 45° shear waves

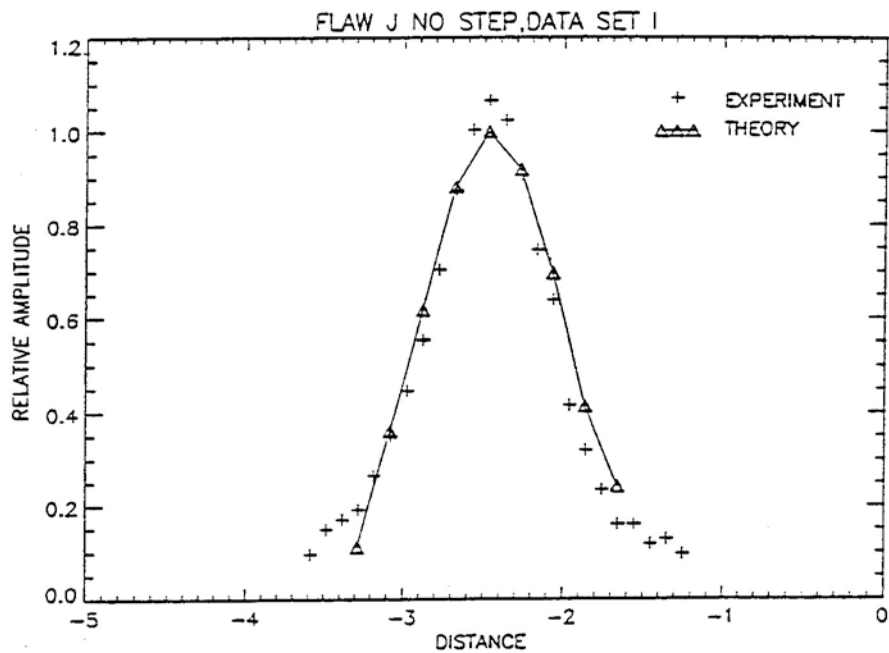


Figure A.22 Comparison of experimental data (Data Set I) with theoretical calculations for eight-cycle 45° shear waves insonifying flaw J no-step

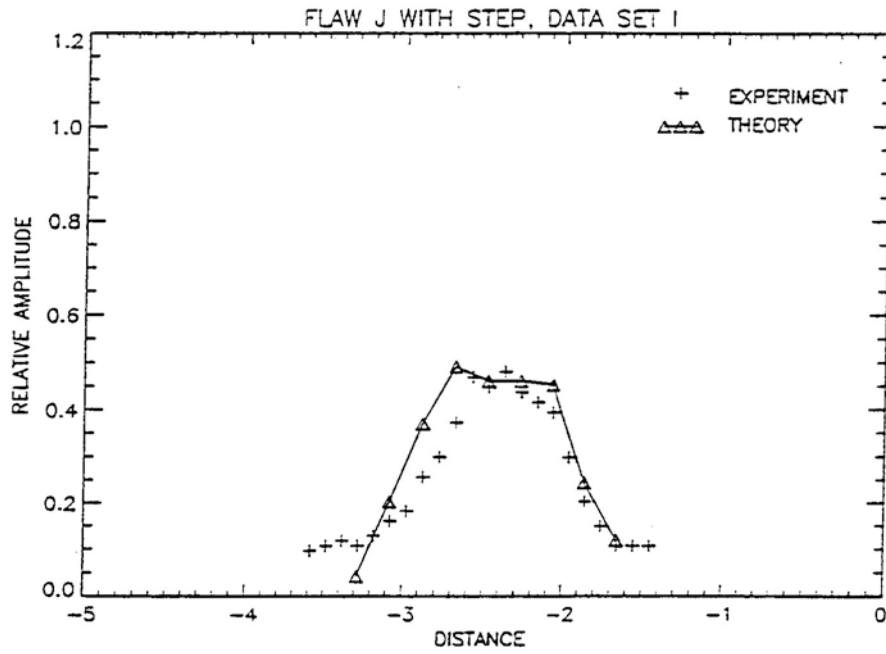


Figure A.23 Comparison of experimental data (Data Set I) with theoretical calculations for eight-cycle 45° shear waves insonifying flaw J with-step

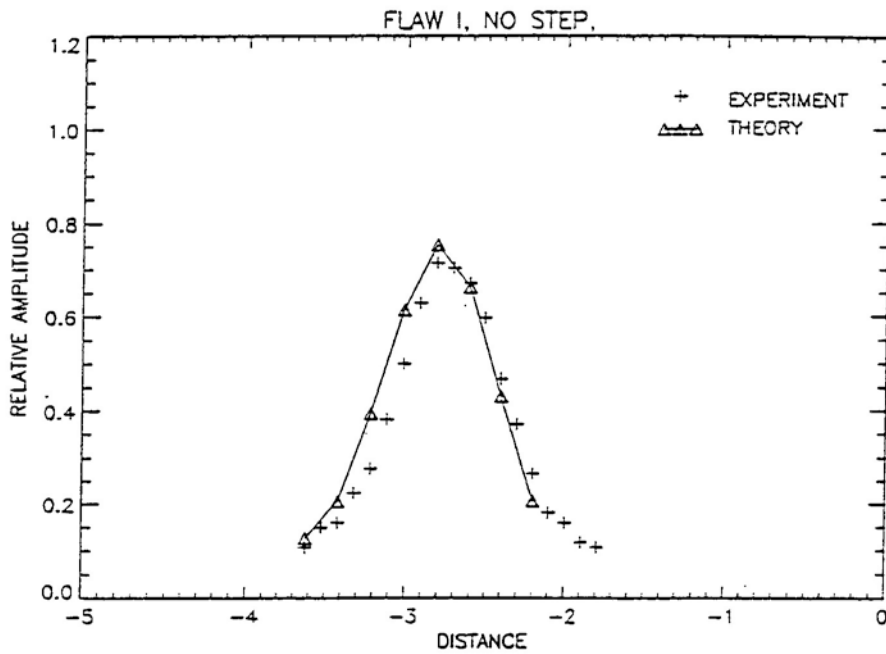


Figure A.24 Comparison of experimental data (Data Set I) with theoretical calculations for eight-cycle 45° shear waves insonifying flaw I no-step

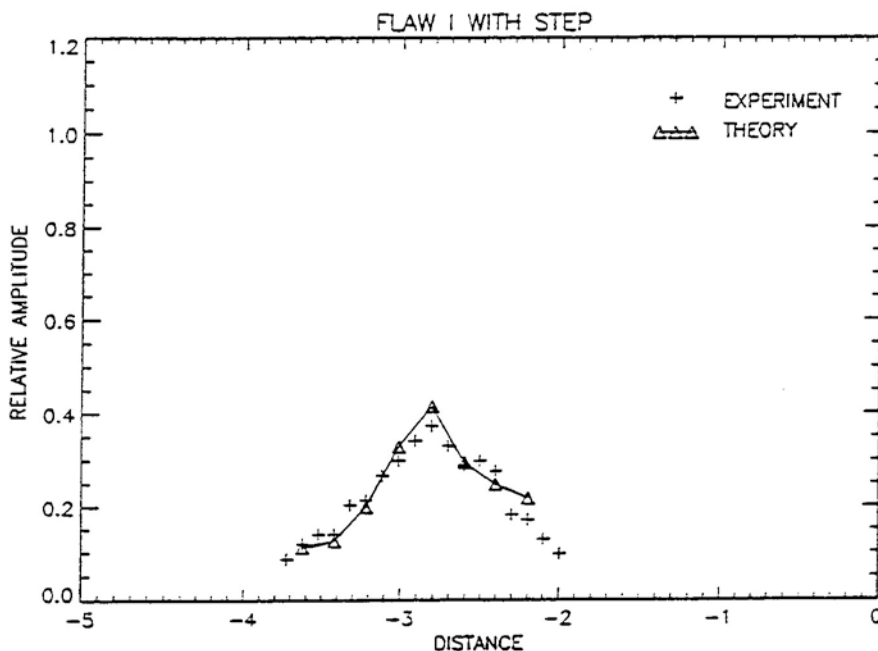


Figure A.25 Comparison of experimental data (Data Set I) with theoretical calculations for eight-cycle 45° shear waves insonifying flaw I with-step

The theoretical calculations were obtained by incrementing the transducer position by 0.2032 cm. The pertinent transducer positions for input to the program were determined by assuming that the peak amplitude will occur when the central ray of the transducer strikes the corner of the flaw. This situation is shown in Figure A.26 for flaw I. The distance AC is given by

$$AC = 7.62 \sin 18.9 + (1.67 - 1.325) = 2.81 \text{ cm}$$

relative to the interface coordinate system located at the step, $x = -2.81$ cm. The theoretical calculation bear out this assumption and Figure A.24 shows a peak amplitude for $x = -2.81$ cm.

The theoretical calculations were also normalized in a similar way. For flaw J no-step the peak amplitude ($x = -2.47$ cm) was 0.346. All theoretical calculations for all flaws (with step and no step) were normalized by dividing by 0.346.

The fact that experimental data can be fit so well with the theoretical calculations **with only one normalization constant** is a very important result. In order to study the

effect of surface roughness in an inservice inspection, one must be able to compare the echo obtained from a flaw when the transducer passes over a smooth surface with that obtained when passing over a rough surface. These results show that the theory can be used not only to predict the change in amplitude for a given flaw, but is also able to predict the change in amplitude for a different flaw.

A.10.3 Data Set I for 45° Shear Waves, Uni-polar Pulse

Data were also obtained by applying a one-cycle negative uni-polar pulse to the transducer. The objective was to test the ability of the Model II code to predict the shape of the echo.

A one-cycle negative uni-polar voltage was applied to the transducer. Figure A.27 shows the reference pulse that is obtained by the reflection from the top surface of a steel plate by an ultrasound beam directed normal to the surface. This pulse shape serves as input to the Model II computer code, as has been discussed.

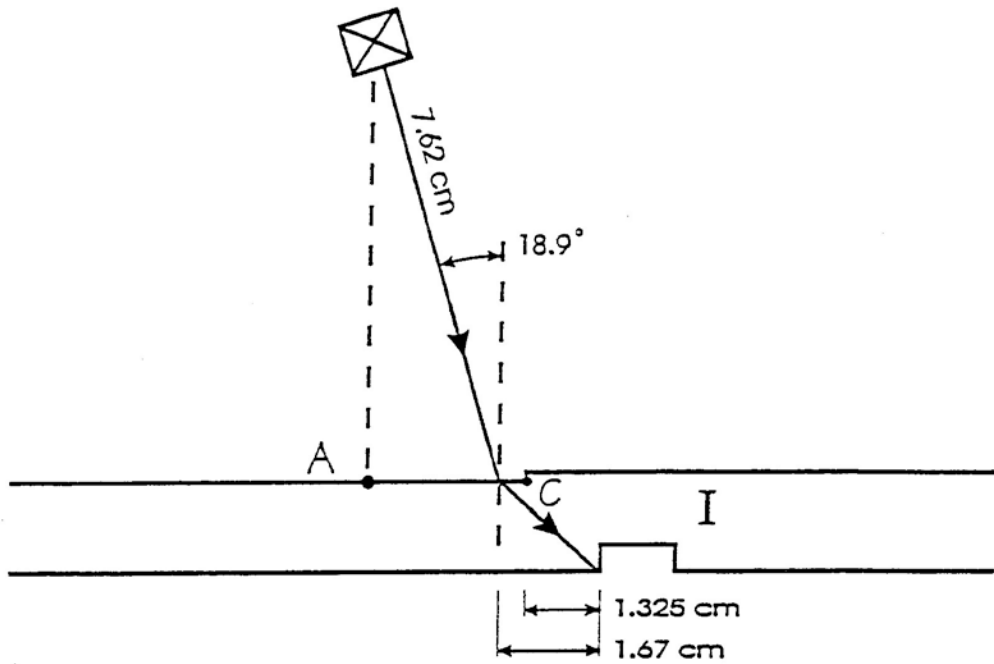


Figure A.26 Diagram showing central ray of the transducer striking the corner of flaw I

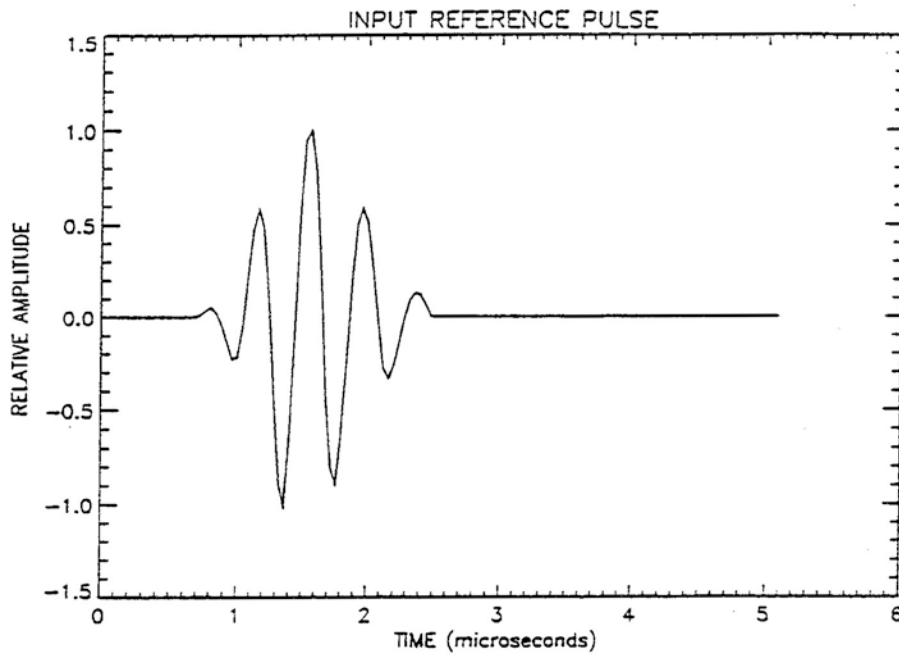


Figure A.27 Reference pulse obtained when a one-cycle bi-polar pulse is applied to the transducer

The theoretical calculations are compared with experimental data for flaw J-no step in Figure A.28 and for flaw J with-step in Figure A.29. The calculations and experimental data are normalized with respect to the peak value for J no-step, as has been described in the preceding section. The agreement between the theoretical calculations and the experimental data is excellent in both cases. The theoretical calculations show that, due to passing through the step discontinuity on the top surface, the pulse shape is broadened and this effect is found experimentally.

A.10.4 Data Set II for 45° Shear Waves, Eight-Cycle Tone Burst

Data Set II was obtained by using larger amplifier settings for the echo signal. Figures A.30 through A.35 show the resulting data, which was normalized using the peak values for J no-step as for Data Set I. The peak voltage for flaw J no-step was 0.612 volts and the experimental data were normalized using this voltage.

There is generally very good agreement between the experimental data from Data Set I and Data Set II. Figures A.32 through A.35 show very good agreement between the theoretical calculations and experimental data for flaw J and flaw I. Figures A.34 and A.35 show that the calculations do not predict as large an amplitude for C no-step as is observed experimentally, while C with-step amplitude is predicted quite accurately by the calculations, using the peak J no-step amplitude for normalization.

In order to use the results of computer calculations to study the effects of surface roughness on an inservice inspection, one will want to compare the signal received from a flaw when the transducer passes over a smooth surface compared to that from a rough surface. The depth of flaw C is 10% of the through-wall thickness. For flaw C let us compare the following ratios:

$$\frac{(\text{peak amplitude for C with-step})_{\text{exp}}}{(\text{peak amplitude for C no-step})_{\text{exp}}} = \frac{0.26}{0.60} = 0.43$$

$$\frac{(\text{peak amplitude for C with-step})_{\text{th}}}{(\text{peak amplitude for C no-step})_{\text{th}}} = \frac{0.25}{0.45} = 0.56$$

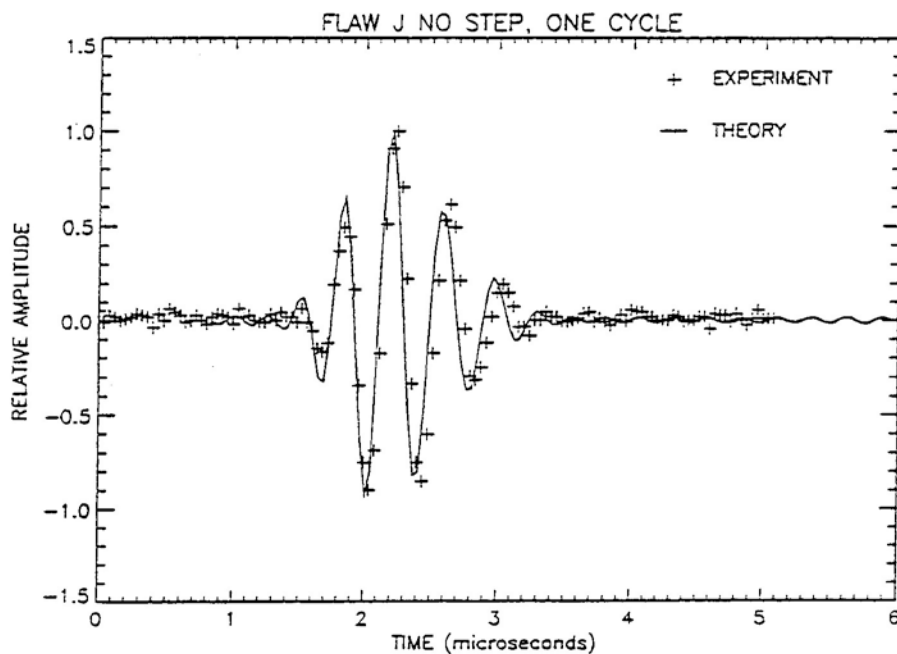


Figure A.28 Comparison of pulse shape predicted by theoretical calculations with experimental data for flaw J no-step

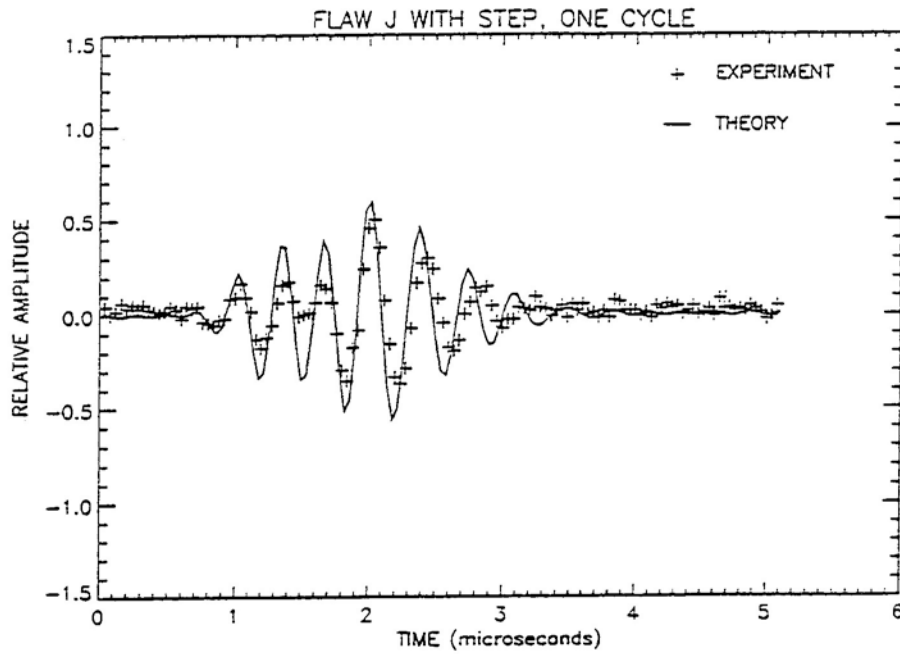


Figure A.29 Comparison of pulse shape predicted by theoretical calculations with experimental data for flaw J with-step

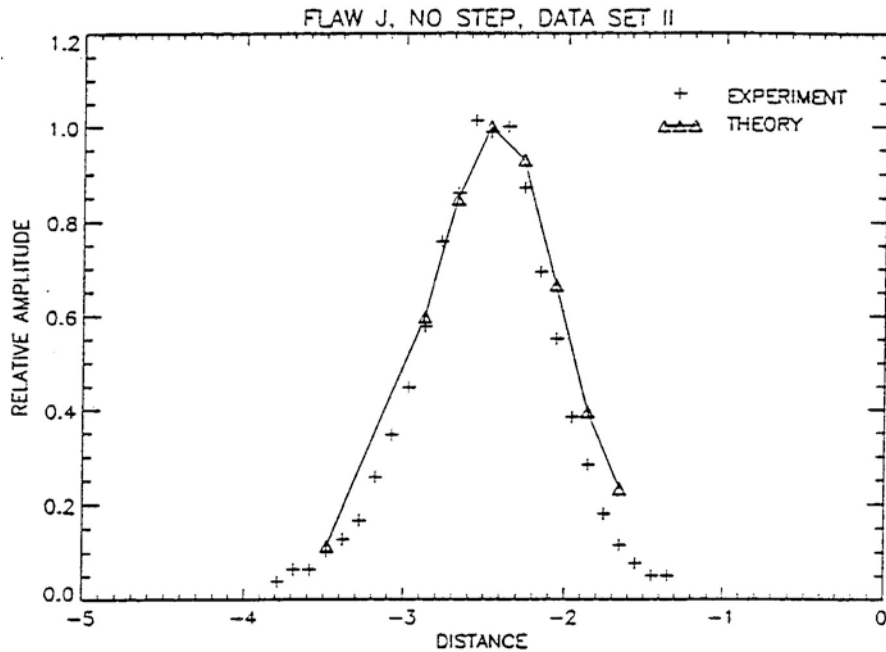


Figure A.30 Comparison of experimental data (Data Set II) with theoretical calculations for eight-cycle 45° shear waves insonifying flaw J no-step

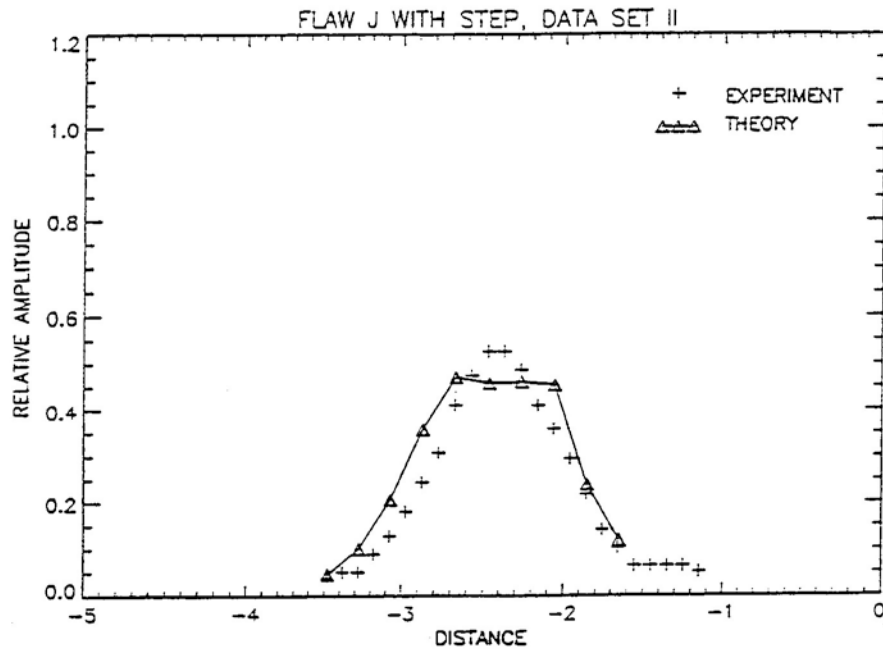


Figure A.31 Comparison of experimental data (Data Set II) with theoretical calculations for eight-cycle 45° shear waves insonifying flaw J with-step

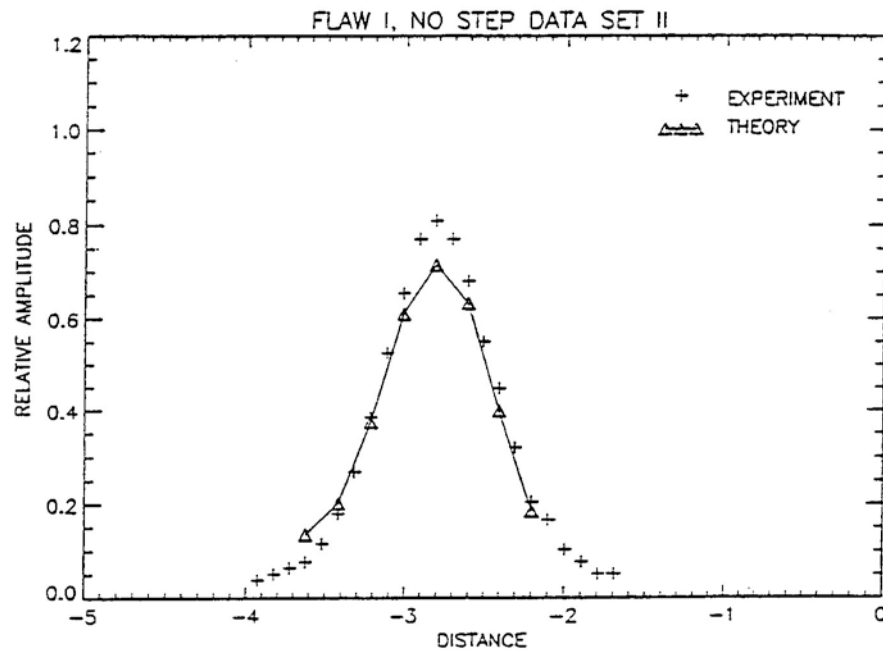


Figure A.32 Comparison of experimental data (Data Set II) with theoretical calculations for eight-cycle 45° shear waves insonifying flaw I no-step

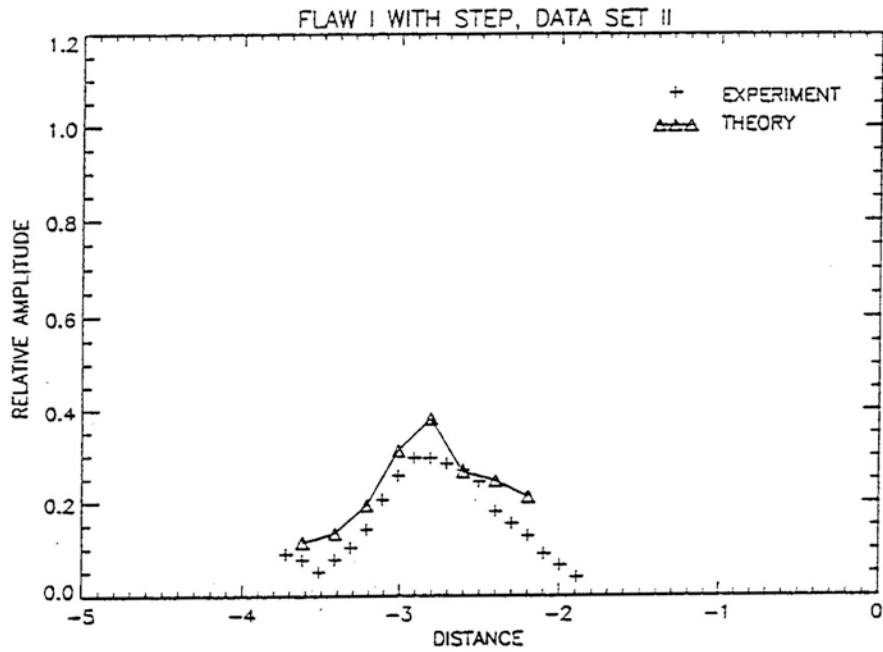


Figure A.33 Comparison of experimental data (Data Set II) with theoretical calculations for eight-cycle 45° shear waves insonifying flaw I with-step

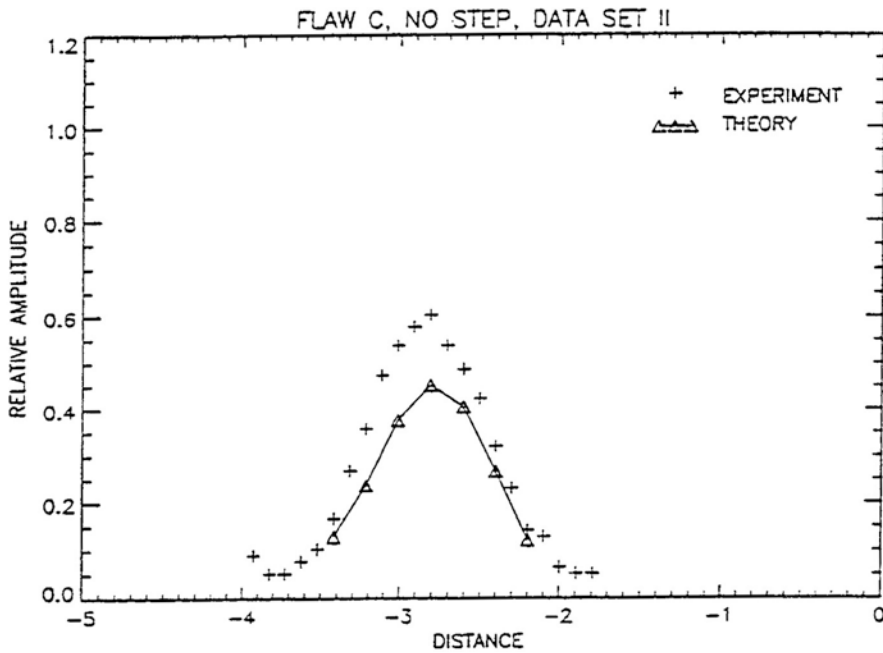


Figure A.34 Comparison of experimental data (Data Set II) with theoretical calculations for eight-cycle 45° shear waves insonifying flaw C no-step

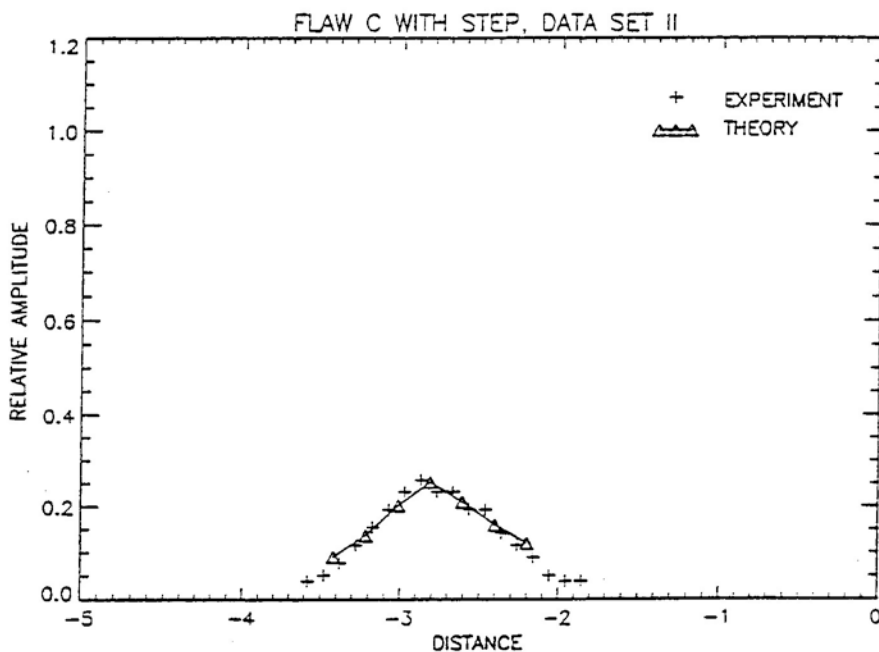


Figure A.35 Comparison of experimental data (Data Set II) with theoretical calculations for eight-cycle 45° shear waves insonifying flaw C with-step

These ratios show that the theoretical calculations overestimate the amplitude of C with-step (compared to C no-step) by about 23%, when compared with experimental data.

A.10.5 45° Longitudinal Waves, Negative Unipolar Pulse

A.10.5.1 Comparison of Pulse Shape

The transducer was oriented so that its central ray made an angle of 10.2° with the vertical. This caused 45° longitudinal rays and 21.7° shear waves to be produced in the steel. In order to eliminate any interference between the longitudinal and shear waves, one-cycle negative unipolar pulse was supplied to the transducer. The data showed that another pulse, interpreted to be a shear wave, arrived about 3 microseconds after the longitudinal pulse. The longitudinal pulse was easily identified by its arrival time and, due to the faster speed of longitudinal waves, was the first echo to arrive.

Figure A.36 compares the experimental data for flaw J no-step with the theoretical predictions of the pulse shape for five transducer positions. Note that the amplitude is expressed in volts rather than normalizing the peak amplitude to 1.0, as was done for the 45° shear data. When $x = -1.37$ cm the central ray of the transducer strikes the base of the flaw. The theoretical calculations were normalized by multiplying by a constant that would give a good fit to the experimental pulse shape at $x = -1.37$. That normalization constant was 15.47 and was used for all of the data shown in Figure A.36.

Figures A.37 through A.41 present similar comparisons for the other cases using the **same** normalization constant for all theoretical curves. The agreement is good for flaw J and I, but for flaw C the experimental data is somewhat larger than predicted by theory. The theoretical calculations predict that the pulse will be spread out due to the ultrasound passing through the step discontinuity and this is observed experimentally. A similar effect was noted for the 45° shear waves in Section A.10.3.

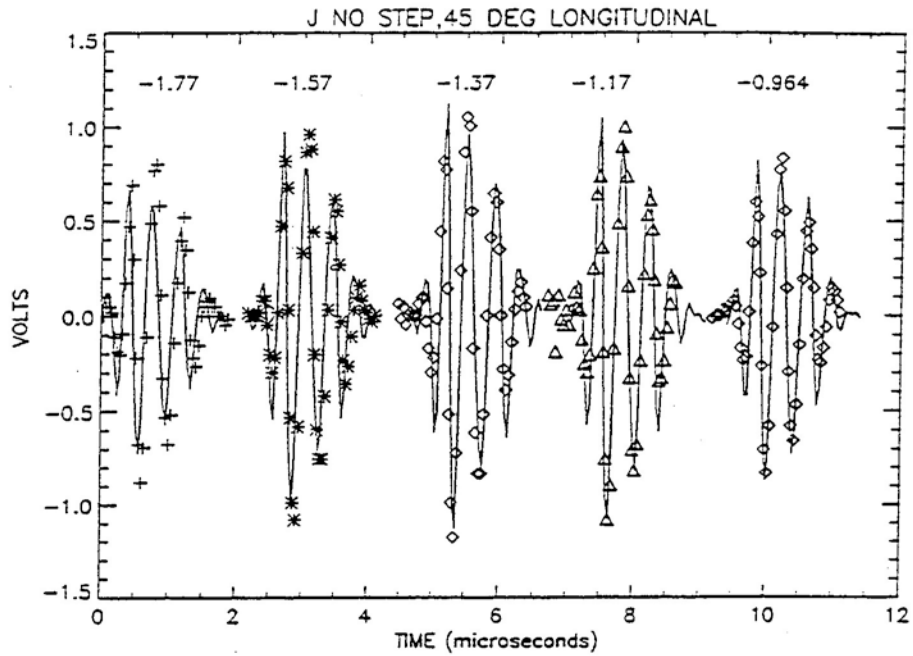


Figure A.36 Comparison of pulse shape predicted by theoretical calculations with experimental data for flaw J no-step for five transducer positions for 45° longitudinal waves

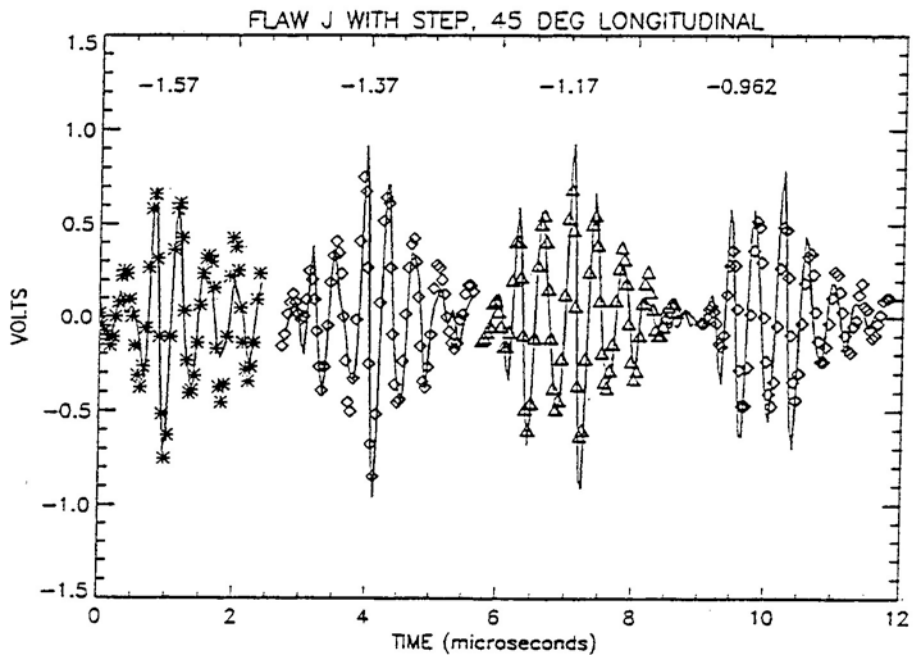


Figure A.37 Comparison of pulse shape predicted by theoretical calculations with experimental data for flaw J with-step for four transducer positions

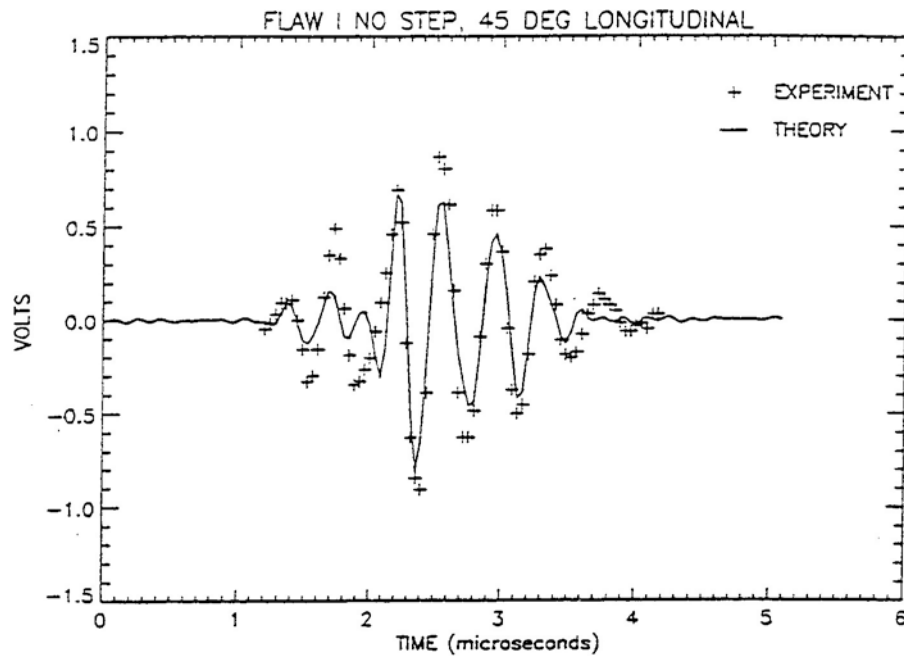


Figure A.38 Comparison of pulse shape predicted by theoretical calculations with experimental data for flaw I no-step for one transducer position

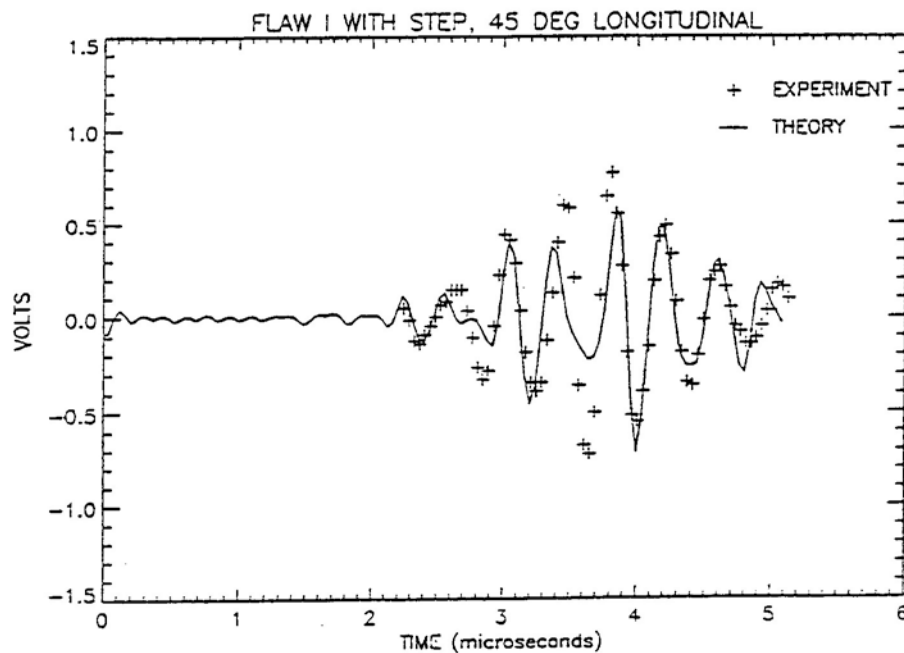


Figure A.39 Comparison of pulse shape predicted by theoretical calculations with experimental data for flaw I with-step for one transducer position

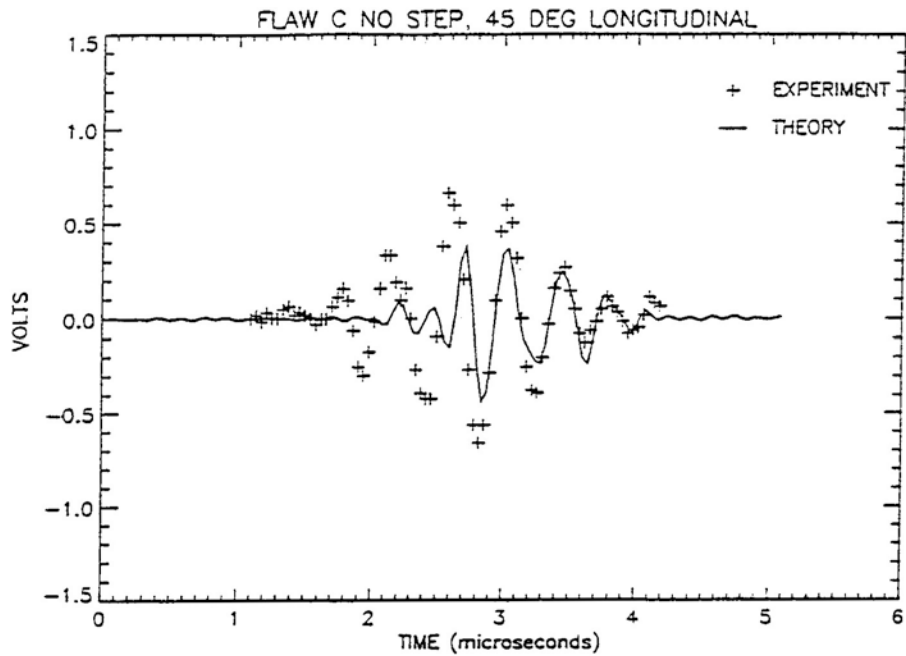


Figure A.40 Comparison of pulse shape predicted by theoretical calculations with experimental data for flaw C no-step for one transducer position

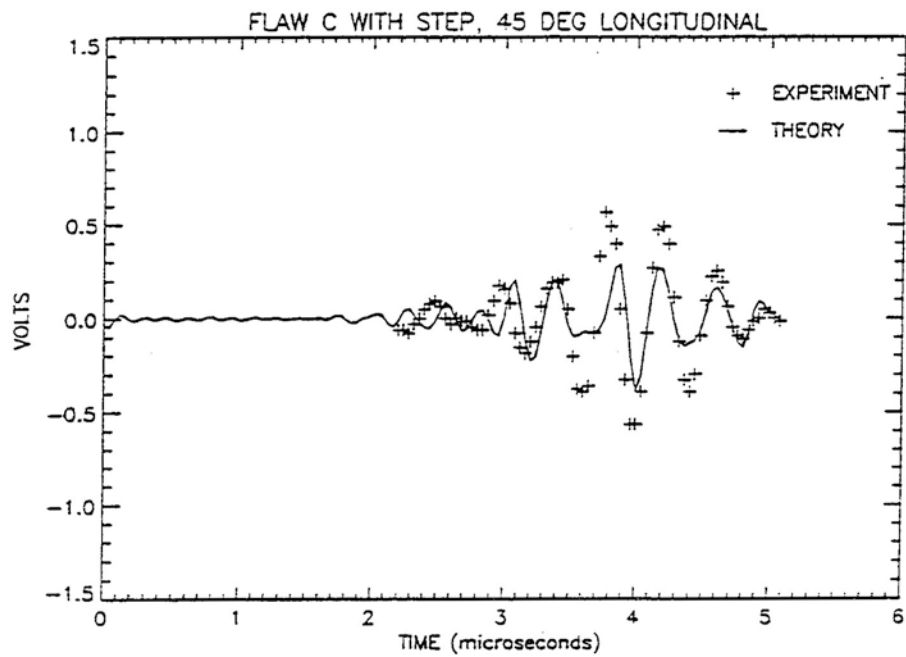


Figure A.41 Comparison of pulse shape predicted by theoretical calculations with experiment data for flaw C with-step for one transducer position

A.10.5.2 Comparison of Peak-to-Peak Amplitude

In order to gain perspective on the comparison between the experimental data and theoretical predictions, the maximum peak-to-peak amplitude obtained experimentally is compared with that predicted by theory in Figures A.42 through A.47. In these figures the solid lines corresponds to a normalization constant of 15.47 for the theoretical curves for all cases. In Figures A.44 and A.45, the normalization constant for the dashed line is 17.55 and in Figures A.46 and A.47 it is 25.07. When the same normalization constant is used for all cases, one finds that for flaw C the experimental data has a larger amplitude than predicted theoretically. However, it is also very important to note, since the normalization constant for the dashed line for flaw C no-step is the same as that for flaw C with-step, one can compare the echo when the transducer passes over a smooth surface with that over a surface with a step discontinuity. Thus, the effect of the step can be accurately measured by these calculations.

A.11 Summary of Results

One of the objectives of this study is to validate the theoretical models, called Model I and Model II, developed at the CNDE at Iowa State University as a result of a cooperative effort between CNDE (through EPRI support) and PNNL (through RES NRC support). Once validated, these models can be used as engineering tools to study the effects of surface conditions and to guide the development of ASME Code recommendations to ensure that surface conditions do not preclude an effective ultrasonic inspection. Currently, there are no ASME Code requirements dealing with surface conditions during an ultrasonic inspection. The detailed summary of the research and conclusions reached to date in this study are as follows:

- Model I describes the propagation of ultrasound:
 - (1) produced by a transducer immersed in water;
 - (2) through a rough top surface on a metal plate,

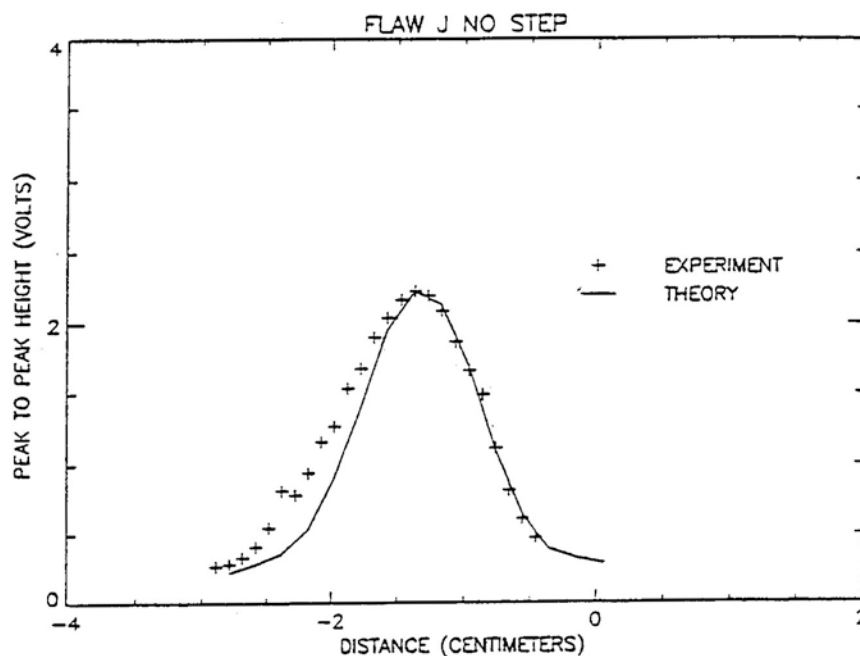


Figure A.42 Comparison of experimental data with theoretical calculations for 45° longitudinal pulse insonifying flaw J no-step

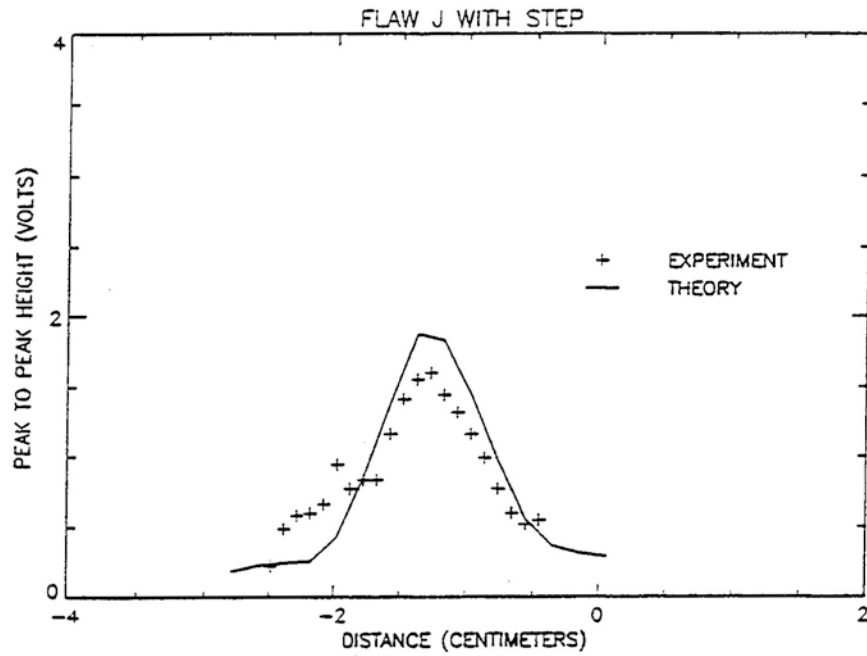


Figure A.43 Comparison of experimental data with theoretical calculations for 45° longitudinal pulse insonifying flaw J with-step

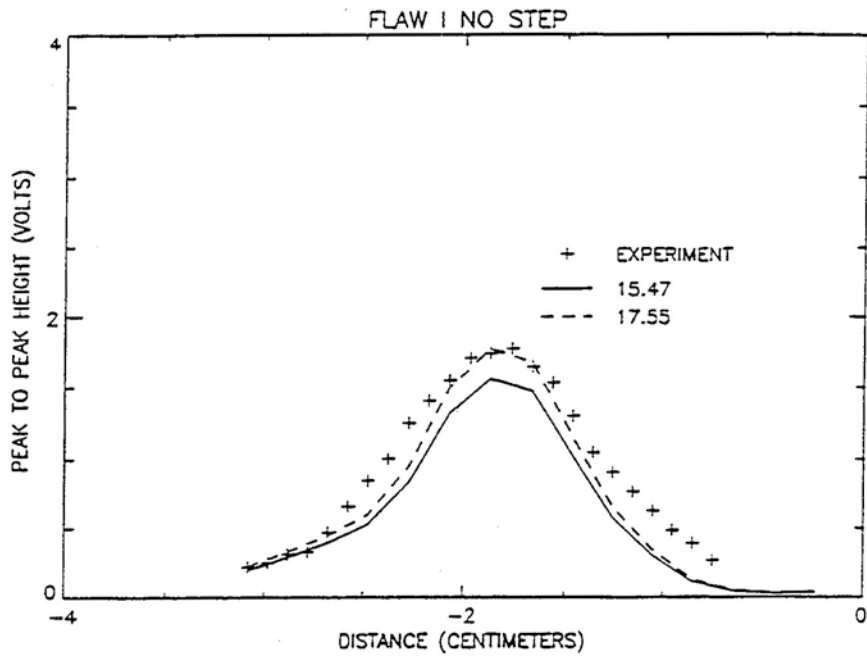


Figure A.44 Comparison of experimental data with theoretical calculations for 45° longitudinal pulse insonifying flaw I no-step

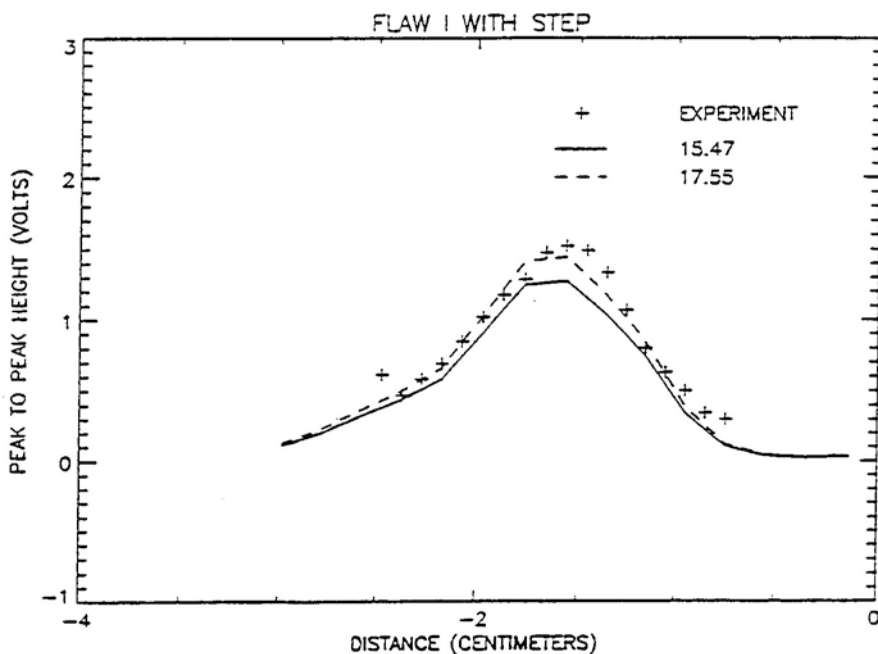


Figure A.45 Comparison of experimental data with theoretical calculations for 45° longitudinal pulse insonifying flaw I with-step

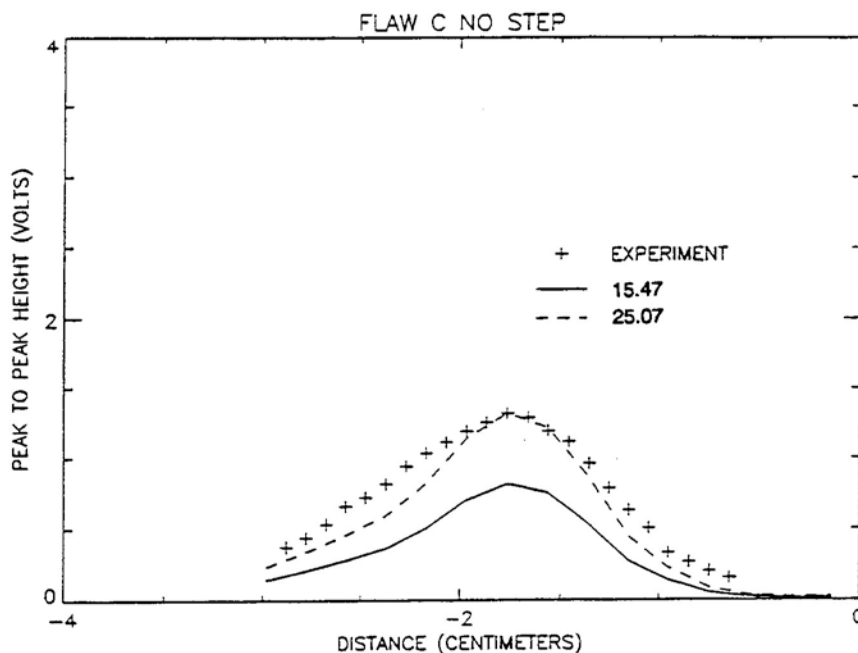


Figure A.46 Comparison of experimental data with theoretical calculations for 45° longitudinal pulse insonifying flaw C no-step

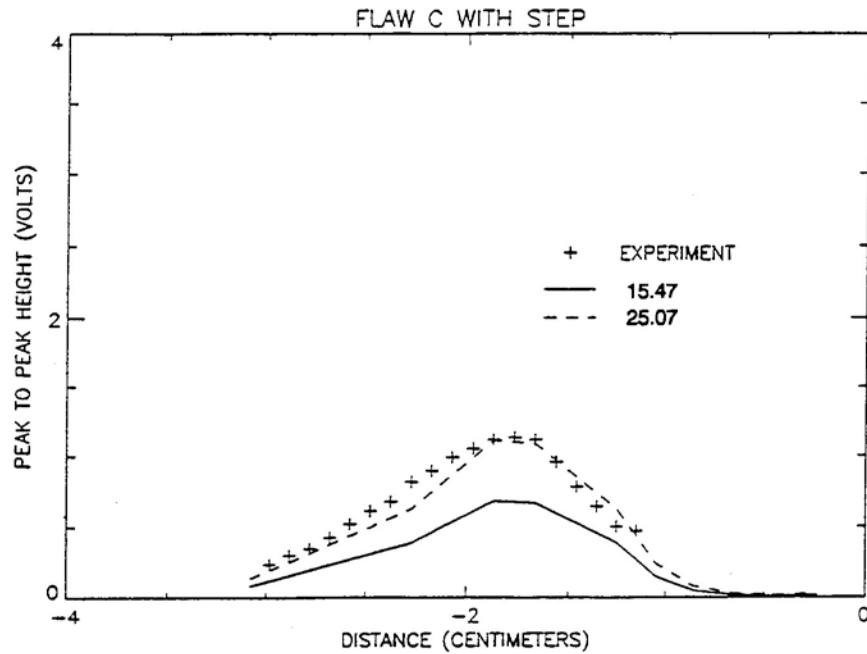


Figure A.47 Comparison of experimental data with theoretical calculations for 45° longitudinal pulse insonifying flaw C with-step

immersed in water; (3) propagation through the metal; and (4) propagation through the bottom surface and into the water. Model I predicts the pressure measured by a microprobe as it scans several millimeters from the bottom surface.

- Model II describes an immersion pulse-echo inspection in which the transducer and metal plate are placed in water in an immersion tank. The ultrasound propagates through a rough top surface, through the metal, and is reflected by a perpendicular flaw on the bottom surface back to the transducer. Model II predicts the pulse-echo response of the transducer for a given transducer location.
- The experiments carried out to validate Model I are as follows:
 - (1) The ultrasound insonified three step discontinuities having depths of 0.152 cm (60 mils), 0.0762 cm (30 mils), and 0.0254 cm (10 mils).

- (2) The ultrasound was first directed normal to each step discontinuity.
- (3) For insonifying each step discontinuity, the ultrasound beam was then oriented to produce 45° longitudinal waves in the steel plate.
- (4) For insonifying each step discontinuity, the ultrasound beam was finally oriented to produce 45° shear waves in the steel plate.

- The comparison between the experimental data and the theoretical calculation for Model I show the following:
 - (1) Very good agreement for the normal orientation for all three step discontinuities.
 - (2) Good agreement for the 45° longitudinal waves for all three step discontinuities. The experimental data shows that the width of the main peak is somewhat wider than predicted by the theoretical calculations. For a 0.0762-cm step

- discontinuity, the theoretical calculations predict a much higher secondary peak than is observed experimentally.
- (3) Very good agreement for the 45° shear waves for all three step discontinuities.
- The experiments carried out to validate Model II are as follows:
 - (1) The ultrasound insonified a step discontinuity with a depth of 0.152 cm. The steel plate had a thickness of 1.67 cm. Data were obtained for the reflection of ultrasound from three flaws: Flaw J (depth = 0.834 cm), Flaw I (depth = 0.318 cm), and Flaw C (depth = 0.169 cm). The length of all flaws was 2.54 cm.
 - (2) Insonification of three flaws using 45° shear waves and eight-cycle, tone-burst pulse.
 - (3) Insonification of three flaws using 45° shear waves and negative uni-polar pulse.
 - (4) Insonification of three flaws using 45° longitudinal waves and negative uni-polar pulse.
 - Theoretical calculations were obtained for flaw J when the ultrasound passed through a smooth top surface and when the ultrasound passed through a step discontinuity. These two situations are called: (1) flaw J-no step and (2) flaw J with step, and similarly, for flaws I and C. Theoretical calculations were obtained for those six possibilities. The theoretical calculations were normalized by dividing all amplitudes by the peak amplitude for flaw J-no step. The experimental data were also normalized in a similar way.
 - In order to study the effects of surface roughness in an inservice inspection, one must be able to compare the echo obtained from a flaw when the transducer passes over a smooth surface with that obtained from passing over a rough surface. Therefore, good agreement between the normalized theoretical curves and the normalized experimental data is important for validation of Model II.
 - Graphs show the normalized amplitude versus the transducer position for the normalized experimental data and the normalized theoretical calculations for 45° shear waves for an eight-cycle, tone-burst pulse. The comparison, using two sets of data, shows the following results: (1) The shape and magnitude of the normalized amplitude is predicted accurately by Model II for flaw J-no step, flaw J with step, flaw I-no step, flaw I with step, flaw C with step. (2) For flaw C no-step, the magnitude of the experimental data at the peak is about 20% higher than predicted by theory.
 - Insonification using 45° shear waves and a negative uni-polar pulse tests the ability of Model II to predict the pulse shape of the echo. Comparison of experimental data and theoretical calculations for flaw J-no step and flaw J with step show excellent agreement of the normalized pulse shapes. The experimental data show that, due to passing through the step discontinuity, the pulse shape is broadened and this effect is accurately predicted by the theoretical calculations.
 - Insonification using 45° longitudinal waves and a negative unipolar pulse shows the following results: (1) Comparison of the echo pulse shape for five transducer positions for flaw J-no step shows good agreement with the theoretical calculations, (2) for flaw J with step, a similar comparison for four transducer positions shows good agreement, (3) for flaw I-no step and flaw I with step for one transducer position, the comparison shows reasonable agreement, and (4) for flaw C-no step and flaw C with step for one transducer position, the comparison shows that the experimental data is larger than predicted by theoretical calculations.
 - In order to obtain a comprehensive view of the data for 45° longitudinal waves using a negative unipolar pulse, graphs of the maximum peak-to-peak amplitude, expressed in volts, were plotted versus transducer position and compared with theoretical calculations. The theoretical curve for flaw J-no step was normalized to the experimental data by multiplying the theoretical values by 15.47. The normalization constant for the other cases, shown in parentheses, are as follows: J with step (15.47), I no-step (17.55), I

Appendix A

with step (17.55), C no-step (17.55), and C with step (17.55). The larger normalization constant indicates that the experimental data is about 13% larger than predicted by theoretical calculations. Even though the normalization constant for flaws I and C is larger than for flaw J, the fact that they are the same for a given flaw shows that the effect of a step can be accurately predicted by these calculations.

- The conclusions resulting from this detailed comparison of experimental results with theoretical calculations are that the Model I code and the Model II code have been validated.

Appendix B

Validation of Model III and Model IV Codes

Appendix B

Validation of Model III and Model IV Codes

B.1 Introduction

Although Model III and Model IV have been considered separate models, the final version of the code combines Model III and Model IV into one code. The only difference is the angle of the crack. For this reason the validation studies will be described in the same chapter.

Appendix B begins by describing the input parameters for the code and includes two different methods for defining the various coordinate systems describing the propagation of ultrasound. Next, data are presented for the validation of Model III for 45° shear waves using the two methods for the input parameters. The two methods are compared. The step height was 0.152 cm. This data showed that the amplitude decreases significantly when the angle of tilt of the transducer wedge is 3° or greater. To investigate this effect more thoroughly, additional data were obtained for angles of tilt between 3° and 5° for 45° shear waves. It is very important to know over what range of step heights the theory is valid. For this reason, experimental data were obtained for 45° shear waves for step heights of 0.229 cm and 0.305 cm. Data were also obtained where 45° longitudinal waves and 60° shear waves were produced in steel. The validation of Model IV was carried out using 45° shear waves for flaw angles ranging from 79° to 101°.

B.2 Program Description for Model III and Model IV Codes

There are two types of input parameters possible, which are called Method 1 and Method 2. The basic difference between these two types of input is that in Method 1 the interface and transmitted coordinate system are fixed in

position at the top of the step. The transmitted plane is also fixed at the top of the step. In Method 2 these coordinate systems and the transmitted plane move with the transducer. The first section describes the input for Method 1 with the exception of two lines. The second section describes the input for these two lines for both methods.

B.2.1 Method 1 Input Parameters

Table B.1 shows the program input for Method 1.

Line 1. Transducer information

radiusx, radiusy:

semi-axis of an elliptical transducer along the x and y axes. For a circular transducer $r_x = r_y = 0.635$ cm.

focusx, focusy:

transducer focal lengths along the x and y axes. For a planar transducer, $\text{focusx} = \text{focusy} = 1.0e30$.

Line 2. Gauss-Hermite (G-H) beam information

nc:

number of terms used in the G-H expansion, $nc = 25$

iphase:

omit(iphase = 0) or retain (iphase = 1) phase factor. iphase = 1 keeps track of phase information or time and time of arrival of pulse, as in an experiment.

Line 3. Transmission through the wedge-couplant interface

ml:

angle in wedge material that the central ray makes with the normal to the wedge base

Table B.1 Example of input file (iblc2.d60) for Method 1 for Model III code^(a)

Line	
1	0.635 0.635 1.E30 1.E30 : radiusx,radiusy,focusx,focusy
2	25 0 : nc,iphase
3	30.0613 18.9050 1.E30 1.E30 1.400 : th1,th2,bx,by,z0
4	20.9050 51.1447 1.E30 1.E30 1.167 : th1,th2,bx,by,z0
5	51.1447 51.1447 1.E30 1.E30 4.957 : th1,th2,bx,by,z0
6	0.2350 0.1420 1.06 1 : v11,vls,rho1,niw
7	0.1480 0.0 1.00 1 : vcl,vcs,rhoc,ncw
8	0.5900 0.3230 7.62 2 : v21,v2s,rho2,ntw
9	0.1480 0.0 1.00 2 : v31,v3s,rho3,nrw
10	0.1480 0.0 1.00
11	0.00 159.095 0.0 -0.4164 0.0 1.0902 : rot. and transl. int. to wedge sys.
12	0.7787 0.0 -0.6274 0.0 : equation of transmitted plane with respect to int. system
13	0.0 128.855 0.0 0.0 0.0 0.0 : rot. and transl. from crack to transm. system
14	0.0 218.855 0.0 2.7925 0.0 3.11 : rot. and transl. from crack sys. to bot. surf. system
15	0.0 90.0 0.0 -0.3175 0.0 -0.7504 : rot. and transl. from crack sys. to bot. surf. system
16	1 0.3175 0.7950 31 31 : ictype, dx, dy, ncx, ncy
17	45 31 0.060 0.1524 21 : nsx, nsy, delgrd, stpht, icode
18	tranb1.dat : transducer efficiency file name
19	0.05 : cone
20	-2.7190 0.2400 15 : XIWTRIN, DELXW, NSC
21	1 : nprt
22	pb1c2.d60 : file name for peak-to-peak output
23	ob1c2.d60 : file name for signal output

(a) This is the input file for the theoretical curve shown in Figure B.9 for a tilt angle of 2° and a step height of 0.152 cm.

th2:
angle in couplant that the central ray emerging from the wedge makes with the normal to the wedge base

bx, by:
radius of curvature of the wedge base in the x and y direction. For a planar wedge base, bx = by = 1.0e30.

z0:
the distance that the central ray travels from the transducer to the wedge base (cm)

Line 4. Transmission through the couplant-top surface interface

th1:
angle in couplant that the central ray makes with the normal to the top surface

th2:
angle in component that the central ray makes with the normal to the top surface

bx,by:
radius of curvature of the top surface in the x and y direction. For a planar surface, bx = by = 1.0e30.

z0:
distance from the bottom of the wedge base, along the central ray, to the top surface of component (cm).

Line 5. Reflection from the bottom surface

Consider a line normal to the bottom surface where the central ray intersects the bottom surface.

th1:
angle between the incident ray on the bottom surface and the normal to the bottom surface

th2:
angle between the reflected ray and the normal. Mode conversion can take place at the bottom surface, but the program only traces one type of ray. If mode conversion takes place, then the second entry will be different from the first.

bx,by:
radius of curvature of the bottom surface in the x and y direction. For a planar bottom surface, $bx = by = 1.0e30$.

z0:
distance along the central ray from the top surface to the point where the central ray intersects the bottom surface (cm)

Line 6. Properties of wedge material

v1l:
longitudinal speed in wedge material (cm/microsec)

v1s:
shear speed in wedge material (cm/microsec)

rho1:
density of wedge material (g/cm^3)

niw:
1 for a longitudinal wave and 2 for a shear wave in wedge material

Line 7. Properties of couplant

vcl:
longitudinal speed in couplant (cm/microsec)

vcs:
shear speed in couplant (cm/microsec)

rhoc:
density of couplant (g/cm^3)

ncw:
1 for a longitudinal wave and 2 for a shear wave in couplant

Line 8. Properties of component

v2l:
longitudinal speed in component (cm/microsec)

v2s:
shear speed in component (cm/microsec)

rho2:
density of component (g/cm^3)

ntw:
1 for a longitudinal wave and 2 for a shear wave in component

Line 9. Properties of material in contact with bottom surface

v3l:
longitudinal speed in material in contact with bottom surface (cm/microsec)

v3s:
shear speed in material in contact with bottom surface (cm/microsec)

rho3:
density of material in contact with bottom surface (g/cm^3)

nrw:
type of wave that is reflected at the bottom, surface.nrw = 1 for longitudinal wave and 2 for a shear wave

Line 10. Properties of material in contact with crack

v4l:
longitudinal speed in material in contact with crack (cm/microsec)

v4s:
shear speed in material in contact with crack (cm/microsec)

rho4:
density of material in contact with crack (g/cm^3)

Line 11. Transformation parameters from the interface coordinate system to the wedge coordinate system

alfal,betal,gammal:
rotational angles

x1,x2,x3:
translational parameters

The goal is that axis z, point in the same direction as axis z_w , as defined in Figure B.1. To accomplish this the interface coordinate system must be rotated by the angle beta 1 about axis y_1 .

The origin of the wedge coordinate system has the coordinates $(x1,x2,x3)$ in the interface coordinate system.

Line 12. Equation of transmitted plane

Same as line 8 for Model II code.

Line 13. Transformation parameters from the interface coordinate system to the transmitted coordinate system

Same as line 9 for Model II code.

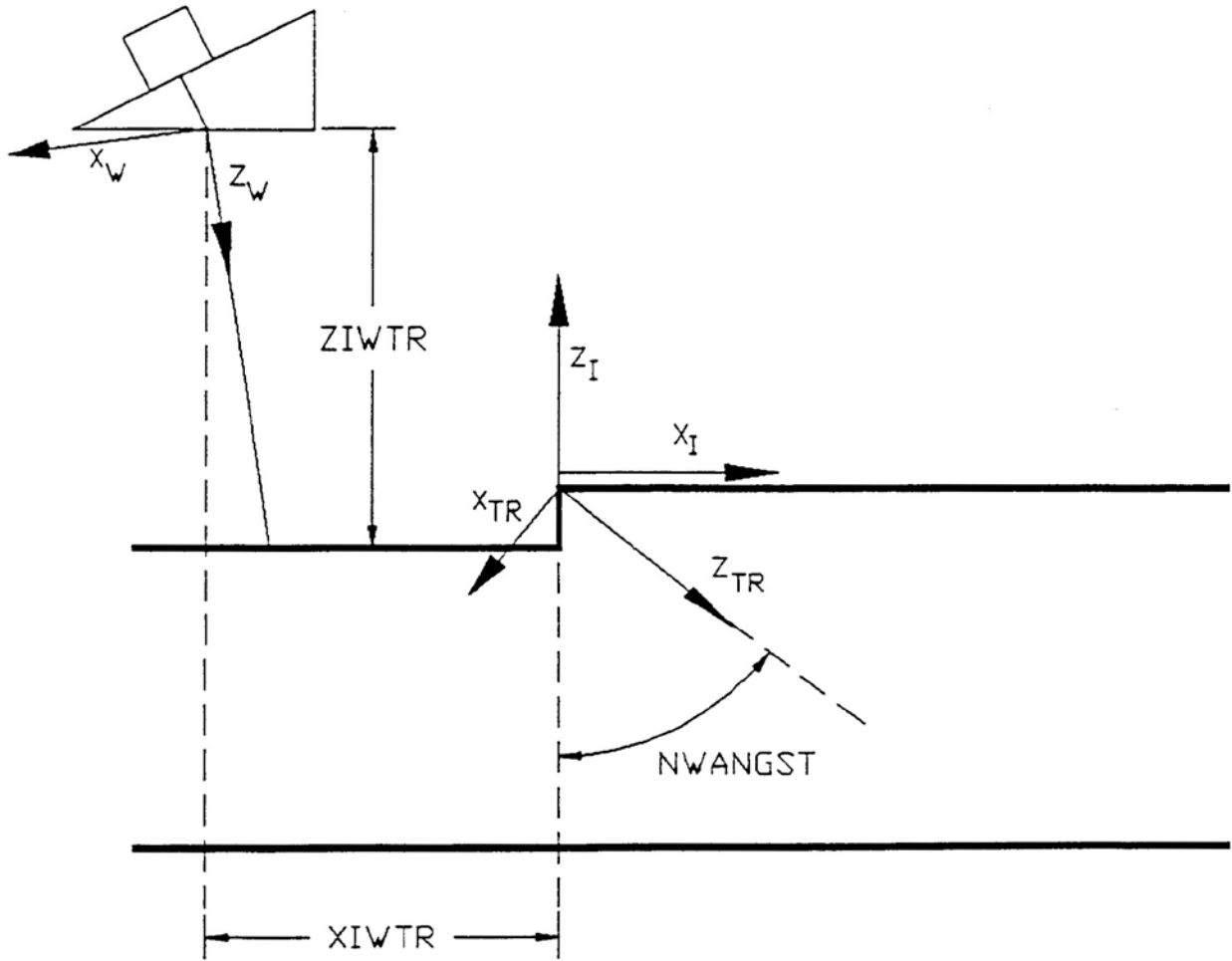


Figure B.1 Definition of wedge, interface, and transmitted coordinate systems for Method 1 input parameters

Line 14. Transformation parameters from the crack coordinate system to the interface coordinate system

See discussion below dealing with Method 1 and Method 2 entries.

Line 15. Transformation parameters from the crack coordinate system to the bottom coordinate system

See discussion below dealing with Method 1 and Method 2 entries.

Line 16. Crack parameters

icotype:

- (1) for a rectangular crack. For a rectangular crack, dx is half of the depth of the crack, dy is half of the length of the crack. The origin of the crack coordinate system is at the center of the rectangle.
- (2) for full elliptical or circular cracks, dx is half of the axis of the ellipse in the x direction and similarly, for dy. For a circular flaw the half length is the radius. The origin of the crack coordinate system is at the center of the flaw
- (3) for a half circle or half ellipse, dx is half of the axis of the ellipse in the x direction and similarly, for dy. For a half circular flaw the half length is the radius. The origin of the crack coordinate system is at the halfway point along the base of the flaw.

ncx,ncy:

number of integration steps over the surface of the flaw in the x and y directions.

Line 17. Definition of rough surface

The rough surface can be defined by generating a file that defines the surface relative to the interface coordinate system at each point in a grid. At each point in the grid the x, y, and z values and the components of a vector normal to the surface are given. The main program then reads this file. Since the calculations are to be carried out only for a step discontinuity, the main section of the program was modified to include this calculation directly in the main section of the code. Table B.I shows the input for the latter case. For Method 1 the interface coordinate system is located at the top of the step.

ngx:

number of points in the grid in the x direction

ngy:

number of points in the grid in the y direction

delgrd:

distance between adjacent grid points (cm)

stpht:

step height (cm)

icode:

specifies features of the code.

The first integer of the code specifies the type of code that is used: 1 indicates reflection at bottom surface, but no mode conversion possible at bottom surface or flaw; 2 indicates reflection at bottom surface, but **with** mode conversion at bottom surface or flaw; and 3 indicates no reflection at bottom surface. The second integer of icode specifies the type of integration over the flaw: 1 indicates the highest level of sophistication, while 3 is the lowest.

Line 18. File name for transducer efficiency information

Same as line 13 for Model II.

Line 19. Frequency amplitude limit

cone:

Limits the amplitude of the frequency that is used in the calculation of the response

Line 20. Scan parameters for Method 1

Define P_{exit} , as the exit point of the central ray from the wedge. The coordinates of P_{exit} in the interface coordinate system are given by (XIWTR,0,ZIWTR). In some cases, a scan occurs in which the only parameter that changes is XIWTR and all other parameters are the same. The theoretical calculations for the validation experiments in the next section are an example.

XIWTRIN:

initial value of XIWTR for the scan

Appendix B

DELXW:

value by which the value of XIWTR increases for the subsequent case

NSC:

number of cases in scan

Line 21. Printout control

nprt = 1 saves each waveform to a file
nprt = 0 doesn't write waveform to a file

Line 22. File name for peak-to-peak output

File name for file that gives the peak-to-peak value of signal for each case in scan.

Line 23. File name for signal output

File name for file that gives the amplitude-versus-time signal for each case in scan.

B.2.2 Parameters for Lines 14 and 15 for Method 1 Input

For the Method 1 input, the interface coordinate and the transmitted coordinate systems are located at the top of the step. The wedge coordinate system is located at the exit point of the ray from the wedge, where the z axis is along the line of the central ray in the water. As the transducer scans, the horizontal distance XIWTR between the interface coordinate system and the exit point on the wedge indicates how the scan is taking place. Figure B.1 shows a diagram where the coordinate systems are defined.

Line 14

In the final version of the code the crack can be at any angle. The angle Θ (or the crack angle CRANGL), defined in Figure B.2, can be less than 90° or greater than 90° . Line 14 of the input to the code gives the relationship between the crack coordinate system and the transmitted system. The crack coordinate system has its z-axis perpendicular to the surface of the crack, with the origin of the crack coordinate system at the center of the rectangular flaw.

The crack coordinate system has to be rotated by angle ANGCRTTR so that ZCR is parallel to ZTR. The angles are shown in Figure B.3.

$$\text{ANGCRTTR} = 360 - \text{CRANGL} - \text{NWANGST} \quad (\text{B.1})$$

The location of the origin of the transmitted system is to be determined in terms of the crack coordinate system. Figure B.2 shows the origin O_{TR} of the transmitted system. A vector VCRTR is drawn from the origin of the crack coordinate system O_{CR} to O_{TR} . The object is to obtain the components of this vector on x_{CR} and z_{CR} .

In terms of the unit vectors \mathbf{I} and \mathbf{k} , the VCRTR is given by

$$\mathbf{VCRTR} = [\text{DBASCR} - \text{CRHALFX} * \text{COS}(\text{CRANGL})] \mathbf{I} + [\text{THKST} - \text{CRHALFX} * \text{SIN}(\text{CRANGL})] \mathbf{k} \quad (\text{B.2})$$

Figure B.2 shows the unit vectors \mathbf{i}_{CR} and \mathbf{k}_{CR} associated with the crack coordinate system, which can be expressed in terms of the unit vector \mathbf{I} and \mathbf{k} .

$$\mathbf{i}_{CR} = -\text{COS}(\text{CRANGL}) \mathbf{I} + \text{SIN}(\text{CRANGL}) \mathbf{k} \quad (\text{B.3})$$

$$\mathbf{k}_{CR} = -\text{SIN}(\text{CRANGL}) \mathbf{I} - \text{COS}(\text{CRANGL}) \mathbf{k} \quad (\text{B.4})$$

The component of VCRTR on \mathbf{i}_{CR} is given by the dot product of these two vectors. Using Eqs. (B.2) and (B.3), we obtain

$$\text{VCRTR}_{x_{cr}} = \mathbf{VCRTR} \cdot \mathbf{i}_{CR} = \text{DBASCR} * \text{COS}(\text{CRANGL}) - \text{CRHALFX} + \text{THKST} * \text{SIN}(\text{CRANGL}) \quad (\text{B.5})$$

Similarly, the component of VCRTR on \mathbf{k}_{CR} is given by the dot product of the vectors. Using Eqs. (B.2) and (B.4), we obtain

$$\text{VCRTR}_{z_{cr}} = \mathbf{VCRTR} \cdot \mathbf{k}_{CR} = \text{DBASCR} * \text{SIN}(\text{CRANGL}) - \text{THKST} * \text{COS}(\text{CRANGL}) \quad (\text{B.6})$$

The terminology used here is somewhat different from that used in the Fortran code. Line 14 of the input file gives the rotation and translational parameters from the crack coordinate system to the transmitted system. Line 14 should read as follows:

$$0.0 \text{ ANGCRTTR} \quad 0.0 \text{ VCRTR}_{x_{cr}} \quad 0.0 \text{ VCRTR}_{z_{cr}}$$

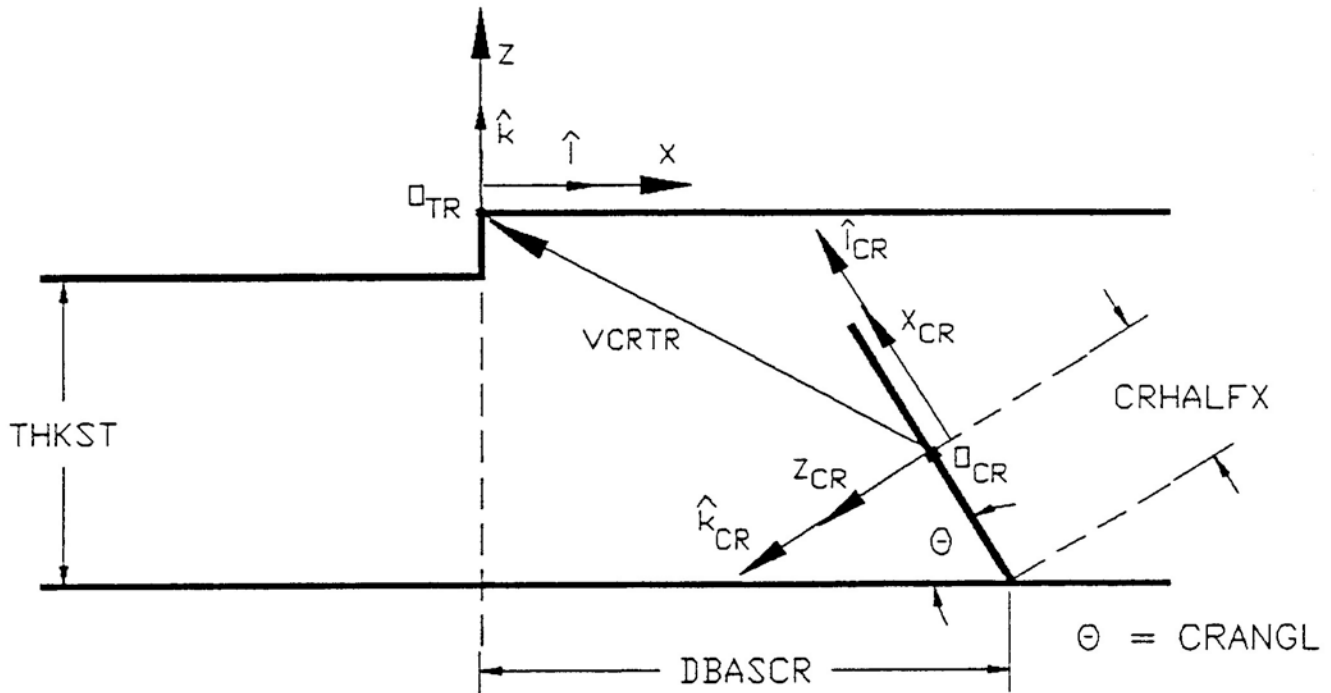


Figure B.2 Definition of the crack coordinate system and its relationship to the origin of the transmitted coordinate system O_{TR} using the vector V_{CRTR} . The parameter $DBASCR$, the distance between the step and the base of the crack, is also defined.

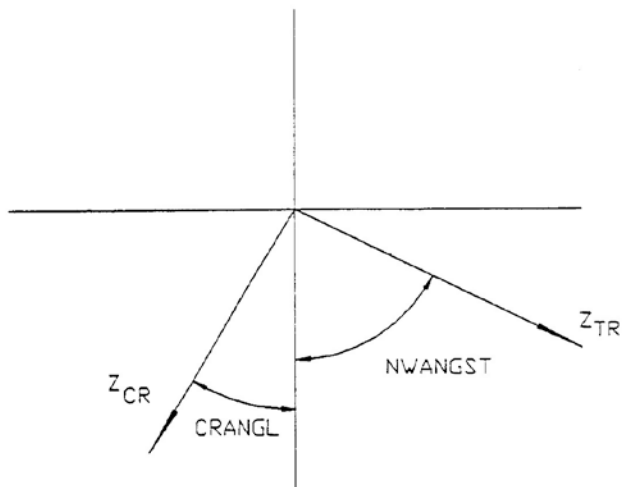


Figure B.3 Diagram showing the angular separation between the z axis of the crack coordinate system and the z axis of the transmitted coordinate system

Line 15

Line 15 of the code describes the rotation and translational parameters from the crack coordinate system to the bottom coordinate system.

The bottom coordinate system is obtained by extending the z-axis of the transmitted coordinate system until it hits the bottom surface. This point on the bottom surface is the origin OB of the bottom coordinate system, as shown in Figure B.4. The z-axis of the bottom coordinate system is perpendicular to the bottom surface.

The crack coordinate system has to be rotated by angle $ANCRBT$ so that z_{CR} is parallel to z_B , as shown in Figure B.5.

$$ANCRBT = 180 - CRANGL \quad (B.7)$$

For the translational parameters, the origin OB is described in terms of the crack coordinate system values. Figure B.4 shows a vector V_{BCR} from the origin of the

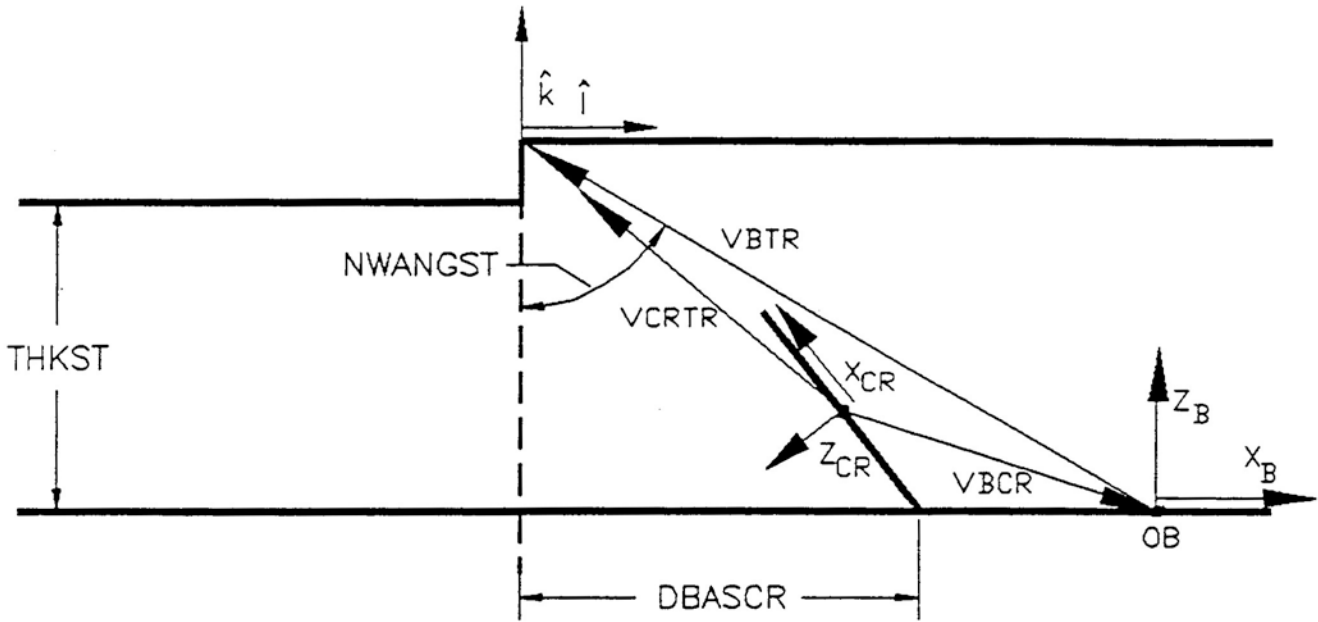


Figure B.4 Definition of the bottom coordinate system and several vectors

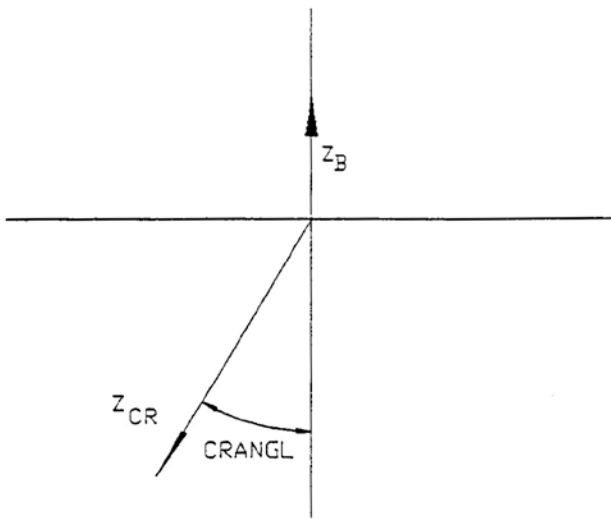


Figure B.5 Diagram showing relationship between the z axis of the bottom coordinate system and the z axis of the crack coordinate system

crack coordinate system to the origin OB. Also shown is the vector **VBTR**, which is defined by

$$\mathbf{VBTR} = -\text{THKST} \cdot \tan(\text{NWANGST}) \mathbf{I} + \text{THKST} \mathbf{k} \quad (\text{B.8})$$

Vector **VCRTR** is given by Eq. (B.2). The relationship between the vectors is given by

$$\mathbf{VBCR} + \mathbf{VBTR} = \mathbf{VCRTR} \quad (\text{B.9})$$

or

$$\mathbf{VBCR} = \mathbf{VCRTR} - \mathbf{VBTR} \quad (\text{B.10})$$

Using Eqs. (B.2) and (B.8),

$$\mathbf{VBCR} = [-(\text{DBASCR} - \text{CRHALFX} \cdot \cos(\text{CRANGL})) + \text{THKST} \cdot \tan(\text{NWANGST})] \mathbf{I} - \text{CRHALFX} \cdot \sin(\text{CRANGL}) \mathbf{k} \quad (\text{B.11})$$

The component of **VBCR** on \mathbf{i}_{CR} is given by the dot product of these two vectors:

$$\text{VBCR}_{\text{xcr}} = \mathbf{VBCR} \cdot \mathbf{i}_{\text{CR}} = \text{DBASCR} \cdot \cos$$

$$\begin{aligned} & (\text{CRANGL}) - \text{CRHALFX} - \text{THKST} * \\ & \text{COS}(\text{CRANGL}) * \text{TAN}(\text{NWANGST}) \end{aligned} \quad (\text{B.12})$$

The component of \mathbf{VBCR} on \mathbf{k}_{CR} is given by the dot product of these two vectors.

$$\begin{aligned} \text{VBCR}_{\text{xcr}} = \mathbf{VBCR} \cdot \mathbf{k}_{\text{CR}} = & \text{DBASCR} * \text{SIN} \\ & (\text{CRANGL}) - \text{THKST} * \text{TAN} \\ & (\text{NWANGST}) * \text{SIN}(\text{CRANGL}) \end{aligned} \quad (\text{B.13})$$

Line 15 of the input file should read as follows:

```
0.0 ANCRBT 0.0 VBCRxcr 0.0 VBCRzcr
```

B.2.3 Method 2

For the Method 2 input, the coordinate systems are defined in a different way from that in Method 1. For Method 2, the origins of the transmitted and interface coordinate systems are located where the central ray strikes the top surface. The transmitted plane passes through the origin of the transmitted coordinate system and it is perpendicular to the z axis of the transmitted system. The bottom coordinate system is located where the z-axis of the transmitted system strikes the bottom surface. These coordinate systems are illustrated in Figure B.6.

For the Method 2 input the transmitted coordinate system and the interface coordinate system MOVES WITH the transducer (in contrast to method 1, where they remained fixed at the top of the step). The horizontal distance between the origins of the interface and transmitted systems and the base of the flaw is called D. Now as the scan takes place, the distance D varies.

For Method 2, Eqs. (B.1) and (B.7) are still valid. In Eqs. (B.5), (B.6), (B.12), and (B.13), the parameter DBASCR (which had a fixed value in Method 1) is replaced by D (which varies in Method 2).

The original version of the updated code from ISU included the ability to scan. This feature was bypassed in the Method 2 input. Instead a loop was set up to read each different set of input parameters. A code was written for PV-WAVE to generate the input file for the designated number of transducer positions (or values of D). The modified version of the ISU code read the set of parameters for each transducer position.

The interface must be described in terms of the interface coordinate system. As the transducer moves, the step is a different distance from the origin of the interface system.

This must be taken into account. The ISU code was modified to take this into account and the interface was calculated, for each transducer position, as a grid of points. The location of the step in the interface coordinate system is given by STPLOC:

$$\text{STPLOC} = \text{D} - \text{HDCRSTP} \quad (\text{B.14})$$

During the loop over the transducer positions, the value of D is changed by a fixed amount with each change of transducer position.

For Method 2, the value of XIWTRIN is a fixed negative value and depends upon the parameters of the experimental setup: the vertical distance between the wedge bottom and the plate surface and the angle of the central ray from the wedge. This value can be calculated.

In previous calculations the transducer position was given by the horizontal distance XPOSST of the exit point from the step. Therefore, it is useful to determine this value. It is given by:

$$\text{XPOSST} = -\text{D} + \text{HDCRSTP} + \text{XIWTRIN} \quad (\text{B.15})$$

The output of the modified code gives the amplitude versus XPOSST. Values of D and HDCRSTP are also listed on the code output.

Lines 14 and 15 have the same definition in Method 1 and Method 2. However, since the coordinate systems and transmitted plane are different in these two methods, the values of these parameters are different (Table B.2).

In the next section the theoretical calculations for Method 1 and Method 2 will be compared. The results will show that very similar results are obtained when the scan covers a distance of about 4 cm and the ray tracing occurs reasonably close to the center of the transmitted plane. However, for a scan covering a greater distance, such as those in Section B.1.3, the Method 2 input parameters must be used. This ensures that the ray tracing occurs near the center of the transmitted plane, where the ray tracing leads to more accurate results.

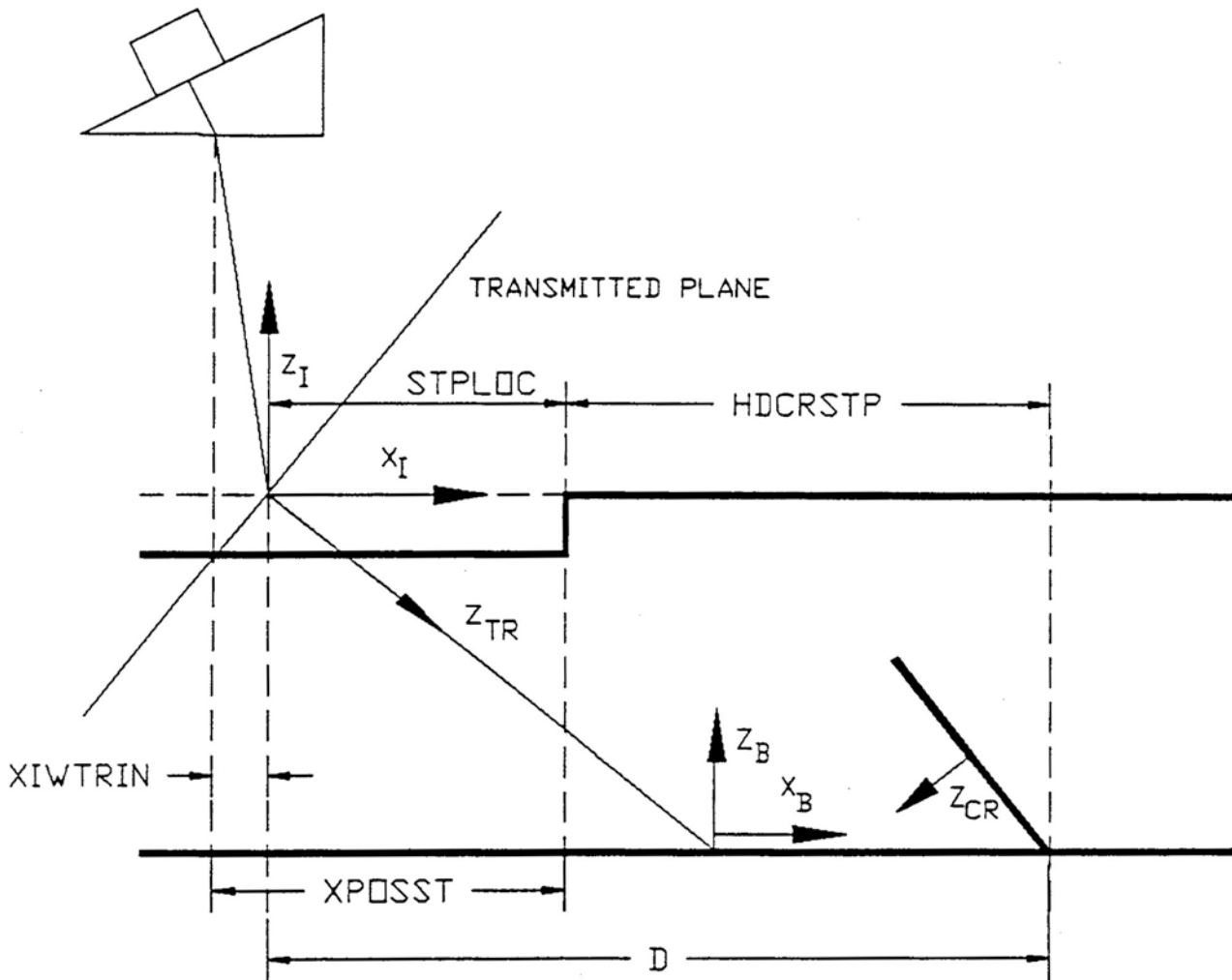


Figure B.6 Definition of interface and transmitted coordinate systems and the location of the transmitted plane for Method 2 input parameters

Table B.2 Example of input file (ib2c2.d60) for Method 2 for Model III code for one transducer position^(a)

Line	
14	0.0 218.855 0.0 2.7925 0.0 5.51: rot. and transl. from crack to transm. system
15	0.0 90.00 0.0 -0.3175 0.0 1.6496: rot. and transl. from crack sys. to bot. surf. sys.

(a) Only lines 14 and 15 are shown. For each transducer position, lines 14 and 15 change.

B.3 Validation of the Model III Code

This chapter is devoted to the validation of the Model III code for 45° shear wave. The first section describes the experimental setup for an immersion experiment that uses an x-y scanner. The second section describes the experiments to investigate the effect of a 0.152 cm (60 mils) step, and also compares two methods of input for the theoretical code. The third section examines in more detail the effect of the tilt angle of the transducer wedge. The fourth section examines the effect of a larger step height—0.229 cm (90 mils) and 0.305 cm (120 mils).

The final section considers how these results affect the ASME Code recommendation.

B.3.1 Experimental Setup using X-Y Scanner

Figure B.7 shows a schematic diagram of the apparatus placed in the immersion tank of an x-y scanner. The plate has a thickness of 3.11 cm and the rectangular flaw has a depth of 0.635 cm and a length of 1.59 cm. The transducer is attached to the wedge and is fastened to the tilted arm of the scanner. The rexolite wedge is designed to produce 45° shear waves in steel. An eight-cycle toneburst signal having a frequency of 2.25 MHz is sent to the transducer. Not shown in the diagram is a knob that can change the angle of inclination of this arm and, hence, change the so-called tilt angle of the wedge. Initially, this knob is adjusted until the wedge is determined to be level. By raising the base of the wedge to about 1 cm from the steel plate, the reverberations of the ultrasound between the wedge base and steel plate can be eliminated. The scan is carried out over about 15 cm and A-scans are obtained at intervals of 0.076 cm. Next, let us consider some features of the experimental data.

Figure B.8 shows the data obtained during a scan for the no-step (smooth surface) level case, where the block shown in Figure B.7 is rotated by 180° and the signal is reflected from the other side of the flaw. As the scan takes place, the first signal to be observed is the scattering from the front end of the block (+ signs). The next signal is the echo from the flaw (diamonds). As the scanning arm continues to move to the right, the next signal is the scattering from the step (asterisks). The signals from the front edge and the step will occur at a smaller time than that from the flaw. The peak-to-peak voltage was extracted from the A-scan for each position in the scan and plotted versus the scan position in Figure B.8. The signals from the front edge and step are used to place the theoretical curve on a graph of the experimental data. In addition, the location of the signal from the flaw, the front edge, and the step can be used to determine the angle of the central ray in the steel.

During a given scan the angle of tilt is constant. For the next scan the scanner arm is adjusted for the desired tilt angle of the wedge and the scan is repeated, and so on. This mimics the tilt of a transducer as it goes over a step in an inservice inspection.

Figure B.9 shows the experimental data for ten scans and the comparison with the theoretical calculations. Here only the signal from the flaw is shown. The top part of the figure shows the data obtained for the no-step cases for five tilt angles of the wedge and the bottom part, for a step height of 0.152 cm. The calculations were carried out using Method 1 input parameters.

B.3.2 Experimental Data for 45° Shear Waves

In order to validate the Model III code, data are obtained when the ultrasound passes through a smooth top surface (often referred to as the no-step case) and when the ultrasound passes through a step discontinuity. For a successful validation the theory should be able to predict the shape of the experimental data and the relative magnitude for each tilt angle compared to the no-step-level case.

The computer code requires a reference signal as input. This signal was obtained by placing the transducer on a 3.18 cm thick piece of rexolite and digitizing the echo that is reflected from the bottom surface. The output of the code is a signal of similar shape, but of different amplitude. Each position of the transducer is a single case for the computer code. The theoretical curve that is plotted in the graphs is the peak-to-peak amplitude for each case versus the position. As discussed in the preceding chapter of Appendix B, there are two types of input parameters for the code relating to the various coordinate systems. M1 (or M2) is used to indicate Method 1 (or Method 2) type of input parameters.

Only **one** normalization constant was used to normalize the theoretical curves to the experimental data. For the level-no-step case, the theoretical curve was multiplied by a constant (NORMCON) so that the theory fit the experimental data, as shown in Figure B.8. Then for the other cases, the theoretical curve was multiplied by the **same** normalization constant. This is a very important consideration because it shows whether or not the theory can predict the magnitude of the response. If so, then using only one constant, all of the theoretical curves should agree in magnitude with the experimental data points.

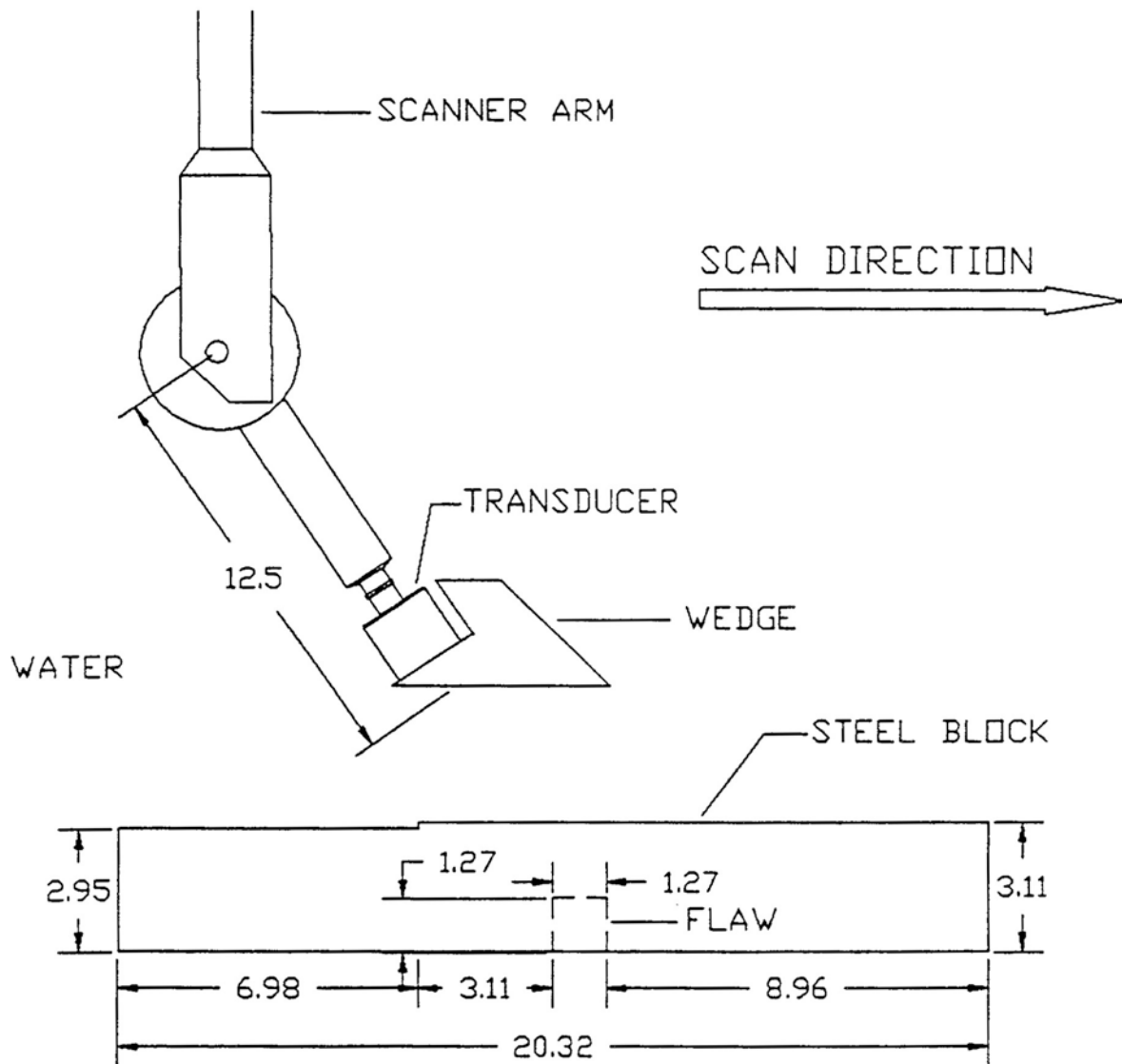


Figure B.7 Schematic diagram of experimental apparatus used in the immersion tank of an x-y scanner. All dimensions are in cm. This distance between the bottom of the wedge and the steel plate is 0.9 cm.

The placement of the theoretical curves is very important. The location of the step (and/or front edge) can be used to place the theoretical curve on the experimental data graphs. The locations of the theoretical curve have not been shifted to the right or left.

The comparison between the theoretical curves and the experimental data in Figure B.9 shows good agreement because the theory is able to predict both the magnitude

and shape quite well in most cases. For a tilt of 1° with-step, the theoretical curve shows two distinct peaks, but the magnitude of one peak is low compared to the experimental data.

In an inservice inspection, one important question is, How much is the amplitude affected when the wedge is tilted to go over a step? Table B.3 shows maximum peak-to-peak voltage for the experimental data. Some interesting

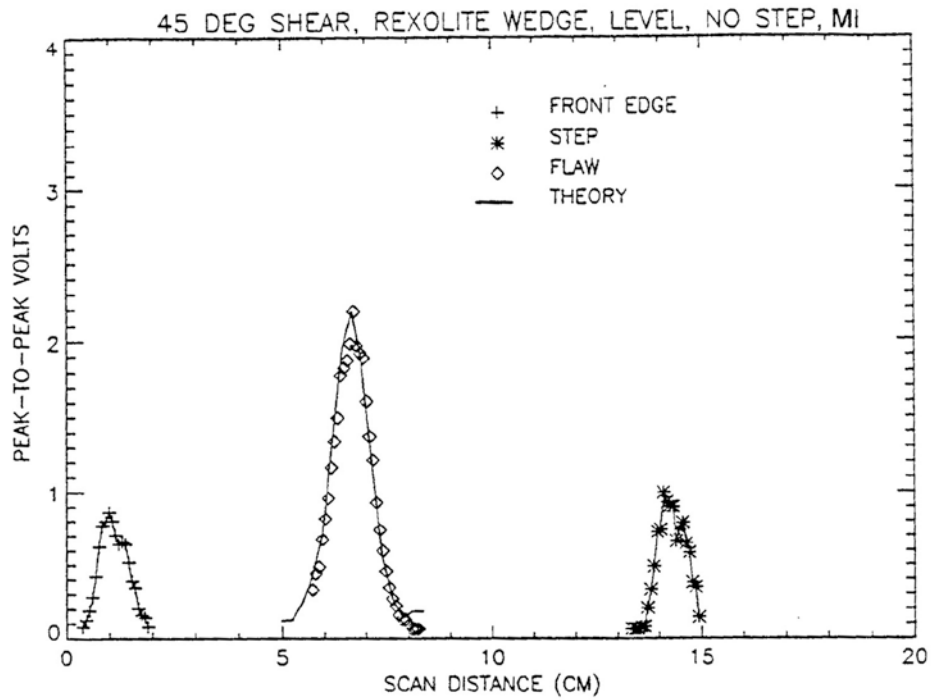


Figure B.8 Comparison of experimental data with theoretical calculations for the level no-step case

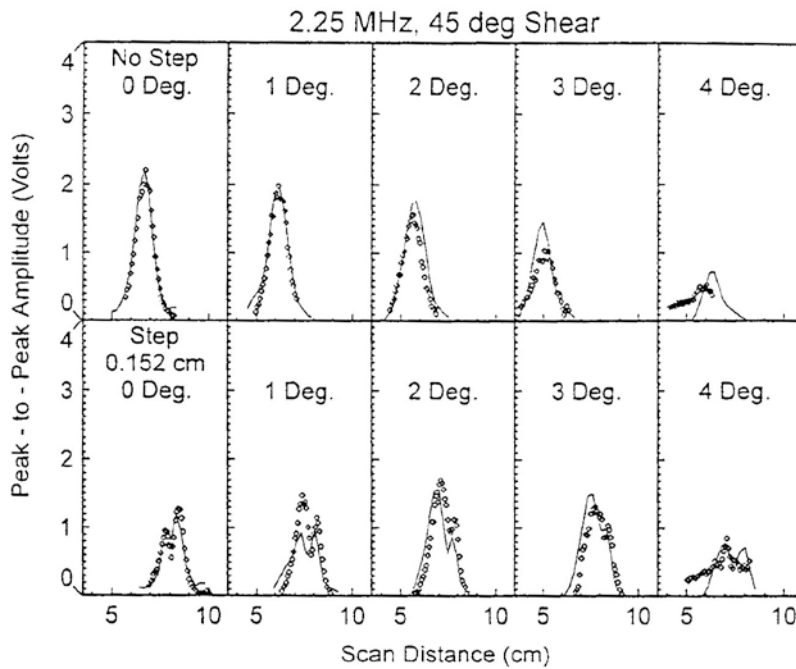


Figure B.9 Comparison of experimental data, shown with diamonds, with theoretical calculations, shown by a solid line. Method 1 input parameters are used for the theoretical calculations.

Table B.3 Summary of the maximum peak-to-peak amplitude for the experimental data in Figures B.8 through B.17^(a)

Tilt angle of wedge	No step peak-to-peak voltage	With step peak-to-peak voltage
0°	1.0	0.55
1°	0.90	0.64
2°	0.68	0.73
3°	0.45	0.59
4°	0.23	0.36

(a) The amplitudes are normalized by dividing each maximum amplitude by the voltage for the no-step level case, 2.2 V.

effects can be seen here. For the no-step case the amplitude for a 4° tilt is less than one-fourth that for the level case, or about a 12 dB drop. Comparing the two level cases, we see that the step causes the amplitude to be reduced by nearly a factor of two. However, when the transducer wedge is tilted by 3° and 4°, the amplitude for cases **with** the step is actually larger than for the no-step cases. These are effects due to constructive or destructive interference.

B.3.2.1 Method 2 Comparison

Figures B.10 through B.13 show the experimental data fitted with theoretical curves obtained using the Method 2 input parameters. Comparison with the corresponding data in Figure B.9 shows that Method 2 gives a somewhat better fit to the amplitude than Method 1. Note that in Figure B.11 the left side of the curve has a shoulder that does not occur for the Method 1 input. Also, in Figure B.13 there are two peaks in contrast to one peak in Figure B.9. So, while there are some minor differences from the two input methods, the overall general agreement is very good.

Method 2 input parameters have been used for the scans carried out in Chapter 3 for modeling an inservice inspection and in Chapter 4 for the investigation of interference effects.

B.3.3 Additional Data from 3° to 5°

Additional data were obtained using the 45° shear rexolite wedge in order to test the theory at larger tilt angles. The data were obtained in the same way as has been described. Data were obtained only for the no-step cases. Figures B.14 through B.19 show the comparison of the theory with the experimental data. When different amplifier gains were used, the data were adjusted to that used for the no-step level case. The location of the signal from the flaw, compared to that from the front edge and the step, indicates that the angle in steel for the no-step level case is 47.1°, rather than 45°. The angle 47.1° and the Method 1 input parameters were used in the theoretical calculations.

Figures B.14 through B.16 show good agreement between the theoretical curves and the experimental data. Table B.4 shows the amplitude of the peak compared to the no-step level case. The values for 3° and 4° are very close to those shown in Table B.3, as would be expected. The comparison in Figure B.17 is reasonable, but the experimental data show a somewhat distorted and wider peak than the theoretical curve. A similar statement can be made for Figure B.18. Figure B.19 for a tilt angle of 5° shows that the amplitude of the theoretical curve is only about half that of the experimental data. Also, the peak for the experimental data is quite wide. The agreement between theory and experiment is considered acceptable for a tilt angle of 4.5°, but not for 5°. Table B.5 shows the angle in steel for the various tilt angles. For a tilt angle of 4.5° the angle in steel is 63.0°, while for 5° it is 65.3°. These results lead to the conclusion that the theory cannot adequately handle angles in steel greater than about 63°.

B.3.3.1 Expected Peak Location

Let us define the "expected peak location" in the scan as the location where the central ray strikes the base of the flaw. The question is, "Is the peak in the experimental data found at the "expected peak location?" Another question is, "Where does the theory predict the maximum amplitude? Is it located at the "expected peak location?"

$$\text{expected peak} = \frac{\text{scan location where the central ray strikes base of flaw}}{\text{scan location}} \quad (\text{B.16})$$

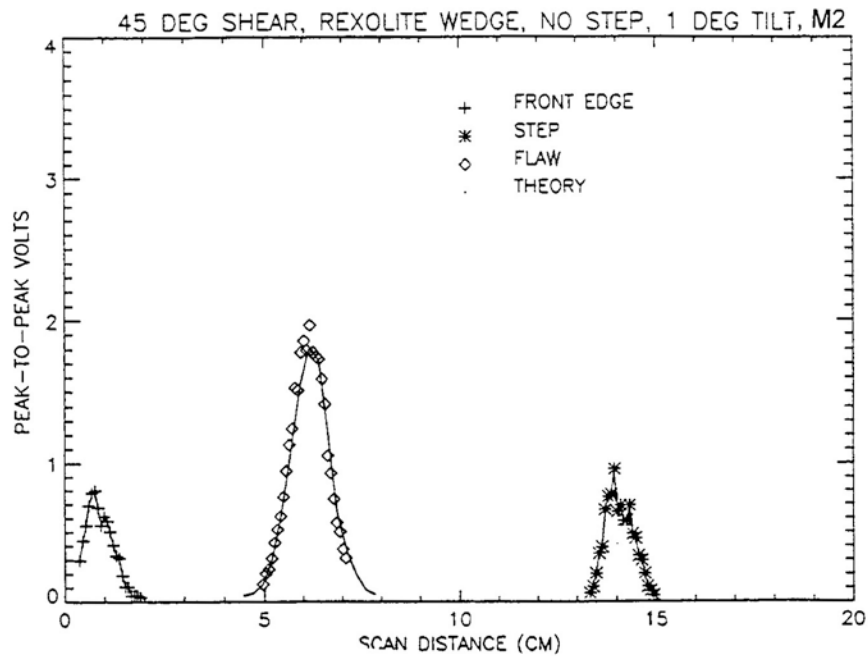


Figure B.10 Comparison of experimental data with theoretical calculations for the no-step case with the transducer wedge tilted by 1°. The Method 2 input parameters were used in the calculation.

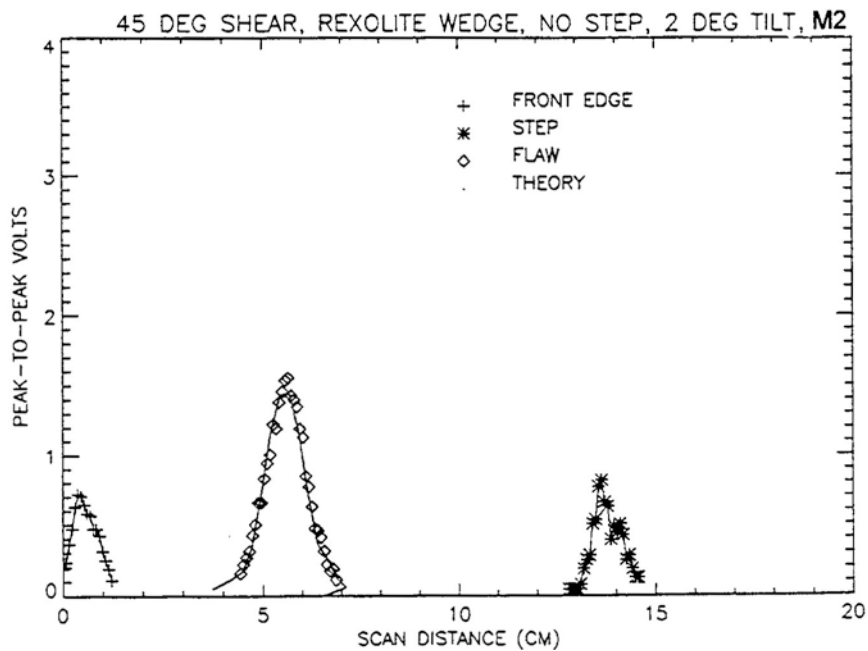


Figure B.11 Comparison of experimental data with theoretical calculations for the no-step case with the transducer wedge tilted by 2°. The Method 2 input parameters were used in the calculation.

Appendix B

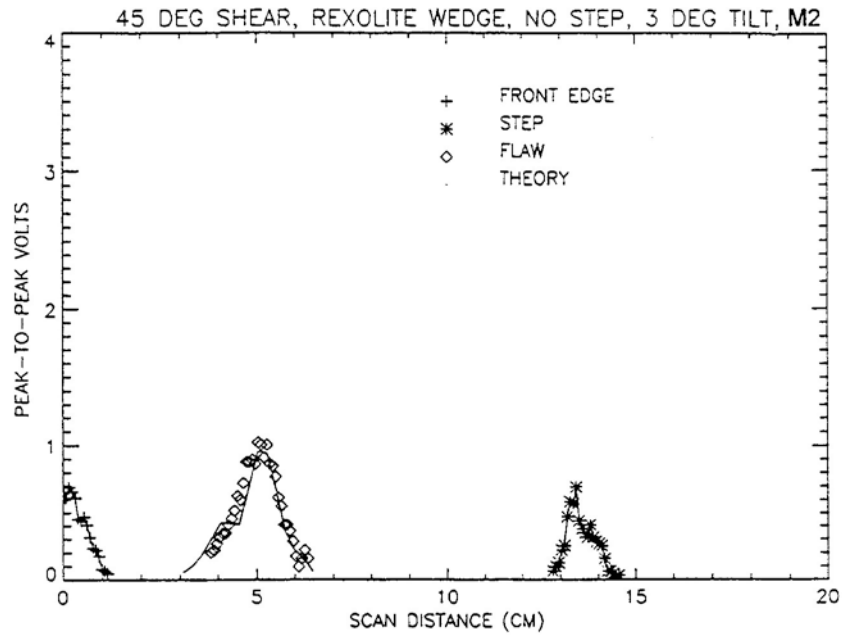


Figure B.12 Comparison of experimental data with theoretical calculations for the no-step case with the transducer wedge tilted by 3°. The Method 2 input parameters were used in the calculation.

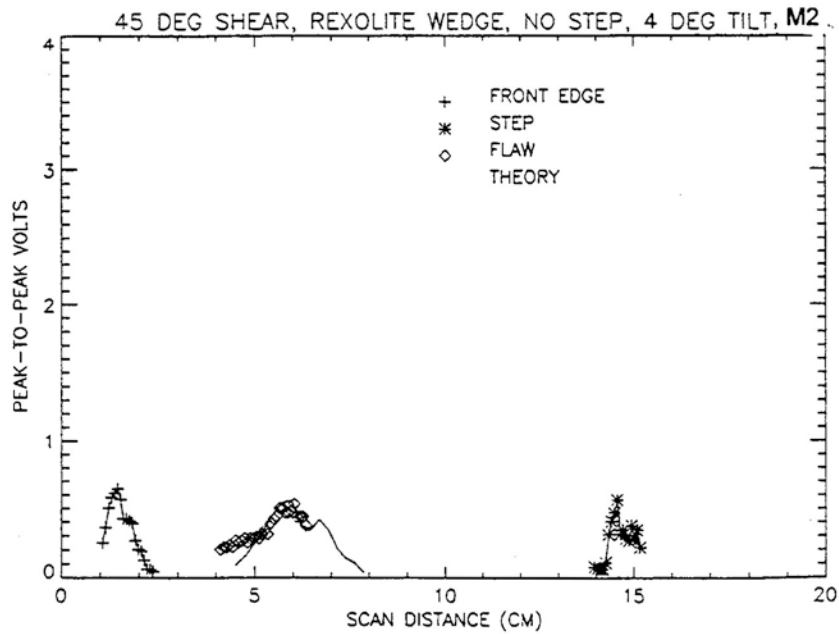


Figure B.13 Comparison of experimental data with theoretical calculations for the transducer wedge tilted by 4° and a step height of 0.152 cm. The Method 2 input parameters were used in the calculation.

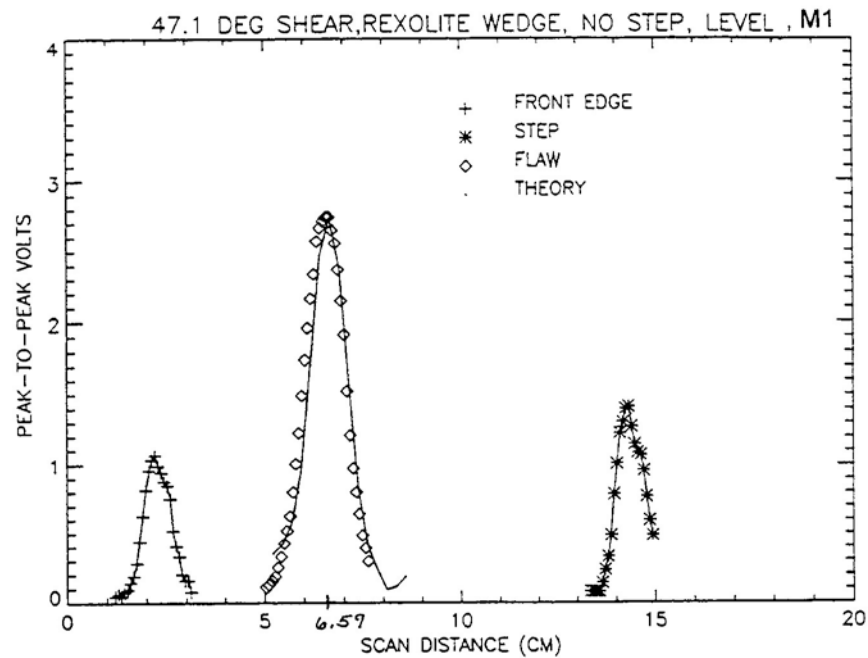


Figure B.14 Comparison of experimental data with theoretical calculations for the level no-step case. Method 1 input parameters were used in the calculation.

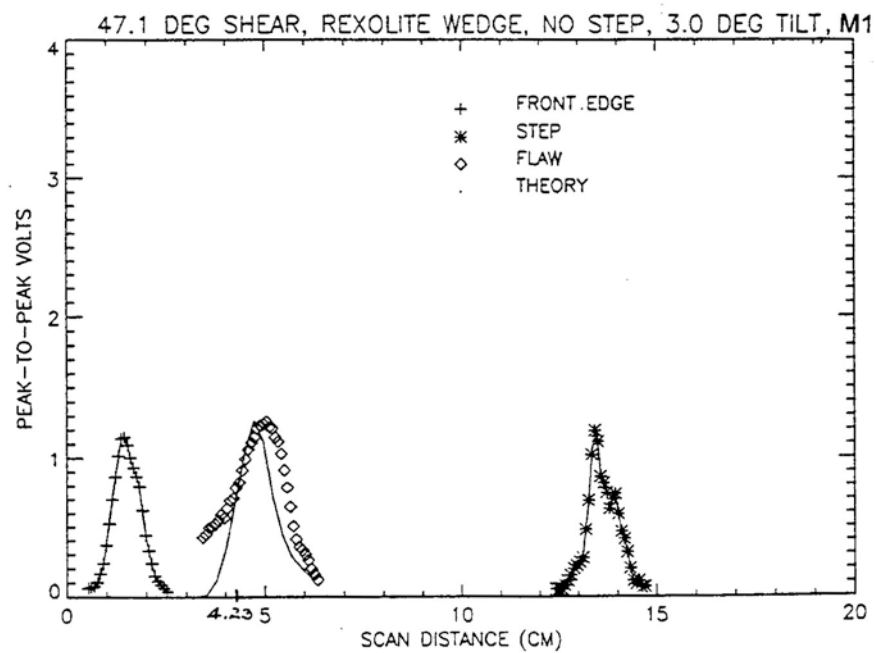


Figure B.15 Comparison of experimental data with theoretical calculations for the no-step case with the transducer wedge tilted by 3°. Method 1 input parameters were used in the calculation.

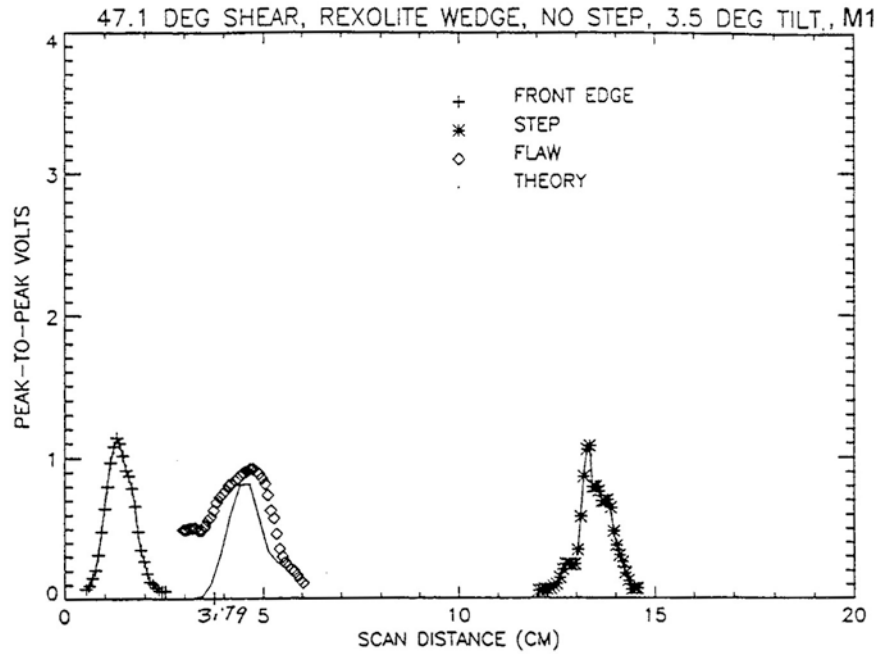


Figure B.16 Comparison of experimental data with theoretical calculations for the no-step case with the transducer wedge tilted by 3.5°. Method 1 input parameters were used in the calculation.

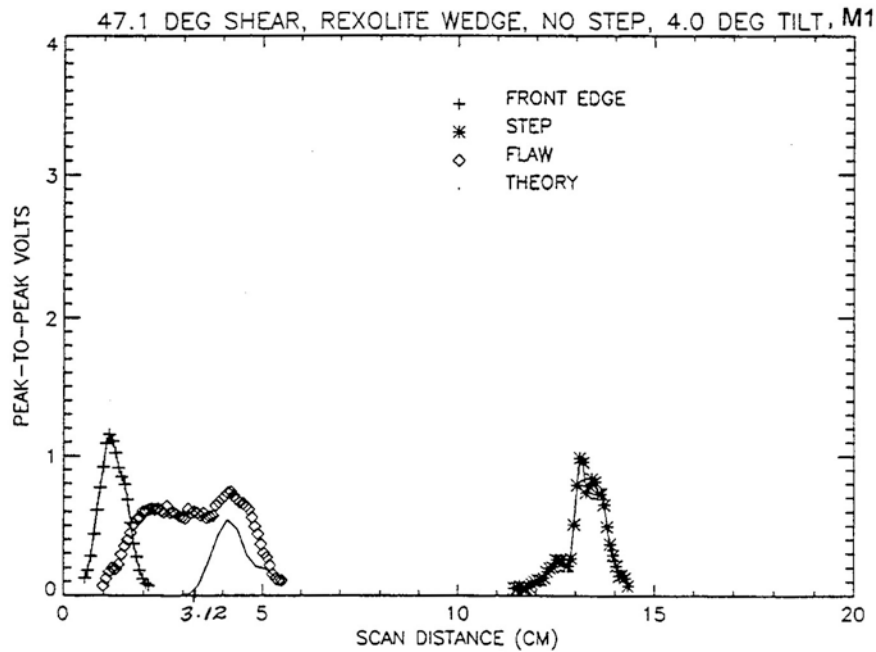


Figure B.17 Comparison of experimental data with theoretical calculations for the no-step case with the transducer wedge tilted by 4°. Method 1 input parameters were used in the calculation.

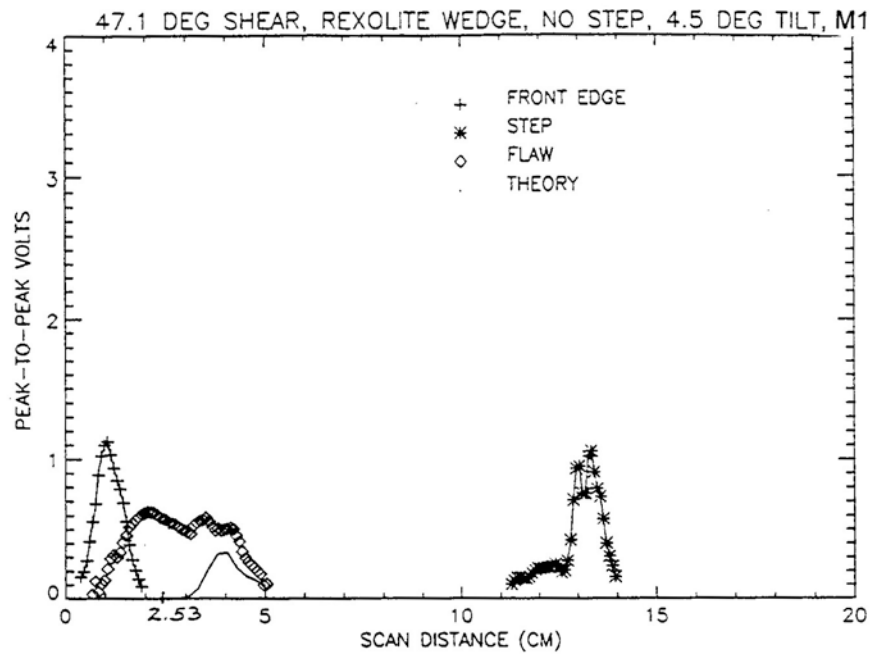


Figure B.18 Comparison of experimental data with theoretical calculations for the no-step case with the transducer wedge tilted by 4.5° . Method 1 input parameters were used in the calculation.

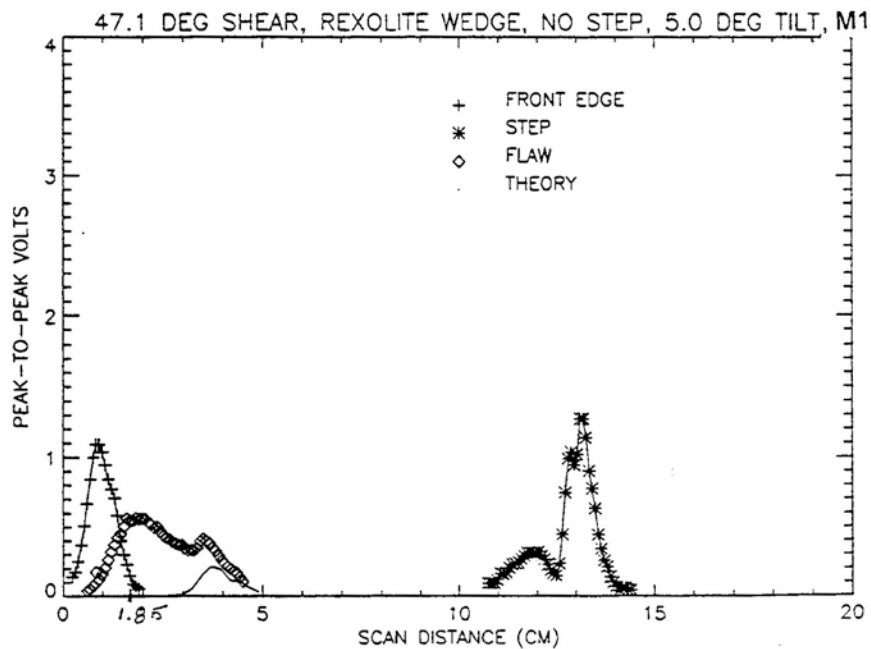


Figure B.19 Comparison of experimental data with theoretical calculations for the no-step case with the transducer wedge tilted by 5° . Method 1 input parameters were used in the calculation.

Table B.4 Summary of the maximum peak-to-peak amplitude for the experimental data in Figures B2.14 through B2.19^(a)

Tilt angle of wedge	No step peak-to-peak voltage
0.0	1.0
3.0	0.48
3.5	0.33
4.0	0.26
4.5	0.19
5.0	0.15

(a) The amplitudes are normalized by dividing each maximum amplitude by the voltage for the no-step level case, 2.7 V.

Figure B.20 shows the connection between the angle in steel and the two positions of the transducer and wedge. The expected peak scan position is given by:

$$\text{Expected peak scan position} = \text{Step scan location} - 4.38 \text{ cm} - 3.11 \tan(\text{ANGST}) \quad (17)$$

where ANGST is the angle in steel that the central ray makes with the normal.

For each tilt angle Table B.5 tabulates the angle Θ_w which is the angle that the central ray makes with the normal in water. Using Snell's law the angle in steel ANGST is determined. Also shown in this table is the step scan

location obtained from the experimental data in Figures B.14 through B.19. Then using Eq. (17) the last column shows the expected peak location in the scan. The expected peak scan location is labeled on the axis of each graph in Figures B.14 through B.19. Table B.5 also shows the scan location for the peak of the theoretical curve. With the exception of the no-step level case, the expected peak location in the scan has a smaller value than is observed experimentally. It is very important to note that the peak location of the experimental data is predicted very well by the theoretical calculations. These results show, that contrary to the commonly held notion, the peak does not necessarily occur when the central ray strikes the base of the flaw.

B.3.4 Experimental Data for Step Heights of 0.229 cm and 0.305 cm

So far the validation experiments for Model III have used only a step height of 0.152 cm. It is very interesting to see what the step height limit might be for the theoretical code. For this reason data were obtained using step height of 0.229 cm (90 mils) and 0.305 cm (120 mils). A steel plate very similar to that shown in Figure B.7 was used and the only difference was that it contained the two larger step heights.

The scans were obtained in a similar manner to the earlier data. Scattering from the step and edges of the plate were used in placing the theoretical curves onto graphs of the experimental data. The plate was oriented so that the ultrasound passed through a smooth top surface in order to obtain a normalization constant. That is, the theoretical

Table B.5 Comparison of expected peak location with that found in the experimental data

Tilt angle	Θ_w	ANGST	Step scan location, cm	Expected peak scan location, cm	Peak location for theoretical curve, cm
0	19.61	47.1	14.33	6.59	6.5
3.0	22.61	57.04	13.41	4.23	4.8
3.5	23.11	58.94	13.34	3.79	4.3
4.0	23.61	60.94	13.11	3.12	4.0
4.5	24.11	63.06	13.03	2.53	3.9
5.0	24.61	65.34	13.00	1.85	3.7

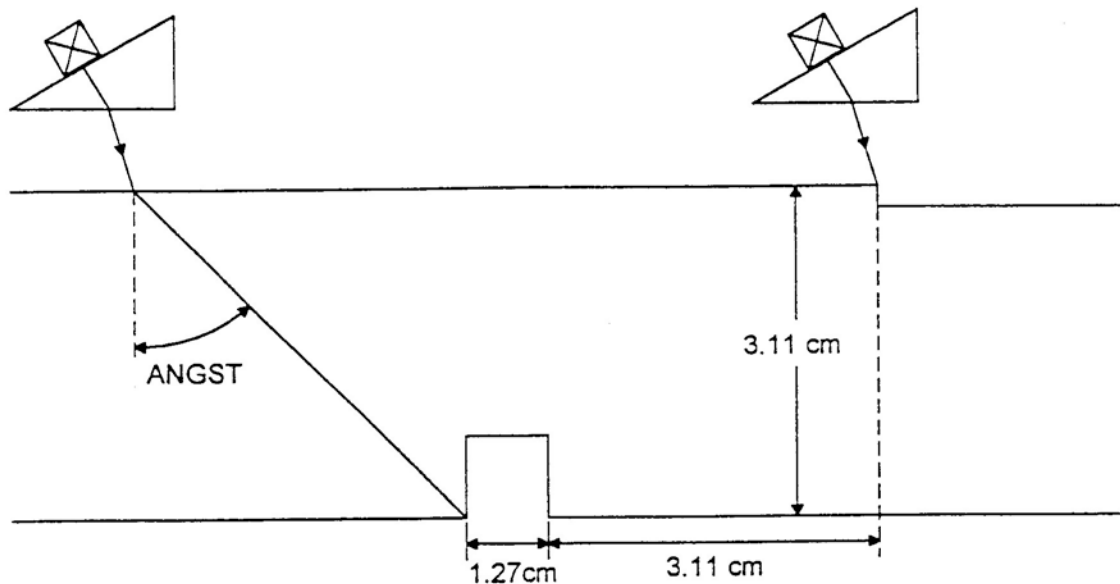


Figure B.20 Diagram to show the connection between the angle of the central in steel and the location of the step in the scan

calculation for this case was carried out and multiplied by the normalization constant so that it fit the experimental data. All of the other calculations shown in Figure B.21 were multiplied by this constant and placed on the graphs of the experimental data.

There is excellent agreement between the experimental data and the theoretical calculations for a step height of 0.229 cm, as shown in the top panel of Figure B.21. However, for a step height of 0.305 cm the comparison in the bottom panel is poor. That is, given the amplitude for the no-step level case, the theory cannot predict the amplitude when ultrasound passes through the 0.305 cm step discontinuity. Therefore, since no other experiments were carried out between a step height of 0.229 cm and 0.305 cm, for time being we shall conclude that the theory cannot be used for a step height greater than 0.229 cm.

The maximum amplitude of the experimental data for both step heights is given in Table B.6. This will be of interest in connection with the ASME Code recommendations. Comparing the normalized amplitudes in Tables B.3 and B.4 for a step height of 0.152 cm with Table B.6, we see that the amplitude varies considerably more for the **smaller** step height of 0.152 cm. This is perhaps an unexpected result.

B.3.5 45° Longitudinal Waves

Experimental data were obtained for 45° longitudinal waves in a manner very similar to that described for 45° shear waves. In this case an acrylic wedge designed to produce 45° longitudinal waves in steel was used and the base of the wedge was about 3 cm above the top surface of a steel plate. Data were obtained using the corner trap (100% through-wall flaw) of a steel plate that was 2.96 cm thick. This signal was much stronger than that from a 0.64 cm-depth flaw used in experiments with 45° shear waves. Since shear waves at 22.8° will also be produced at the same time as 45° longitudinal waves, data for the shear waves were also obtained. Data were not obtained for propagation through a step, since the ability of the code to describe this has already been validated. Data were obtained when the base of the wedge was level and also when the wedge was tilted from 1° through 2° in steps of 0.5°.

Figure B.22 shows the comparison between the experimental data and the theoretical calculations for both longitudinal and shear signals. The experimental data for the longitudinal waves is given by asterisks, and the shear waves, by plus signs. The theoretical calculations were

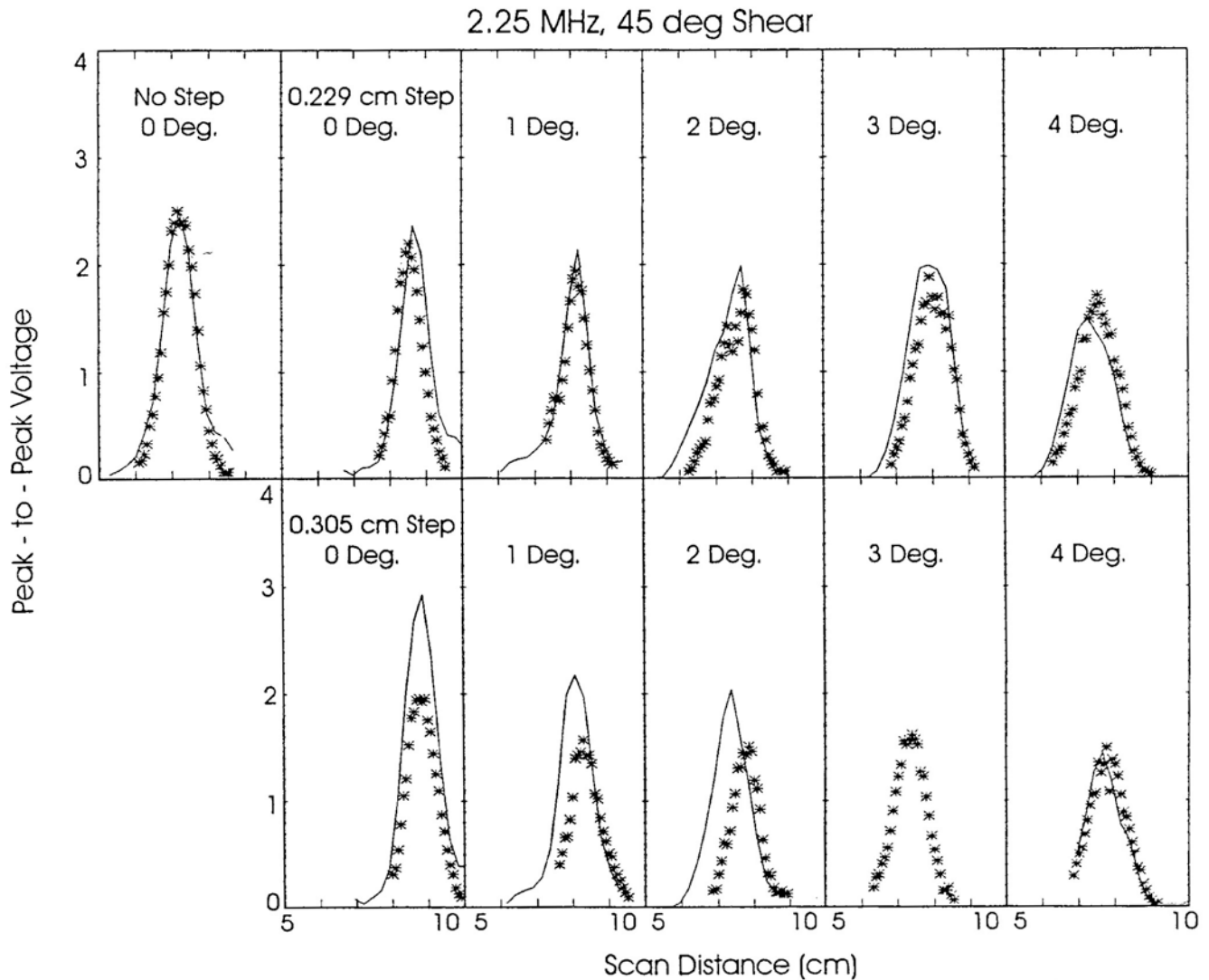


Figure B.21 Comparison of experimental data with theoretical calculations for step heights of 0.229 cm and 0.305 cm

carried out using the code that includes mode conversion at the bottom surface and at the crack. For the level case the theoretical curve was placed upon the experimental data to yield a good fit to the data and the normalization constant was obtained. The normalization constant for the longitudinal waves is 7.725 and that for the shear waves is 3.420. It is not understood why these two normalization constants are so different. The theoretical curves were multiplied by the appropriate normalization constant and placed upon the graphs of the experimental data.

Figure B.22 shows that excellent agreement between theory and experiment result for both longitudinal and shear waves.

It is very interesting to note that, when the wedge is tilted by 2°, the signal due to longitudinal waves is becoming quite broad. Data were not obtained at a larger tilt angle for this reason. Snell's law shows that, when the wedge is tilted by 2°, the angle in steel is 57.5°.

Table B.6 Summary of the peak-to-peak amplitude for the experimental data for the 0.229 cm step and the 0.305 cm step, shown in Figure B.21^(a)

Case	Normalized Amplitude
no step, level	1.00
0.229 cm, level	0.88
0.229 cm, 1°	0.76
0.229 cm, 2°	0.72
0.229 cm, 3°	0.76
0.229 cm, 4°	0.68
0.305 cm, level	0.76
0.305 cm, 1°	0.64
0.305 cm, 2°	0.40
0.305 cm, 3°	0.64
0.305 cm, 4°	0.56

(a) The amplitudes are normalized to the no-step level case by dividing each amplitude by that of the no-step level case, 2.5 volts.

B.3.6 60° Shear Waves

Experiments were carried out using 60° shear waves. The steel plate was 3.11 cm thick with a flaw 0.635 cm in depth and 1.59 cm long. The flaw was located so that when the central ray passed through the top of the step it traveled to the base of the flaw. Data were obtained when the wedge was level, and when it was tilted to 0.5° to 2.0° in 0.5° increments. Data were obtained for a smooth surface and when there was a 0.152 cm step on the surface. As before, the no-step level case was used to obtain the normalization constant and it was then used to place all theoretical curves on the experimental data. The results show poor agreement between the theoretical curves and the experimental data. The theory predicted larger amplitudes than were obtained in the experimental data. These results suggest that the theory is not valid when the angle in steel is about 60° or larger.

B.4 Validation of Model IV

The computer code permits the flaw to be at an angle other than 90°. The experiments for such angles were very similar to those already described. Through-wall flaws were obtained by machining the ends of the steel blocks (3.11 cm thick) at angles of 90°, 89°, 87°, 85°, 83°, 81°, and 79°. Turning a block upside-down yields the complementary angles of 91°, 93°, 95°, etc. The rexolite wedge was designed to produce 45° shear waves in steel and the frequency is 2.25 MHz. The angle in steel was determined to be 43.7°, which indicates that the wedge was not precisely level. The base of the wedge was 0.9 cm above the plate.

Figure B.23 shows the comparison of the theoretical calculations with the experimental data. All of the data is for a smooth top surface. The code was used that included reflection from the bottom surface and takes into account mode conversion at the flaw surface. The theoretical curves were normalized to the data in the way described previously.

Some observations about the comparison between theory and experiment are as follows:

- (1) Agreement is better for angles less than 90° than for those greater than 90°.
- (2) It was surprising that the theoretical maximum amplitude for 89° is about 10% greater than that for 90°. The experimental data shows that the amplitudes are about the same.
- (3) It was surprising that the theoretical maximum amplitude for 9° is 14% smaller than that at 90°.
- (4) At 95° the theoretical maximum amplitude is only about 60% of the experimental value.
- (5) At 97° the theoretical maximum amplitude is less than half that of the experimental data. Similar statements can be made for 99° and 101°.

The through-wall flaw perhaps represents an extreme case for the model. An analogy can be made between transducers and flaw sizes. Consider two transducers of the

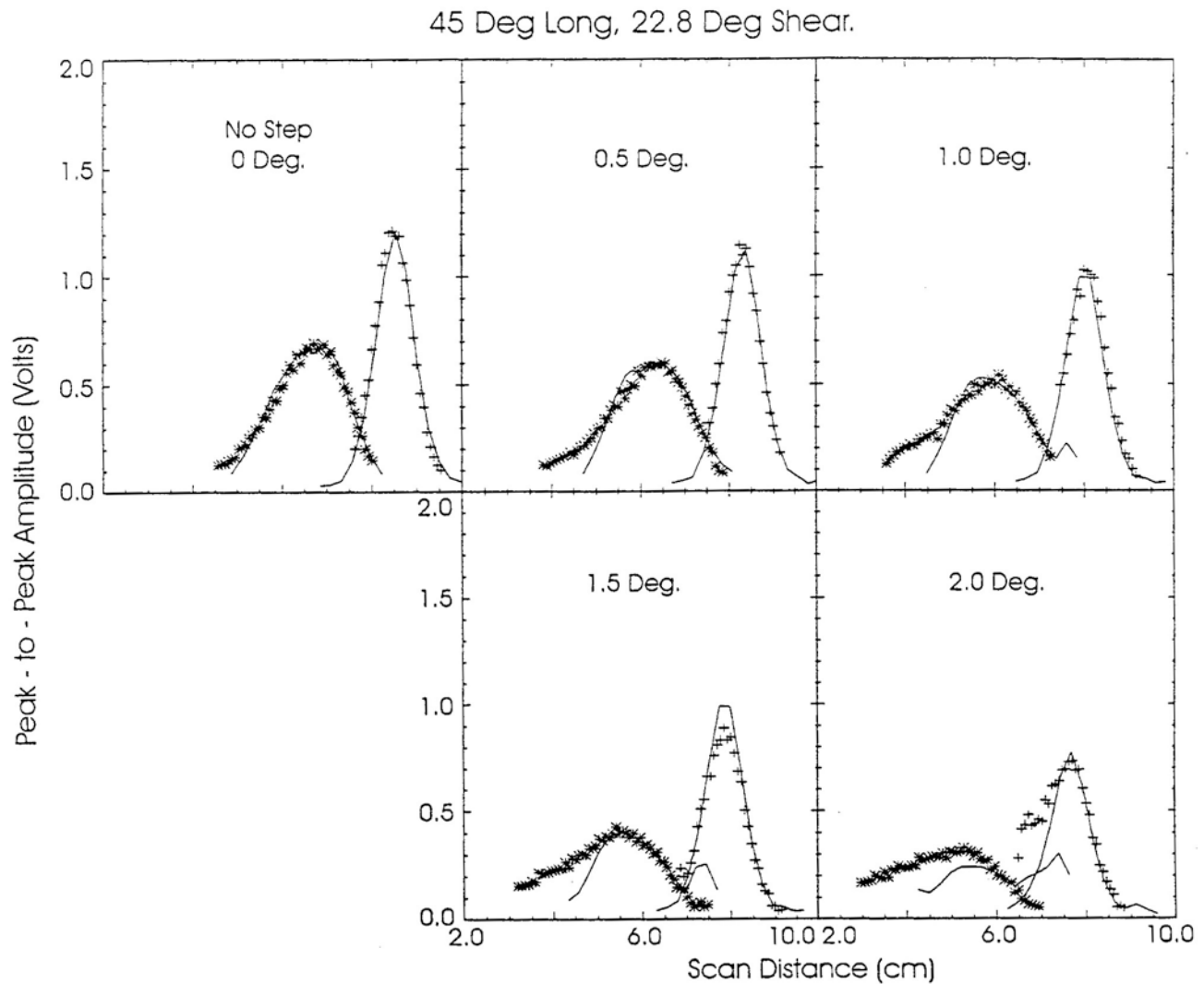


Figure B.22 Experimental data for 45° longitudinal waves and 22.8° shear waves. The solid lines show the corresponding theoretical calculations.

same frequency having diameters of 0.64 cm and 2.54 cm. There will be much more beam divergence for the smaller diameter transducer than for the larger one. A similar statement can be made for flaws. A small flaw will show much more beam divergence than a large flaw. For a through-wall flaw this means that the amplitude will drop off rapidly as the angle departs from 90°, since they are not corner traps. It would be very interesting to compare experimental data for a small flaw depth with theoretical calculations and see if better agreement results in a less extreme case. Such experiments have not been carried out.

Based upon the limited set of experimental data, the conclusion is that the code can successfully predict the results of an in-service inspection when the flaw angle is 90° or less, but not for angles greater than 90°.

B.5 Conclusion

The results of the validation studies show that Model III is validated for 45° shear waves in steel when the transducer wedge is tilted up to 5°. The experimental data were

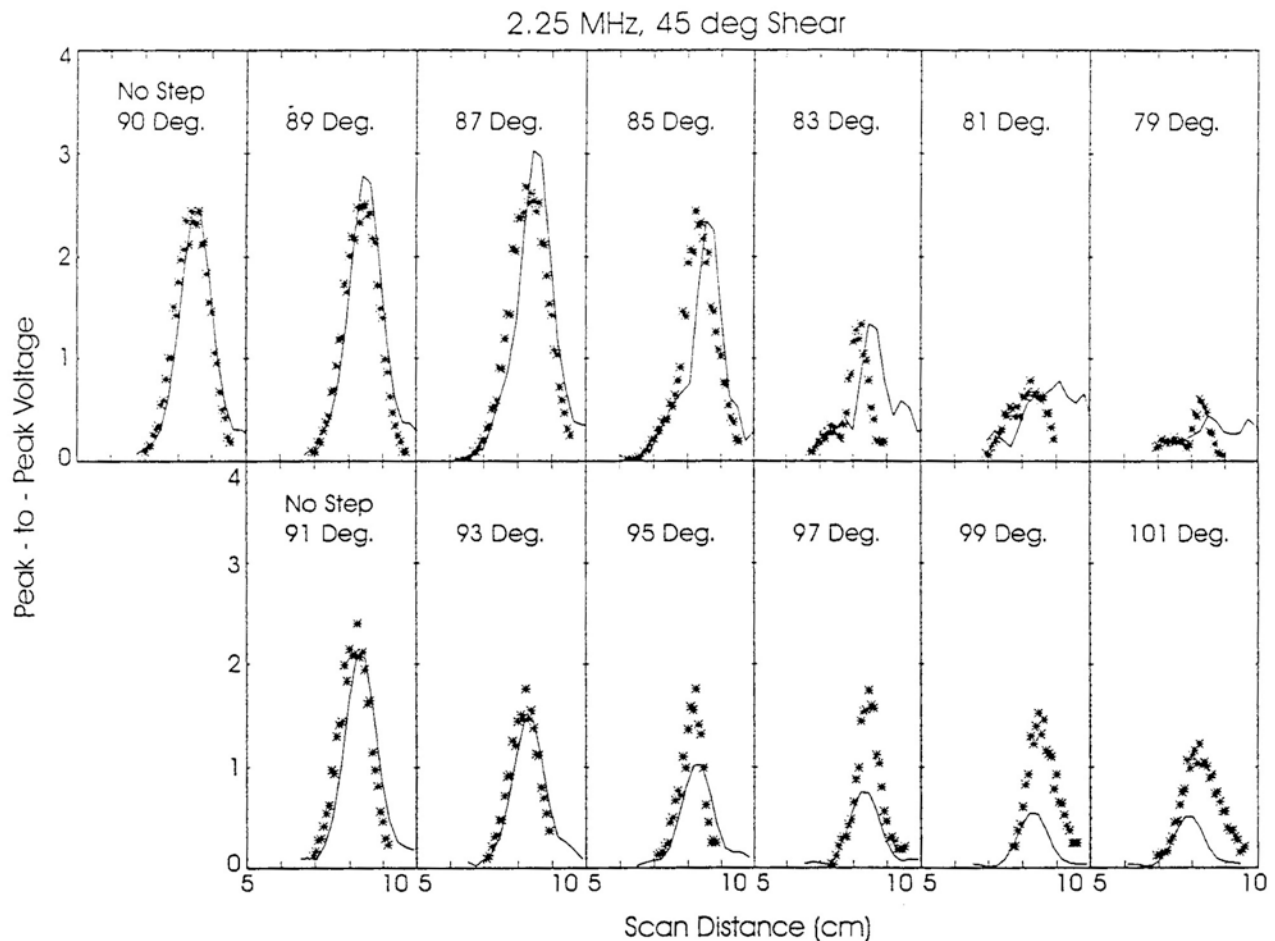


Figure B.23 Comparison of experimental data with theoretical calculations for 45° shear waves striking flaws at an angle. The frequency is 2.25 MHz.

compared with theoretical calculations using both Method 1 and Method 2 input parameters and both input methods gave very good agreement to the data. In the validation studies the ultrasonic waves travel quite close to the top of the step in order to reach the flaw located on the bottom surface. However, in the calculation described in Chapter 3 "Modeling an Ultrasonic Inservice Inspection" the ultrasonic waves can be farther away from the top of the step. In this case, Method 2 must be used for accurate calculations. The reason is that the ray tracing will be more accurate for shorter distances between the transmitted plane and the top surface. (See Figure B.6). Step heights of 0.229 cm and 0.305 cm were investigated using 45° shear waves. The data show very good

agreement for a step height of 0.229 cm and poor agreement for 0.305 cm. Thus, the theory can be used in engineering studies as long as the step height is 0.229 cm or less.

Experiments were carried out in which 45° longitudinal waves were produced in steel. Very good agreement resulted when the wedge was tilted by 2° or less. However, at 2° the experimental data showed a very broad peak, while the theoretical calculations did not show quite as broad a peak. The result is that the transducer wedge cannot be tilted by more than 2° to obtain good data when using 45° longitudinal waves in steel.

Appendix B

Experiments were carried out using 60° shear waves but the theory could not predict the magnitude of the experimental data. Thus, the theoretical models are not validated for 60° shear waves.

Experimental data were obtained using 45° shear waves in steel and the flaw was at angles ranging from 79° to 101° . The conclusion is that Model IV is valid when the flaw angle is 90° or less, but not for angles larger than 90° .

BIBLIOGRAPHIC DATA SHEET

(See instructions on the reverse)

1. REPORT NUMBER
(Assigned by NRC, Add Vol., Supp., Rev.,
and Addendum Numbers, If any.)

NUREG/CR-6589
PNNL-11751

2. TITLE AND SUBTITLE

The Effects of Surface Condition on an Ultrasonic Inspection:
Engineering Studies Using Validated Computer Model

3. DATE REPORT PUBLISHED

MONTH	YEAR
April	1998

4. FIN OR GRANT NUMBER

B2289 and W6275

5. AUTHOR(S)

M. S. Greenwood

6. TYPE OF REPORT

Technical

7. PERIOD COVERED *(Inclusive Dates)*

8. PERFORMING ORGANIZATION - NAME AND ADDRESS *(If NRC, provide Division, Office or Region, U.S. Nuclear Regulatory Commission, and mailing address; if contractor, provide name and mailing address.)*

Pacific Northwest National Laboratory
Richland, WA 99352

9. SPONSORING ORGANIZATION - NAME AND ADDRESS *(If NRC, type "Same as above"; if contractor, provide NRC Division, Office or Region, U.S. Nuclear Regulatory Commission, and mailing address.)*

Division of Engineering Technology
Office of Nuclear Regulatory Research
U.S. Nuclear Regulatory Commission
Washington, DC 20555-0001

10. SUPPLEMENTARY NOTES

D. A. Jackson, NRC Project Manager

11. ABSTRACT *(200 words or less)*

This report documents work performed at Pacific Northwest National Laboratory (PNNL) on the effects of surface roughness on the reliability of an ultrasonic inservice inspection. The primary objective of this research is to develop ASME Code recommendations in order to limit the adverse effects of a rough surface and thereby increase the reliability of ultrasonic inservice inspections. In order to achieve this objective, engineering studies were conducted that included experimental validation of computer codes, developed at the Center for Nondestructive Evaluation (CNDE) at Iowa State University as a result of a cooperative effort between the Electric Power Research Institute (EPRI) and the Nuclear Regulatory Commission. The basic problem associated with a rough surface in an inservice inspection is that as the transducer rotates slightly to accommodate the rough surface, the beam direction in the metal changes and the time-of-flight of the echo changes as well. One problem is the excessive weld crown, where weld material protrudes above the adjoining surfaces. In this research this condition is modeled by considering a step discontinuity on the top surface. CNDE developed several models of increasing complexity in order to model an inservice inspection. This report describes the validation of four computer codes. These codes were used to mimic an inservice inspection in order to understand effects associated with rotation of the transducer as it traverses a step discontinuity. Studies resulted in ASME Section XI Code recommendations.

12. KEY WORDS/DESCRIPTORS *(List words or phrases that will assist researchers in locating the report.)*

ultrasonic testing, ultrasonic modeling, inservice inspection, nondestructive testing, nondestructive examination, nondestructive evaluation

13. AVAILABILITY STATEMENT

unlimited

14. SECURITY CLASSIFICATION

(This Page)

unclassified

(This Report)

unclassified

15. NUMBER OF PAGES

16. PRICE



Federal Recycling Program